Dissertation

submitted to the

Combined Faculty of Mathematics, Engineering and Natural Sciences

of Heidelberg University, Germany

for the degree of

Doctor of Natural Sciences

Put forward by

Ahmed Elghandour Shetiwy

born in Dakahliya, Egypt

Oral examination: December 06, 2023

Thermodynamic and Magnetic Studies on Correlated Electron Systems with Competing Interactions

Referees: Prof. Dr. Rüdiger Klingeler

Prof. Dr. Maurits W. Haverkort

Thermodynamic and Magnetic Studies on Correlated Electron Systems with Competing Interactions

In this work the ground states and thermodynamic properties of selected materials with competing magnetic interactions are investigated mainly by heat capacity and magnetization studies down to low temperatures and in high magnetic fields. Due to replacement of Mn^{2+} by Ni^{2+}, competing magnetic anisotropies and mixed spins in $Ni_{0.25}Mn_{0.75}TiO_3$ yield a suppression of long-range magnetic order as compared to its undoped parent compound and a spin-reoriented low-temperatures phase appears. While short-ranged magnetic order persists up to about $4 \times T_N$, glass-like behavior, a quasi-linear temperature dependence of the specific heat and the presence of weakly-coupled moments highlight the unusual ground state and its thermal excitations. Geometric frustration is studied in the example of the disordered pyrochlore structure $Ho_2Zr_2O_7$ and is evidenced by the absence of long-range magnetic order at least down to $T = 280$ mK. The analysis of residual entropy excludes a spin ice state in $Ho_2Zr_2O_7$. Instead, it exhibits a disordered ground state with short-ranged antiferromagnetic correlations and a spin-frozen state below $T = 0.6$ K is found. Magnetic frustration is also relevant in the hexagonal systems Nd_3BWO_9 and Pr_3BWO_9 in which the rare earth ions form a distorted Kagomé lattice. Again, no long-range magnetic order appears in Pr_3BWO_9 at least down to $T = 90$ mK while Nd_3BWO_9 orders antiferromagnetically at $T_N = 0.3$ K. In the former, specific heat shows a Schottky anomaly at $T = 5.7(4)$ K. Magnetic entropy changes in both systems suggest an effective $J_{\text{eff}} = 1/2$ orbital ground state. While Nd_3BWO_9 exhibits field-induced spin freezing at $T^* = 4.3$ K as shown by AC-susceptibility data, Pr_3BWO_9 does not show such field-induced anomalies. A narrow $\frac{1}{3}$-magnetization plateau is observed in Nd_3BWO_9 at ~ 0.8 T whereas in Pr_3BWO_9, the magnetization increases monotonically with increasing the field with no signs of plateaus. In both systems, the theoretical saturation magnetization is not reached even in high-magnetic fields of $B = 58$ T and no further magnetization plateaus appear in the high field regime.

Thermodynamische und magnetische Untersuchungen an Korrelierte Elektronensysteme mit konkurrierenden Wechselwirkungen

In der vorliegenden Arbeit werden die Grundzustände und thermodynamischen Eigenschaften ausgewählter Materialien mit konkurrierenden magnetischen Wechselwirkungen vor allem mittels Messungen der Wärmekapazität und der statischen und dynamischen Magnetisierung bei tiefen Temperaturen und in hohen Magnetfeldern untersucht. Durch die Substitution von Mn^{2+} durch Ni^{2+} ergeben sich in $Ni_{0.25}Mn_{0.75}TiO_3$ konkurrierende magnetische Anisotropien und gemischte Spins, was zur Unterdrückung der langreichweitigen magnetischen Ordnung im Vergleich zur undotierten Ausgangsverbindung und der Bildung einer Spin-reorientierten Niedrigtemperaturphase führt. Während kurzreichweitige magnetische Ordnung bis etwa $4 \times T_N$ beobachtet wird, zeigen glasartiges Verhalten, eine quasi-lineare Temperaturabhängigkeit der spezifischen Wärme und das Vorhandensein schwach gekoppelter Momente bei tiefen Temperaturen Besonderheiten des Grundzustandes und der thermischen Anregungen. Geometrische Frustration wird am Beispiel der ungeordneten Pyrochlorstruktur $Ho_2Zr_2O_7$ untersucht und zeigt sich u.a. durch die Abwesenheit von langreichweitiger magnetischer Ordnung bis mindestens $T = 280$ mK. Die ermittelte residuelle Entropie schließt einen Spin-Eis-Grundzustand in $Ho_2Zr_2O_7$ aus. Stattdessen zeigt das System einen ungeordneten Grundzustand mit kurzreichweitigen antiferromagnetischen Korrelationen, und einen spin-gefrorenen Zustand unterhalb von $T = 0.6$ K. Magnetische Frustration ist auch in den hexagonalen Systemen Nd_3BWO_9 und Pr_3BWO_9 relevant, in denen die Seltenerd-Ionen ein verzerrtes Kagomé-Gitter bilden. Auch Pr_3BWO_9 zeigt zumindest bis $T = 90$ mK keine langreichweitige magnetische Ordnung, während Nd_3BWO_9 bei $T_N = 0.3$ K antiferromagnetisch ordnet. In Pr_3BWO_9 zeigt die spezifische Wärme eine Schottky-Anomalie bei ca. 6 K. In beiden Systemen weisen die magnetischen Entropieänderungen auf einen effektiven orbitalen $J_{eff} = 1/2$ Grundzustand hin. Externe Magnetfelder führen in Nd_3BWO_9 zum Einfrieren der Spins unterhalb von $T^* = 4.3$ K wohingegen Pr_3BWO_9 keine entsprechenden feldinduzierten Anomalien in der AC Suszeptibilität aufweist. In Nd_3BWO_9 wird ein schmales $\frac{1}{3}$-Magnetisierungsplateau bei ~ 0.8 T beobachtet, während in Pr_3BWO_9 die Magnetisierung mit steigendem Feld monoton und ohne Anzeichen von Plateaus ansteigt. In beiden Systemen wird die theoretische Sättigungsmagnetisierung auch bei hohen Magnetfeldern von $B = 58$ T nicht erreicht und es treten keine weiteren Magnetisierungsplateaus auf.

Contents

Chapter 1

Introduction

The contemporary uses of magnetic materials as vital components in various technological devices, including MRI machines, electric vehicle motors, information storage, and magnetic sensors, just to name a few, exemplify the fruits of ongoing experimental and theoretical research efforts aimed at understanding the magnetic phases of matter on the microscopic level. In 1895, Pierre Curie suggested that permanent magnets naturally goes into a ferromagnetic state when they cooled below a critical temperature [1]. A decade later, Pierre Weiss proposed that magnetic moments within a substance experience a huge internal field created by the remaining moments in the system, aligning the individual moments [2]. The Curie-Weiss work paved the way for studying microscopic magnetism, especially following the discovery of the electron's spin angular momentum in the Stern-Gerlach experiment [3] and the development of quantum mechanics. While Weiss' field is not a physical reality, it served as a useful approximation to describe the interatomic Coulomb interaction. Heisenberg utilized this in the formalism of his Hamiltonian for ferromagnetic exchange, which results in a ferromagnetic order in three dimensions [4]. Néel extended the concept of ordered spin states in ferromagnets (FMs) to include antiferromagnets (AFMs) [5, 6]. Anderson developed the theory of antiferromagnetism by introducing the concept of Superexchange interactions [7]. Antiferromagnet research saw a notable rise when Bednorz and Müller grew an insulating antiferromagnet called lanthanum barium copper oxide, doped it to draw between 6% and 22% of the electrons out of the planes, and it became a superconductor [8]. The work at hand is also concerned with insulating antiferromagnets, though not superconductors. Instead, it explores the exotic properties of materials, such as spin ice, classical and quantum spin liquids, driven by competing interactions in antiferromagnets. Specifically, this work is dedicated to investigating the magnetic ground states of spin systems characterized by competing interactions.

These competitions can exhibit varying degrees of influence, ranging from relatively mild effects that marginally shift the onset of long-range magnetic (Néel temperature) order by a few Kelvin degrees, to considerably stronger influences that suppress ordering down to millikelvin temperatures or even result in unconventional, ground states. The primary experimental approach chosen for studying the magnetic ground state of these systems involved measuring heat capacity within a temperature range of 50 mK to 300 K and applying magnetic fields of up to 14 T. Heat capacity measurements are backed up by magnetization studies in static, dynamic, and pulsed-fields.

One might question the significance of measuring specific heat at low temperatures and wonder why it matters. Heat capacity C of a system represents the rate at which its entropy S changes with temperature, scaled by temperature ($C = T\frac{dS}{dT}$). Entropy is connected to the system's excited energy states through the partition function, which means that heat capacity is influenced by the sum of energy states within the system. Consequently, the heat capacity is not sensitive to individual energy states unless only one specific state is excited when heat (energy) is added. In any given material, multiple modes of excitations exist. For instance, in a ferromagnetic metal, the electrons and the lattice vibrations (phonons) exhibit different temperature dependencies in their specific heats. The electronic system's specific heat changes with temperature linearly ($C \propto T$), while the lattice system's specific heat, at T, changes with the cube of temperature ($C \propto T^3$). Furthermore, for the metal ferromagnetic properties, a portion of the overall specific heat arises from quantized spin waves (magnons), which have a temperature dependence of $C \propto T^{3/2}$. If the metal is antiferromagnetic, the temperature dependence of magnons would resemble that of the phonons, following $C \propto T^3$.

This dissertation is structured as follows: *Chapter 1* titled "Introduction" compromises the opening and the general remarks about the work. *Chapter 2* titled "Theoretical Background" focuses on the essential concepts for studying magnetic materials with competing interactions. It emphasizes how different modes of excitations in a substance appear in the heat capacity theory. *Chapter 3* titled "Experimental methods" introduces the basic principles behind the experimental tools used in this work, with a special emphasis on heat capacity technique. *Chapter 4* titled "Magnetic anisotropy, magnetoelastic coupling, and the magnetic phase diagram of $Ni_{0.25}Mn_{0.75}TiO_3$" presents experimental results on the mixed spin antiferromagnet, $Ni_{0.25}Mn_{0.75}TiO_3$. The specific heat capacity, thermal expansion, magnetostriction, and magnetization measurements (DC, AC, and pulsed field, up to 50 T) were employed to address the questions: what is the magnetic ground state of $Ni_{0.25}Mn_{0.75}TiO_3$ given the antiferromagnetic nature of parent compounds $MnTiO_3$, and $NiTiO_3$ with easy magnetic axes parallel to c and easy-plane-like anisotropy perpendicu-

lar to the c axis, respectively. What is the impact of 25% $NiTiO_3$ doping on the ordering temperature of $MnTiO_3$, $T_N = 64$ K. How is the magnetic entropy consumed in the doped version compared to the pure one? Thermal expansion reveals magnetoelastic coupling in the system. Lastly, an anisotropic magnetic phase diagram for $Ni_{0.25}Mn_{0.75}TiO_3$ is constructed. *Chapter 5* titled "Spin freezing and slow spin dynamics in $Ho_2Zr_2O_7$" presents experimental results on the geometrically frustrated magnet, $Ho_2Zr_2O_7$. The system adopts the defected-fluorite structure, which makes it a platform to investigate the spin ice state. Heat capacity and DC magnetization measurements were utilized to study the magnetic ground state of the system at low temperatures down to 280 mK. Further, AC magnetization was used to investigate the system's spin dynamics. *Chapter 6* titled "Low-temperature magnetization and heat capacity of RE_3BWO_9; RE = Nd and Pr" presents experimental results on Nd_3BWO_9, and Pr_3BWO_9, distorted kagomé systems. These systems represent a platform to realize new spin-liquid state, avoiding the drawbacks found in 3d-transition metal-based kagomé systems. The ground state of Nd_3BWO_9, and Pr_3BWO_9 were studied by the specific heat capacity, and magnetization measurements (DC, AC, and pulsed field, up to 60 T). *Chapter 6* titled "Summary" is the final chapter, which concludes this work by summarizing the discussed topics of this dissertation.

Chapter 2

Theoretical Background

The material covered in sections from 2.1 to 2.5 is primarily derived from "Magnetism in Condensed Matter" by Blundell [9] and "Magnetism and Magnetic Materials" by Coey [10]. Additionally, Simon's book [11] has been revisited for insights.

Section 2.6 draws mainly from "Introduction to Frustrated Magnetism" [12], specifically focus chapters 1 and 6. In addition to this, it incorporates insights from Ramirez's Annual Review on Frustrated Magnetism [13], as well as relevant content from Blundell [9].

Lastly, section 2.7 predominantly relies on the content presented in the book "The Specific Heat of Matter at Low Temperatures" by Tari [14]. It also incorporates insights from books by Pobell [15] and Gopal [16].

2.1 Single-Atom Hamiltonian

The Hamiltonian $\mathcal{H}$ of N electrons localized to a nucleus is given by:

$$\mathcal{H} = \sum_{i=1}^{N} \left(\frac{p_i^2}{2m_e} - \frac{Ze^2}{r_i} + \sum_{j=1, j\neq i}^{N} \frac{e^2}{2|r_i - r_j|} \right), \tag{2.1}$$

where the first and second terms are the kinetic and potential energy of a single electron, respectively. The third term represents the mutual interactions between two electrons. p_i and r_i, r_j are the momentum operator and distance from the nucleus for the i^{th} or j^{th} electron, respectively. m_e and Z are the electron's mass and the atomic number, respectively. This description is built on the assumption that the nucleus spin has much smaller magnetic moments than the electron's spin as the mass of the proton ($\approx 1.67 \times 10^{-27}$ kg) is roughly four orders of magnitude larger than that of the electron. Consequently, electrons

are the main source of magnetic moments in solids and the nuclear magnetism can often be neglected. In the mean-field approximation, the electron at site i^{th} is subjected to an effective electrostatic potential, $V_i(r_i)$, resulting from the left electrons. Therefore, the Hamiltonian $\mathcal{H}$ in 2.1 can be simplified to:

$$\mathcal{H} = \sum_{i=1}^{N} (\frac{p_i^2}{2m_e} - \frac{Ze^2}{r_i} + V_i(r_i)) \tag{2.2}$$

The eigenfunction ψ of the simplified Hamiltonian is given by:

$$\psi_{n,l,m_l,m_s}(r,\theta,\phi) = R_{n,l}(r) Y_l^{m_l}(\theta,\phi)\chi(m_s), \tag{2.3}$$

where $R_{n,l}(r)$, $Y_l^{m_l}(\theta,\phi)$, $\chi(m_s)$ are the radial, angular, and spin parts, respectively. Further, $n = 1, 2, ...$ is the principal quantum number and it reflects the main energy levels occupied by the electron, $l = 0, 1, ..., n-1$ for a given n is the angular momentum quantum number and it describes the general shape or region an electron occupies. The magnetic quantum number m_l takes values $-l$ to $+l$ i.e., $m_l = 2l + 1$, and it describes the orbital orientation in space. Finally, the spin quantum number $m_s = \pm s$ describes the electron spin.

2.2 An Atom in a Magnetic Field

The magnetic moments in solids are associated with electrons. The microscopic theory of magnetism is based on the quantum mechanics of electronic angular momentum, which has two distinct sources – orbital motion and spin. The Hamiltonian of an atom consists of N electrons in a magnetic field is given by:

$$\mathcal{H} = \sum_{i=1}^{N} ((\vec{P}_i + e\vec{A}(\vec{r}_i))^2/2m_e + V(i)) + g\mu_B \vec{B} \cdot \vec{S}, \tag{2.4}$$

where $\vec{r}_i$ is the position of the i^{th} electron in the atom, $\vec{P}_i$ its momentum, $\vec{A}$ is the magnetic vector potential. The first and the second terms represent the electron's kinetic and potential energy, respectively. The third term is the Zeeman energy of the electronic spin. Expanding Eq. 2.4 gives:

$$\mathcal{H} = \sum_{i=1}^{N} (\frac{\vec{P}_i^2}{2m_e} + V(i) + \frac{e}{2m_e}(\vec{P}_i \cdot \vec{A} + \vec{A} \cdot \vec{P}_i) + \frac{e^2}{2m_e}\vec{A}^2(\vec{r}_i)) + g\mu_B \vec{B} \cdot \vec{S}, \tag{2.5}$$

Using the gauges $\vec{A} = \frac{1}{2}\vec{B} \times \vec{r}$, $\vec{B} = \vec{\nabla} \times \vec{A}$, and knowing that the vectors $\vec{P}_i$ and $\vec{A}$ commute, the third term in Eq. 2.5 can be rewritten as:

$$\frac{e}{2m_e}(2\vec{A} \cdot \vec{P}_i) = \frac{e}{2m_e}(2\frac{1}{2}\vec{B} \times \vec{r}) \cdot \vec{P}_i \tag{2.6}$$

$$= \frac{e}{2m_e}\vec{B} \cdot (\vec{r} \times \vec{P}_i) \tag{2.7}$$

$$= \frac{e}{2m_e}\vec{B} \cdot \vec{L} \tag{2.8}$$

$$= \mu_B \vec{B} \cdot \vec{L} \tag{2.9}$$

Now, inserting $\mu_B \vec{B} \cdot \vec{L}$ into Eq. 2.4 and rearranging gives:

$$\mathcal{H} = \sum_{i=1}^{N}(\frac{\vec{P}_i^2}{2m_e} + V(i)) + \mu_B \vec{B} \cdot (\vec{L} + g\vec{S}) + \frac{e^2}{2m_e}\sum_{i=1}^{N}(\vec{A}^2(\vec{r}_i)) \tag{2.10}$$

$$= \mathcal{H}_0 + \mu_B \vec{B} \cdot (\vec{L} + g\vec{S}) + \frac{e^2}{8m_e}\sum_{i=1}^{N}(\vec{B} \times \vec{r}_i)^2 \tag{2.11}$$

The first term $\mathcal{H}_0$ represents the unperturbed Hamiltonian, the second and the third terms correspond to the paramagnetic and diamagnetic moments, respectively. Note, the paramagnetic term is linear in $\vec{B}$, whereas the diamagnetic term is quadratic in $\vec{B}$.

2.3 The Brillouin Function

The Brillouin function is primarily used to estimate the magnetization (M) of an ideal paramagnet, showing how it depends on both the applied magnetic field (B) and the total angular momentum quantum number (J). To derive the Brillouin function, assume an applied magnetic field $\mathbf{B}$ along z direction. The z-component of angular momentum (m_J) can take any of the $2J + 1$ possible values from $-J$ to J. These values correspond to different energies, induced by the external field $\mathbf{B}$, which can be expressed as:

$$E = -m_J g_J \mu_B B, \tag{2.12}$$

where g is the g-factor, μ_B is the Bohr magneton; an illustrative example of this relation is shown in Fig. 2.1. The thermodynamic average of $\langle m_J \rangle$ is given by:

$$\langle m_J \rangle = \frac{\sum_{-J}^{J} m_J e^{\frac{m_J g_J \mu_B B}{k_B T}}}{\sum_{-J}^{J} e^{\frac{m_J g_J \mu_B B}{k_B T}}} \tag{2.13}$$

$$= \frac{\sum_{-J}^{J} m_J e^{m_J x}}{\sum_{-J}^{J} e^{m_J x}} \tag{2.14}$$

$$= \frac{1}{Z}\frac{\partial Z}{\partial x}, \tag{2.15}$$

where $x = \frac{m_J g_J \mu_B B}{k_B T}$ is a dimensional less ratio of Zeeman energy to the thermal energy, and the normalization factor $Z = \sum_{-J}^{J} e^{\frac{m_J g_J \mu_B B}{k_B T}}$ is the partition function [1]. In case of a material with n magnetic moments per unit volume, the magnetization M can be expressed as:

$$M = n g_J \mu_B \langle m_J \rangle \tag{2.16}$$

$$= \frac{n g_J \mu_B}{Z}\frac{\partial Z}{\partial B}\frac{\partial B}{\partial x} \tag{2.17}$$

$$= n k_B T \frac{\partial ln Z}{\partial B}, \tag{2.18}$$

since Z is a geometric progression [2] so the series can be explicitly summed and gives:

$$Z = \frac{sinh[(2J+1)\frac{x}{2}]}{sinh[\frac{x}{2}]} \tag{2.19}$$

with the substitution $y = xJ = \frac{g_J \mu_B J B}{k_B T}$, the magnetization reads as follows:

$$M = M_{sat} B_J(y), \tag{2.20}$$

where the saturation magnetization $M_{sat} = n g_J \mu_B J$, and the Brillouin function is given by:

$$B_J(y) = \frac{2J+1}{2J} coth(\frac{2J+1}{2J} y) - \frac{1}{2J} coth \frac{y}{2J} \tag{2.21}$$

[1] To derive the formula $\frac{1}{Z}\frac{\partial Z}{\partial x}$, the fundamental property of the exponential function, $\frac{\partial (e^{ax})}{\partial x} = a e^{ax}$ was employed.

[2] A geometric progression is a sequence of numbers in which each term after the first is found by multiplying the previous term by a fixed, non-zero number called the "common ratio." Mathematically, a geometric progression is defined as follows: a, ar, ar^2, ar^3, Where: "a" is the first term in the sequence. "r" is the common ratio.

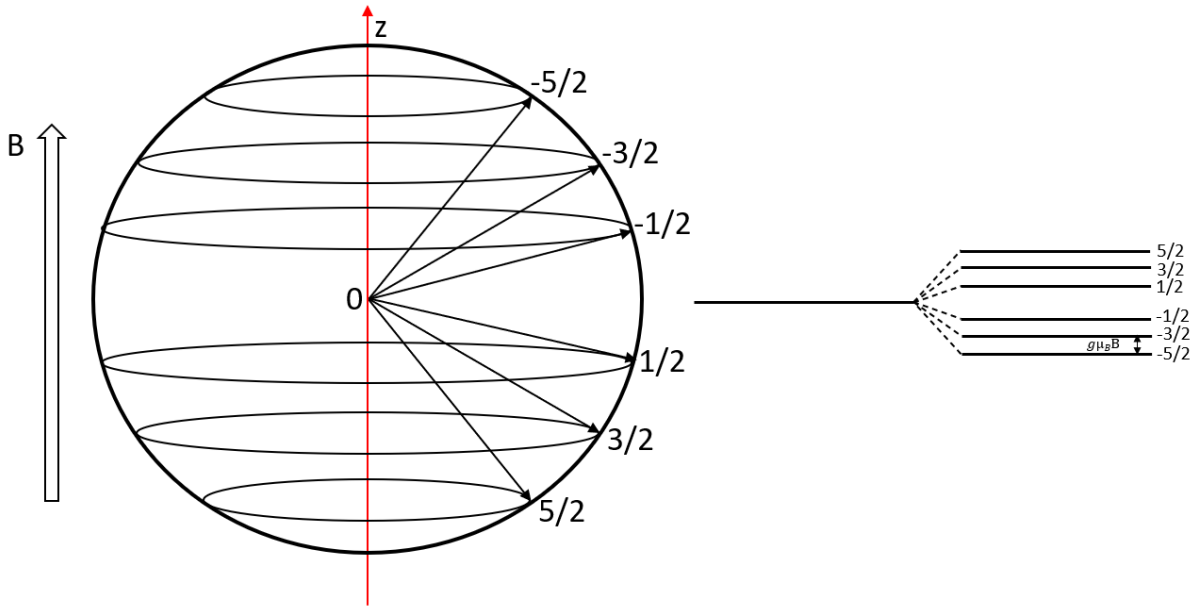

Figure 2.1: A quantum moment $J = 5/2$ under applied magnetic field B along z-direction. A sketch of Zeeman shift is shown on the right.

2.4 Hund's Rule and Ions Ground state

Hund proposed an empirical rule to determine the lowest-energy state of an ion:

1. First, maximize S for the electronic configuration. This means electrons occupy different orbitals to minimize their Coulomb repulsion, and fulfill Pauli exclusion principle.

2. Afterward, maximize L consistent with S. It means that the electrons orbit in the same direction whenever possible.

3. Finally, couple L and S to form J, whereas $J = L - S$ if the shell is less than half full, and $J = L + S$ if the shell is more than half full. When the shell is exactly half full, $L = 0$ and $J = S$. This rule attempts to minimize the spin-orbit coupling energy.

After determination of S, L, and J, the ion ground state can be expressed as ${}^{2S+1}L_J$, where L is not a number but rather a symbol according to the list in table 2.1.

2.5 Spin-Orbit Coupling

The point view of a single electron tells that it has an orbital angular momentum (l), and a spin angular momentum (s), which may be coupled by spin–orbit interaction to create a

Table 2.1: Letters corresponding to L values used in an ion ground state nomenclature.

L	0	1	2	3	4	5
-	S	P	D	F	G	H

total electronic angular momentum j. The magnetic moment m of the resultant j is given by:

$$m = \gamma j, \tag{2.22}$$

where γ is the gyromagnetic ratio. In multielectron picture and from the electron's perspective, the nucleus orbits around the electron at a speed of v, forming a current loop with $I_{nuc} = Zev/2\pi r$ and generating a magnetic field at the center, given by $\mu_0 I_{nuc}/2r$. This magnetic field, $B_{so} = \mu_0 Zev/4\pi r^2$, causes the spin-orbit interaction with the electron's intrinsic magnetic moment. The resulting interaction energy, $E_{so} = -\mu_B B_{so}$, can be expressed in terms of the Bohr radius $r = \frac{a_0}{Z}$, and Bohr magneton as:

$$E_{so} \approx -\frac{\mu_0 \mu_B^2 Z^4}{4\pi a_0^3} \tag{2.23}$$

The Hamiltonian of the spin–orbit coupling of a single electron is given by :

$$\mathcal{H}_{so} = \lambda \hat{\mathbf{l}}.\hat{\mathbf{s}}, \tag{2.24}$$

where λ is the spin–orbit coupling energy, $\hat{\mathbf{l}}$, and $\hat{\mathbf{s}}$ are dimensionless operators.

According to Hund's third rule, the spin-orbit coupling in multielectron systems (ions) is generally weak and depends on shell filling. Despite its weakness, spin-orbit coupling in magnetic ions leads to phenomena like magnetocrystalline anisotropy and magnetostriction. Its significance increases with heavier ions, as demonstrated in Eq. 2.23. For multielectron systems, the spin-orbit coupling Hamiltonian is expressed as:

$$\mathcal{H}_{so} = (\zeta/\hbar^2)\hat{\mathbf{l}}.\hat{\mathbf{s}}, \tag{2.25}$$

where ζ is positive for the first half of the $3d$ or $4f$ series and negative for the second half.

2.6 Competing Interactions

Considering site disorder and frustration as independent controlling parameters of the ground state of insulating magnets, interrelationships among different magnet classes emerge, as illustrated in Fig. 2.2. From this prospective, ferromagnets, antiferromag-

nets, ferrimagnets have weak frustration and low site disorder. Spin glasses exhibit high frustration and high site disorder. Geometrically frustrated magnets have high frustration, and little or no site disorder.

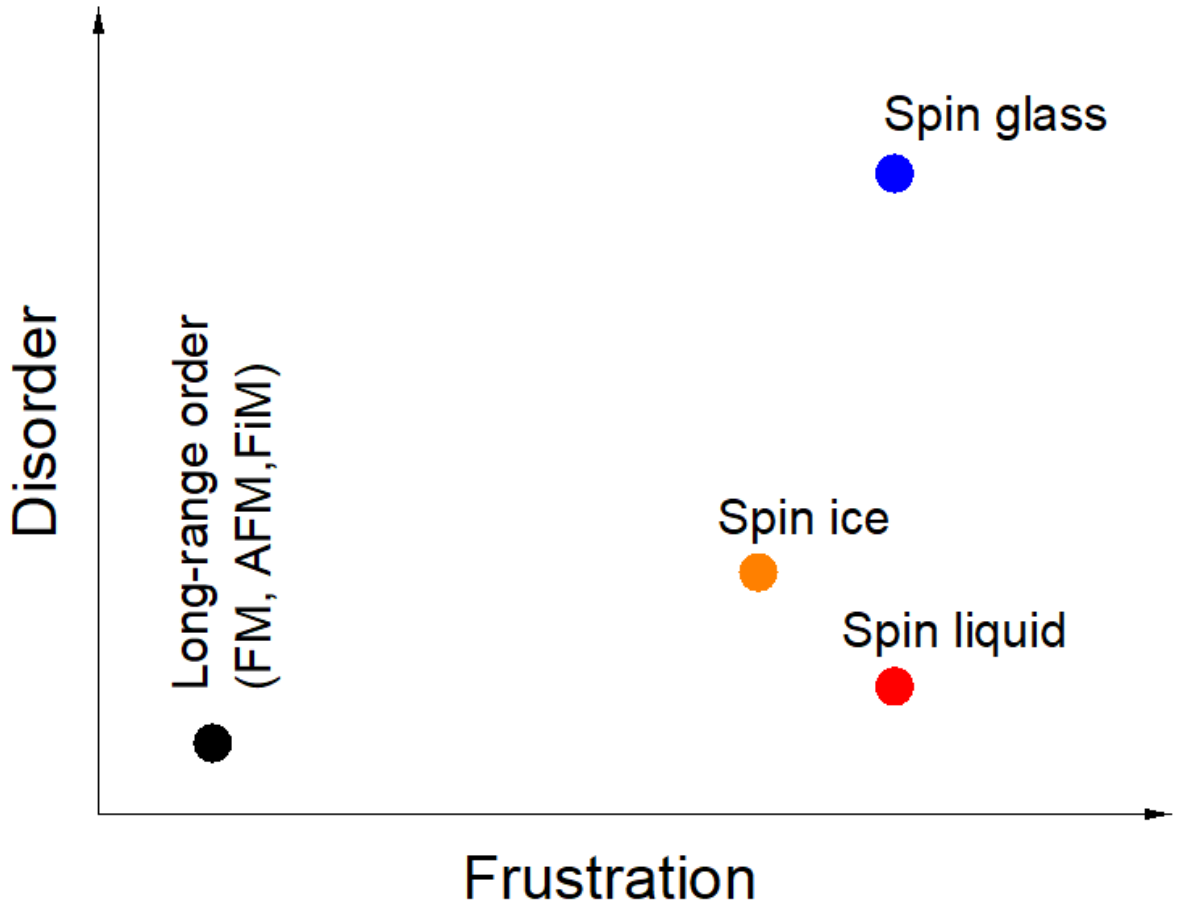

Figure 2.2: Couple of magnetic ground states as a function of site disorder and frustration. The acronyms AFM, FM, and FiM correspond to ferromagnets, antiferromagnets, ferrimagnets, respectively.This sketch is motivated by a similar concept in [13].

2.6.1 Frustrated Antiferromagnets

To introduce frustrated antiferromagnets, it is useful to revisit the behavior of unfrustrated antiferromagnets. In bipartite AFM, the lattice is divided into two sublattices with interpenetrating sites. One sublattice's nearest neighbors are exclusively from the other sublattice. The classical ground state is a two-sublattice Néel state, where spins on one sublattice share an orientation, and on the other sublattice, spins have the opposite orientation as shown in Fig. 2.4 (a). In such systems, under ideal conditions, the ground state exhibits only long-wavelength spin waves (magnons) as the primary low-energy excitations. These are Goldstone modes, which arise due to symmetry breaking in ground

states. These modes have a linear frequency dependence, $\omega(k)$, at small k. This semi-classical picture applies to quantum systems with $S \geq 1$, and fluctuations are considered using harmonic spin wave theory. In this approximation, the sublattice magnetization at low temperatures is reduced from its classical ground state value by:

$$\delta M_{\text{sublattice}} = \frac{1}{\Omega} \int_{BZ} \frac{zJS}{\hbar\omega(k)} \left[\langle n(k) \rangle + \frac{1}{2} \right] d^3k - \frac{1}{2} \tag{2.26}$$

where Ω is volume of the Brillouin zone, z is the number of nearest neighbour sites, $n(k)$ the number of thermally excited spin waves at wavevector k, and $1/2$ is the zero-point contribution. Frustrated antiferromagnets have Hamiltonians with competing interactions, preventing simultaneous energy minimization. They are intriguing due to their potential to violate Néel order. Such systems tend to exhibit many low-frequency modes, because of the term $\frac{zJS}{\hbar\omega(k)}$ in Eq. 2.26, which enables effective excitations that suppress ordered moments, even at very low temperatures.

2.6.2 Geometrically Frustrated Lattices

In solids with frustrated triangular lattices (see Fig. 2.3 (a)), long-range magnetic ordering is often delayed to lower temperatures (or even completely suppressed) than expected due to near-neighbor interactions. The final ordered state (if there is any) results from a delicate balance of factors, including deviations from perfect triangular symmetry and interactions with second or higher-order nearest neighbors.

Two-dimensional frustrated structures with triangular lattices of edge-sharing or corner-sharing, illustrated in Fig. 2.3 (c, and d), respectively exhibit diverse magnetic ground state. Specifcially, the ground state depends on the spin's magnitude, orbital occupancy, the distances between magnetic ions, and the crystalline field effect from the surrounding non-magnetic ions. The synthesis of transition-metal compounds with edge-sharing lattices is feasible, whereas it is a challenge to synthesize rare-earth (RE) compounds with pure planar edge-sharing. 2D-compounds based on triangle corner-sharing lattices have been studied more than that of edge sharing, as the former is more susceptible to magnetic frustration. A typical example of corner-sharing lattices are kagomé systems.

Extending magnetic lattice into three dimensions (3D), results in a diverse set of frustrated lattices. Most of these 3D frustrated lattices are built out of tetrahedra blocks. Among these, rare earth oxide pyrochlores have been studied extensively, owing to their substantial geometrically frustrated lattice, and the feasibility of growing large single crystals using the floating zone crystal growth method. In $A_2B_2O_7$ pyrochlores, both the A and B sublattices

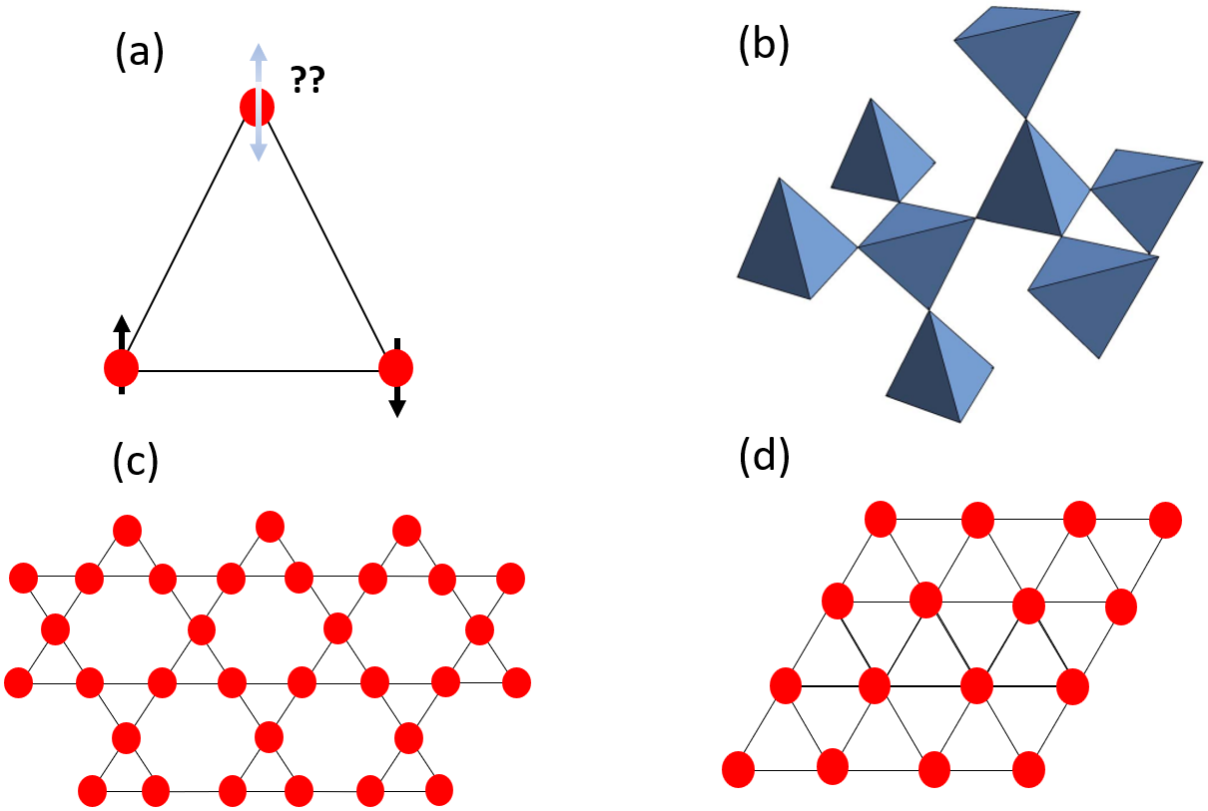

Figure 2.3: (a) Frustration in the triangle-lattice antiferromagnet, (b) Network of corner-sharing tetrahedrons forming Pyrochlore lattice, (c) Network of corner-sharing triangles forming Kagomé lattice, and (d) Network of edge-sharing triangles forming Kagomé lattice. Note, the red spheres represent the magnetic ions.

consist of corner-sharing tetrahedra that interconnect within the structure as depicted in Fig. 2.3 (b). In the majority of the studied pyrochlores, the magnetic atoms occupy the A-sites, which can be easily diluted through solid solutions such as $(Ho_{2-x}Y_x)Ti_2O_7$. This structure modification serves multiple purposes: it allows the isolation of single ion effects from collective effects, and it alleviates some of the frustration by eliminating competing magnetic interactions on nearest neighbor sites.

2.6.3 Revealing Frustration by Macroscopic Probes

Antiferromagnet with two sub-lattice case can be represented by the Hamiltonian:

$$H = -J_{\mathrm{nn}} \sum_{\langle i,j \rangle} \mathbf{S}_i \cdot \mathbf{S}_j, \tag{2.27}$$

where the negative sign of the exchange interaction J_{nn} reflects the antiferromagnetic nature of the interactions, S_i the spin operators at sites j, and the sum runs over neighbouring

pairs ij of sites. The high-temperature magnetic susceptibility in this case follows by the classical Curie–Weiss law:

$$\chi = \frac{C}{T - \theta_W}, \tag{2.28}$$

where C is the Curie-constant, θ_W is the Weiss-temperature. The ordering temperature of this antiferromagnet, T_N, appears as singularities in the specific heat $C(T)$, and the magnetic susceptibility $\chi(T)$ or its corresponding derivatives $\partial(\chi T)/\partial T$. The value of T_N is given from the mean-field solution to the Hamiltonian in 2.27 as:

$$\Theta_W = \frac{1}{3} z S(S+1) |J_{\mathrm{nn}}| \tag{2.29}$$

Fitting the magnetic susceptibility $\chi(T)$ at high temperatures to Eq. 2.28, yields θ_W;

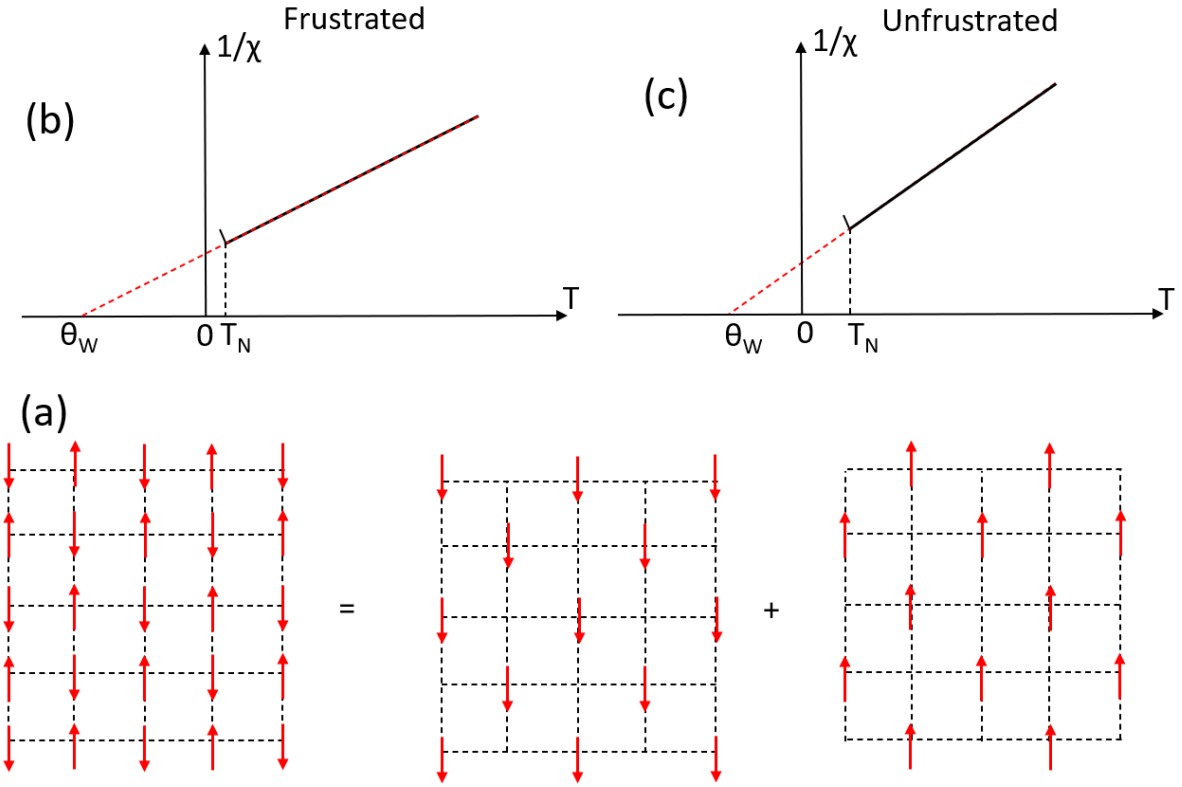

Figure 2.4: (a) An antiferromagnet with bipartite lattice; the red arrows represent spins with nearest neighbor antiferromagnetic interactions. (b), and (c) are sketches of $1/\chi$ versus temperature (T) for frustrated and unfrustrated antiferromagnets, respectively. The red dashed lines represent Curie-Weiss fits. Note that in the case of frustrated antiferromagnet $\theta_W >> T_\mathrm{N}$, while in unfrustrated ones $\theta_W \approx T_\mathrm{N}$.

which is positive (negative) for ferromagnetic (antiferromagnetic) exchange interactions, and its value reflects the strength of these interactions. Further, θ_W, and T_N are used to

quantify the magnetic frustration factor, f, according to the empirical relation:

$$f = \frac{|\theta_W|}{T_N}, \tag{2.30}$$

Note, the values of T_{N} and $|\theta_W|$ are comparable in case of unfrustrated antiferromagnts, whereas in the frustrated antiferromagnts $|\theta_W|$ can be much larger than T_{N} as depicted in Fig. 2.4 (b) and (c).

2.7 Heat Capacity

2.7.1 Lattice Specific Heat

Dulong-Petit Law

In a solid, atoms or molecules occupy regular lattice positions, which can be approximated as masses connected by springs. At low temperatures, their vibrations are represented by simple harmonic oscillations. A harmonic oscillator in thermal equilibrium has an internal energy of k_BT, with half as kinetic energy and half as potential energy. In three dimensions, this yields an internal energy of $3k_BT$, or $3RT$ for one mole of oscillators ($R = N_Ak_B$). The heat capacity is $C = 3R$; this empirical relation is known as Dulong-Petit Law. For a compound A_nB_m, Dulong-Petit's law extends as:

$$C = (n + m)3R$$

This shows that specific heat depends on the number of atoms in the compound, not only their masses.

Phonons Distribution Function

In the quantum mechanical treatment of the lattice, motivated by Planck's quantization assumption of the photons, the energy levels of an oscillator are discrete and described by $E_n = (n + \frac{1}{2})\hbar\omega$; $\frac{1}{2}\hbar\omega$ is the zero point energy. Further, the probability of finding the oscillator in the quantum state n with energy E_n is given by:

$$P_n = \frac{e^{\frac{-E_n}{k_BT}}}{\sum_n e^{\frac{-E_n}{k_BT}}} \tag{2.31}$$

$$= e^{\frac{-n\hbar\omega}{k_BT}}[1 - e^{\frac{-\hbar\omega}{k_BT}}] \tag{2.32}$$

Subsequently, the mean value of n in thermal equilibrium is given by:

$$\langle n \rangle = \sum_n n P_n = \frac{1}{[e^{\frac{\hbar\omega}{k_B T}} - 1]} \tag{2.33}$$

Einstein-Debye Models

In the Einstein model, the solid lattice is treated as a large number of independent three-dimensional oscillators, all vibrating with the same angular frequency ω_{Ein}. Thus at thermal equilibrium and for$N$ oscillators at temperature T, the internal energy is given by:

$$E = 3sRT[\frac{1}{2}\frac{\hbar\omega_{Ein}}{k_B T} + \frac{\frac{\hbar\omega_{Ein}}{k_B T}}{e^{\frac{\hbar\omega_{Ein}}{k_B T}} - 1}], \tag{2.34}$$

where s is the number of atoms per mole, and R is the general gas constant. Taking the first derivative of the internal energy with respect to temperature, yields heat capacity according to the formula:

$$C = 3sR[\frac{x_{Ein}^2 e^{x_{Ein}}}{(e^{x_{Ein}} - 1)^2}], \tag{2.35}$$

where $x_{Ein} = \frac{\hbar\omega_{Ein}}{k_B T}$. The last equation can be expressed as a function of Einstein temperature Θ_{Ein} according to the relation:

$$C(\frac{\Theta_{Ein}}{T}) = 3sR[(\frac{\Theta_{Ein}}{T})^2 \frac{e^{\frac{\Theta_{Ein}}{T}}}{(e^{\frac{\Theta_{Ein}}{T}} - 1)^2}], \tag{2.36}$$

where $\Theta_{Ein} = \frac{\hbar\omega_{Ein}}{k_B}$ is the characteristic temperature below which the thermal excitations of the oscillators freeze out. The Einstein model, as described in Eq. 2.36, fits the heat capacity of many solids within the high-temperature regime ($T \gg \Theta_{Ein}$), and for high temperatures it agrees with the classical value derived from the Dulong-Petit law. However, at lower temperatures ($T \ll \Theta_{Ein}$), the model's predictions diverge from the observed heat capacity behavior.

In the Debye model, instead of treating atoms as independent harmonic oscillators each of them with frequency ω_{Ein}, Debye assumed the collective motion of atoms for small wave vectors, represented by sound waves in a material, as harmonic oscillators with frequencies depend on the wave vector k through the dispersion relation $\omega(k) = v_{so}|k|$; v_{so} is the speed of sound in solids. In this picture, the displacement δX of an atom at position X and time t reads as $\delta X = X_0 e^{i(k.X - \omega t)}$; X_0, ω, k are the amplitude, the angular frequency, and the wave vector, respectively. The later is related to the wavelength via $|k| = \frac{2\pi}{\lambda}$. In this

model, the internal energy of the system is described as:

$$E = 3\sum_{k}(\frac{1}{2}\hbar\omega(k) + \frac{\hbar\omega(k)}{e^{\frac{\hbar\omega(k)}{k_B T}} - 1}) \tag{2.37}$$

and the heat capacity is given by:

$$C = 9Rs\left(\frac{T}{\Theta_D}\right)^3 \int_0^{x_D} \frac{x^4 e^x dx}{(e^x - 1)^2} = 9Rs\left(\frac{T}{\Theta_D}\right)^3 D\left(\frac{\Theta_D}{T}\right), \tag{2.38}$$

where Debye temperature $\Theta_D = \frac{\hbar v_{so}}{k_B}(\frac{6\pi^2 Ns}{V})^{1/3}$, and $D(\frac{\Theta_D}{T})$ is the Debye function. A detailed derivation of Debye specific heat model of solids can be found in [14, 16, 17]. Finally, to estimate the phononic contribution to the total heat capacity of the solids with more than one atom, a heat capacity model comprising Debye and Einstein terms is used to fit the heat capacity data at temperatures greater than the transition temperature.

$$c^{ph} = n_{\mathrm{D}} D\left(\frac{T}{\Theta_D}\right) + n_{\mathrm{E}} E\left(\frac{T}{\Theta_E}\right) \tag{2.39}$$

2.7.2 Electronic Specific Heat

In the classical theory, the equipartition law predicts electron contribution to high temperature heat capacity as $3R/2$. However, the experimental data reports total heat capacity as $3R$ at room temperature, primarily due to lattice heat capacity. Hence, electronic specific heat at room temperature should be negligible. This contradiction is resolved in quantum theory, where the Pauli exclusion principle and Fermi-Dirac electron distribution were considered.

In the quantum theory, not all electrons gain $k_B T$ energy when an electron gas is heated. Only those near the Fermi energy within a range of $k_B T$ are excited. Thus, the fraction of thermally excited electrons at temperature T is proportional to $\frac{T}{T_F}$. For an assembly of N electrons, the average thermal energy is $\Delta E \approx N k_B T \frac{T}{T_F}$, and the electronic specific heat is given by:

$$C^e = \frac{1}{3}\pi^2 k_B^2 \eta(E_F) T \tag{2.40}$$

$$= \gamma T, \tag{2.41}$$

where the electron density of states $\eta(E_F)$ is expressed in (States/eV atom), the coefficient of the electronic specific heat γ in units of J/mol K^2. The relation between γ and the electron's mass is given by: $\gamma = \frac{k_B^2}{3\hbar^2} V k_F m_e$. At low temperatures, the total heat capacity

can be expressed as $C = \gamma T + \beta T^3$. The determination of γ and, consequently, the density of states η, is typically achieved through a plot of C/T against T^2, where the slope of this plot provides the value of β, and thus, the Debye temperature Θ_D, while the intercept yields the value of γ.

2.7.3 Magnetic Specific Heat

Specific Heat of Magnons

The spin wave theory can be explained using Heisenberg Hamiltonian:

$$\mathcal{H} = -2\sum_i J_{ex}(r_{i,i+1}) S_i . S_{i+1}, \tag{2.42}$$

where $J_{ex}(r_{i,i+1})$ is an isotropic exchange interaction which depends only on the distance between the interacting spins, $r = r_{i+1} - r_i$. Rewriting the Hamiltonian for a linear ferromagnetic chain with nearest neighbor (nn) spin interactions only, the Hamiltonian of the i^{th} spin in this chain is given by:

$$\mathcal{H} = -2\sum_i J_0 S_i \cdot (S_{i-1} + S_{i+1}), \tag{2.43}$$

where J_0 is the nearest neighbor exchange interaction, which is assumed to be constant throughout the chain. Note, S_i has a moment $\mu_i = -g\mu_B S_i$, and its energy in magnetic field is $E(\mu_i) = -\mu_i \cdot B$. In this picture, S_i is exposed to an effective magnetic field B_{eff} originating from S_{i-1} and S_{i+1} according to the formula:

$$B_{eff} = \frac{-2J_0}{g\mu_B(S_{i-1} + S_{i+1})} \tag{2.44}$$

In an external magnetic field B, each μ_i has a torque $\tau = \mu_i \times B$. This torque is equivalent to the rate of change of S_i according to the formula:

$$\frac{dS_i}{dt} = (\frac{2J_0}{\hbar}) S_i \times (S_{i-1} + S_{i+1}) \tag{2.45}$$

The solution of Eq. 2.45 yields the dispersion relation of this ferromagnetic chain by the relation:

$$\omega_k = \frac{2J_0 S a^2}{\hbar} k^2 \tag{2.46}$$

and it can be generalized for three dimensional ferromagnets (FM):

$$\omega_k = F_l \frac{2J_{ex}Sa^2}{\hbar}k^2, \tag{2.47}$$

where J_{ex} the magnitude of the exchange interaction and F_l is a constant varies according to the crystal structure type. For three dimensional antiferromagnets(AFM) the dispersion relation is given by:

$$\omega_k = F_l \frac{2J'_{ex}Sa}{\hbar}k, \tag{2.48}$$

The general remarks of the dispersion relations of FM and AFM systems can be summarized as follows:

- In FM systems, the dispersion relation has two magnon modes for each value of k.
- In AFM systems, there is only one magnon modes for each value of k.
- In AFM systems, the magnons dispersion relation has the same form as phonons. Consequently, the heat capacity of AFM magnons follows $C \propto T^3$ at low temperatures.

Similar to photons and phonons, magnons are described by Planck's distribution and the mean value of n magnons with wave vector k is given by:

$$\langle n_k \rangle = \frac{1}{[e^{\frac{\hbar\omega_k}{k_B T}} - 1]} \tag{2.49}$$

In case of FM, the number of magnons (density of magnons) with frequencies between ω and $\omega + d\omega$ is given by:

$$D(\omega) = \frac{V_m}{4\pi^2}(\frac{\hbar}{2JSa^2F_l})^{3/2}\omega^{1/2}, \tag{2.50}$$

where V_m is the volume of the crystal. The energy of magnons is given by:

$$E = \int \hbar\omega D(\omega)\langle n_k \rangle d\omega \tag{2.51}$$

Now, substitution of ω_k, $D(\omega)$, and $\langle n_k \rangle$ into Eq. 2.51, then taking the derivative of the energy with respect to T gives the magnetic specific heat of a ferromagnet according to the formula:

$$C = l_{FM}R(\frac{k_B T}{2J_{ex}S})^{3/2}, \tag{2.52}$$

Likewise, the magnetic specific heat of an antiferromagnet is given by:

$$C = l_{AFM} R(\frac{k_B T}{2J'_{ex} S})^3, \tag{2.53}$$

where $l_{FM,AFM}$ is a constant depends on the lattice type.

Specific Heat in Mean-Field Approximation

As mentioned earlier, the exchange interaction can be considered as the interplay between the magnetic moment of the ion at the site i^{th} and the effective field $B_{eff} = \frac{-2J_0}{g\mu_B(\sum S)}$ produced by the remaining spins in the crystal. In Weiss molecular field model, the phenomenological molecular field is given by:

$$B_{mf} = \frac{-2J_0 z}{N(g\mu_B)^2} N g\mu_B \langle S_i \rangle \tag{2.54}$$

$$= \lambda M, \tag{2.55}$$

where z is the number of the nearest neighbor spins (S_{nn}) around the central spin S_i, N is the number of spins per unit volume, λ is a temperature independent constant, and the magnetization resulting from all the spins $M = Ng\mu_B\langle S_i \rangle$. In a zero field the change in magnetic energy per mole is given by:

$$dE = -V_m B_{mf} dM = -V_m \lambda M dM, \tag{2.56}$$

where V_m is the molar volume. Taking the derivative of E with respect to the temperature yields the specific heat according to the relation:

$$C = -V_m \frac{\lambda}{2} \frac{dM^2}{dT} \tag{2.57}$$

$$= -V_m \frac{\lambda}{2} (M_{sat})^2 \frac{d[(M/M_{sat})^2]}{dT}, \tag{2.58}$$

Note that in the last equation, at absolute zero temperature ($T = 0$), the magnetization (M) equals its saturation value (M_{sat}), leading to C approaching zero. However, as temperature rises and approaches the transition temperature, the derivative $\frac{d[(M/M_{sat})^2]}{dT}$ increases, reaching its peak just below the transition temperature. Beyond the transition temperature, according to the Weiss model, magnetization (M) drops to zero abruptly, causing the specific heat to attain its maximum value at the transition temperature and then sharply decrease to zero. The magnetic specific heat at the transition temperature

can be expressed as:

$$C^{mag} = 5R\frac{J(J+1)}{(J+1)^2+J^2} \tag{2.59}$$

2.7.4 Schottky Specific Heat

An ion with total angular momentum $\hbar J$ initially exhibits a $(2J + 1)$-fold degenerate energy level. However, in a solid, this degeneracy can be altered by the crystalline electric field. Similarly, in the case of a nucleus with spin $\hbar I$, the initial $(2I + 1)$-fold degeneracy is affected by a magnetic field from the surrounding electrons. The specific heat of a system with such discrete energy levels shows a broad peak, a phenomenon known as Schottky anomaly.

Starting with the case of a two-level system such as a magnet with $S = \frac{1}{2}$ in a magnetic field B, this system has two possible energy levels, E_1 and E_2 separated by $\Delta = \frac{E_2-E_1}{k_B}$ and its partition function can be written as:

$$Z = \sum_{1}^{2} e^{\frac{-E_i}{k_B T}} \tag{2.60}$$

and it average thermal energy at temperature T is expressed as:

$$E = k_B T^2 (\frac{\partial ln Z}{\partial T}) \tag{2.61}$$

$$= E_1 + \frac{k_B \Delta}{1 + e^{\frac{\Delta}{T}}} \tag{2.62}$$

Taking the first derivative of the last equation with respect to T and and multiplying it by Avogadro number N_A yields Schottky heat capacity according to the formula:

$$C_{\text{Sch}} = R(\frac{\Delta}{T})^2 \frac{e^{\frac{\Delta}{T}}}{[1 + e^{\frac{\Delta}{T}}]^2} \tag{2.63}$$

In Eq. 2.63, as temperature decreases, C_{Sch} exponentially approaches zero, while at high temperatures, it follows a T^{-2} behaviour. Specifically, at very low temperatures ($T \ll \Delta$), the upper level remains barely populated, resulting in negligible transition probability between the levels, causing C_{Sch} to tend to zero as T approaches zero. Conversely, at high temperatures ($T \gg \Delta$), both levels are nearly equally populated, leading to insignificantly low transition probabilities once again, causing C_{Sch} to approach zero as T approaches zero. Only when T is on the order of Δ, the transitions between levels occur, leading to Schottky anomaly in the specific heat. The two-level system can be extended into a

multi-level system with n discrete levels having degeneracies g_0, g_1, g_2, ..., g_n, and energy separations E_1, E_2, E_3, ..., E_n from the ground state. In that case Schottky heat capacity is expressed as:

$$C_{\text{Sch}} = R(\frac{\Delta}{T})^2 \frac{(\frac{g_0}{g_1})e^{\frac{\Delta}{T}}}{[1+(\frac{g_0}{g_1})e^{\frac{\Delta}{T}}]^2} \tag{2.64}$$

2.8 Normalization of the Debye Temperature

To estimate excess specific heat, like the Schottky term, in a substance, an isomorphic substance with similar electronic and lattice structures can be used. The heat capacity of the isomorphic substance separates lattice and electronic terms from the total specific heat. However, for accuracy, a correction for molar mass differences between the isomorphic substance and the substance under investigation at high temperatures is required. Accordingly a normalization of the substance's Debye temperature to that of the isomorphic substance can be performed as follows: In solids, the mean square displacement $\langle u^2 \rangle$ of an atom at temperature T is related to Debye temperature Θ_D by $\langle u^2 \rangle = K\frac{T}{M\Theta^2}$; M is the mass of the atom and K is a constant. Assuming that all the atoms in the solid have the same $\langle u^2 \rangle$, then for a binary compound A_nB_m, $M_A\Theta_A^2 = M_B\Theta_B^2$; $n+m$ represent the number atoms per formula unit. Further, the specific heat of a binary compound can be described by two Debye parameters, one for each type of atom according to the relation:

$$C_v = nf(\frac{\Theta_A}{T}) + mf(\frac{\Theta_B}{T}), \tag{2.65}$$

Recalling that $C_v = \frac{12\pi^4}{5}(\frac{Rs}{\Theta^3})T^3$ gives $\frac{n+m}{\Theta_{AB}^3} = \frac{n}{\Theta_A^3} + \frac{m}{\Theta_B^3}$, and the atoms mass ratio is given as:

$$n(\frac{M_A}{M_B})^{3/2} + m = (n+m)\frac{\Theta_B^3}{\Theta_{AB}^3} \tag{2.66}$$

Likewise for the isomorphic compound:

$$n(\frac{M_W}{M_X})^{3/2} + m = (n+m)\frac{\Theta_X^3}{\Theta_{WX}^3} \tag{2.67}$$

From the last two equations a mass normalization relation with respect to Debye temperature can be written as:

$$\frac{\Theta_{W_nX_m}^3}{\Theta_{A_nB_m}^3} = \frac{nM_A^{3/2} + nM_B^{3/2}}{nM_W^{3/2} + nM_X^{3/2}} \tag{2.68}$$

Chapter 3

Experimental Methods

3.1 Heat Capacity

The measurement of the heat capacity of solids at low temperatures provide information on the electronic, magnetic, and lattice degrees of freedom. Heat capacity measurements enable comparisons between statistical theoretical models and the experimental results. As the former compute the density of states and energy levels in a certain material, which lead to predictions of heat capacity values. In the present work, the heat capacity of several solid samples was measured at constant pressure using the Quantum Design (QD) heat capacity option, where the heat capacity is given by:

$$C_p = \left(\frac{dQ}{dT}\right)_p, \tag{3.1}$$

where dQ is a heat input that causes a subsequent temperature rise dT in the sample.

3.1.1 Thermal-Relaxation Method

In the course of this work, the heat capacity is measured using a thermal-relaxation calorimeter. In this method, during a heat capacity measurement, a known amount of heat is applied at constant power $P(t)$ for a fixed time, and then this heating period is followed by a cooling period of the same duration. Afterward, the heat capacity software chooses between "The Simple Model" and "The Two-Tau Model" to estimate the heat capacity of the sample.

In the simple model, a very high thermal coupling between the sample and the platform is assumed i.e., the sample is supposed to have the same temperature as the platform during the measurement. The Heat Capacity software uses this model to estimate heat

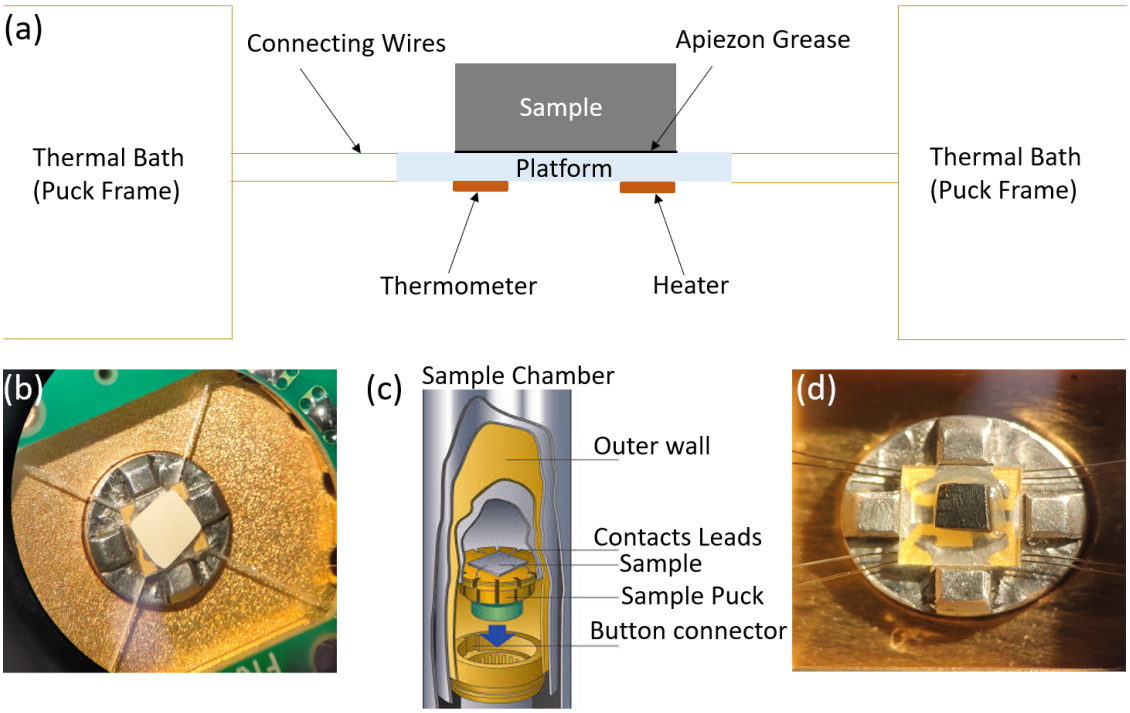

Figure 3.1: (a) Sketch of the thermal connections to sample and sample platform in PPMS heat capacity option, (c) Cartoon of the sample chamber which is taken from [18], (b) and (d) are images of polycrystalline, and single crystal samples mounted on the different platforms used for measuring heat capacity with dilution refrigerator and standard heat capacity option, respectively. Images in (b) and (d) are examples of samples fixed onto the heat capacity platform using N-grease for measurements using the dilution refrigerator (DR), and the standard heat capacity option, respectively.

capacity of the addenda and of most samples. In this model, the power $P(t)$ applied to the platform via the thin-film heater is given by:

$$P(t) = C_{\text{tot}} + K_w(T - T_{\text{b}}), \tag{3.2}$$

where C_{tot} is the total heat capacity of the sample and sample platform; K_w is the thermal conductance of the supporting wires; T is the temperature of the platform, and T_b is the temperature of the thermal bath (puck frame). The heater power $P(t)$ is equal to P_0 during the heating regime of the measurement and equal to zero during the cooling one. The solution of Eq. 3.2 yields a characteristic time constant $\tau = \frac{C_{\text{tot}}}{K_w}$, i.e., based on the τ value the heat capacity can be estimated.

The Two-Tau model is used only when there is a very poor thermal coupling between the sample and the platform. The poor thermal coupling produces a significant temperature difference between the two during the measurement. To account for this problem, the two-

tau model simulates the effect of heat flowing between the sample platform and sample, and the effect of heat flowing between the sample platform and puck by the following equations:

$$C_{\text{platform}}\frac{dT_p}{dt} = P(t) - K_w(T_p(t) - T_b) + K_g(T_{\text{sample}}(t) - T_p(t)) \tag{3.3}$$

$$C_{\text{sample}}\frac{dT_{\text{sample}}}{dt} = -K_g(T_{\text{sample}}(t) - T_p(t)), \tag{3.4}$$

where C_{platform} is the heat capacity of the sample platform, C_{sample} is the heat capacity of the sample, K_g is the thermal conductance of the grease, $T_p(t)$, and T_{sample} are temperatures of the platform and sample, respectively.

3.1.2 Measurement Routine and Sample Mounting

In the course of this work, the heat capacity measurements were performed in two steps. First, a background measurement known as an 'addenda' was conducted prior to measuring the heat capacity of the sample. During the addenda measurement, the heat capacity of the sample platform, along with a specific amount of grease, was measured. The grease was evenly spread onto the sapphire platform in a thin layer, covering an area that matches the contact surface with the sample. The quantity of grease used varied based on the size and geometry of the sample. Note, the excessive grease on the platform leads to a reduction in thermal diffusivity, thereby compromising the accuracy of the addenda measurement.

Following the completion of the addenda measurement, the grease on the platform was heated, using a heat gun with temperature of 50 degrees Celsius for approximately 10 sec, to ensure thorough spreading of the grease. Subsequently, samples with an area of less than $4\,\text{mm}^2$ and masses of a few milligrams were gently pressed onto the grease, as illustrated in Fig. 3.1 (b and d). It is important to emphasize that the sample's flattest and smoothest surface is essential to achieve the highest possible thermal coupling with the platform. Subsequent to this step, the heat capacity measurement was performed for both the sample and the addenda. The heat capacity software calculates the sample's heat capacity by subtracting the addenda measurement from the total heat capacity measurement.

The PPMS standard heat capacity option is capable of measuring the sample's heat capacity from 1.8 K to 400 K and in different applied magnetic fields in the range $0\ \text{T} \leq B \leq 14\ \text{T}$. The sample is cooled to the lowest temperature and allowed to equilibrate for ≈ 2 hours. This ensures that both the sample and the platform are at the same temperature during the measurement. Afterwards, the turbo pump evacuates the sample chamber and the measurement begins. The temperature increase and the number of data points are se-

lected according to the anticipated phase transition. Generally in zero field measurement, a reasonable number of data points are required at temperature ranges far above the phase transition temperatures. This facilitates the fitting of the data to lattice models.

To measure heat capacity at temperatures below 1.8 K and down to 50 mK, the PPMS is equipped with the dilution refrigerator (DR) probe. The following points must be considered during the measurement of heat capacity using the DR probe:

- Similar to the standard option, the addenda measurement is required prior to the sample's measurement.
- At 0.05 K $\leq T \leq$ 0.5 K, vibrations of the DR generates substantial vibrational warming of the sample platform. Therefore, isolation of the DR-cart from the floor during this regime is necessary.
- At $T < 1$ K in magnetic fields of several Tesla, the thermometer on the platform of the puck used with DR produces temperature errors of up to 20%, therefore measuring the addenda in the same fields will be applied during the sample measurement is necessary.

3.2 Thermal Expansion and Magnetostriction

Thermal expansion and magnetostriction data shown in this work were measured by means of a three-terminal high-resolution capacitance dilatometer in a home-built setup placed inside a Variable Temperature Insert (VTI) of an Oxford magnet system [19, 20]. With this dilatometer, the relative length changes dL_i/L_i measurements were performed in the temperature range of 2 K to 300 K and in magnetic fields up to 15 T, applied along the direction of the measured length changes. The linear thermal expansion coefficients, $\alpha_i = 1/L_i \times dL_i(T)/dT$, were obtained. In addition, the field-induced length changes, $dL_i(B_i)$, were measured at different fixed temperatures between 2 and 40 K and in magnetic fields up to 15 T. The longitudinal magnetostriction coefficients, $\lambda_i = 1/L_i \times dL_i(B_i)/dB_i$, were derived. The measurements were done mostly by Lukas Gries (KIP, Heidelberg University), and some of the data are documented in [21].

3.3 Magnetometry

In the present work, magnetization measurements were performed in DC-field, AC-field, and pulsed-field modes. For the DC and AC measurements, two commercially available

devices from Quantum Design, namely Magnetic Property Measurement System (MPMS-3), and Physical Property Measurement System (PPMS) were used. To measure the magnetization at magnetic fields higher than 14 T (the upper limit of the PPMS), the pulsed-field measurements were performed.

3.3.1 DC-Field Magnetization

In the present work, DC-field measurements encompass two distinct approaches for investigating the DC moment of the sample. The first approach investigates temperature dependence of the sample's DC-moment at a constant DC magnetic field, and the second investigates its field dependence at a constant temperature.

In the temperature dependence measurements, the DC moment was obtained in two ways either after cooling the sample in the external magnetic measurement field (field-cooled; FC) or by applying the magnetic field after cooling the sample to the lowest temperature (zero-field-cooled; ZFC). The target magnetic field was held constant for $\simeq 60$ S prior to the start of the temperature sweep, and the magnetic moment was recorded upon raising the temperature with sweep rates of 0.4-1 K/min depending on the interest. In the field dependence measurements (isothermal), the target sample temperature was held constant for 1 to 3 min prior to the start of the field sweep with rates of 50–100 Oe/s.

In MPMS-3 and PPMS, the DC magnetic moment is detected by moving the sample through a pickup coil. This motion induces a voltage in a pickup coil. The time-dependent induced voltage is given by:

$$V_{\text{coil}} = \frac{d\Phi}{dt} = 2\pi f C m A \sin(2\pi f t), \tag{3.5}$$

where C is a coupling constant, m is the DC magnetic moment of the sample, A is the amplitude of oscillation, and f is the frequency of oscillation.

MPMS-3 pickup coil is incorporated with a superconducting quantum interference device (SQUID) and it detects the moment using two modes: (a) a DC mode where the sample is singularly moved with a large scan length (30 mm) with a scan time of 4 s, (b) a vibrating sample magnetometer (VSM) mode where the sample is vibrated at a frequency of 14 Hz and a small amplitude $A \leq 5$ mm. While PPMS uses the VSM mode as a separate option, and the moment is directly detected by the pickup coil without a SQUID. The sample is vibrated at a frequency of 40 Hz and a small amplitude $A \leq 5$ mm. The measurements details of the DC magnetization and different modes found in the respective manuals [22, 23].

The samples (polycrystalline pressed pellets and single crystals) were chosen to be < 3 mm in length and width. They were sandwiched between two quartz spacers within a brass holder. In case of measurements below 1.8 K down to 400 mK, the MPMS-3 was equipped with the iQuantum He3 probe and the moment was recorded only using DC mode. The samples were fixed by Apiezon N-Grease onto the flat surface of a straw drink.

3.3.2 AC-Field Magnetization

AC-field magnetization measurement involves applying an AC field (B_{ac}) to a sample and measuring the resulting AC moment. Unlike DC-field magnetization measurements where the sample moment is constant in time, AC measurements reveal sample's moment time-dependence. The field of the time-dependent moment generates a current in the pickup coils, enabling measurement without needing to move the sample. At low frequencies, the AC magnetization is given by:

$$M_{\mathrm{ac}} = \frac{dM}{dB} \cdot B_{\mathrm{ac}} \cdot \sin(\omega t), \tag{3.6}$$

where B_{ac} is the amplitude of the driving field, ω is the driving frequency, and the susceptibility $\chi = \frac{dM}{dB}$ is the slope of the isothermal magnetization M(B) curve. At higher frequencies, the AC moment of the sample does not follow along the DC magnetization curve due to dynamic effects in the sample. Thus, the AC magnetic susceptibility measurement yields two quantities: the magnitude of the susceptibility, $\chi = dM/dB$, and the phase shift, φ (see Fig. 3.2 (a, b)) and it can be described as $\chi_{\mathrm{ac}} = \chi' + i\chi''$, where χ' is the in-phase component (real part), and χ'' is the out-of-phase (imaginary part). The two components are given by:

$$\chi' = \frac{dM}{dB} \cdot \cos(\varphi) \tag{3.7}$$

$$\chi'' = \frac{dM}{dB} \cdot \sin(\varphi) \tag{3.8}$$

In the present work, AC-field magnetization measurements were performed using ACMSII, and AC options of PPMS and MPMS-3, respectively. In measurements using MPMS-3, the 5-point measurement mode was utilized, unless stated otherwise. This mode provides a calibrated measurement with temperature drift compensation, which makes it slower in sweeping temperature in comparison to the 3-point mode. The measurements details of the AC-susceptibility and different modes found in the respective manuals [22, 24]. The samples were chosen to be < 3 mm in length and width. They were fixed by Apiezon N-grease onto the flat surface of a quartz sample holder as shown in Fig. 3.2 (d, c)).

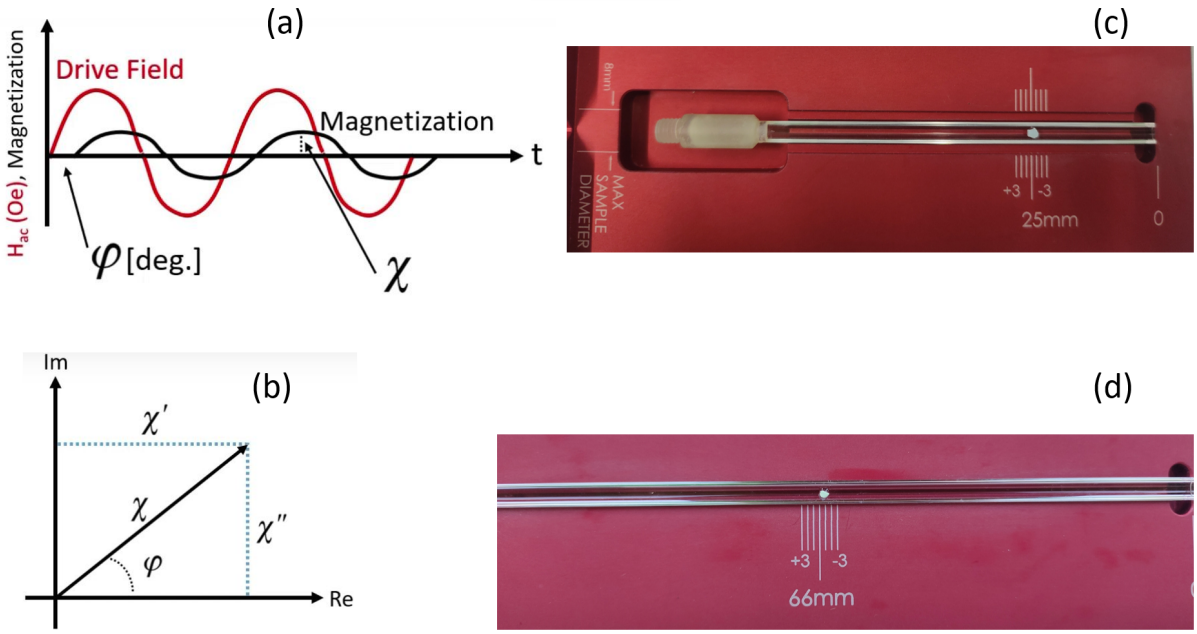

Figure 3.2: Sketches in (a) and (b) demonstrate the basic theory of the AC-field magnetization. The sketches are taken from [22]. Images in (c) and (d) are examples of samples fixed onto quartz holders using N-grease for measurements using PPMS, and MPMS-3, respectively.

3.3.3 Pulsed-Field Magnetization

The magnetization of samples in magnetic fields higher than 14 T (the upper limit of the PPMS) were measured at the High Field Magnet Laboratory Dresden (HLD) at the Helmholz Zentrum Dresden Rossendorf (HZDR) in pulsed-fields up to 60 T by an induction method using a coaxial pickup coil system [25]. The samples were loaded into a Kapton straw with 1.8 mm diameter and sealed with wooden plugs. The pulsed-field magnetization data were calibrated using static-field magnetization data obtained by means of MPMS-3 or PPMS. The measurements were supervised by Dr. Sven Luther.

Chapter 4

Magnetic Anisotropy, Magnetoelastic Coupling, and the Magnetic Phase Diagram of $Ni_{0.25}Mn_{0.75}TiO_3$

The present chapter has been published as a regular article in Physical Review B under the title "Magnetic anisotropy, magnetoelastic coupling, and the magnetic phase diagram of $Ni_{0.25}Mn_{0.75}TiO_3$" [26].

- A. Elghandour is first and corresponding author of the manuscript. He performed most of the measurements, analysed the data, and composed the figures and the manuscript draft.
- L. Gries performed the thermal expasnion and magnetostriction studies and was involved in their analysis and discussion.
- The single crystal under study was grown by K. Dey who also was involved in the XRD analysis (Fig. 1b).
- L. Singer carried out Energy-dispersive X-ray spectroscopy (EDS) measurements for sample characterisation.
- M. Uhlarz, M. Hoffmann. and S. Spachmann conducted measurements of pulsed field magnetization.
- R. Klingeler supervised the project and supported data analysis and manuscript writing.

Editors' Suggestion

Magnetic anisotropy, magnetoelastic coupling, and the magnetic phase diagram of $Ni_{0.25}Mn_{0.75}TiO_3$

A. Elghandour,[1,*] L. Gries,[1] L. Singer,[1] M. Hoffmann,[1] S. Spachmann,[1] M. Uhlarz,[2] K. Dey,[1,†] and R. Klingeler[1,‡]

[1]*Kirchhoff Institute for Physics, Heidelberg University, INF 227, 69120 Heidelberg, Germany*

[2]*Dresden High Magnetic Field Laboratory (HLD-EMFL), Helmholtz-Zentrum Dresden-Rossendorf, 01328 Dresden, Germany*

(Received 3 March 2023; accepted 1 June 2023; published 5 July 2023)

Thermodynamic and magnetic studies on high-quality single crystals are used to investigate the magnetic phase diagram and magnetostructural coupling in the mixed-spin system $Ni_{0.25}Mn_{0.75}TiO_3$. Clear anomalies in the thermal expansion at the spin ordering and spin reorientation temperatures,T_N and T_R, evidence pronounced magnetoelastic effects. The magnetic entropy is released mainly above T_N implying considerable short range magnetic order up to about $4 \times T_N$. This is associated with a large regime of negative thermal expansion of the c axis. Both T_N and T_R exhibit the same sign of uniaxial pressure dependence, which is positive (negative) for pressure applied along the b (c) axis. The magnetic phase diagrams are constructed and the uniaxial pressure dependencies of the ordering phenomena are determined. For magnetic fields $B \parallel b$ axis, a sign change and splitting of anomalies implies further magnetic phases. In addition to short-range magnetic order well above T_N, competing anisotropies yield a glasslike behavior as evidenced by a maximum in AC-χ ($T_{SG} \simeq 3.7$ K) and quasilinear temperature dependence of c_p. High-field magnetization up to 50 T demonstrates that in addition to antiferromagnetically ordered spins there are also only weakly coupled moments at 2 K with a sizable amount of about 15% of all Mn^{2+} spins present in the material. The observed changes in the pressure dependence and the magnetostrictive effects shed light on the recently observed flop of electric polarization from $P \parallel c$ to $P \parallel a$ [Phys. Rev. B **90**, 144429 (2014)], in particular, suggesting that the magnetoelectric effect is not directly related to magnetostriction.

DOI: 10.1103/PhysRevB.108.014406

I. INTRODUCTION

Mixed antiferromagnetic (AFM) systems with competing magnetic anisotropies have been extensively studied with regard to their underlying physics and as a platform to realize spin-glass states [1–5]. In such mixed AFM systems where, e.g., a magnetic ion (M) is partly substituted by another one (N), i.e., forming $M_{1-x}N_x$, long-range magnetic order appears in the vicinity of $x = 0$ and $x = 1$, whereas, it is suppressed at intermediate doping levels. The spin arrangement in the AFM long-range-ordered state is basically that of the parent compounds but with two different AFM sublattices resulting from the induced modulation around the magnetic ions [6,7] and the difference in their ionic radii [8,9]. A typical example is mixed ilmenite-structured titanates, $A_xMn_{1-x}TiO_3$ (A = Fe, Co, and Ni), where the substituent A is randomly distributed in the structure. Although, at intermediate x, spin-glass-like phases are observed, AFM long-range order evolves near the end sides of the phase diagrams and is suppressed in the doped systems [10–18]. The parent compounds $ATiO_3$ (A = Mn, Fe, Co, Ni) crystallize in a hexagonal lattice with space-group $R\bar{3}$ [19]. $MnTiO_3$ exhibits G-type AFM order with the crystallographic direction c as the magnetically easy axis [20]. In contrast, $FeTiO_3$, $NiTiO_3$, and $CoTiO_3$ show A-type AFM order with an easy-plane-like anisotropy perpendicular to the c axis [20–23]. This implies not only different exchange interactions, but also competing anisotropies in the mixed systems $A_xMn_{1-x}TiO_3$.

Experimental studies on $Ni_xMn_{1-x}TiO_3$ started three decades ago by Ito *et al.* [13] and Yoshizawa *et al.* [14] to address theoretical predictions [1,6] on the mixed AFM compounds and revived after the discovery of linear magnetoelectric effect (ME) in $MnTiO_3$ [24]. The general trends in $Ni_xMn_{1-x}TiO_3$ upon increasing the Ni-content x are as the following [13,15]: Initially, G-type AFM order is suppressed, and a spin-reoriented phase appears around $x \sim 0.2$. Specifically, at $x = 0.33$, G-type AFM order evolves at $T_N = 27.6$ K and spin reorientation at $T_R = 17.5$ K. The latter is accompanied by a flop in the electric polarization [18]. At intermediate concentrations, $0.38 \leqslant x \leqslant 0.45$, a spin-glass phase emerges [15–17,25]. Within this glassy phase and particularly at $x = 0.42$, $Ni_xMn_{1-x}TiO_3$ exhibits a linear ME [15,16]. Further increasing the Ni content to $x \geqslant 0.48$ results in an A-type AFM long-range-ordered phase, which does not show ME [18].

Here, we report detailed thermodynamic and magnetic studies on $Ni_{0.25}Mn_{0.75}TiO_3$ single crystals grown by the optical floating-zone technique. Our dilatometric studies provide quantitative information on magnetoelastic coupling in the mixed AFM system. These investigations have been motivated by recent studies on the parent compounds $MnTiO_3$ and $NiTiO_3$, which display pronounced thermal expansion

*ahmed.elghandour@kip.uni-heidelberg.de

†Present address: Clarendon Laboratory, University of Oxford, Parks Road, Oxford, OX1 3PU, United Kingdom.

‡klingeler@kip.uni-heidelberg.de

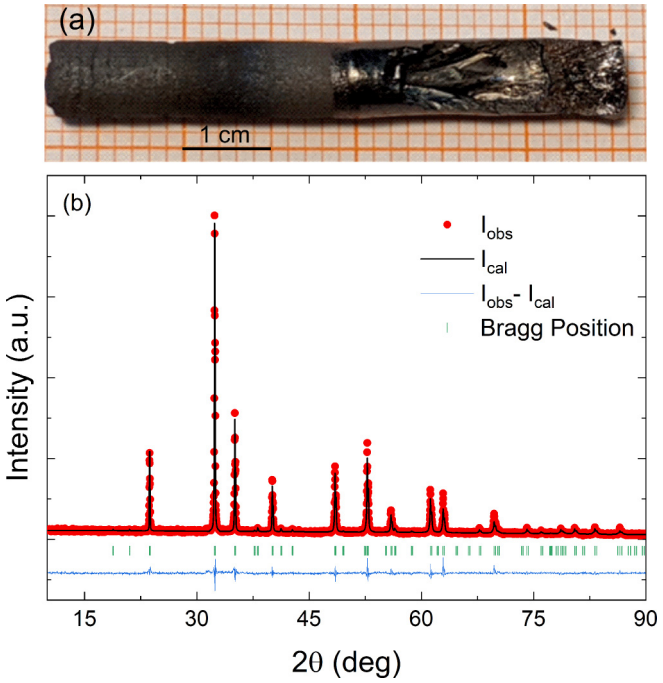

FIG. 1. (a) Picture of the $Ni_{0.25}Mn_{0.75}TiO_3$ boule grown under a 5-bar argon atmosphere. (b) Rietveld refinement fit (black line) of the room temperature XRD pattern (red markers) of a powdered $Ni_{0.25}Mn_{0.75}TiO_3$ single crystal. The difference between the observed and the calculated pattern is shown in blue. Vertical ticks in green denote the allowed Bragg positions of the ilmenite phase.

and magnetostriction anomalies associated with magnetic ordering and spin reorientation [26–28]. The present thermodynamic data elucidate magnetoelastic coupling in the *G*-type AFM-ordered phase and in the spin reoriented phase of $Ni_{0.25}Mn_{0.75}TiO_3$. Sharp anomalies in the thermal expansion and magnetostriction coefficients enable us to construct the magnetic phase diagrams and to identify an additional magnetic phase, thereby illustrating the interplay of spin and structure in the mixed anisotropic system under study. We also find that short-range correlations persist up to about $4 \times T_N$.

II. SINGLE-CRYSTAL GROWTH AND EXPERIMENTAL METHODS

Macroscopic single-crystals of $Ni_{0.25}Mn_{0.75}TiO_3$ were grown by the floating-zone technique in a high-pressure optical furnace [29,30] (HKZ, Scidre). Figure 1(a) shows a representative $Ni_{0.25}Mn_{0.75}TiO_3$ boule grown in Ar atmosphere at 5-bar pressure (Ar flow of 0.3 l/min) and at a growth rate of 12 mm/h with counterrotating rods at 10–25 rpm. The employed polycrystalline feed rods were made from stoichiometric amounts of NiO, MnO_2, and TiO_2 precursors similar to the procedure described in Ref. [26]. The single-crystal growth parameters were optimized in a series of growth experiments at various Ar:O_2 atmosphere mixtures, pressures, growth rates, and rotation speeds [31]. The phase purity of the grown crystals was confirmed by powder XRD (pXRD) studies of pulverized single crystals using a Bruker D8 Advance ECO diffractometer with Cu $K\alpha$ radiation [Fig. 1(b)]. The simulation of the pXRD data was performed by means of Rietveld refinements using the FULLPROF suite 2.0 [32] [see Fig. 1(b) and Table I). The composition was investigated by energy dispersive x-ray spectroscopy (EDX) using a JEOL JSM-7610F scanning electron microscope with a Thermo Scientific UltraDry silicon drift x-ray detector. The analysis yields a Ni:Mn ratio of 0.235(5):0.765(5), whereas, the ratio (Ni+Mn):Ti agrees to 1 within the error bars. Finally, from the grown boule, millimeter-sized grains were obtained, oriented for measurements along the [010], [$2\bar{1}0$], and [001] crystallographic axes and cut to cuboids. Their crystallinity was confirmed by Laue diffraction in backscattering geometry. The crystal structure was studied by means of single-crystal XRD at 100 K with Mo $K\alpha$ radiation (λ = 0.71073 Å) using an Agilent Technologies Supernova-E CCD four-circle diffractometer. The structural refinements confirm the $R\bar{3}$ space group and improve the accuracy of the crystallographic parameters. The obtained lattice parameters and relevant crystallographic information are listed in Table II.

TABLE I. Fractional atomic coordinates, Wyckhoff positions, and site occupation of $Ni_{0.25}Mn_{0.75}TiO_3$ as obtained from the refinement of powder XRD measurements at 300 K. The overall factor is set as B_{ov} = 2.278 55 and the isotropic Debye-Waller factor B_{iso} is fixed to zero. [Space-group: *R*-3 (148), $a = b$ = 5.113 259 Å, c = 14.147 032 Å (χ^2 = 2.82), $\alpha = \beta = 90°$, $\gamma = 120°$.]

Atom	Site	*x*	*y*	*z*	Occ
Ni	6*c*	0	0	0.35474	0.07999
Mn	6*c*	0	0	0.35474	0.25333
Ti	6*c*	0	0	0.14201	0.33333
O	18*f*	0.33329	0.04030	0.23906	1.00000

The obtained lattice parameters are in between the values for the parent compounds $MnTiO_3$ (a = 5.133 93(6) Å, c = 14.268 79(15) Å [31]) and $NiTiO_3$ (a = 5.0304 Å, c = 13.7862 Å [26]) and are slightly larger than the values found for x = 0.33 (5.12 and 14.15 Å) [18]. The reduced unit-cell volume upon increasing the Ni^{2+} concentration can be attributed to negative chemical pressure due to the different ionic radii of Mn^{2+} (0.83 Å) and Ni^{2+} (0.69 Å) [33]. By means of the lattice parameters of the end members, Vegard's law can be used to further confirm the doping level of $x \simeq 0.25$.

TABLE II. Selected crystallographic parameters from the EDX studies and from refinement of single-crystal XRD data obtained at 100 K.

Composition from EDX (Ni:Mn)	0.235(5):0.765(5)
Molar mass	151.69 g/mol
Crystal system, space group	Trigonal, $R\bar{3}$ (no. 148)
Unit cell:	
a	5.10799(4) Å
c	14.12863(11) Å
Calculated density	4.739 g/cm^3
Reflections collinear/independent	14886/1066 (R_{int} = 0.023)
Goodness-of-fit on F^2	1.172

The magnetization was studied by means of the Magnetic Properties Measurement System (superconducting quantum interference device, Quantum Design) and the Physical Properties Measurement System (PPMS-vibrating-sample magnetometer, Quantum Design) on an oriented single crystal of $Ni_{0.25}Mn_{0.75}TiO_3$ in the temperature range of 2 to 300 K and in magnetic fields up to 7 and 14 T, respectively. At low applied magnetic fields, both field-cooled (FC) and zero-field-cooled (ZFC) protocols were applied where the sample was cooled either in the external measurement field or the field was applied after cooling to the lowest temperature. The AC magnetization was measured in the temperature range from 2 to 40 K with 9-Oe AC excitation field, up to 3-T DC magnetic fields and frequencies ranging from 2 to 10 kHz, using the ACSMII option of the PPMS. Pulsed-magnetic-field magnetization was measured up to 50 T at Helmholtz Zentrum Dresden-Rossendorf by an induction method using a coaxial pick-up coil system [34]. The pulse raising time was 7 ms. The pulsed-field magnetization data were calibrated using static magnetic-field magnetization data obtained by means of PPMS. The specific-heat capacity was measured in the temperature range of 1.8–300 K using the heat-capacity option of the PPMS. High-resolution dilatometry measurements were performed by means of a three-terminal high-resolution capacitance dilatometer in a home-built setup placed inside a Variable Temperature Insert of an Oxford magnet system [35,36]. With this dilatometer, the relative length changes dL_i/L_i along the crystallographic b and c directions, respectively, were measured on an oriented cuboid-shaped single crystal of dimensions $2.400(2) \times 2.128(2) \times 0.559(2)\,\mathrm{mm}^3$. Measurements were performed in the temperature range of 2–300 K and in magnetic fields up to 15 T, applied along the direction of the measured length changes. The linear thermal expansion coefficients $\alpha_i = 1/L_i dL_i(T)/dT$ were obtained. In addition, the field-induced length changes, $dL_i(B_i)$, were measured at different fixed temperatures between 2 and 40 K and in magnetic fields up to 15 T. The longitudinal magnetostriction coefficients, $\lambda_i = 1/L_i dL_i(B_i)/dB_i$, were derived.

III. EVOLUTION OF MAGNETIC ORDER AT $B = 0$ T

In zero magnetic field, $Ni_{0.25}Mn_{0.75}TiO_3$ exhibits two magnetic phase transitions as evidenced by the static magnetic susceptibility and the specific heat in Fig. 2. Specifically, there is a jumplike feature in the specific-heat c_p/T at $T_N = 34.8(6)$ K and a rather symmetric hump at $T_R \sim 14.8(4)$ K [see Fig. 2(c)]. The jump at T_N amounts to $\Delta c_p \approx 0.54(11)$ J/(mol K). The magnetic nature of both transitions is evident from associated anomalies in the static magnetic susceptibility and its derivative as shown in Figs. 2(a) and 2(b), respectively. At high temperatures, the magnetic susceptibility χ_i along the different crystallographic axes i obey a Curie-Weiss-like behavior (see Fig. 1 in the Supplemental Material (SM) [37]). At T_N, χ_c displays a clear kink whereas only very small anomalies are observed for the other directions, thereby confirming the easy magnetic c axis in the long-range -ordered phase below T_N. This is particularly evident when Fisher's specific-heat $\partial(\chi T)/\partial T$ is considered, which is proportional to the magnetic specific heat [38]. It displays a λ-shaped behavior only for the $B \parallel c$ axis [Fig. 2(b)]. Upon further cooling, the

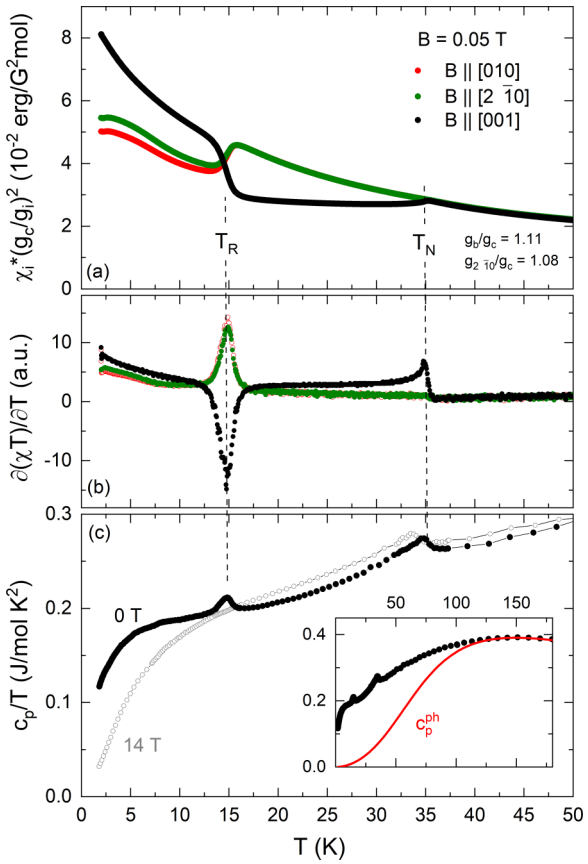

FIG. 2. (a) Static magnetic susceptibility $\chi = M/B$, of $Ni_{0.25}Mn_{0.75}TiO_3$ as a function of temperature measured along three different crystallographic directions at applied magnetic-field $B = 0.05$ T. The data have been normalized to the c-axis g factor as fitted to the high-temperature behavior. (b) Corresponding derivatives $\partial(\chi T)/\partial T$. (c) Specific-heat capacity, represented by c_p/T, measured both at zero magnetic field and at $B \parallel = 14$ T. The inset shows the zero-field specific-heat data over an extended temperature range, including an estimated representation of the phononic background (see the text). The vertical dashed lines mark the onset of the long-range magnetic ordering at T_N and the spin reorientation at T_R.

jumplike features, visible in the magnetic susceptibility χ_i at T_R, suggest rotation of the spins into the ab plane. We note the discontinuous nature of the anomaly at T_R.

Fitting χ_c between 175 and 300 K by means of an extended Curie-Weiss law including a temperature-independent term, χ_0, yields the Curie constant $C = 3.5(2)$ erg K mol^{-1} G^2, the Weiss temperature $\Theta = -112(6)$ K, and $\chi_0 = 8.05 \times 10^{-4}$ erg mol^{-1} G^{-2}. Differences in the static magnetic susceptibilities χ_i at high temperatures can be explained by the ratio g_{010}:$g_{2\bar{1}0}$:$g_{001} \simeq 2$:1.94:1.8 of the corresponding g factors (g_i) (see Fig. 2 in the SM). The large negative value of the Weiss temperature indicates the presence of dominant antiferromagnetic exchange interactions, aligning with the previously recorded neutron-scattering results on $Ni_{0.33}Mn_{0.67}TiO_3$ [18]. The effective moment $\mu_{\mathrm{eff}} \approx 5.2(1)\mu_B$ is derived from the Curie constant. It agrees well with the expected value calculated using the g-factors g_{Mn} and g_{Ni} of the parent compounds [26,39].

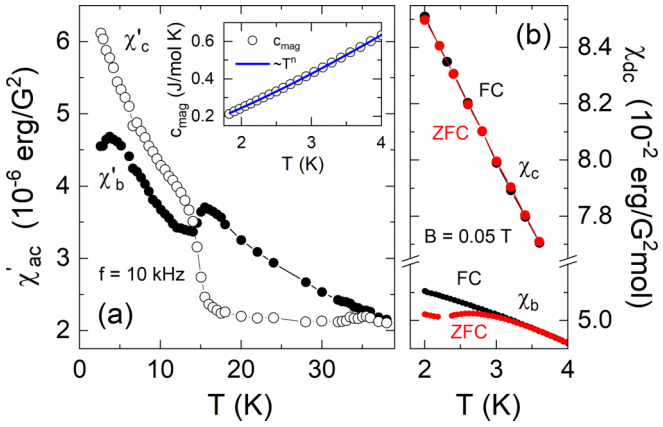

FIG. 3. (a) Real part of AC magnetic susceptibility of $Ni_{0.25}Mn_{0.75}TiO_3$ measured along the crystallographic b and c axes at $f = 10$ kHz. The inset: Magnetic specific heat at low temperatures. The (blue) line represents a fit to the data (see the text). (b) Static magnetic susceptibility measured along the crystallographic b and c axes at $B = 0.05$ T, highlighting the differences between FC and ZFC measurements.

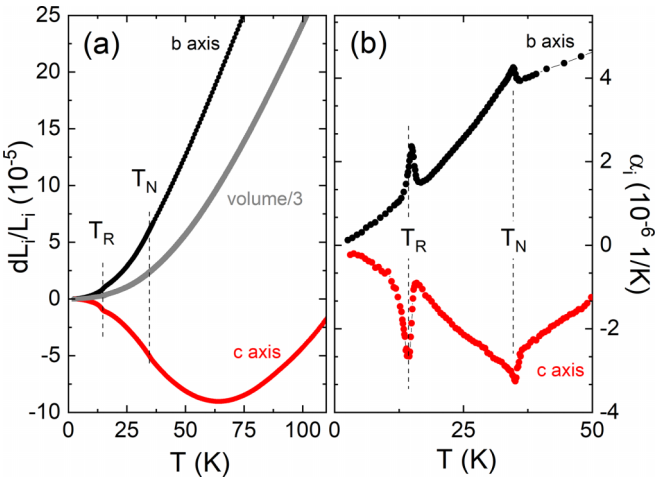

FIG. 4. (a) Relative length changes dL_i/L_i ($i = b$ and c), of $Ni_{0.25}Mn_{0.75}TiO_3$ measured along the crystallographic i axis in zero applied magnetic field; light gray markers represent the relative volume changes. (b) Corresponding uniaxial thermal expansion coefficients α_i. The dashed lines mark T_N and T_R.

AC magnetic susceptibility studies confirm the anomalies at T_N and T_R, but do not indicate any frequency dependence in the regime of $2.5 \leqslant f \leqslant 10$ kHz (see Fig. 3 in the SM). We also do not observe any finite dissipative signal χ''. In χ_b', apart from the anomalies observed at T_N and T_R, we observe an additional broad maximum at $T^* \approx 3.7$ K as depicted in Fig. 3(a) T^* corresponds to the beginning of a thermal hysteresis region seen in χ_b between the ZFC and the FC data as shown in Fig. 3(b). In contrast, no thermal hysteresis is observed in χ_c and χ_c'. In the same temperature regime, the magnetic specific heat shows no anomaly but follows a $c_p(T) \propto T^n$ behavior with $n \approx 1.3(1)$ [see the inset of Fig. 3(a)]. We note that the observed exponent n does not correspond to the expectations $c_p(T) \propto T^3$ describing the low-temperature magnon excitations in a long-range-ordered three-dimensional (3D) antiferromagnet [40].

The onset of long-range magnetic order at T_N and spin reorientation at T_R are associated with distinct lattice changes as demonstrated by clear anomalies in the thermal expansion (see Fig. 4). In addition, the thermal expansion exhibits an anisotropic behavior up to the highest measured temperatures. The evolution of magnetic order is signaled by kinks in the relative length changes dL_i/L_i at T_N and by slightly λ-shaped anomalies in its corresponding thermal expansion coefficients α_i. Although there is a positive thermal expansion of the b axis in the whole temperature regime under study, the c axis initially shrinks upon heating and expands only above $T = 60$ K. Opposite trends for the different axes are also observed for the actual anomalies in α_i at T_N, which show opposite signs. Qualitatively, the anomalies in α_i imply a positive uniaxial pressure dependence ($\partial T_{N/R}/\partial p_b > 0$) of T_N and T_R, whereas, both are suppressed by uniaxial pressure applied along the c axis.

A. Magnetic phase diagram

Applying magnetic fields up to 15 T hardly changes the long-range-ordering temperature T_N but significantly affects the spin-reoriented phase and the associated transition temperature T_R. This is clearly visible in the specific-heat data shown in Fig. 2(c). At $B = 14$ T, whereas, the anomaly at T_R is completely suppressed, the one at T_N is only very slightly shifted to lower temperatures. Due to pronounced magnetoelastic coupling in $Ni_{0.25}Mn_{0.75}TiO_3$, which is evidenced in Fig. 4, the magnetic-field effects on the phase boundaries can be very well traced by thermal expansion and magnetostriction measurements. As displayed in Fig. 5, applying a field of $B = 1$ T yields a significant decrease (increase) of T_R when applied along the b axis (c axis). Notably, for the $B \parallel b$ axis, the anomaly at T_R changes its sign from positive to negative for $B \geqslant 1$ and up to $B = 14$ T [see Fig. 5(a)]. At low magnetic fields, the phase transition is also detected in the static magnetic susceptibility χ_b, which displays a noticeable jumplike feature at T_R and a corresponding peak in $\partial(\chi T)/\partial T$. However, these anomalies become weaker as the

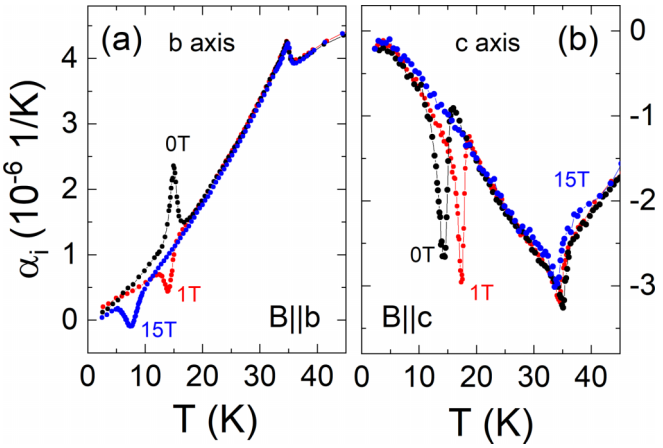

FIG. 5. Temperature dependence of the thermal expansion coefficient α_i ($i = b$ and c), measured at different applied magnetic fields along (a) the b axis, and (b) the c axis.

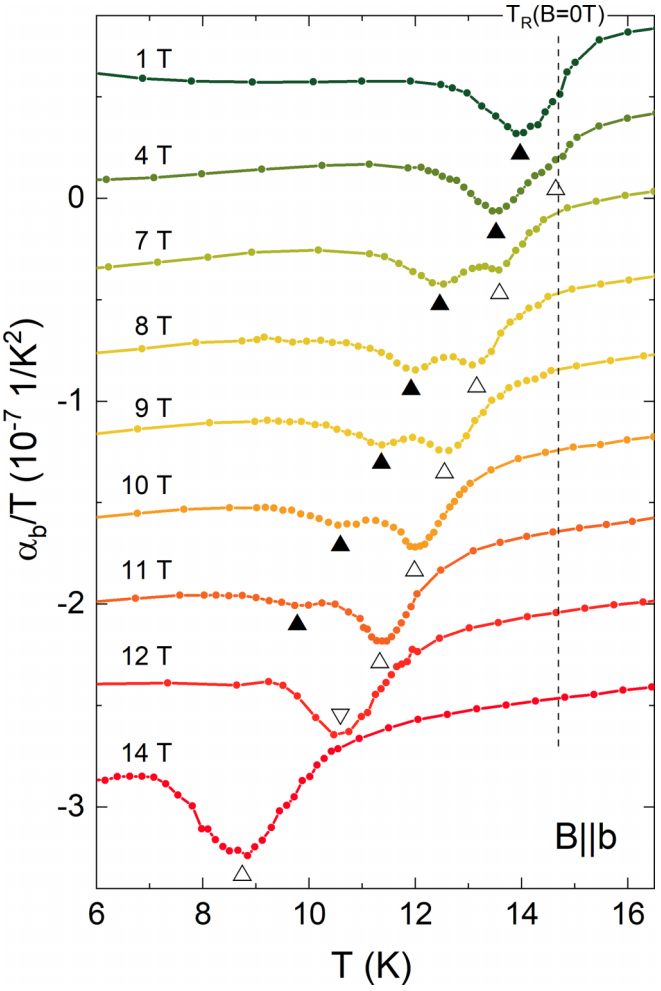

FIG. 6. Thermal expansion coefficient α_b/T at different magnetic fields $B \parallel b$ axis. Triangles mark two features as discussed in the text; the dashed line displays $T_R(B = 0\ \mathrm{T})$.

magnetic field gradually increases and completely vanish at magnetic-fields $B \parallel b \geqslant 0.8$ T (see Fig. 4 in the SM). The data, hence, imply that the sign change in α_b at T_R is accompanied by the disappearance of the anomalies observed in χ_b.

The evolution of the anomaly observed at T_R in α_b, $B \parallel b \geqslant 1$ T, is shown in Fig. 6. After the anomaly changed sign as evidenced by the data obtained at $B = 1$ T, an additional feature appears, which is only faint at 1 T but increases for larger fields, yielding two clearly separated features split by more than 1 K at 7 T. Both the emerged (marked by filled triangles) and the initial (marked by open triangles) features shift to lower temperatures with increasing the applied magnetic field, which indicates their antiferromagnetic nature. In addition, the emerged feature becomes more pronounced for higher fields, whereas, the initial one decreases until it is not detectable anymore above 11 T (see Fig. 6). In contrast, the thermal expansion and magnetization data signal a significant shift of T_R to higher temperatures when applying the $B||c$ axis so that the phase boundary merges into T_N slightly above 2 T (see Fig. 9, and Figs. 5 and 9 in the SM).

The G-type AFM phase appearing at zero magnetic field in the temperature regime $T_R < T < T_N$ (i.e., AF1 in Fig. 9)

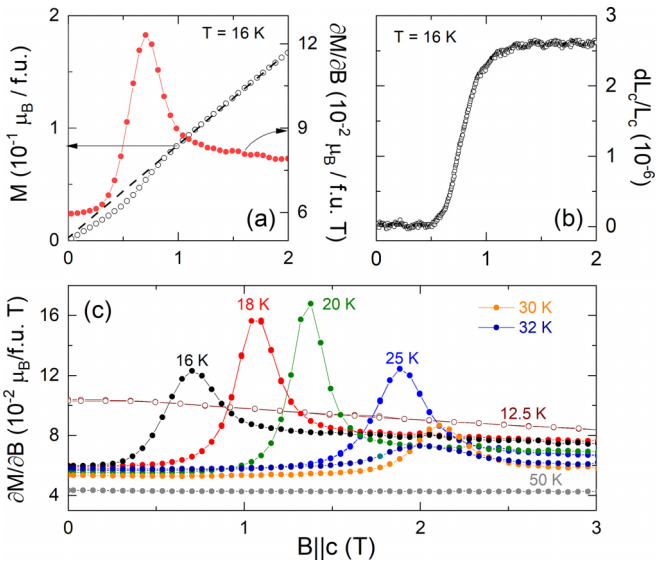

FIG. 7. (a) Isothermal magnetization, measured at 16 K, for the $B \parallel c$ axis and corresponding magnetic susceptibility $\partial M/\partial B$. The dashed line linearly extrapolates the high-field behavior to zero field. (b) Magnetostriction dL_c/L_c, at $T = 16$ K as a function of the magnetic-field $B \parallel c$ axis. (c) Magnetic susceptibility for the $B \parallel c$ axis in the temperature regime of 16 K $\leqslant T \leqslant$ 50 K. Peaks are associated with the spin-flip transition at B_{c2}.

is further investigated by magnetization and magnetostriction studies presented in Fig. 7. At $T = 16$ K, when the spins are predominately parallel to the c axis [18], magnetic fields $\parallel c$ yield a spin-flop-like transition at $B_{\mathrm{SF}} = 0.62(8)$ T [see Fig. 7(a)]. The critical field B_{SF} associated with this transition into the spin-reoriented phase (AF2 in Fig. 9) is signaled by the peaks in $\partial M/\partial B$. Upon heating, it shifts towards higher

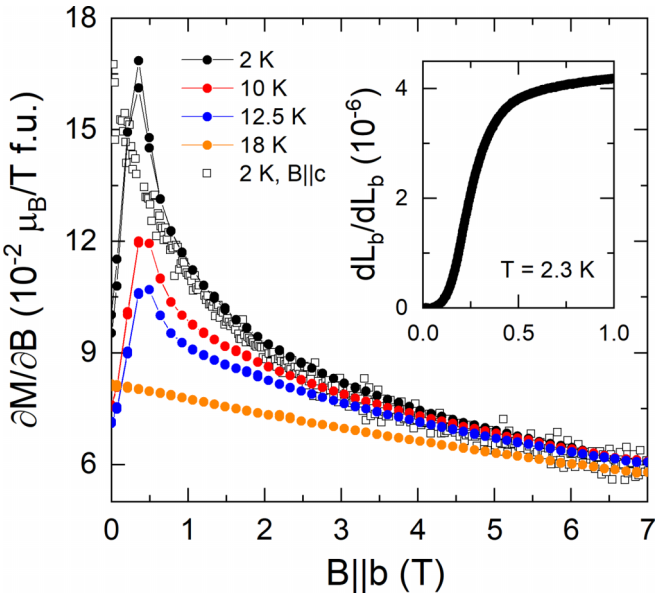

FIG. 8. Magnetic susceptibility $\partial M/\partial B$ in the temperature regime of 2 K $\leqslant T \leqslant$ 18 K for $B \parallel b$ axis. The peaks signal B_{c1} (see the text). Open squares show $\partial M/\partial B$ at 2 K with the $B \parallel c$ axis. The inset: Magnetostriction $dL_b/L_b(B \parallel b)$ at $T = 2.3$ K.

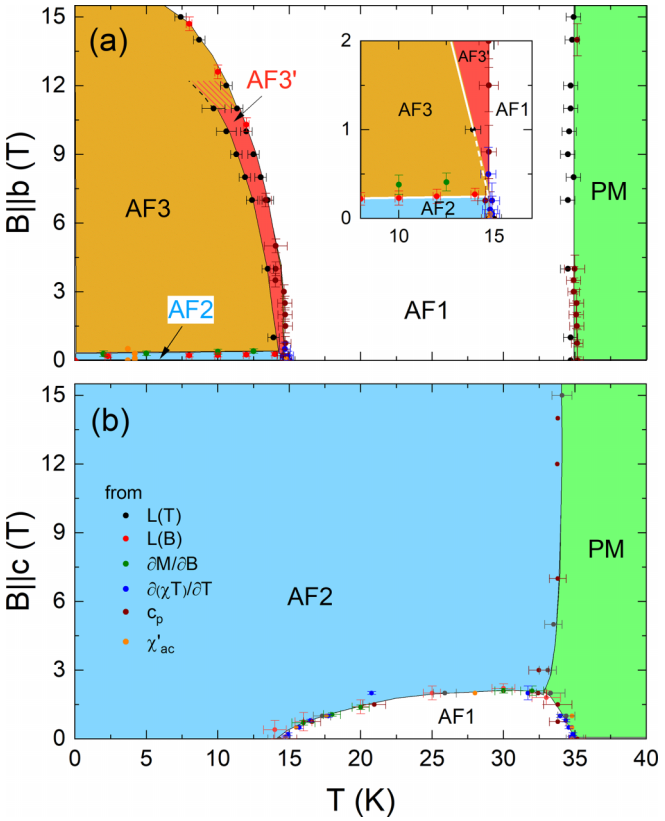

FIG. 9. Magnetic phase diagram of $Ni_{0.25}Mn_{0.75}TiO_3$ derived from magnetization $M(T, B)$, thermal expansion, and magnetostriction $L(T, B)$, χ_{ac}, and specific-heat data for the (a) $B \parallel b$ and (b) $B \parallel c$ axes. The insert in (a) shows the enlarged region around 15 K. The colors distinguish paramagnetic (PM), G-type AF (AF1), spin-reoriented AF (AF2), and field-induced AF phases (AF3/AF3′). T_N, T_R, B_{SF}, and B_{c1} are the associated phase boundaries described in the text.

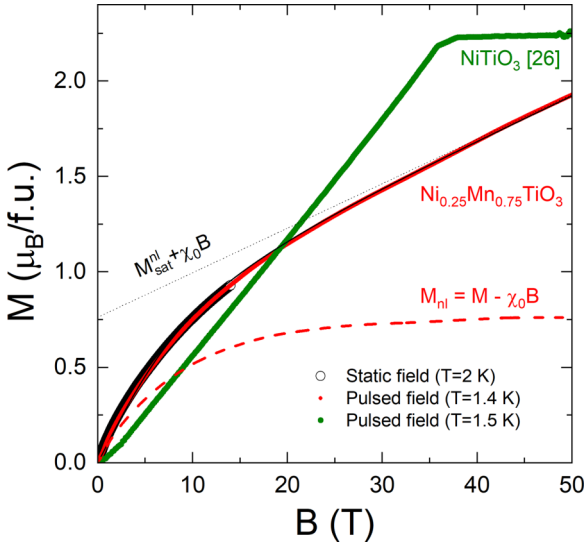

FIG. 10. Magnetization of $NiTiO_3$ (from Ref. [26]) and $Ni_{0.25}Mn_{0.75}TiO_3$ up to 50 T. Open circles show the averaged static field magnetization of $Ni_{0.25}Mn_{0.75}TiO_3$ single crystals measured up to 14 T. Pulsed-field data are from up sweeps. The data of $Ni_{0.25}Mn_{0.75}TiO_3$ are well described by the sum of a modified Brillouin function and a linear term $\chi_0 B$ (see the text). The dashed line shows the nonlinear magnetization $M_{nl} = M - \chi_0 B$.

fields and disappears above T_N [see Fig. 7(c)]. The metamagnetic transition is also characterized by a sharp increase of the c axis length amounting to $\Delta L_c/L_c = 2.6 \times 10^{-6}$ [Fig. 7(b)]. Below T_R, $B \| c$ does not drive a spin-flop transition [Fig. 7(c)], which agrees to the suggested spin rotation. In contrast, for $B \| b$ a metamagnetic transition appears only below T_R at a critical field of $B_{C1} \sim 0.4$ T, which barely depends on the temperature (Fig. 8). The high-field phase for $B \parallel b$ is labeled AF3 in Fig. 9). Again, the metamagnetic transition is associated with anomalous length changes (Fig. 8, the inset), amounting to $\Delta L_b/L_b = 3.9 \times 10^{-6}$ at $T = 2.3$ K.

The observed clear features in magnetization, thermal expansion, magnetostriction, and specific heat enable us to construct the magnetic phase diagrams for both $B \| b$ and $B \| c$ as shown in Fig. 9. For $B \| c$, the G-type antiferromagnetic phase with spins $\| c$ evolving in zero field at T_N (AF1 phase) forms a distinct dome bounded by $T_R(B)$ and $B_{SF}(T)$ towards the spin-reoriented AF2 phase [see Fig. 9(b)]. The transition AF1 to AF2 is associated with significant lattice changes. In the field region of the dome, T_N is visibly suppressed by $B \parallel c$, but it increases for higher fields ($B \parallel c > 2\,T$), which implies the relevance of critical fluctuations around the tricritical point. A field-driven magneto-structural transition is also observed for $B \| b$ where the low-field AF2 phase is separated by a rather field-independent phase boundary $B_{c1}(T)$ from the AF3 phase. Note, AF2 and AF3 phases feature uniaxial pressure dependencies of opposite sign. In contrast to T_N, which only very weakly depends on $B \parallel b$, AF3 is considerably suppressed and we extrapolate the upper critical field $B_c^{AF3} \simeq 17(2)$ T. Notably, starting from B_{c1}, an intermediate phase AF3′ appears. The thermal-expansion anomaly size associated with the phase boundary between AF3 and AF3′ continuously decreases when increasing $B \parallel b$ and cannot be detected above 11 T in our dilatometric data. This behavior suggests the decrease in the pressure dependence or negligible associated specific-heat changes. Since the boundary AF3/AF3′ is not associated with a clear anomaly in the magnetization, we neither can trace it by magnetic measurements in this regime of the phase diagram.

Lastly, our data reveal the presence of weakly coupled magnetic moments at low temperatures. In contrast to $NiTiO_3$ which magnetization increases linearly up to the saturation field as expected for an long-range-ordered AFM [26], magnetization of $Ni_{0.25}Mn_{0.75}TiO_3$ exhibits pronounced right-bending behavior (see Fig. 10). Note, that the pulsed-field powder magnetization data perfectly agree with the single-crystal studies up to 14 T. The data can be described by the sum of a modified Brillouin function B_S and a linear term, i.e., $M_{sat}B_S(x) + \chi_0 B$; $x = g\mu_B SB/[k_B(T + \Theta^*)]$ with M_{sat} as the saturation magnetization of the right-bending term, spin S, field-independent susceptibility χ_0, Boltzmann constant k_B, Bohr magneton μ_B, and the g factor. Θ^* is a parameter to account for magnetic interactions between the weakly coupled moments. The linear term mainly reflects the response of the long-ranged AF-ordered phase. The nonlinear term $M_{nl}(B) = M(B) - \chi_0 B$ implies the presence of rather weakly

coupled spins saturating already at intermediate fields. $M_{\rm sat}$ is the fully saturated moment of the weakly coupled spins. Phenomenologically, using $g = 1.99$ and $S = 5/2$ of the Mn^{2+} spins, the data are described by $\Theta^* = 15.5$ K, $M_{\rm sat} = 0.75$ μ_B/f.u., and $\chi_0 = 0.023$ μ_B/(T f.u.). The value of $M_{\rm sat}$ may be read from the data without fitting, and it clearly exceeds the fully saturated moment of all Ni^{2+} spins in $Ni_{0.25}Mn_{0.75}TiO_3$ ($S = 1$, $g = 2.14$, $M_{\rm sat}^{\rm Ni} \simeq 0.53$ μ_B/f.u.) [41] so that $M_{\rm nl}(B)$ cannot be attributed only to the Ni^{2+} subsystem. Attributing $M_{\rm nl}(B)$ to only Mn^{2+} spins would imply that about 15% of them are only weakly coupled. As will be pointed out below, this value might further increase at higher temperatures. In general, the observation of weakly coupled moments is in accordance with the observed low-temperature behavior of the static magnetic susceptibility displayed in Fig. 2(a) where for $B \parallel c$ a Curie-like increase is observed in the AFM-ordered phase. Concomitantly, both $\chi_{[010]}$ and $\chi_{[2\bar{1}0]}$ increase upon cooling below T_N, too, which behavior differs from what is expected in conventional antiferromagnets as it shows much larger magnetization with respect to the paramagnetic phase.

IV. DISCUSSION

Our data imply the evolution of long-range antiferromagnetic order at $T_N \simeq 35$ K and reorientation of the spin direction at $T_R \simeq 15$ K. This agrees to the sequence of phase transitions reported in the established phase diagram of $Ni_xMn_{1-x}TiO_3$ [13,15]. As compared to the mother compound $MnTiO_3$, which shows $T_N \simeq 64$ K, the tendency for long-range magnetic order is significantly reduced by Ni doping. Although our results fit the expected phase boundary $T_N(x)$, we find T_R in between the two temperatures proposed as the start and the end temperatures of the spin rotation in Ref. [13]. The onset of long-range magnetic order in $Ni_{0.25}Mn_{0.75}TiO_3$ at T_N is signaled by clear anomalies in $\chi_{B\parallel c}$, c_p, and thermal expansion (Figs. 2 and 4), which confirms the easy magnetic c axis and, in particular, shows significant magnetoelastic coupling. The negative thermal expansion along the c axis as well as strong magnetic-field effects on the specific heat well above T_N suggest the presence of short-range-ordering phenomena in the paramagnetic phase. The presence of short-range magnetic correlations above T_N results in associated magnetic entropy changes, which can be estimated by comparison with the bare lattice contribution. The latter may be obtained by fitting the specific heat well above T_N by an appropriate phononic model. This results in very similar phonon specific heat as found in $MnTiO_3$. Since, in the following, we will compare the entropy changes in $Ni_{0.25}Mn_{0.75}TiO_3$ and $MnTiO_3$, for the following entropy analysis, we employ the phonon specific heat from Ref. [28] and account for the different atomic masses by multiplying with 1.015 [see Fig. 11(a)].

Subtracting the lattice contribution from the measured specific heat gives the magnetic specific heat $c_p^{\rm mag}$. Integrating $c_p^{\rm mag}/T$ yields the magnetic entropy changes $\Delta S_{\rm m} = 12.3(7)$ J/(mol K), which is close to the full expected magnetic entropy of $0.75R \ln 6 + 0.25R \ln 3 \approx 13.4$ J/(mol K). Notably, our analysis implies magnetic entropy changes up to about 130 K, i.e., persistence of short-range magnetic order up to about $\simeq 4T_N$. The presence of considerable short-range magnetic order is further confirmed by the fact that the

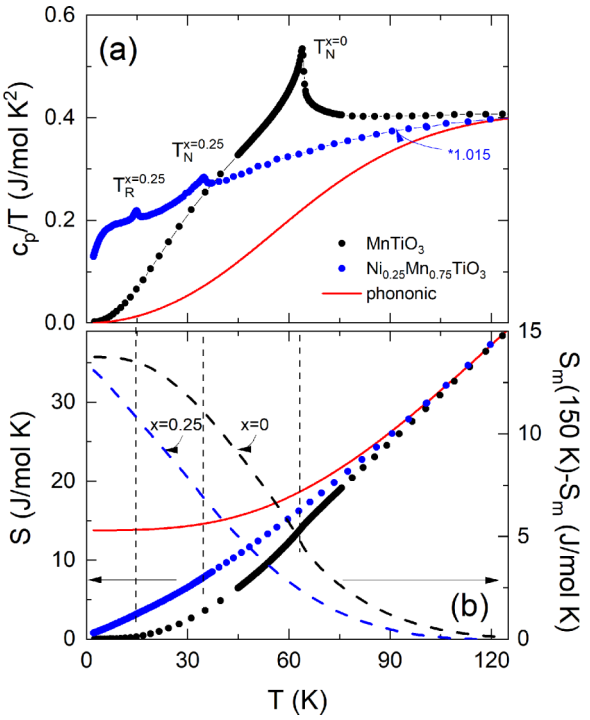

FIG. 11. (a) Temperature dependence of the specific-heat c_p/T of $Ni_xMn_{1-x}TiO_3$ with $x = 0$, i.e., $MnTiO_3$ (from Ref. [28]), and $x = 0.25$ measured at $B = 0$ T. The $Ni_{0.25}Mn_{0.75}TiO_3$ data are multiplied by 1.015 to account for the atomic mass difference. The red line presents the lattice contribution $c_p^{\rm ph}$ of $MnTiO_3$. (b) Corresponding entropy changes (left ordinate) derived from integrating c_p/T. $S_{\rm ph}(T)$ (red line) and $S_{x=0.25}(T)$ (blue circles) are shifted to match $S_{x=0}(T)$ above 120 K (see the text). Right ordinate: Changes in the magnetic entropy for both doping levels with respect to its value at 150 K.

observed anomaly Δc_p, at T_N, is rather small as it only amounts to a few percent of the value predicted by mean-field theory. Quantitatively, the specific-heat jump at T_N amounts to $\Delta c_p = 0.54(11)$ J/(mol K), which is only a very small fraction ($\approx$3%) of the expected mean-field value $\Delta c_p = R\frac{5S(S+1)}{S^2+(S+1)^2} \approx 18.9$ J/(mol K) [42]. Note, that the actual jump size associated with the measured anomaly can be even smaller as it may be superimposed by critical fluctuations. Such a small specific-heat anomaly implies significant short-range spin order above T_N and/or considerable spin disorder below T_N.

Our experimental data show short-range magnetic order well above T_N as well as weakly coupled moments and a glasslike behavior at low temperatures. In Fig. 11(b), we illustrate how magnetic entropy is consumed upon cooling by comparing the specific heat and entropy changes appearing in $Ni_{0.25}Mn_{0.75}TiO_3$ and $MnTiO_3$ [28] alongside the lattice contributions. In $MnTiO_3$, the specific-heat data illustrate a typical example of evolution of 3D long-range magnetic order. In $Ni_{0.25}Mn_{0.75}TiO_3$, at high temperatures, the specific-heat data are similar to those of $MnTiO_3$, which we attribute to the lattice. The main effects of 25% Ni doping are as follows: (1) Suppression of T_N and of the anomaly size as discussed above. (2) Upon cooling below T_N, in $Ni_{0.25}Mn_{0.75}TiO_3$, the entropy is consumed in a quasilinear manner, which qualitatively

differs from the behavior in $MnTiO_3$. This is particularly visible in Fig. 11(b), where in addition to the measured total entropy changes, the relative changes in the magnetic entropy with respect to the value at high temperature are shown. The figure illustrates how different magnetic order evolves in $Ni_{0.25}Mn_{0.75}TiO_3$ as compared to $MnTiO_3$. (3) In $Ni_{0.25}Mn_{0.75}TiO_3$, the low-temperature behavior exhibits a quasilinear behavior for $T \lesssim 4$ K where we find $c_p \sim T^{1.3}$ as shown in the inset of Fig. 3(a). This contrasts a T^3 behavior expected for a 3D AFM, which is observed in $MnTiO_3$. Quasilinear behavior of c_p at low temperatures was previously reported for the spin-glass state of $Ni_{0.42}Mn_{0.58}TiO_3$ [15] and for canonical spin-glass systems, such as CuMn [43] and ScGd [44].

The presence of considerable magnetic disorder evidenced by our analysis of the entropy changes qualitatively agrees with the observation of weakly coupled magnetic moments and a glassylike feature in the AC magnetic susceptibility ($T_{SG} \simeq 3.7$ K). For $Ni_{0.4}Mn_{0.6}TiO_3$, Solanki *et al.* observe a similar feature at 9.1 K and report an XY-like spin-glass state with quasi-two-dimensional antiferromagnetic order [17]. By inelastic neutron scattering studies, they conclude the presence of short-range-ordered antiferromagnetic clusters with short-lived spin correlations in the XY-like SG state. The latter observation may be associated with the presence of weakly antiferromagnetically coupled moments in $Ni_{0.25}Mn_{0.75}TiO_3$ as demonstrated by in the high-field magnetization data in Fig. 10. Our findings also raise the question of the origin of the glasslike behavior. One may speculate about a dynamic process, which involves partial freezing of weakly coupled moments at low temperatures resulting in the (at 1.4 K) experimentally observed number of weakly coupled moments. This scenario implies that the number of weakly coupled moments increases upon heating. However, our M vs B data do not enable us to distinguish the response of weakly coupled moments from the entire magnetic response at higher temperatures. The observed number of about 15% of all Mn^{2+} spins present in the material at 1.4 K may, hence, increase at higher temperatures.

Magnetoelastic coupling is further analyzed by quantifying and comparing the thermal expansion and the heat-capacity anomalies in α_i and c_p. The ratio of these quantities yields the uniaxial and hydrostatic pressure dependencies of the associated ordering phenomena by exploiting the Clausius-Clapeyron relation for discontinuous phase transitions and the Ehrenfest relation for continuous ones [45,46]. In $Ni_{0.25}Mn_{0.75}TiO_3$, we consider the anomaly at T_N a continuous phase transition, and its size has been determined by means of a same area construction [47]. At $T_N(B = 0\ \mathrm{T})$ this yields $\Delta\alpha_b = 0.5(1) \times 10^{-6}$ (1/K) and $\Delta\alpha_c = -0.80(15) \times 10^{-6}$ (1/K) (see Figs. 7 and 10 in the SM [37]). Using these values as well as $\Delta c_p = 0.54(11)$ J/(mol K) and the molar volume $V_m = 3.215 \times 10^{-5}$ m^3/mol, the Ehrenfest relation,

$$\left.\frac{\partial T_N}{\partial p_i}\right|_B = T_N V_m \frac{\Delta\alpha_i}{\Delta c_p} \tag{1}$$

yields $\partial T_N/\partial p_b = 1.1(3)$ and $\partial T_N/\partial p_c = -1.7(5)$ K/GPa for uniaxial pressure applied along the b and the c axes, respectively. Furthermore, T_N depicts a small positive hydrostatic pressure dependence of $\partial T_N/\partial p = 0.4(5)$ K/GPa as qualitatively shown by the anomaly in the volume thermal-expansion coefficient at T_N.

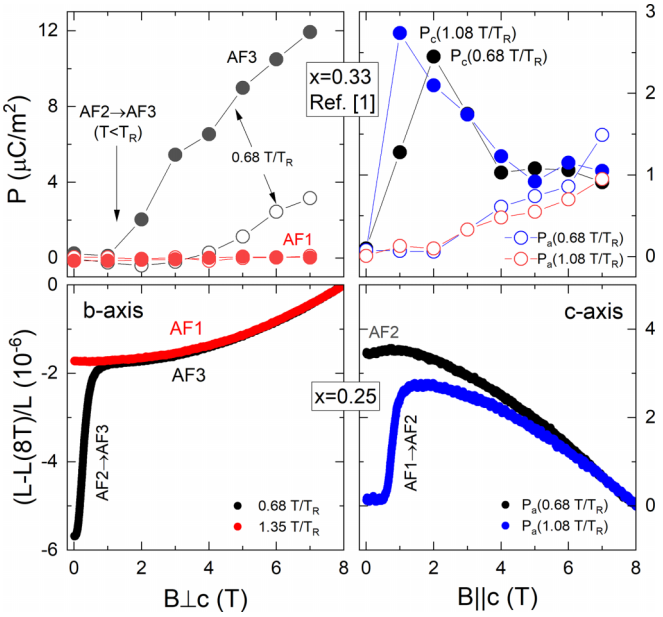

FIG. 12. Magnetic-field dependence of electric polarization ($x = 0.33$, data from Ref. [18] (upper panel; open/filled markers show P_a/P_c) and magnetostriction (lower panel; $x = 0.25$) in $Ni_xMn_{1-x}TiO_3$. In order to compare the results, the data are shown for same values of reduced temperature T/T_R, using $T_R(x = 0.33) = 17.5$ K [18] and $T_R(x = 0.25) = 14.8$ K.

The uniaxial pressure dependencies of T_R are derived from the corresponding jumps $\Delta L_b/L_b = -2.0(2) \times 10^{-6}$, $\Delta L_c/L_c = 3.1(2) \times 10^{-6}$, and $\Delta S = -0.027(3)$ J/(mol K). Using the Clausius-Clapeyron relation for a discontinuous phase transition [45],

$$\left.\frac{\partial T_R}{\partial p_i}\right|_B = V_m \frac{\Delta L_i/L_i}{\Delta S} \tag{2}$$

yields the uniaxial pressure dependencies $\partial T_R/\partial p_b = 2.3(4)$ and $\partial T_R/\partial p_c = -3.7(5)$ K/GPa. Following the phase boundary $T_R(B)$ [AF1 $\rightarrow$ AF2/AF′ in Fig. 9(a)], the signs of the thermal expansion anomalies change at $B \simeq 1$ T implying opposite uniaxial pressure dependencies for AF1 $\rightarrow$ AF2 and AF1 $\rightarrow$ AF3′. The observed changes in pressure dependence and, in particular, the magnetostrictive effects shed light on the recently observed flop of electric polarization from $P \parallel c$ to $P \parallel a$ in $Ni_{0.33}Mn_{0.67}TiO_3$ [18]. Chi *et al.* [18] associate the linear ME response with rotation of the collinear spins away from the c axis for $T < T_R$. Comparison of polarization and magnetostriction data at the same reduced temperatures T/T_R yields the following observations (see Fig. 12): For $B \perp c$, (1) the jump in length at the transition AF2$\rightarrow$ AF3 indicates the onset of finite ME effect. (2) Although magnetostriction is indiscernible in AF3 and AF1, a finite field-induced polarization appears only in AF3, whereas, it is negligible in AF1. (3) For $B \| c$, both AF1 and AF2 show the ME effect and P_c peaks at 1 to 2 T. However, whereas, for $T > T_R$ there are anomalies both in P_c and L_c for $T < T_R$, the peak in P_c is not associated

with a jump in $L(B)$. From (1)–(3), we conclude that magnetoelastic coupling is prominent and yields distinct structural anomalies at the phase boundaries as well as differences in the magnetostrictive response of the different magnetic phases and, correspondingly, the different ME regimes. However, observation (2) suggests that the ME effect in $Ni_xMn_{1-x}TiO_3$ may not be directly related to magnetostriction.

V. CONCLUSIONS

To conclude, we report detailed dilatometric, specific heat, and magnetic studies on macroscopic single crystals of $Ni_{0.25}Mn_{0.75}TiO_3$grown by means of the optical floating-zone method. Our data imply the evolution of long-range magnetic order at $T_N \simeq 35$ K and a spin reorientation at $T_R \simeq 15$ K. The latter is of discontinuous nature and attributed to competing magnetic anisotropies of Mn^{2+} and Ni^{2+} magnetic moments. We find clear anomalies in the length changes at the phase boundaries, indicating pronounced magnetoelastic coupling and sizable pressure dependencies of the associated ordering phenomena, respectively, energy scales. Quantitatively, our analysis yields $\partial T_N/\partial p_b = 1.1(3)$, $\partial T_N/\partial p_c = -1.7(5)$, $\partial T_R/\partial p_b = 2.3(4)$, and $\partial T_R/\partial p_c = -3.7(5)$ K/GPa. Applying magnetic-fields $B \parallel b$ axis yields a sign change in the uniaxial pressure dependence signaling different low-temperature phases. Splitting of the anomalies implies the presence of an intermediate phase AF3′. In addition, our experimental data show short-range magnetic order well above T_N as well as at low-temperatures, weakly coupled moments, and a glass- behavior ($T_{SG} \simeq 3.7$ K). The number of weakly coupled moments is sizable and might be attributed to about 15% of all Mn^{2+} spins present in the material. Glasslike behavior is seen in AC-χ and is further evidenced by quasilinear T dependence of c_p at low temperatures. The observed changes in pressure dependence and, in particular, the magnetostrictive effects shed light on the recently observed flop of electric polarization from $P \parallel c$ to $P \parallel a$ [18], suggesting that the ME effect in $Ni_xMn_{1-x}TiO_3$ appearing at intermediate-doping x does not have a direct magnetostrictive origin.

ACKNOWLEDGMENTS

We are grateful to H. Wadepohl from the Inorganic Chemical Institute of Heidelberg University for performing single-crystal diffraction studies. We acknowledge support by BMBF via the Project SpinFun (Project No. 13XP5088) and by Deutsche Forschungsgemeinschaft (DFG) under Germany's Excellence Strategy EXC2181/1-390900948 (the Heidelberg STRUCTURES Excellence Cluster) and Project No. KL 1824/13-1. L.G. and K.D. acknowledge support by IMPRS-QD. A.E. acknowledges support by DAAD through the GSSP Program. We acknowledge support of the HLD at HZDR, member of the European Magnetic Field Laboratory.

[1] D. Sherrington and S. Kirkpatrick, Phys. Rev. Lett. **35**, 1792 (1975).
[2] M. Kobayashi, K. Katsumata, T. Satō, and Y. Miyako, J. Phys. Soc. Jpn. **46**, 1467 (1979).
[3] S. Murayama, K. Yokosawa, Y. Miyako, and E. F. Wassermann, Phys. Rev. Lett. **57**, 1785 (1986).
[4] G. C. DeFotis, D. S. Mantus, E. M. McGhee, K. R. Echols, and R. S. Wiese, Phys. Rev. B **38**, 11486 (1988).
[5] T. Ono, T. Kato, H. Tanaka, A. Hoser, N. Stüßer, and U. Schotte, Phys. Rev. B **63**, 224425 (2001).
[6] F. Matsubara and S. Inawashiro, J. Phys. Soc. Jpn. **42**, 1529 (1977).
[7] M. Igarashi and K. Nagata, J. Magn. Magn. Mater. **90-91**, 363 (1990).
[8] Y. Ishikawa and S.-i. Akimoto, J. Phys. Soc. Jpn. **13**, 1110 (1958).
[9] L. Bevaart, E. Frikkee, J. Lebesque, and L. De Jongh, Solid State Commun. **25**, 539 (1978).
[10] A. Ito, H. Aruga, E. Torikai, M. Kikuchi, Y. Syono, and H. Takei, Phys. Rev. Lett. **57**, 483 (1986).
[11] A. Ito, H. Aruga, M. Kikuchi, Y. Syono, and H. Takei, Solid State Commun. **66**, 475 (1988).
[12] T. Kurihara, T. Komai, A. Ito, and T. Goto, J. Phys. Soc. Jpn. **60**, 2057 (1991).
[13] A. Ito, H. Kawano, H. Yoshizawa, and K. Motoya, J. Magn. Magn. Mater. **104-107**, 1637 (1992).
[14] H. Yoshizawa, H. Kawano, H. Mori, S. Mitsuda, and A. Ito, Physica B **180-181**, 94 (1992).
[15] Y. Yamaguchi, T. Nakano, Y. Nozue, and T. Kimura, Phys. Rev. Lett. **108**, 057203 (2012).
[16] Y. Yamaguchi and T. Kimura, Nat. Commun. **4**, 2063 (2013).
[17] R. S. Solanki, S.-H. Hsieh, C. H. Du, G. Deng, C. W. Wang, J. S. Gardner, H. Tonomoto, T. Kimura, and W. F. Pong, Phys. Rev. B **95**, 024425 (2017).
[18] S. Chi, F. Ye, H. D. Zhou, E. S. Choi, J. Hwang, H. Cao, and J. A. Fernandez-Baca, Phys. Rev. B **90**, 144429 (2014).
[19] J. B. Goodenough and J. J. Stickler, Phys. Rev. **164**, 768 (1967).
[20] G. Shirane, S. J. Pickart, and Y. Ishikawa, J. Phys. Soc. Jpn. **14**, 1352 (1959).
[21] R. Newnham, J. Fang, and R. Santoro, Acta Crystallogr. **17**, 240 (1964).
[22] H. Kato, Y. Yamaguchi, M. Ohashi, M. Yamada, H. Takei, and S. Funahashi, Solid State Commun. **45**, 669 (1983).
[23] M. Hoffmann, K. Dey, J. Werner, R. Bag, J. Kaiser, H. Wadepohl, Y. Skourski, M. Abdel-Hafiez, S. Singh, and R. Klingeler, Phys. Rev. B **104**, 014429 (2021).
[24] N. Mufti, G. R. Blake, M. Mostovoy, S. Riyadi, A. A. Nugroho, and T. T. M. Palstra, Phys. Rev. B **83**, 104416 (2011).
[25] T. Müller, Order and disorder in the charge and spin structures of YFe2O4-δ and Ni0. 42Mn0. 58TiO3, Ph.D. thesis, RWTH Aachen University, 2018.
[26] K. Dey, S. Sauerland, J. Werner, Y. Skourski, M. Abdel-Hafiez, R. Bag, S. Singh, and R. Klingeler, Phys. Rev. B **101**, 195122 (2020).
[27] K. Dey, S. Sauerland, B. Ouladdiaf, K. Beauvois, H. Wadepohl, and R. Klingeler, Phys. Rev. B **103**, 134438 (2021).

[28] L. Gries, M. Jonak, A. Elghandour, K. Dey, and R. Klingeler, Phys. Rev. B **106**, 174425 (2022).
[29] W. Hergett, C. Neef, H. Wadepohl, H.-P. Meyer, M. M. Abdel-Hafiez, C. Ritter, E. Thauer, and R. Klingeler, J. Cryst. Growth **515**, 37 (2019).
[30] C. Neef, H. Wadepohl, H.-P. Meyer, and R. Klingeler, J. Cryst. Growth **462**, 50 (2017).
[31] K. Dey, Single-crystal growth, magnetic and thermodynamic investigations of ilmenite titanates and lanthanum nickelates, Ph.D. thesis, Heidelberg University, 2021.
[32] J. Rodríguez-Carvajal, Physica B **192**, 55 (1993).
[33] R. D. Shannon, Acta. Crystallogr., Sect. A: Cryst. Phys., Diffr., Theor. Gen. Crystallogr. **32**, 751 (1976).
[34] Y. Skourski, M. D. Kuz'min, K. P. Skokov, A. V. Andreev, and J. Wosnitza, Phys. Rev. B **83**, 214420 (2011).
[35] R. Küchler, A. Wörl, P. Gegenwart, M. Berben, B. Bryant, and S. Wiedmann, Rev. Sci. Instrum. **88**, 083903 (2017).
[36] J. Werner, W. Hergett, M. Gertig, J. Park, C. Koo, and R. Klingeler, Phys. Rev. B **95**, 214414 (2017).
[37] See Supplemental Material at http://link.aps.org/supplemental/10.1103/PhysRevB.108.014406 for additional ac and dc magnetization, specific heat, thermal expansion, and magnetostriction data. It also shows how the anomaly sizes have been determined.
[38] M. E. Fisher, Philos. Mag. **7**, 1731 (1962).
[39] Y. Syono, S.-I. Akimoto, Y. Ishikawa, and Y. Endoh, J. Phys. Chem. Solids **30**, 1665 (1969).
[40] L. J. de Jongh, D. Betts, and D. Austen, Solid State Commun. **15**, 1711 (1974).
[41] Here, we used the Ni content as determined by EDX; using the nominal Ni content does not change the conclusion.
[42] A. Tari, *The Specific Heat of Matter at Low Temperatures* (World Scientific, Singapore, 2003).
[43] W. Fogle, J. Ho, and N. Philipps, J. Phys. Colloq. **39**, C6-901 (1978).
[44] R. Caudron, P. Costa, J. Lasjaunias, and B. Levesque, J. Phys. F: Met. Phys. **11**, 451 (1981).
[45] T. Barron and G. White, in *Heat Capacity and Thermal Expansion at Low Temperatures* (Springer, Berlin, 1999), pp. 153–223.
[46] R. Klingeler, B. Büchner, S.-W. Cheong, and M. Hücker, Phys. Rev. B **72**, 104424 (2005).
[47] R. Küchler, Thermische Ausdehnung und divergierendes Grüneisenverhältnis in Schwere-Fermionen-Systemen, Dissertation, Technische Universität Dresden, Dresden, 2005.

Supplemental Information: Magnetic anisotropy, magnetoelastic coupling and the magnetic phase diagram of $Ni_{0.25}Mn_{0.75}TiO_3$

A. Elghandour,[1,*] L. Gries,[1] L. Singer,[1] M. Hoffmann,[1] M. Uhlarz,[2] K. Dey,[1,†] and R. Klingeler[1,‡]

[1] *Kirchhoff Institute for Physics, Heidelberg University, INF 227, 69120 Heidelberg, Germany*

[2] *Dresden High Magnetic Field Laboratory (HLD-EMFL), Helmholtz-Zentrum Dresden-Rossendorf, 01328 Dresden, Germany*

PACS numbers:

The Supplemental information contains:

- Magnetization data: dc and ac magnetic susceptibilities, and the effect of applied magnetic field on both of them.
- Heat capacity data: magnetic field effects and an illustration of how the equal-area construction used to estimate the entropy jump-height.
- Thermal expansion data: magnetic field effects and an illustration of how the equal-area construction used to estimate anomaly heights at the phase transitions.

---

* Electronic address: ahmed.elghandour@kip.uni-heidelberg.de
† Current address: Clarendon Laboratory, University of Oxford, Parks Road, Oxford, OX1 3PU, United Kingdom
‡ Electronic address: klingeler@kip.uni-heidelberg.de

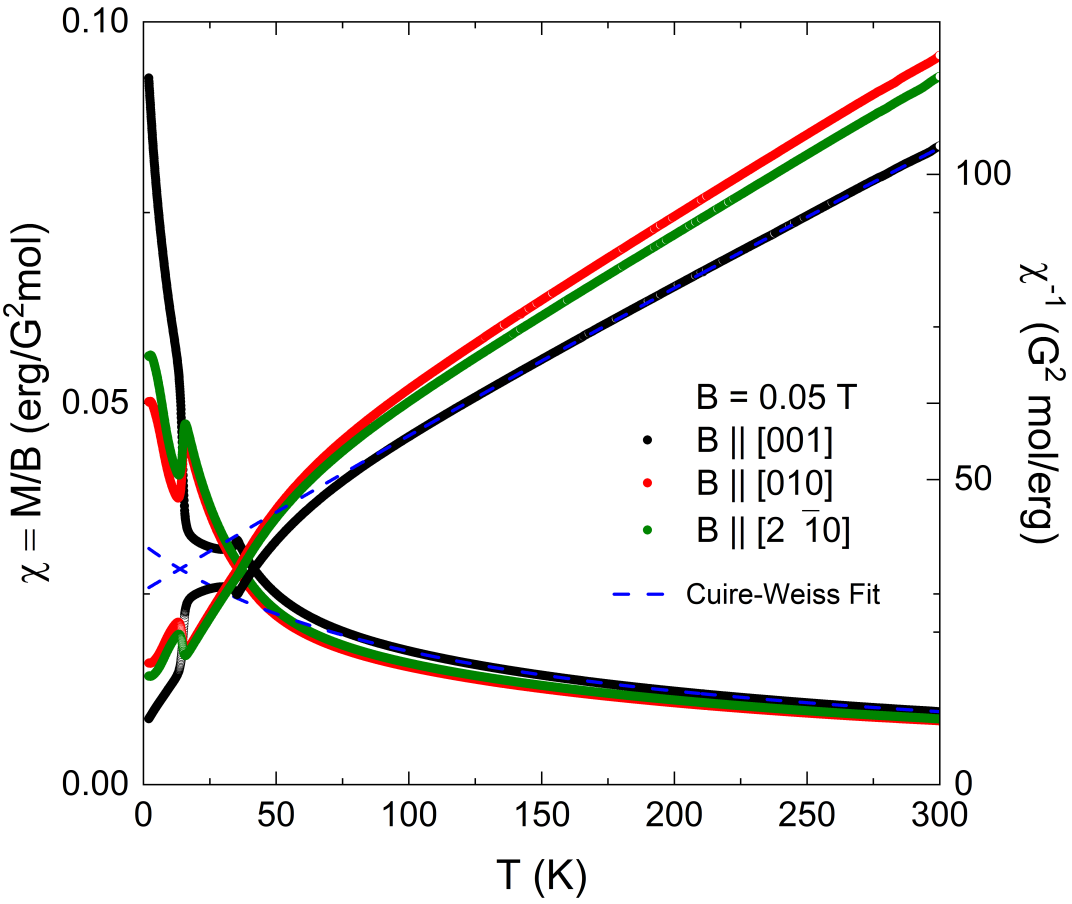

FIG. 1: Temperature dependence of static magnetic susceptibility $\chi = M/B$ of $Ni_{0.25}Mn_{0.75}TiO_3$ measured at B = 0.05 T applied along the three crystallographic axes and the corresponding inverse magnetic susceptibility. The dashed blue lines represent the Curie-Weiss fit of the data measured along c axis. Fitting parameters are given in the main manuscript text.

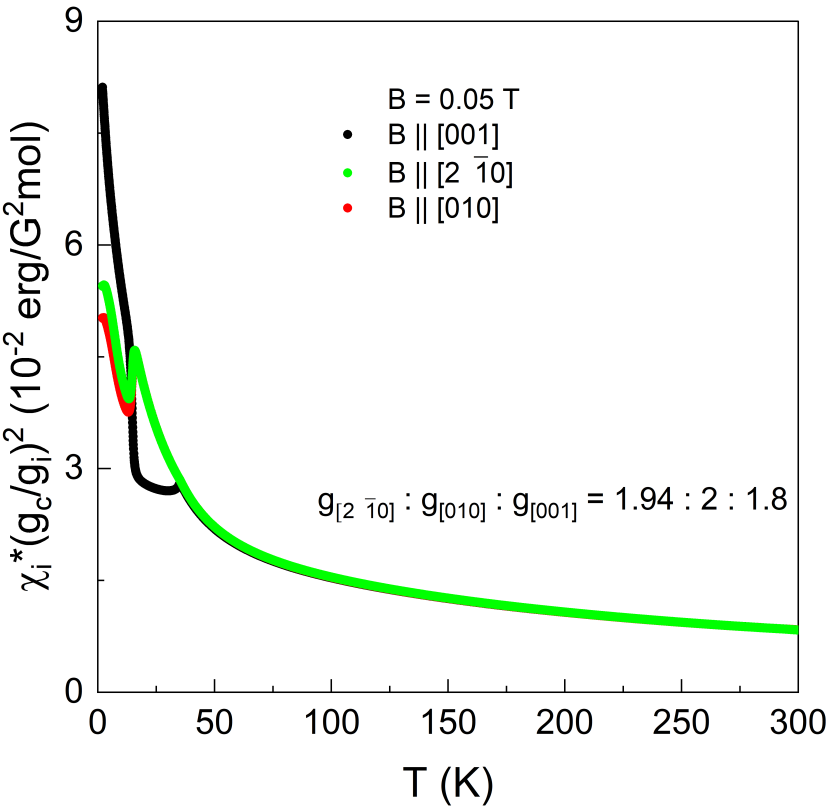

FIG. 2: Temperature dependence of the static magnetic susceptibility of $Ni_{0.25}Mn_{0.75}TiO_3$ measured at B = 0.05 T applied along the three crystallographic axes. The data have been normalized to the c axis results to show almost isotropic at $T \ll T_N$. The resulting ratio of the g factors is displayed.

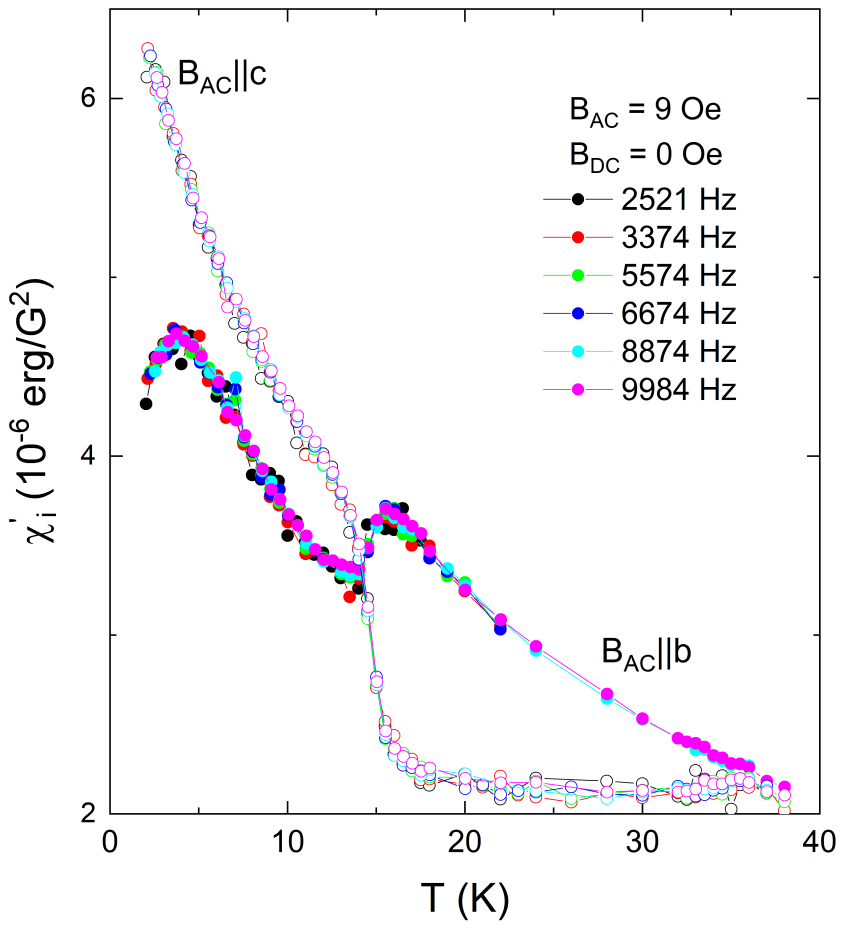

FIG. 3: Temperature dependence of the real part of AC magnetic susceptibility $\chi^{'}$ of $Ni_{0.25}Mn_{0.75}TiO_3$ measured at different frequencies. The data measured along the b and c axes confirm the anomalies at T_N and T_R. Additionally, the data reveal a broad hump at $T^* \approx 3.7\ K$, which is only visible along b axis and which does not change with frequency in the accessible regime.

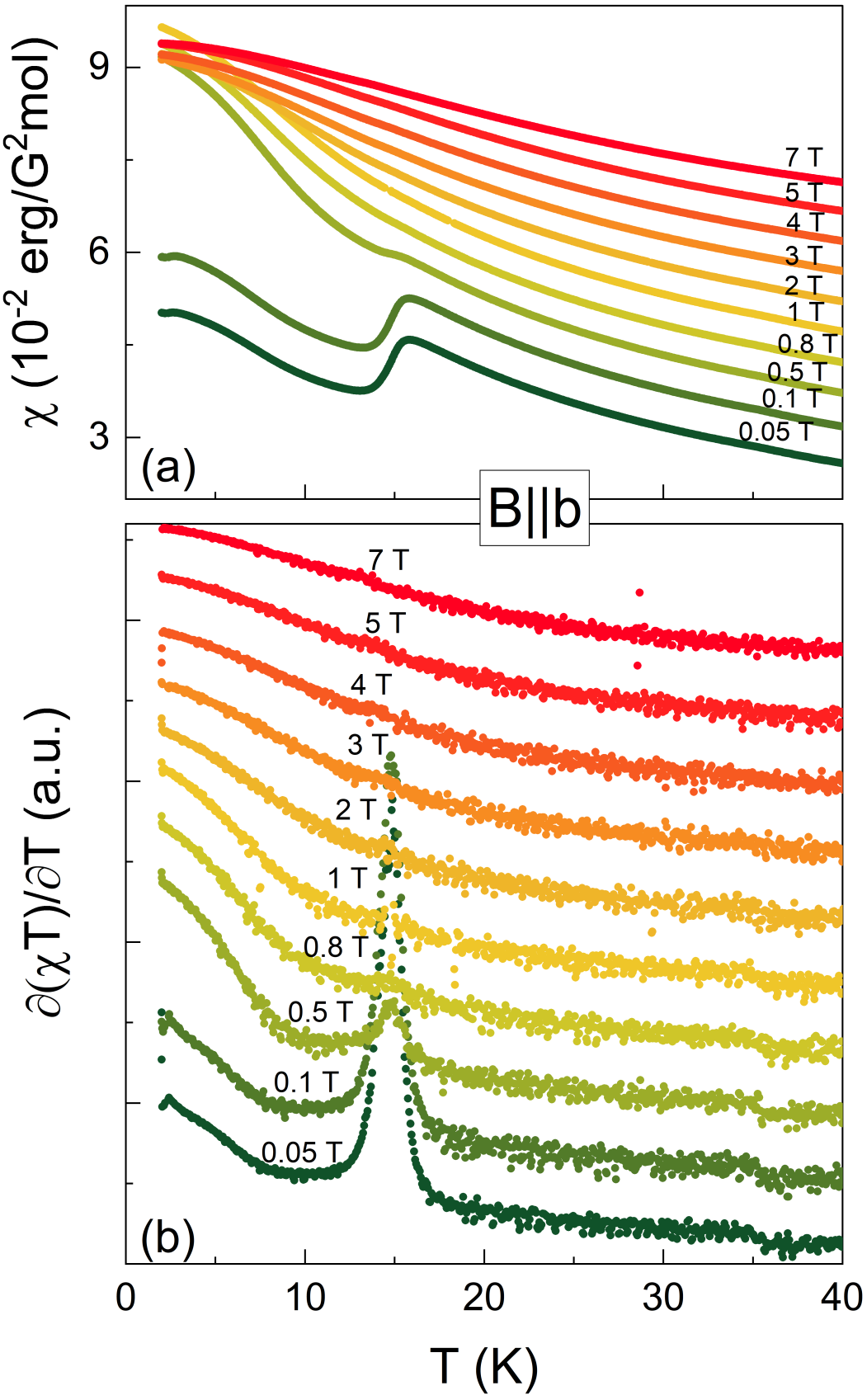

FIG. 4: Temperature dependence of static magnetic susceptibility, $\chi = M/B$, of $Ni_{0.25}Mn_{0.75}TiO_3$ measured along the b axis at applied magnetic fields $0.05\ T \leq B \leq 7\ T$, and (b) the corresponding Fischer's magnetic specific heat $\partial(\chi T)/\partial T$.

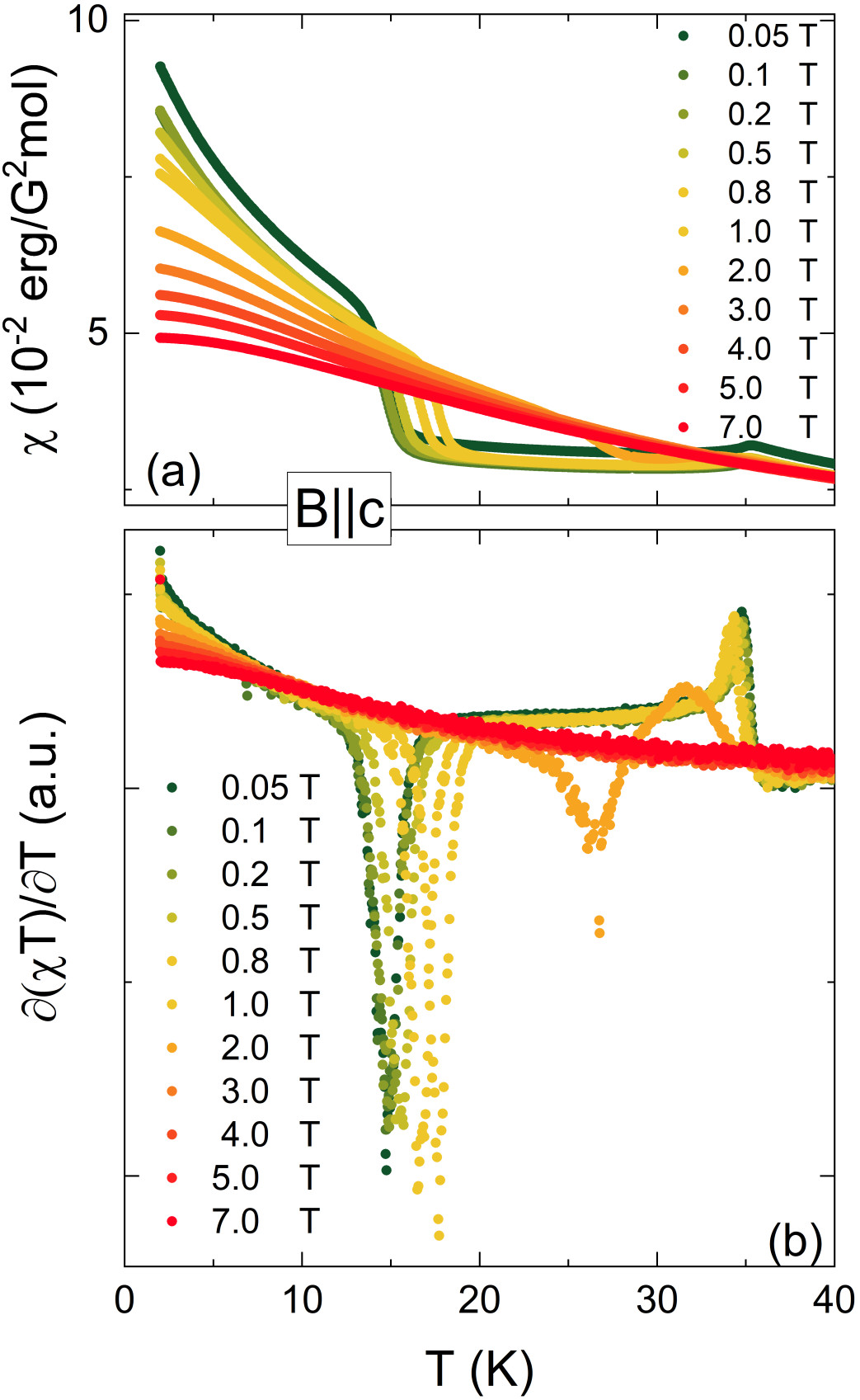

FIG. 5: Temperature dependence of static magnetic susceptibility, $\chi = M/B$, of $Ni_{0.25}Mn_{0.75}TiO_3$ measured along c axis at applied magnetic fields $0.05\ T \leq B \leq 7\ T$, and (b) the corresponding Fischer's magnetic specific heat $\partial(\chi T)/\partial T$.

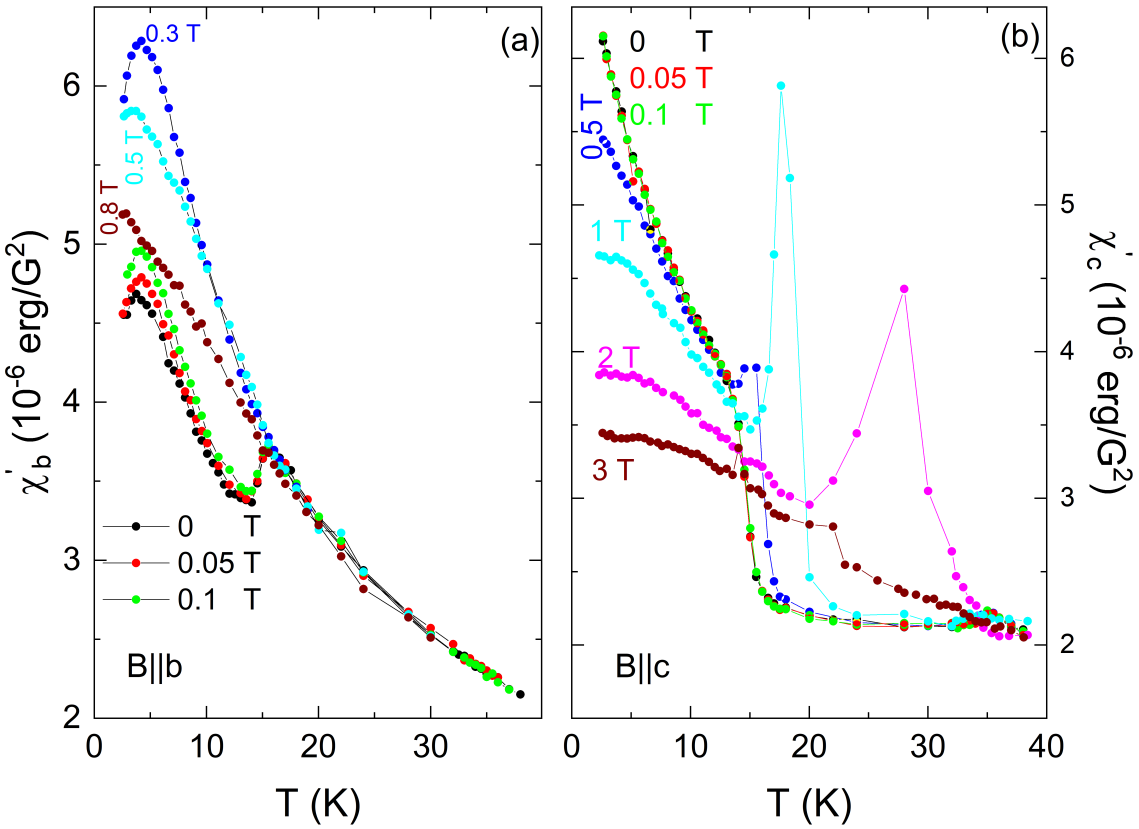

FIG. 6: Temperature dependence of the real part of AC magnetic susceptibility $\chi^{'}$ of $Ni_{0.25}Mn_{0.75}TiO_3$ measured along the b and c axes at a frequency of 10 kHz. The amplitude of the ac magnetic field is 9 Oe and measurements have been done in external DC magnetic fields between 0 and 3 T.

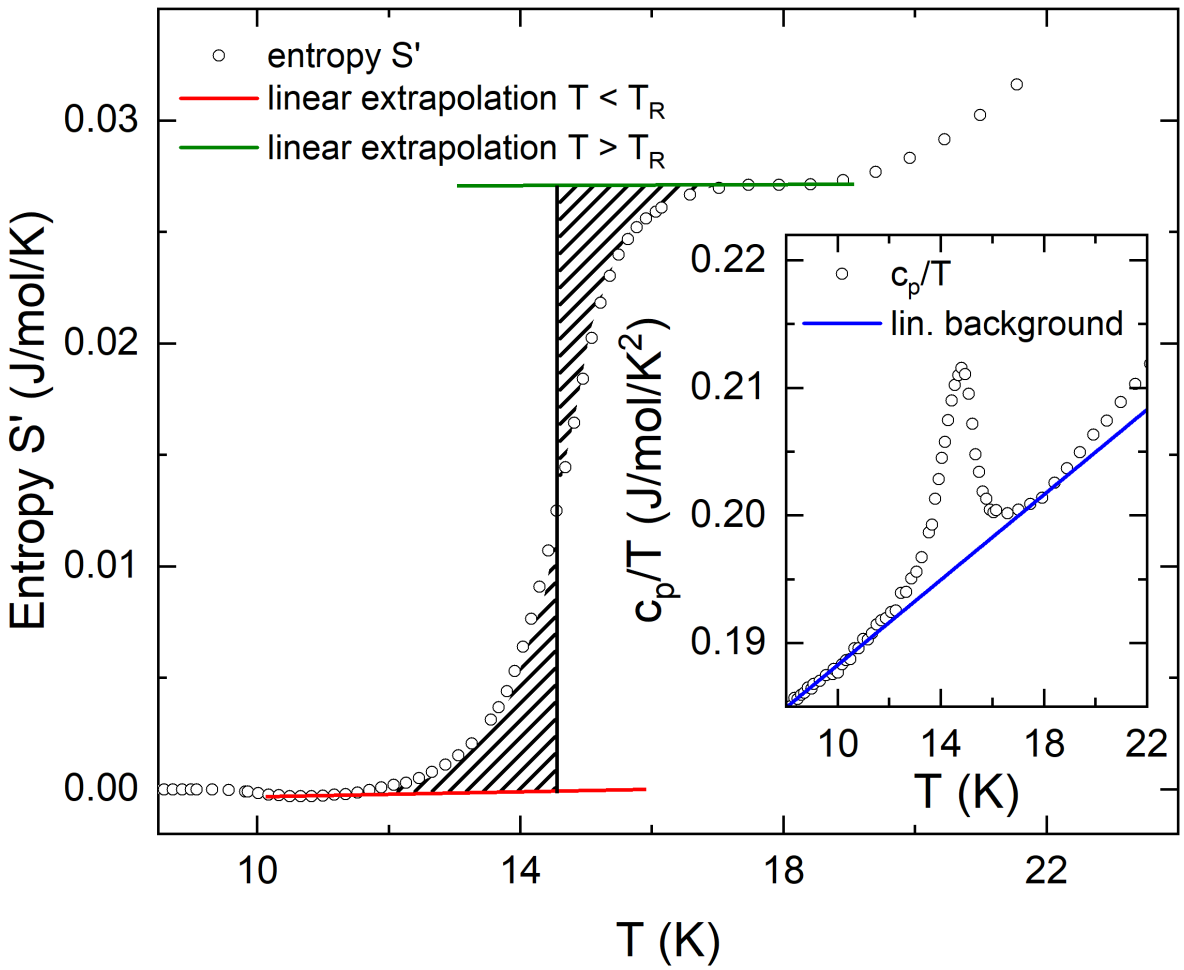

FIG. 7: Same area construction for the jump in entropy S at T_{R}. The entropy has been calculated by integrating the background corrected heat capacity c_p/T. The coloured lines are linear extrapolations of the intervals below and above T_{R}. Inset: c_p/T data with the used linear background (blue) in the temperature regime around T_{R}.

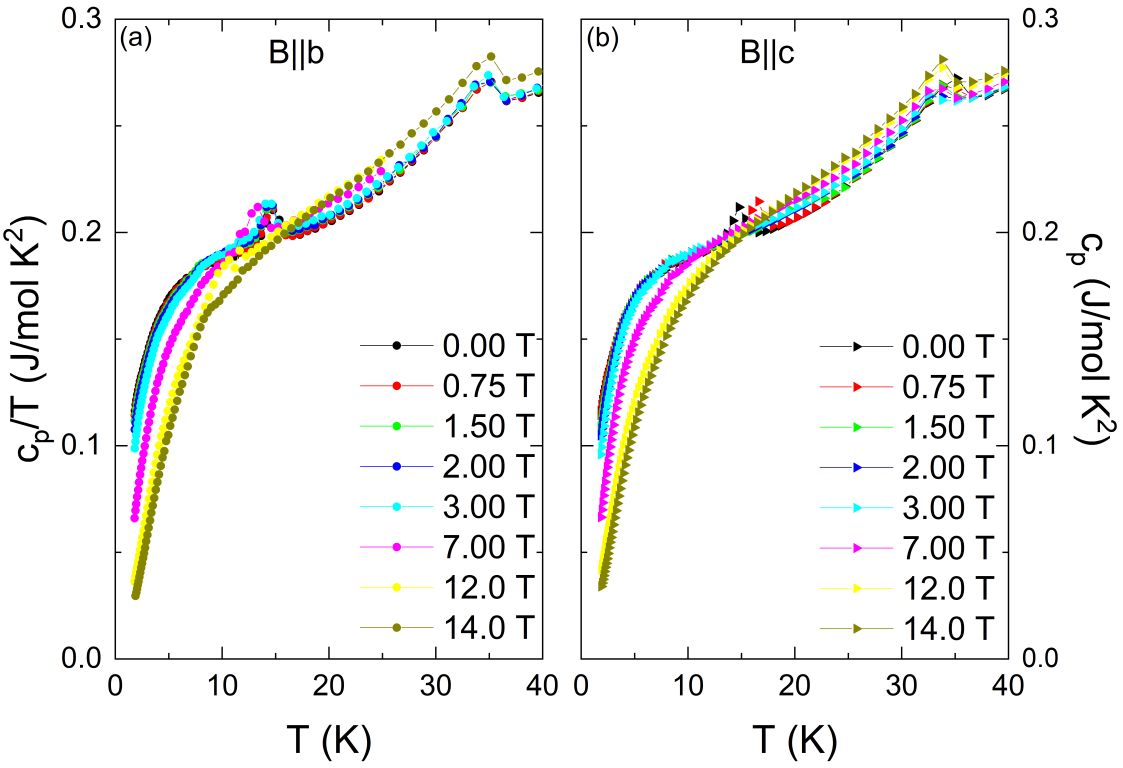

FIG. 8: Temperature dependence of the heat capacity measured (a) along the b axis and (b) along the c axis in applied magnetic fields $0\ T \leq B \leq 14\ T$. We note that the anomaly at $T_{\rm N}$ is hardly affected by the applied field, while the anomaly observed at $T_{\rm R}$ significantly changes in the magnetic field range under study.

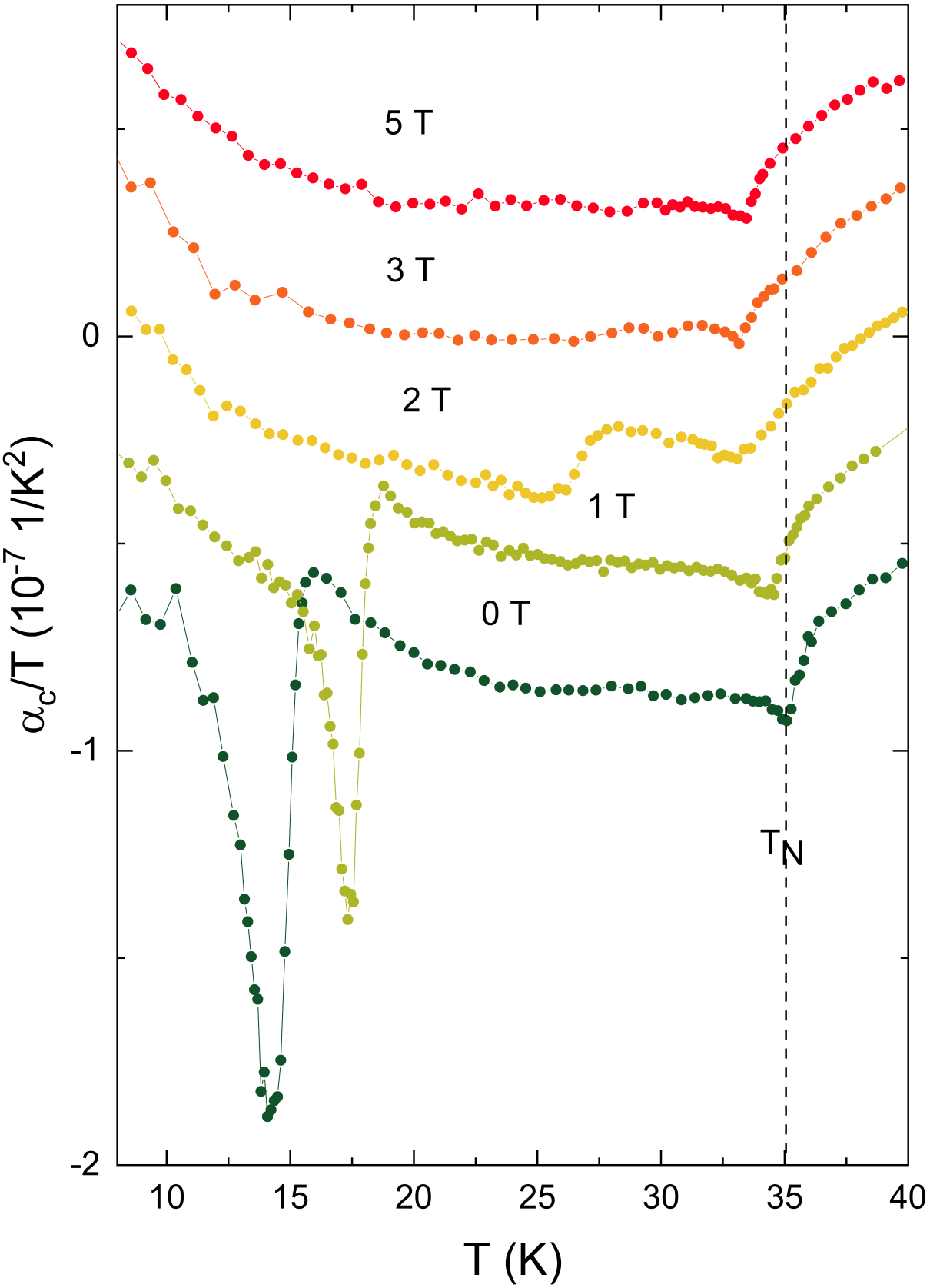

FIG. 9: Thermal expansion coefficient α_c divied by temperature in various external magnetic fields applied along the c axis. The dashed line marks $T_N(B = 0\ \mathrm{T})$.

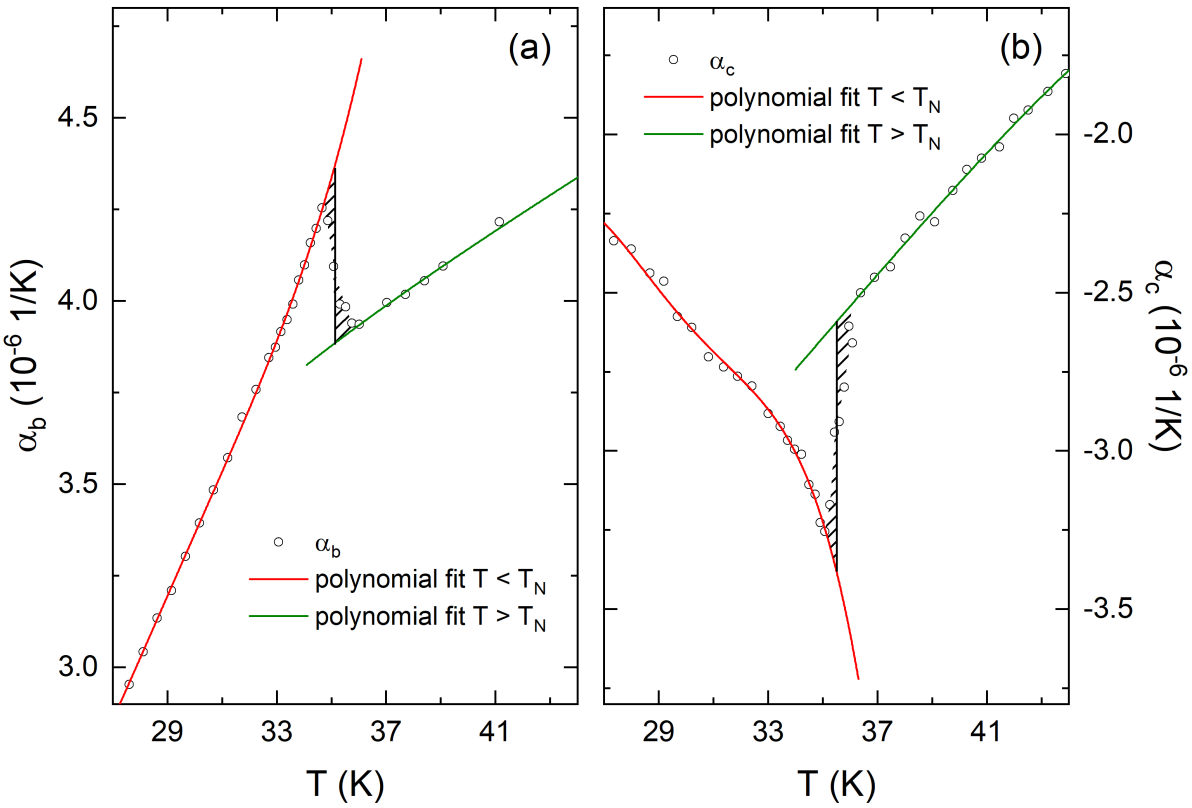

FIG. 10: Same area construction to determine T_N and the associated jumps in the thermal expansion coefficient measured along the crystallographic (a) b and (b) c axes. The extrapolations of α below (red line) and above (green line) T_N have been acquired by fitting polynomials of fourth order to the data.

Chapter 5

Spin Freezing and Slow Spin Dynamics in $Ho_2Zr_2O_7$

The following chapter consists of two main parts:

1. The first part, titled "Field induced spin freezing and low temperature heat capacity of disordered pyrochlore oxide $Ho_2Zr_2O_7$" [27] has been published as a regular article in the Journal of Physics: Condensed Matter.

2. The second part (sections 5.1 - 5.5) is an original work.

The author contributions of part I are as following:

- Sheetal and C. Yadav synthesized the samples, performed the measurements except the specific heat measurements at low temperatures and wrote the manuscript.

- A. Elghandour measured the specific heat capacity data below 4 K presented in Fig. 5 and 6. Further measurements at higher temperature have been done, too, but are not included in the manuscript.

IOP Publishing Journal of Physics: Condensed Matter
J. Phys.: Condens. Matter **34** (2022) 245801 (7pp) https://doi.org/10.1088/1361-648X/ac5fd8

Field induced spin freezing and low temperature heat capacity of disordered pyrochlore oxide $Ho_2Zr_2O_7$

Sheetal[1], **A Elghandour**[2], **R Klingeler**[2] **and C S Yadav**[1,*]

[1] School of Basic Sciences, Indian Institute of Technology Mandi, Mandi-175075 (H.P.), India
[2] Kirchhoff Institute of Physics, Heidelberg University, INF 227, D-69120 Heidelberg, Germany

E-mail: shekhar@iitmandi.ac.in

Received 3 February 2022, revised 12 March 2022
Accepted for publication 22 March 2022
Published 7 April 2022

Abstract

Spin ice materials are the model systems that have a zero-point entropy as $T \to 0$ K, owing to the frozen disordered states. Here, we chemically alter the well-known spin ice $Ho_2Ti_2O_7$ by replacing Ti sites with isovalent but larger Zr ion. Unlike the $Ho_2Ti_2O_7$ which is a pyrochlore material, $Ho_2Zr_2O_7$ crystallizes in disordered pyrochlore structure. We have performed detailed structural, ac magnetic susceptibility and heat capacity studies on $Ho_2Zr_2O_7$ to investigate the interplay of structural disorder and frustrated interactions. The zero-field ground state exhibits large magnetic susceptibility and remains dynamic down to 300 mK without showing Pauling's residual entropy. The dynamic state is suppressed continuously with the magnetic field and freezing transition evolves ($\sim$10 K) at a field of $\sim$10 kOe. These results suggest that the alteration of chemical order and local strain in $Ho_2Ti_2O_7$ prevents the development of spin ice state and provides a new material to study the geometrical frustration based on the structure.

Keywords: frustrated magnetism, pyrochlores, spin freezing

(Some figures may appear in colour only in the online journal)

1. Introduction

Beginning with the identification of unusual disordered ground state in magnetic materials, frustration becomes a source of fascination among the scientists. In these systems, pyrochlore $A_2Ti_2O_7$ (A = Dy, Ho) as an exemplar of three-dimensional frustration continues to be the central topic of research due to the observation of water ice-like highly degenerate macroscopic ground state [1, 2]. $Dy_2Ti_2O_7$ and $Ho_2Ti_2O_7$ are the well-known spin ice materials that possess the finite residual entropy at the lowest temperature which is equivalent to the Pauling's value of water ice [2, 3]. Apart from the spin-ice behavior below $\sim$2 K, $Dy_2Ti_2O_7$ also shows a strong frequency-dependent spin-freezing at $\sim$16 K [4, 5]. However no such feature is seen for the $Ho_2Ti_2O_7$ which distinguishes the spin dynamics of $(Ho/Dy)_2Ti_2O_7$ [6, 7].

In order to understand the spin-ice state, researchers have begun to look outside the present structural map scenario by forming the stuffed pyrochlores by placing a non-magnetic atom or the atoms with smaller moments in the pyrochlore lattice [8–14]. In pyrochlore oxide $A_2B_2O_7$, various combinations of A and B site ions are employed to replace the existing spin ice state and disorder the symmetry of available crystal structure. The zirconate and hafnates pyrochlore provides a new avenue to look for a similar magnetic ground state. The stability of the pyrochlore structure can be empirically investigated in terms of atomic radii ratio (r_A/r_B) of the respective A and B ions [15]. The stable pyrochlore structure can be realized only for the range of $1.48 \leqslant r_A/r_B \leqslant 1.71$ ratio, and any deviation from this value disturbs the structural symmetry [15, 16]. For comparison, the radius ratio for $Dy_2Zr_2O_7$ and $Ho_2Zr_2O_7$ lies between 1.39 and 1.44, which is smaller than the nominal range for pyrochlore structure. These materials exhibit disordered pyrochlore structures and show the

* Author to whom any correspondence should be addressed.

absence of low-temperature magnetism of rare-earth moments. For example, $Pr_2Zr_2O_7$ exhibits spin ice-like correlations and strong quantum fluctuations [8, 9]. $Nd_2Zr_2O_7$ reveals the coexistence of an ordered and fluctuating Coulomb phase at low-temperature [10]. $Dy_2Zr_2O_7$, $Tb_2Hf_2O_7$ and $Pr_2Hf_2O_7$ remain dynamic down to 100 mK [11–13]. However the $Dy_2Zr_2O_7$ and $Pr_2Hf_2O_7$ have been shown to exhibit glassy transition at ∼90 mK [11, 17]. $Nd_2Hf_2O_7$ shows a long-range antiferromagnetic state ($T_N \sim 0.55$ K) with an all-in-all-out (AIAO) spin configuration [18]. Recent research also shows the loss of spin ice ground state due to a large chemical disorder induced by the stuffing of pyrochlores [11, 19].

There are few reports on the evolution of structure and magnetism of the magnetically diluted pyrochlore lattice under the application of magnetic field [16, 20, 21]. It was found that the structural disorder and spin ice state can be stabilized in disordered pyrochlores either by the application of magnetic field or by suitable choice of non-magnetic substitution over A site [16, 19]. $Dy_2Zr_2O_7$ shows the stabilization of spin-ice entropy in the presence of the magnetic field, and $Nd_2Zr_2O_7$ shows a field-induced one-dimensional quantum chain in AIAO [19, 20]. The substitution of non-magnetic La^{3+} ion in $Dy_2Zr_2O_7$ induces the structural change from disordered pyrochlore to a stable pyrochlore structure and observation of spin freezing at $H = 0$ Oe similar to the field-induced spin freezing of $Dy_2Zr_2O_7/Ho_2Ti_2O_7$ and the well-known spin ice system $Dy_2Ti_2O_7$ [16, 22]. In our previous work, we have reported the complete magnetic and structural phase diagram of $Dy_2Zr_2O_7$ and the evolution of pyrochlore phase and spin freezing transition on diluting $Dy_2Zr_2O_7$ by non-magnetic La over Dy. Further, pressure effects exhibit weak pyrochlore-type ordering in case of $Ho_2Zr_2O_7$ and $Er_2Zr_2O_7$ [21].

In this paper, we have studied a less explored disordered pyrochlores zirconate $Ho_2Zr_2O_7$ and discussed its structural, magnetic, and thermodynamic properties. We observe that with the stuffing of Zr on the Ti site, the spin ice character is completely lost. The large susceptibility and heat capacity values reveal a very dynamic ground state down to 300 mK. However, we found evidence of field-induced spin freezing at ∼10 K similar to the spin ice $Ho_2Ti_2O_7$ [7]. This also rules out the importance of high-temperature spin freezing in the formation of spin ice state below 1 K in $Dy_2Ti_2O_7$ [4].

2. Experimental details

The polycrystalline $Ho_2Zr_2O_7$ and $La_2Zr_2O_7$ compounds were prepared by solid-state reaction method using stoichiometric amounts of Ho_2O_3 (⩾99.99% purity), La_2O_3 (⩾99.999% purity) and ZrO_2 (99% purity). The raw oxides were pre-heated at 500 °C at weighed at 100 °C to avoid moisture because of their hygroscopic nature. The stoichiometric mixture of constituent oxides is heated twice at 1350 °C for 50 h with intermediate grindings, and the final heat treatment was given in the pellet form at the same temperature [19]. X-ray diffraction (xrd) experiment was performed using Rigaku x-ray diffractometer with Cu K_α source of wavelength 1.5406 Å in the 2θ range of 10–90°. The crystal structure and phase purity were confirmed by performing Rietveld refinement of the powder sample using Fullprof Suit software and the graphical interface Vesta [23]. The magnetic measurements were carried out using Quantum Design built magnetic property measurement system. Heat capacity measurements were measured using Quantum Design built physical property measurement system (PPMS) down to 1.8 K. Low temperature (300 mK to 4 K) specific heat measurements were performed using the dilution refrigerator option of PPMS using a relaxation method on a pressed pellet of ∼11.32 mg.

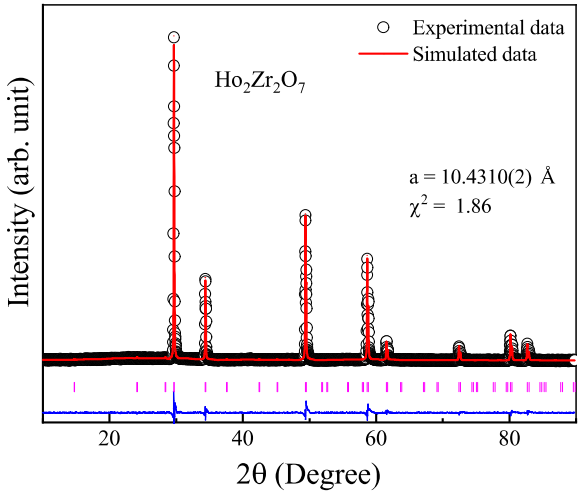

Figure 1. Room temperature x-ray powder diffraction pattern along with the Rietveld refined simulated data for $Ho_2Zr_2O_7$. As seen from the figure, the superstructure peaks corresponding to pyrochlore phase are missing.

Table 1. Positional parameters of $Ho_2Zr_2O_7$.

Atom	Wyckoff position	Fractional coordinates
Ho	16d	0.5, 0.5, 0.5
Zr	16c	0, 0, 0
O	48f	0.3726(17), 0.125, 0.125
O′	8b	0.375, 0.375, 0.375

3. Results and discussion

X-ray powder diffraction characterized the $Ho_2Zr_2O_7$ in single phase without any detectable impurity (see figure 1). Modeling of the xrd data with the cubic space group is consistent with the disordered pyrochlore structure and gives an excellent fit with $Fd\bar{3}m$ space group. The obtained crystallographic parameters are listed in table 1. Similar to the $Dy_2Zr_2O_7$ the xrd pattern of $Ho_2Zr_2O_7$ consists of only the main peaks of pyrochlore structure and the remaining superstructure peaks expected at $2\theta = 14°, 27°, 36°, 42°$ etc are missing [19, 24]. This behavior is consistent with the r_A/r_B ratio (∼1.40) of the compound, which is less than the value at which a stable pyrochlore structure is expected to evolve ($1.48 \leqslant r_A/r_B \leqslant 1.72$). Figure 2 shows the crystal structure of stable pyrochlore (a), disordered pyrochlore (b) and a comparison of fluorite and pyrochlore structure (c).

Unlike the configuration of oxygen atoms in the pyrochlore structure, the oxygen atoms locally form a perfect cube around

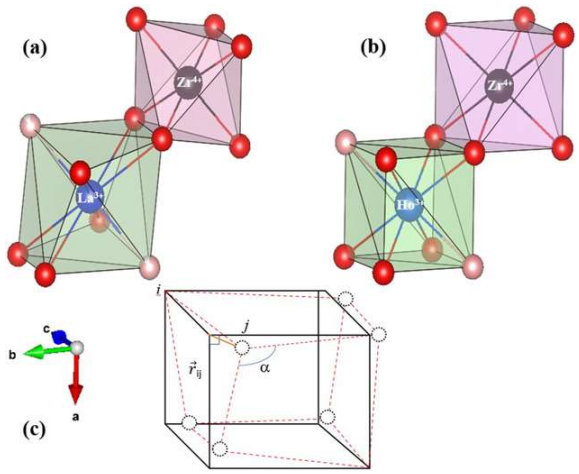

Figure 2. Coordination of A^{3+} and B^{4+} ions in $A_2B_2O_7$. (a) Pyrochlore structure: O^{2-} ions around A^{3+} (blue) rare-earth ion and B^{4+} (black) transition-metal ion form the distorted cube and octahedra respectively. The two types of oxygen are shown in red and light red color. (a) Pyrochlore (b) disordered pyrochlore structure of $Ho_2Zr_2O_7$. (c) Shows the difference between cubes of the fluorite and pyrochlore structures. For fluorite $\alpha = 90°$ (angle between O–A–O) and all the oxygens are equivalent to the central ion. The $\vec{r}_{ij}$ is the unit vector showing displacement of O^{2-} ion from the ideal position. The deviation from fluorite structure can be parameterized in term of $\vec{r}_{ij}$.

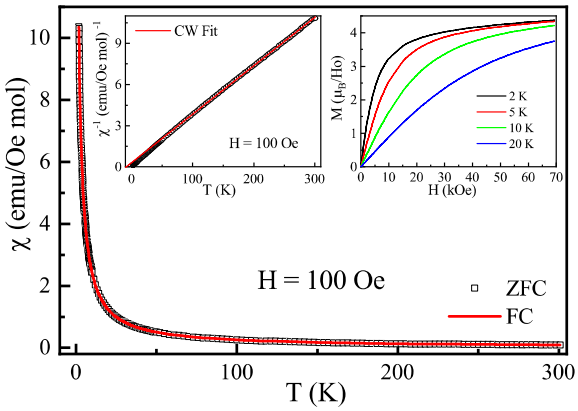

Figure 3. Temperature dependence of dc susceptibility in the range $T = 1.8$–300 K. The left inset shows Curie–Weiss fit to the inverse susceptibility data above 300 K. The right inset depicts isothermal magnetization as a function of the applied field showing a saturation moment of ∼4 μ_B/Ho ion at 2 K in addition to a finite slope indicating admixture of higher crystal field (CF) levels.

both the A and B sites in fluorite structure. The structural change from fluorite to pyrochlore phase, which consists of ordered oxygen vacancies, results in the shift in x-coordinate of 48f oxygen site. The variation in α and $\vec{r}_{ij}$ values can be used as a distortion parameter to study the difference between these structures. Depending on the choice of A and B atoms, the crystal symmetry changes and modifies the distortion parameters. It is worth mentioning that the pyrochlore compound $La_2Zr_2O_7$ with $\alpha = 108.65(19)$ and $|\vec{r}_{ij}| > 0$, shows a change of 12.96% from fluorite structure ($\alpha = 90$ and $|\vec{r}_{ij}| = 0$). In $Ho_2Zr_2O_7$, the obtained $\alpha = 91.085(10)$ and percentage deviation are 0.934%, indicating a small deformation from the fluorite structure.

Fitting of the inverse susceptibility data collected at 100 Oe above 80 K (left inset of figure 3) by Curie–Weiss law yields an antiferromagnetic Curie–Weiss temperature $\theta_{CW} \sim -10.7$ (4) K and effective magnetic moment $\mu_{eff} \sim 7.6$ (05) μ_B/Ho. Though the spin ice pyrochlore systems show crystal field anisotropy, phenomenologicaly the low-temperature (below $T = 30$ K) behavior can again be described by a Curie–Weiss law with the parameters viz $\theta_{CW} \sim -0.5$ K and $\mu_{eff} \sim 7.2$ μ_B/Ho. These parameters are similar to that for $Dy_2Zr_2O_7$. Here, it is worthy to mention that a ferromagnetic $\theta_{CW} \sim +1.9$ K was reported for the clean pyrochlore $Ho_2Ti_2O_7$ system [25]. The isothermal magnetization as a function of applied field for $Ho_2Zr_2O_7$ at various temperatures is shown in the right inset of figure 3. The saturation magnetization (M_s) at the maximum field (70 kOe) is comparatively less compared to the $Ho_2Ti_2O_7$ ($M_s \sim 5$ μ_B/Ho), which is half of the free-ion value and is due to the presence of strong crystal field anisotropy. These data indicate that $Ho_2Zr_2O_7$ exhibits strong anisotropic behavior like other systems such as $Ho_2Ti_2O_7$, $Dy_2Ti_2O_7$ and $Dy_2Zr_2O_7$ [19, 25, 26].

Figure 4 shows the ac susceptibility data for $Ho_2Zr_2O_7$ collected between the temperature range 1.8–40 K, at $H_{ac} = 2$ Oe, $f = 931$ Hz and in various dc magnetic fields ($H = 0$–30 kOe). Measurement of the real part of ac susceptibility in the absence of dc magnetic field shows paramagnetic-like behavior down to 1.8 K (figure 4(a)), similar to the behavior of spin ice $Ho_2Ti_2O_7$, which exhibits spin freezing anomaly at ∼16 K in the presence of magnetic field [3]. The large susceptibility value suggests the large spin dynamics down to the lowest measuring temperature. No anomaly appears up to 8 kOe except that of reduction in the magnitude of susceptibility, which indicates slowing down the spin dynamics with the field. A broad hump-like feature shows up at $H = 10$ kOe (around 10 K), and it shifts to higher temperatures with increasing the applied magnetic field. It is worthy of mentioning that $Dy_2Zr_2O_7$ shows the freezing anomaly in the presence of dc field of 5 kOe. Here, this feature is not seen even up to the field of 8 kOe, which is consistent with the large structural disorder in $Ho_2Zr_2O_7$ compared to $Dy_2Zr_2O_7$. It suggests that $Ho_2Zr_2O_7$ requires the higher field to slow down the spin dynamics induced by the large chemical disorder with Zr substitution at the Ti site. It is to note that the structurally ordered $Ho_2Ti_2O_7$ system shows the thermally activated high-temperature spin freezing behavior in the presence of a magnetic field, which rules out the importance of these features in the formation of spin ice state at low-temperature [27]. Inset of figure 4(a) shows the ac susceptibility data collected at various frequencies between 10 Hz–1 kHz in a field of 10 kOe. The frequency dependence of freezing anomaly is characterized by calculating the Mydosh parameter ($p = \delta T/T_f \ln f$), which comes out to be 0.18. This large value rules out the spin-glass behavior for which p values range between 0.005 to 0.01 and show the unusual spin freezing in these systems [28].

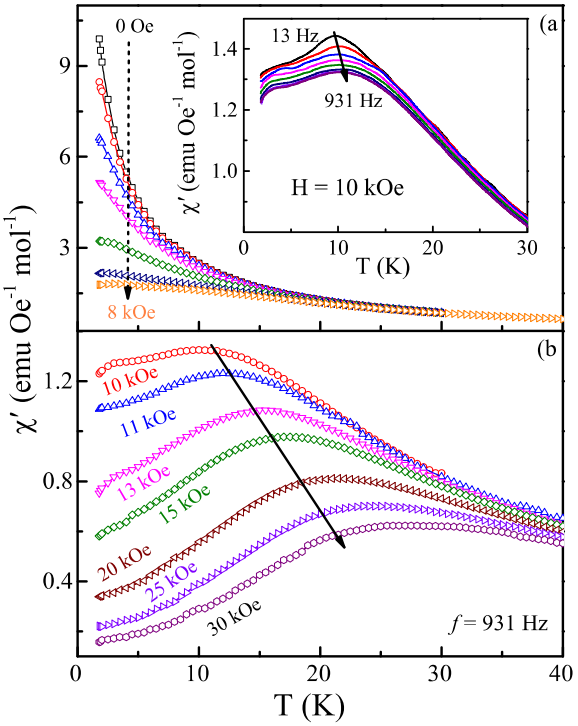

Figure 4. Real part of ac susceptibility data at 931 Hz in the presence of dc magnetic field ($H \leqslant 30$ kOe). Inset shows the frequency dependence of χ' at 10 kOe at various frequencies ranges between 10 Hz to 1 kHz.

The specific heat of $Ho_2Zr_2O_7$ down to 300 mK (shown in figure 5(a)) does not show any evidence of phase transition. Instead, the low-temperature heat capacity of the Ho based pyrochlore system shows an increase below $T = 1$ K, which is attributed to the anomalously large hyperfine coupling between the nuclear magnetic moment and effective magnetic field ($H_{\rm eff}$) at the Ho nucleus, leading to the ambiguities in the exact estimation of the magnetic heat capacity ($C_{\rm m}$). The magnetic heat capacity $C_{\rm m}$ is extracted by subtracting the phonon contributions ($C_{\rm L}$), nuclear contributions ($C_{\rm N}$) and magnetic Schottky anomaly ($C_{\rm sch}$) in case of field data from the total heat capacity (shown in figure 5(b)) [29, 30]. The lattice/phononic contribution to heat capacity was estimated by fitting the high-temperature data by using both Einstein and Debye models (and Schottky term in field data) [19]. The value of Debye temperature ($\Theta_{\rm D}$) and Einstein temperature ($\Theta_{\rm E}$) were obtained as 122 K and 305 K, respectively. For $Ho_2Ti_2O_7$, the $C_{\rm m}$ was extracted by subtracting the estimated nuclear contribution ($C_{\rm N}$) for the pyrochlore oxide Ho_2GaSbO_7 (which shows a peak at $T = 0.3$ K) [3]. Blöte *et al* estimated that the $C_{\rm N}$ arises due to the splitting of eight nuclear levels of holmium (nuclear isospin $I = 7/2$) with the theoretical maximum of $C_{\rm N} \sim 0.9R$ at $T = 0.3$ K [31]. The obtained value of $C_{\rm m}$ for $Ho_2Ti_2O_7$ using this methodology reveals the same characteristic feature of spin ice as observed for $Dy_2Ti_2O_7$ [32]. Further, the theoretical studies using Monte-Carlo simulation give magnetic entropy values within $\sim$2% of $R[\ln 2 - (1/2)\ln 3/2]$, which agrees well with the ambit of spin ice materials [33]. Such a small variance from the Pauling entropy value could be reasonably accounted for any slight deviations in the hyperfine parameters of $4f$ electrons of rare-earth ions (depending upon ionic surrounding, electric field gradient, etc). Ramon *et al* extracted the nuclear contribution in $Ho_2Zr_2O_7$ by subtracting the nuclear contribution for Ho metal [34]. However, as the low temperature residual magnetic entropy is one of the important quantities to identify the formation of spin ice state, it is necessary to carefully deal with the fitting models to extract the magnetic contribution. Therefore, we have not restricted ourselves to the approaches used by Bramwell *et al*, and Ramon *et al* only for our disordered pyrochlore oxide $Ho_2Zr_2O_7$ because of its modified crystal field spacing associated with the change in lattice and electronic structure. It was found that the hyperfine interactions of Ho spin lead to a nuclear anomaly at $\sim 0.3 \pm 0.02$ K [6, 35, 36]. In contrast, the peak position in $Ho_2Zr_2O_7$ is slightly shifted to a higher temperature of 0.5 K. The subtraction of nuclear part in $Ho_2Zr_2O_7$ is also an approximation as it overshadows the magnetic contribution below $T = 1.5$ K. We have discussed three possible methods to extract the $C_{\rm m}$ for $Ho_2Zr_2O_7$ by subtracting the $C_{\rm N}$ (shown in figure 5(c)) to illustrate the generic effect of structural symmetry and electronic distribution on the heat capacity.

First, the $C_{\rm m}$ was obtained by subtracting the nuclear hyperfine contribution $C_{\rm N1}$ used in the previous reports in case of isostructural Ho_2GaSbO_7 and $Ho_2Ti_2O_7$ [3, 31]. The obtained $C_{\rm m}$ gives a dynamic ground state crossing the entropy limit of $R\ln 2$, expected for the maximum possible states. However, it is hard to rely on this estimation method due to the difference in structural symmetry and effective magnetic moment of $Ho_2Zr_2O_7$ and Ho_2GaSbO_7. Additionally, the observed heat capacity in the systems viz Ho metal, $Ho_2Ti_2O_7$, Ho_2GaSbO_7 pyrochlore, $HoCrO_3$ distorted perovskite, shows a variation of $\sim$2–6% in the peak position and magnitude of $C_{\rm N}$ [6, 35–37]. Therefore in the second case, we have fixed the peak position to 0.3 K and tried to fit the $C_{\rm N}$ of $Ho_2Zr_2O_7$ ($I = 7/2$) using the equation [38]

$$C_{\rm N} = \frac{R\sum_{i=-I}^{I}\sum_{j=-I}^{I}(W_i^2 - W_iW_j)e^{\frac{-W_i-W_j}{kT}}}{(kT)^2\sum_{i=-I}^{I}\sum_{j=-I}^{I}e^{\frac{-W_i-W_j}{kT}}} \qquad (1)$$

where R is universal gas constant, $W_i/k = a'i + P[i^2 - I(I+1)/3]$, $a' = 0.299 \pm 0.002$ K is measure of the strength of hyperfine interactions and P represents the quadrupole coupling constant which is negligible in case of holmium. The obtained nuclear hyperfine contribution $C_{\rm N2}$ is shown in figure 5(c). Remarkably, the additional constraints due to the substitution of Zr for Ti could account for the change in hyperfine interactions, the resulting peak position and magnitude of $C_{\rm N}$. In the third case, we have used the hyperfine interaction model ($C_{\rm N3}$) to fit the raw data without approximating the magnitude or the nuclear peak position. We estimated that the total uncertainty in the extracted data is more than $\sim$10% due to the uncertainty in the subtraction of nuclear spin contribution. Figures 5(d) and (e) shows the extracted $C_{\rm m}$ data at $H = 0$ and 5 kOe where $C_{\rm m1}$, $C_{\rm m2}$, $C_{\rm m3}$ are the extracted magnetic contributions according to the three different fitting approaches

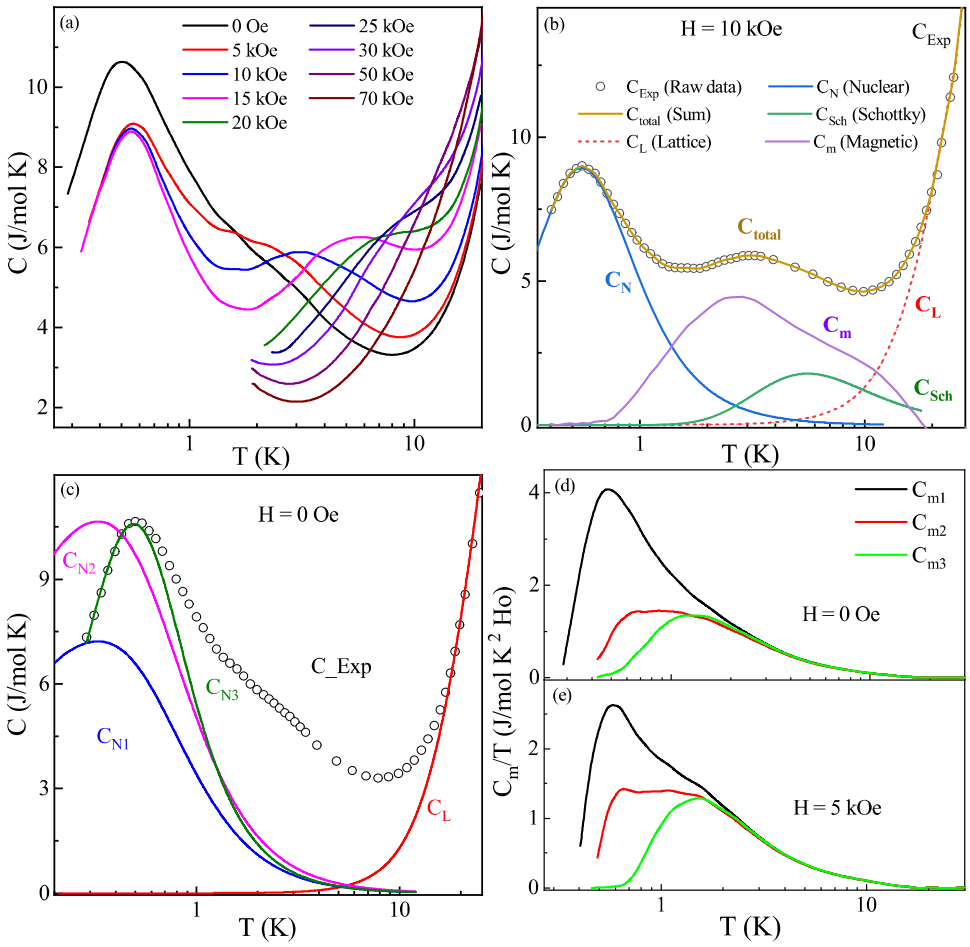

Figure 5. (a) Temperature dependence of heat capacity data at various magnetic fields between 0–70 kOe. (b) Heat capacity data analysis of $Ho_2Zr_2O_7$ at $H = 10$ kOe using various fitting models. (c) Nuclear heat capacity data analysis of $Ho_2Zr_2O_7$ at $H =$ Oe using three different approaches as explained in the main text. (d) and (e) Shows the temperature dependence of C_m/T at $H = 0$, 5 kOe. The components C_{m1}, C_{m2} and C_{m3} represent the magnetic heat capacity extracted using the different approaches discussed in the main text.

and correspondingly the ΔS_{m1}, ΔS_{m2}, ΔS_{m3} are the magnetic entropy changes (shown in figure 6(a)).

The recovered entropy of (ΔS_m) was calculated by integrating the C_m/T from $T = 0.3$–12 K. We have plotted ΔS_m of $Ho_2Zr_2O_7$ obtained at $H = 0$ from the above mentioned three methods along with the ΔS_m for spin ice $Ho_2Ti_2O_7$ taken from reference [3] in figure 6(a). In the absence of a magnetic field, the ΔS_m (third case) is comparatively lower than for the disordered state value of $R \ln 2$ corresponding to the maximum possible 2^N states available to N spins, which indicates that the residual entropy is small compared to the spin ice value as T goes to zero. The $Ho_2Ti_2O_7$ is reported to show Pauling's value of water ice $(R/2)\ln(3/2)$ at zero magnetic field [3]. The integrated entropy for $Ho_2Zr_2O_7$ is larger than that for $Ho_2Ti_2O_7$, indicating a significant decrease in the zero-point entropy. It is to mention that the heat capacity fitting performed for an even larger temperature range up to 35 K did not show evidence of missing entropy. The increase in entropy is understood from the chemical alteration of the pyrochlore structure with Zr substitution. The partial replacement of Dy or Ho site in $(Dy/Ho)_{2-x}Y_xTi_2O_7$ by non-magnetic Y, Lu strongly affect the spin ice state, however, the lattice structure remains intact [6, 39]. Figure 6(b) shows the recovered value of ΔS_m at various magnetic fields taken at $T = 12$ K. Application of a magnetic field to the degenerate ground state restored some of the missing entropy, presumably due to the lifted degeneracy of the ground state as the applied field breaks the system's symmetry. An additional peak appears at $T > 3$ K on switching the magnetic field and shift to higher temperatures with an increase in the magnetic field. This also shows a continuous decrease in magnetic entropy, leading to a non-magnetic ground state at 70 kOe. We have also fitted the heat capacity data of $Ho_2Ti_2O_7$ taken from reference [3] using the same hyperfine model (inset of figure 6(b)). Amazingly, the extracted magnetic entropy is significantly lower ($\sim$12%) than the expected value for the spin ice systems. Thus the approach of using the nuclear contribution of Ho_2GaSbO_7 by Blöte *et al* is not a good choice for the estimation of magnetic heat capacity of $Ho_2Ti_2O_7$ compound. Similarly, the use of estimated nuclear heat capacity of $Dy_3Ga_5O_{12}$ garnet to $Dy_2Ti_2O_7$ is suggested to be

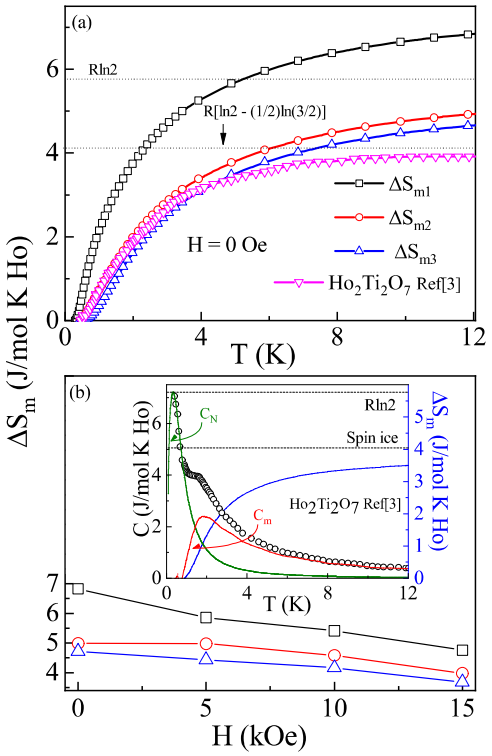

Figure 6. (a) Temperature dependence of extracted magnetic entropy (ΔS_{m1}, ΔS_{m2} and ΔS_{m3} extracted using three methodologies) of $Ho_2Zr_2O_7$ at $H = 0$ Oe and zero field data of spin ice $Ho_2Ti_2O_7$ taken from the reference [3]. (b) Variation in the magnetic entropy of $Ho_2Zr_2O_7$ in reference [3] as a function of applied field. Inset shows the heat capacity data (symbol) of $Ho_2Ti_2O_7$ fitted (green) with hyperfine model (equation (1)), extracted magnetic heat capacity (red) and the magnetic entropy (blue).

incorrect due to the difference between the magnitude of moments ($Dy_3Ga_5O_{12}$: $\mu_{eff} \sim 4.5\ \mu_B$ and $Dy_2Ti_2O_7$: $\mu_{eff} \sim 9.8\ \mu_B$) [32].

In conclusion, $Ho_2Zr_2O_7$ with its disordered pyrochlore structure shows the presence of spin freezing at $T \sim 10$ K on the application of the magnetic field. Unlike the spin ice systems, the heat capacity and susceptibility indicate large spin dynamics at the lowest measuring temperature and the absence of Pauling residual entropy. These studies show that the low-temperature magnetic state of pyrochlores systems can be significantly altered by frustration and structural disorder. We have further analyzed the low-temperature heat capacity and discussed the error arising from the estimation of nuclear contribution in holmium based system. We observed that the use of the hyperfine model (equation (1)) for the estimation of nuclear heat capacity leads to the significant correction in the residual spin ice entropy of the $Ho_2Ti_2O_7$. The disordered pyrochlore zirconates provide an excellent family of materials for further investigation, for the role of induced disorder on the spin dynamics and the creation/propagation of monopole–antimonopole excitations in the frustrated systems. The low-temperature neutron scattering technique would be important for the identification of true magnetic ground state in $Ho_2Zr_2O_7$.

Acknowledgment

We thank AMRC, Indian Institute of Technology Mandi for the experimental facility. Sheetal acknowledged IIT Mandi and MHRD India for the HTRA fellowship. We acknowledge financial support by BMBF via the Project Spin-Fun (13XP5088) and by Deutsche Forschungsgemeinschaft (DFG) under Germany's Excellence Strategy EXC2181/1-390900948 (the Heidelberg STRUCTURES Excellence Cluster) and through Project KL 1824/13-1.

Data availability statement

All data that support the findings of this study are included within the article (and any supplementary files).

ORCID iDs

Sheetal https://orcid.org/0000-0002-4766-0108
A Elghandour https://orcid.org/0000-0001-8289-2644
R Klingeler https://orcid.org/0000-0002-8816-9614
C S Yadav https://orcid.org/0000-0002-0664-5489

References

[1] Matsuhira K, Hinatsu Y and Sakakibara T 2001 Novel dynamical magnetic properties in the spin ice compound $Dy_2Ti_2O_7$ *J. Phys.: Condens. Matter* **13** L737
[2] Ramirez A P, Hayashi A, Cava R J, Siddharthan R and Shastry B 1999 Zero-point entropy in 'spin ice' *Nature* **399** 333
[3] Bramwell S *et al* 2001 Spin correlations in $Ho_2Ti_2O_7$: a dipolar spin ice system *Phys. Rev. Lett.* **87** 047205
[4] Snyder J, Slusky J, Cava R J and Schiffer P 2001 How 'spin ice' freezes *Nature* **413** 48
[5] Snyder J, Ueland B, Slusky J, Karunadasa H, Cava R J and Schiffer P 2004 Low-temperature spin freezing in the $Dy_2Ti_2O_7$ spin ice *Phys. Rev.* B **69** 064414
[6] Lau G, Freitas R, Ueland B, Muegge B, Duncan E, Schiffer P and Cava R 2006 Zero-point entropy in stuffed spin-ice *Nat. Phys.* **2** 249
[7] Ehlers G, Cornelius A, Orendac M, Kajnakova M, Fennell T, Bramwell S and Gardner J 2002 Dynamical crossover in 'hot' spin ice *J. Phys.: Condens. Matter* **15** L9
[8] Kimura K, Nakatsuji S, Wen J, Broholm C, Stone M, Nishibori E and Sawa H 2013 Quantum fluctuations in spin-ice-like $Pr_2Zr_2O_7$ *Nat. Commun.* **4** 1934
[9] Wen J-J *et al* 2017 Disordered route to the coulomb quantum spin liquid: random transverse fields on spin ice in $Pr_2Zr_2O_7$ *Phys. Rev. Lett.* **118** 107206
[10] Petit S *et al* 2016 Observation of magnetic fragmentation in spin ice *Nat. Phys.* **12** 746
[11] Ramon J, Wang C, Ishida L, Bernardo P, Leite M, Vichi F, Gardner J and Freitas R 2019 Absence of spin-ice state in the disordered fluorite $Dy_2Zr_2O_7$ *Phys. Rev.* B **99** 214442
[12] Sibille R *et al* 2017 Coulomb spin liquid in anion-disordered pyrochlore $Tb_2Hf_2O_7$ *Nat. Commun.* **8** 892
[13] Anand V, Islam A, Samartzis A, Xu J, Casati N and Lake B 2018 Optimization of single crystal growth of candidate quantum spin-ice $Pr_2Hf_2O_7$ by optical floating-zone method *J. Cryst. Growth* **498** 124
[14] Anand V, Tennant D and Lake B 2015 Investigations of the effect of nonmagnetic Ca substitution for magnetic Dy on spin-freezing in $Dy_2Ti_2O_7$ *J. Phys.: Condens. Matter* **27** 436001

[15] Mouta R, Silva R and Paschoal C 2013 Tolerance factor for pyrochlores and related structures *Acta Crystallogr.* B **69** 439

[16] Sheetal and Yadav C S 2021 Evolution of spin freezing transition and structural, magnetic phase diagram of $Dy_{2-x}La_xZr_2O_7$ ($0 \leqslant x \leqslant 2.0$) *Sci. Rep.* **11** 19832

[17] Anand V *et al* 2016 Physical properties of the candidate quantum spin-ice system $Pr_2Hf_2O_7$ *Phys. Rev.* B **94** 144415

[18] Anand V, Bera A, Xu J, Herrmannsdörfer T, Ritter C and Lake B 2015 Observation of long-range magnetic ordering in pyrohafnate $Nd_2Hf_2O_7$: a neutron diffraction study *Phys. Rev.* B **92** 184418

[19] Sheetal , Ali A, Rajput S, Singh Y, Maitra T and Yadav C S 2020 Emergence of weak pyrochlore phase and signature of field induced spin ice ground state in $Dy_{2-x}La_xZr_2O_7$; $x = 0, 0.15, 0.3$ *J. Phys.: Condens. Matter* **32** 365804

[20] Xu J, Islam A, Glavatskyy I, Reehuis M, Hoffmann J-U and Lake B 2018 Field-induced quantum spin-1/2 chains and disorder in $Nd_2Zr_2O_7$ *Phys. Rev.* B **98** 060408

[21] Zhang F, Lang M, Becker U, Ewing R and Lian J 2008 High pressure phase transitions and compressibilities of $Er_2Zr_2O_7$ and $Ho_2Zr_2O_7$ *Appl. Phys. Lett.* **92** 011909

[22] Ehlers G, Cornelius A, Fennell T, Koza M, Bramwell S and Gardner J 2004 Evidence for two distinct spin relaxation mechanisms in 'hot' spin ice $Ho_2Ti_2O_7$ *J. Phys.: Condens. Matter* **16** S635

[23] Rodríguez-Carvajal J 1990 FULLPROF: a program for Rietveld refinement and pattern matching analysis *Satellite Meeting on Powder Diffraction of the XV Congress of the IUCr* vol 127 (Toulouse, France)

[24] Mandal B, Garg N, Sharma S M and Tyagi A 2006 Preparation, xrd and Raman spectroscopic studies on new compounds $RE_2Hf_2O_7$ (RE = Dy, Ho, Er, Tm, Lu, Y): pyrochlores or defect-fluorite? *J. Solid State Chem.* **179** 1990

[25] Harris M J, Bramwell S, McMorrow D, Zeiske T and Godfrey K 1997 Geometrical frustration in the ferromagnetic pyrochlore $Ho_2Ti_2O_7$ *Phys. Rev. Lett.* **79** 2554

[26] den Hertog B C and Gingras M J 2000 Dipolar interactions and origin of spin ice in Ising pyrochlore magnets *Phys. Rev. Lett.* **84** 3430

[27] Shukla M, Upadhyay R, Tolkiehn M and Upadhyay C 2020 Robust spin-ice freezing in magnetically frustrated $Ho_2Ge_xTi_{2-x}O_7$ pyrochlore *J. Phys.: Condens. Matter* **32** 465804

[28] Binder K and Young A P 1986 Spin glasses: experimental facts, theoretical concepts, and open questions *Rev. Mod. Phys.* **58** 801

[29] Lal S, Mukherjee K and Yadav C 2018 Effect of crystalline electric field on heat capacity of $LnBaCuFeO_5$ (Ln = Gd, Ho, Yb) *Solid State Commun.* **270** 130

[30] Ku S *et al* 2018 Low temperature magnetic properties of $Nd_2Ru_2O_7$ *J. Phys.: Condens. Matter* **30** 155601

[31] Blöte H, Wielinga R and Huiskamp W 1969 Heat-capacity measurements on rare-earth double oxides $R_2M_2O_7$ *Physica* **43** 549

[32] Henelius P, Lin T, Enjalran M, Hao Z, Rau J, Altosaar J, Flicker F, Yavorskii T and Gingras M 2016 Refrustration and competing orders in the prototypical $Dy_2Ti_2O_7$ spin ice material *Phys. Rev.* B **93** 024402

[33] Den Hertog B, Gingras M J, Bramwell S T and Harris M J 1999 Comment on Ising pyrochlore magnets: low temperature properties, 'ice rules', and beyond by R Siddharthan *et al* *Phys. Rev. Lett.* **83** 1854

[34] Ramón J G A 2020 Geometrically frustrated magnetism in the pyrochlore $Er_2Ti_{2-x}Sn_xO_7$ and in the disordered fluorites $R_2Zr_2O_7$ (R = Dy, Ho, Tb) *PhD Thesis* Universidade de São Paulo

[35] Kumar C, Xiao Y, Nair H, Voigt J, Schmitz B, Chatterji T, Jalarvo N and Brückel T 2016 Hyperfine and crystal field interactions in multiferroic $HoCrO_3$ *J. Phys.: Condens. Matter* **28** 476001

[36] Nagata S, Sasaki H, Suzuki K, Kiuchi J and Wada N 2001 Specific heat anomaly of the holmium garnet $Ho_3Al_5O_{12}$ at low temperature *J. Phys. Chem. Solids* **62** 1123

[37] Krusius M, Anderson A and Holmström B 1969 Calorimetric investigation of hyperfine interactions in metallic Ho and Tb *Phys. Rev.* **177** 910

[38] Lounasmaa O 1962 Specific heat of holmium metal between 0.38 and 4.2 K *Phys. Rev.* **128** 1136

[39] Snyder J, Ueland B, Mizel A, Slusky J, Karunadasa H, Cava R and Schiffer P 2004 Quantum and thermal spin relaxation in the diluted spin ice $Dy_{2-x}M_xTi_2O_7$ (M = Lu, Y) *Phys. Rev.* B **70** 184431

5.1 Introduction

Research in rare-earth pyrochlore magnets has been revived by the discovery the spin ice state in Ising-like frustrated pyrochlore titanates, namely $Ho_2Ti_2O_7$ and $Dy_2Ti_2O_7$ [28, 29]. The spin ice state is an analogous to the degenerate ground state of the solid ice water, where inequality of the hydrogen bonds results in finite entropy even as the temperature decreases towards zero [30, 31]. Likewise, on a pyrochlore lattice, the spin orientation of the rare-earth magnetic ions form a '2-in-2-out' configuration resembling the '2-near-2-far' one in water ice.

Rare-earth oxides with the formula $RE_2Zr_2O_7$ with RE = Ce, Pr, Nd, Gd, Tb, Dy, or Ho magnetic ions have been extensively studied aiming at observing spin ice states or other novel ground states forming in strongly geometrically frustrated lattices. While the canonical spin ice systems $Ho_2Ti_2O_7$ and $Dy_2Ti_2O_7$ crystallize in an ordered-fluorite (pyrochlore) structure with space group $Fd\overline{3}m$, depending on the ratio r_{RE}/r_{Zr} of ionic radii of RE^{3+} and Zr^{4+}, $RE_2Zr_2O_7$ crystallizes either in the pyrochlore or a defected-fluorite structure [32]. Accordingly, $RE_2Zr_2O_7$ systems with RE = Ce, Pr, Nd, Gd, adopt a pyrochlore structure, whereas those with RE = Tb, Dy, Ho magnetic ions exhibits defected-fluorite structure. For light RE ions, the systems tend to form quantum ground states [33]. For instance, $Ce_2Zr_2O_7$ has been reported a quantum spin-liquid system with minimum magnetic and non-magnetic disorder [34–36]. $Pr_2Zr_2O_7$ exhibits a dynamic magnetic ground state with no long-range magnetic order and Pr^{3+} moments freeze below $T = 300$ mK [37]. In $Nd_2Zr_2O_7$, Nd^{3+} ions exhibit a single-ion crystal-field ground state of Ising-anisotropic dipolar-octuplar doublet-type and the system evolves long-range antiferromagnetic order at $T_N \simeq 0.4$ K with an 'all-in-all-out' (AIAO) configuration [38–40]. In contrast, $RE_2Zr_2O_7$ systems with quasi-classical large spins do not show long-range magnetic order down to very low temperatures. For example, $Tb_2Zr_2O_7$ exhibits a dynamic magnetic ground state at least down to $T = 0.1$ K with collective antiferromagnetic correlations while a spin-glass transition appears at $T = 2.5$ K [41]. Similarly, $Dy_2Zr_2O_7$ exhibits a dynamic magnetic ground state down to $T = 0.04$ K which is characterized by collective antiferromagnet correlations while Dy^{3+} moments freeze at $T = 1$ K [42].

In this chapter, we report on the origin of spin freezing in $Ho_2Zr_2O_7$ which does not evolve magnetic long-range order at least down to 280 mK [27]. To be specific, we investigate the spin dynamics and magnetic field induced relaxation processes at relatively high temperatures, which mediates complete freezing of the spins below $T = 0.6$ K. Our results show that the spin freezing is preceded by two slow spin relaxation processes at $T_{g1} = 7(1)$ K and $T_{g2} = 0.9(1)$ K [43] similar to the canonical spin ice $Ho_2Ti_2O_7$ [44] and $Dy_2Ti_2O_7$ [45].

5.2 Experimental Details

The DC magnetization of $Ho_2Zr_2O_7$ polycrystalline sample, pelletized into a thin flat disc with a mass of 7.8(2) mg, was measured in the temperature range of 1.8 to 60 K and in magnetic fields up to 4 T by means of the Magnetic Properties Measurement System (MPMS3, Quantum Design). For measurements down to 400 mK, the MPMS-3 was equipped with the iQuantum He-3 probe. The DC magnetization were obtained in two ways: (a) after cooling the sample in the external magnetic measurement field (field-cooled; FC), and (b) by applying the magnetic field after cooling the sample to the lowest temperature (zero-field-cooled; ZFC). Note, prior to each isothermal DC magnetization measurement, the sample's temperature was elevated to $T = 10$ K in the absence of a magnetic field, then cooled to the target temperature before a magnetic field was applied.

The AC magnetization was measured in the temperature range of 1.8 to 60 K, with a 7 - 9 Oe AC excitation field, up to 4 T DC magnetic fields, and frequencies ranging from 10 Hz to 200 Hz using the AC option of the MPMS-3. For measurements at $f > 1$ KHz the ACSMII option of the Physical Properties Measurement System (PPMS, Quantum Design) was employed.

5.3 Experimental Results

5.3.1 Slow Spin Dynamics Above 1.8 K

Figure 5.1 (a) shows the temperature dependence of the real part, $\chi'_{\rm ac}$, of the AC magnetic susceptibility measured at different frequencies ($B_{ac} = 0.7$ mT) in zero DC magnetic field as well as the static magnetic susceptibility $\chi_{\rm dc} = M/B$ measured at $B = 0.1$ T. Upon cooling, $\chi'_{\rm ac}$ increases monotonically following a Curie-Weiss-like behaviour. The data show no frequency dependence in the regime 10 Hz $\leq$ $f \leq 10$ kHz and $\chi'_{\rm ac}$ coincides with $\chi_{\rm dc}$. Similarly, $\chi''_{\rm ac}$ presented in Fig. 5.1 (b) does not show any anomalies either.

The Curie-Weiss behaviour of $\chi_{\rm dc}$ is highlighted in the inset of Fig. 5.1 (a). Fitting the data by an extended Curie-Weiss law $\chi_{\rm dc} = C/(T + \Theta) + \chi_0$ yields the Weiss temperature $\Theta = -3(1)$ K. From the obtained Curie constant C we deduce the effective magnetic moment $\mu_{\rm eff} \simeq 9.5(1)\ \mu_{\rm B}/{\rm Ho}^{3+}$ in good agreement with Ref. [43] and with the expected free ion value. The sign of the estimated Weiss temperature and its small value indicate the presence of a weak antiferromagnetic coupling of a few Kelvins, which agrees well with previous reports [43]. Using a mean-field approach and assuming only nearest-neighbor (nn) couplings, the average exchange interaction $J_{\rm nn}$ between Ho^{3+} moments can be estimated

using the relation [46]:

$$J_{nn} = \frac{3\Theta_W}{zJ(J+1)}, \tag{5.1}$$

where the number of the nearest neighbors is $z = 6$ and the total angular momentum $J = 8$ yields $J_{nn} = -20(2)$ mK, which is in a good agreement with previous reports [43].

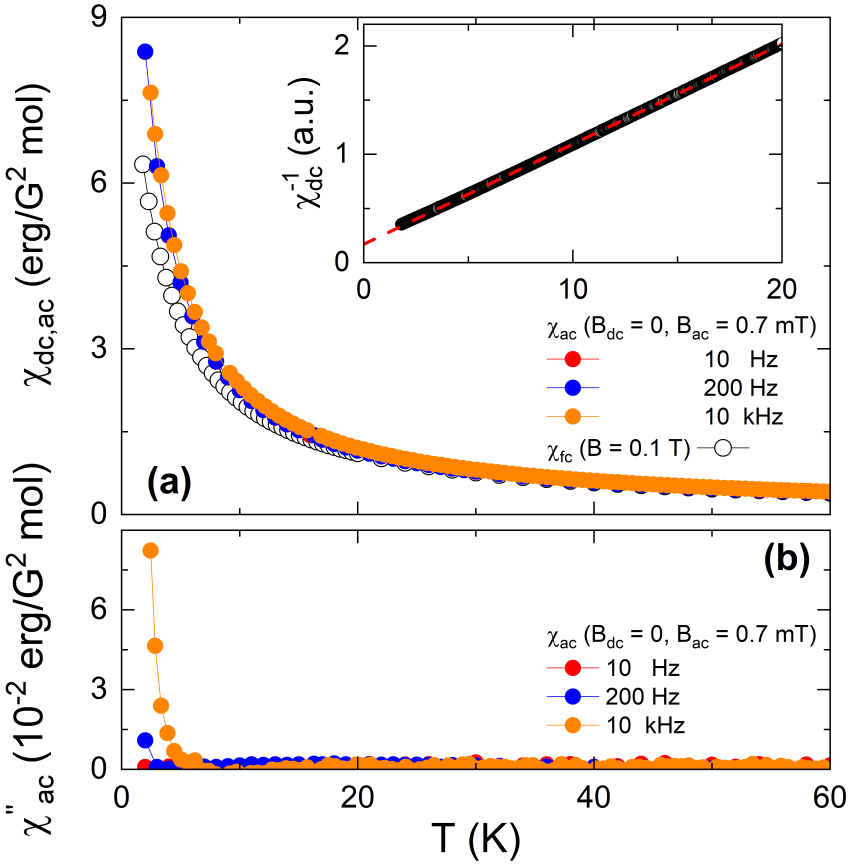

Figure 5.1: Temperature dependence of (a) the real part $\chi'_{\rm ac}$ and (b) the imaginary part $\chi''_{\rm ac}$ of the AC magnetic susceptibility of $Ho_2Zr_2O_7$ measured at different frequencies 10 $\leq f \leq$10 kHz, 0.7 mT AC excitation field, and $B_{\rm dc} = 0$ T. Black open circle in (a) represent the static magnetic susceptibility $\chi_{\rm dc} = M/B$ measured at $B = 0.1$ T. Inset: Inverse of the $\chi_{\rm dc}$ (black solid circles) and an extended Curie–Weiss law fit to the data (dashed red line).

Figure 5.1 (b) shows the temperature dependence of the imaginary part, $\chi''_{\rm ac}$, of the AC magnetic susceptibility measured at different frequencies ($B_{\rm ac} = 0.7$ mT) in zero dc magnetic field. $\chi''_{\rm ac}$ data show no anomalies consistent with the paramagnetic behaviour [47] inferred from its corresponding $\chi'_{\rm ac}$.

Applying external DC magnetic fields results in a more complex behavior of both $\chi'_{\rm ac}$ and $\chi'_{\rm ac}$ as shown in Fig. 5.2. The data imply significant dissipative effects at $B_{\rm dc} = 1$ T below

about 22 K and non-linear field dependence of the susceptibility is probed in $\chi'_{\rm ac}$ up to $\sim$ 30 K, at f = 10 Hz. Note, that in the same temperature regime, DC magnetization shows CW behaviour and very weak exchange interactions of $J_{\rm nn} \simeq 20(2)$ mK. The main features, at $B_{\rm dc} = 1$ T, are a broad hump and decrease upon cooling in $\chi'_{\rm ac}$ and a peak in $\chi''_{\rm ac}$ centered at $T_{\rm g1} = 7(1)$ K. The features agree with the Kramer-Kronig relations and shift to higher temperatures with increasing the field. The data in Fig. 5.2 hence imply dc-field induced relaxation process. Similar observations of field-induced processes indeed are typical for the canonical spin ice systems and have been reported for $Dy_2Ti_2O_7$ [45] and $Ho_2Ti_2O_7$ [44] as evidenced by features respectively peaks in $\chi'_{\rm ac}$ and $\chi''_{\rm ac}$ at 15(1) K. Similar data are also reported for $Tb_2Ti_2O_7$ at 20 K [48] and recently for $Tb_2Zr_2O_7$ [41] where a peak in $\chi''_{\rm ac}$ is centered at 25(1) K.

From the AC magnetization measurements, we observe that $\chi'_{\rm ac}$ and $\chi''_{\rm ac}$ are frequency independent in the absence as well as the presence of DC magnetic field as shown in Fig. 5.1. The above mentioned field-induced anomalies in $\chi'_{\rm ac}$ also show up in the DC magnetization as displayed in Fig. 5.3 where both the $\partial(\chi)/\partial T$ (with $\chi = M/B$) and $\partial(\chi')/\partial T$ (measured at f = 40 Hz) are displayed for different applied DC fields. Both quantities exhibit the same trends. Specifically, the magnetic field induces a peak, which is gradually suppressed and shifted to higher temperatures upon increasing the field. Note, the peak in the DC data appears at lower temperatures as compared to f = 40 Hz AC data. Further, the absolute magnitude of the peaks in $\partial(\chi')/\partial T$ is smaller than that of $\partial(\chi)/\partial T$. A similar behaviour was observed in $Tb_2Ti_2O_7$ [48] and has been attributed to the development of correlated clusters coupled through dipolar interactions, similar to domains in a ferromagnet. Note, there is no bifurcation between the ZFC and FC protocols in the DC magnetization data.

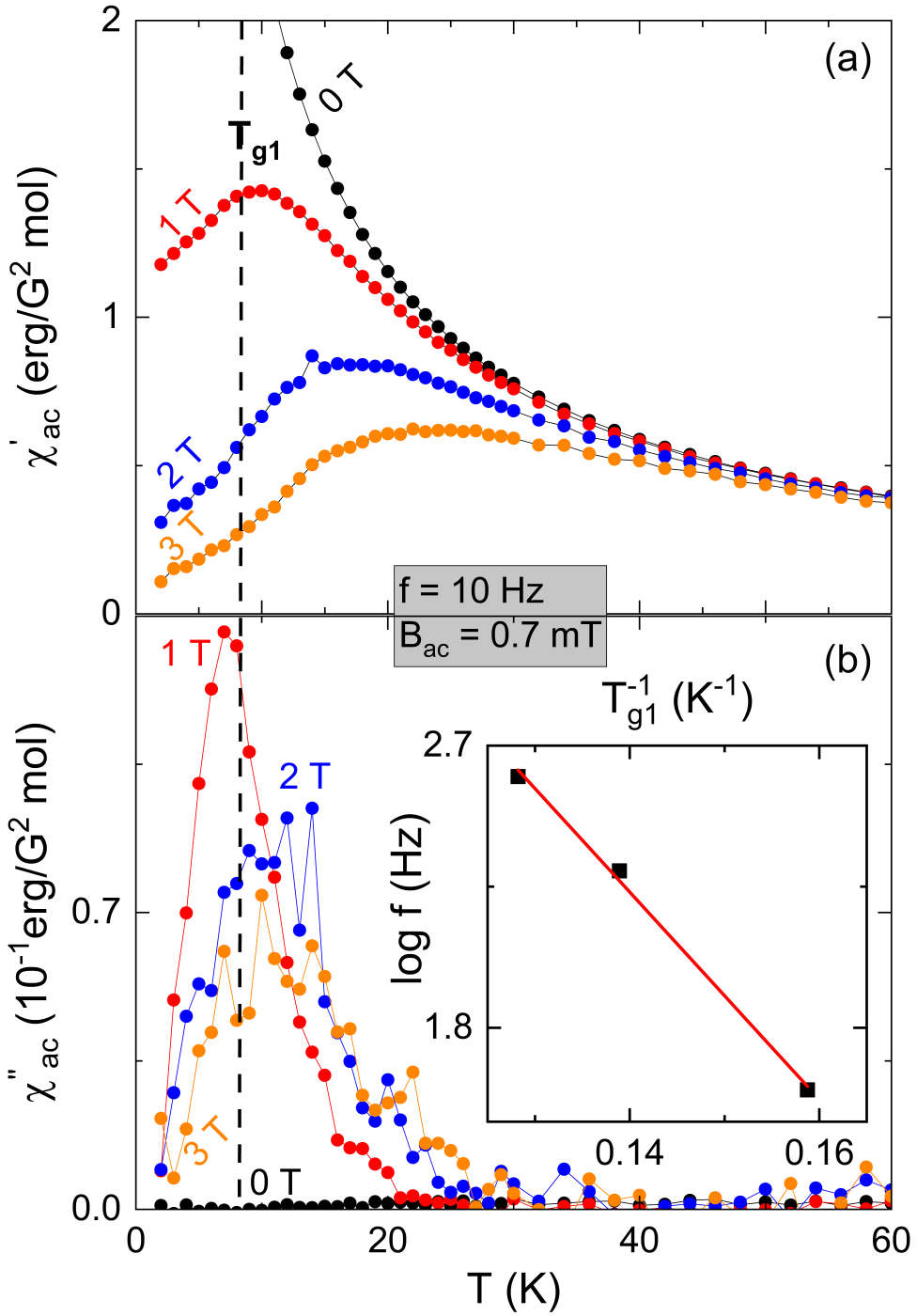

Figure 5.2: Temperature dependence of (a) the real part χ'_{ac} and (b) the imaginary part χ''_{ac} of the AC magnetic susceptibility of $Ho_2Zr_2O_7$ measured at different static magnetic fields $0 \leq B \leq 3$ T, 0.7 mT AC excitation field, and $f = 10$ Hz. Inset: Logarithm of the measurement frequency versus the inverse of the freezing temperature obtained at $B_{dc} = 1$ T. The red line is a fit by means of Arrhenius law. The dashed line guides the eye to follow the magnetic field effect on the induced anomalies T_{g1}.

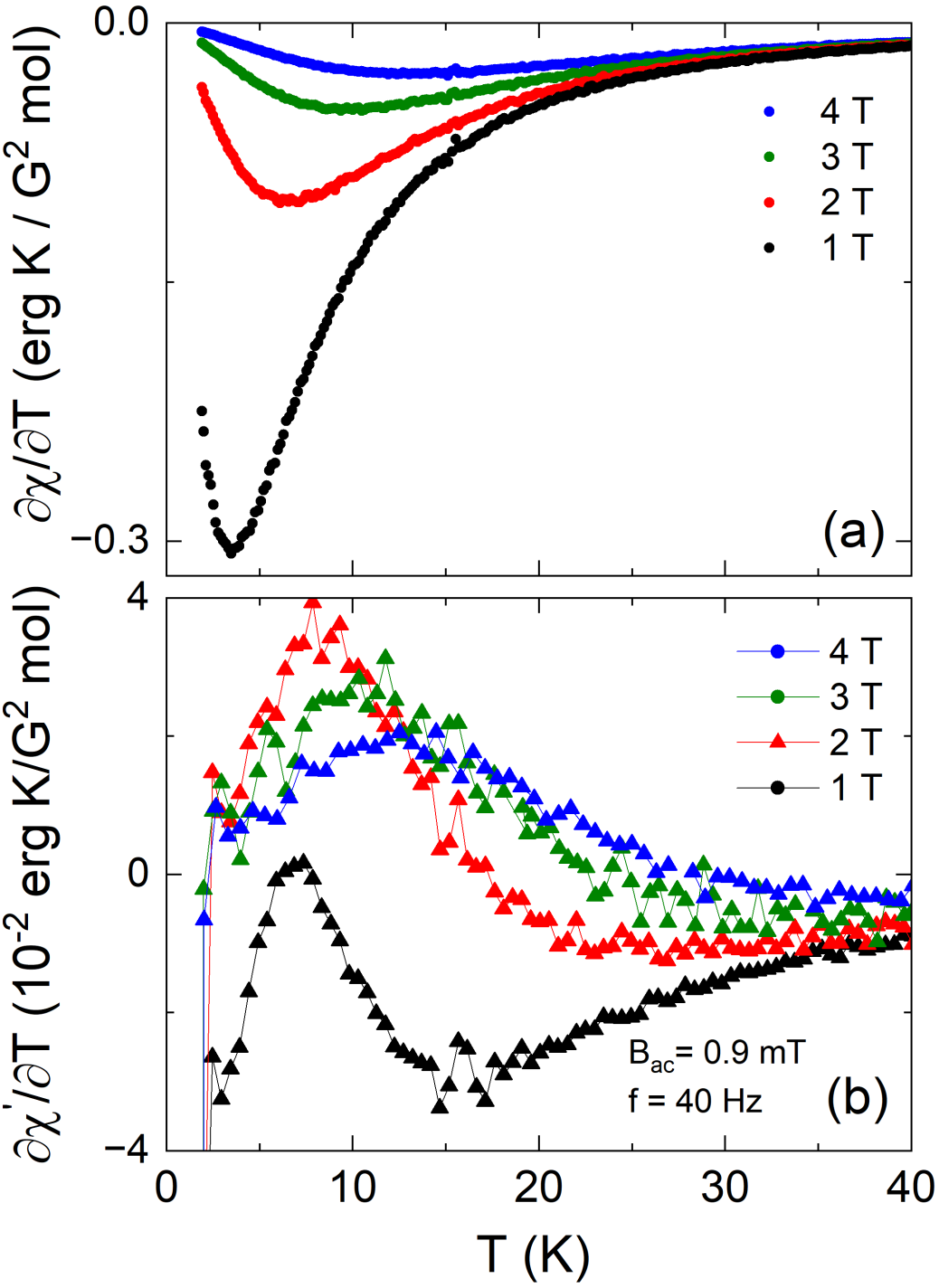

Figure 5.3: Temperature dependence of the derivative of (a) the real part, $\partial(\chi')/\partial T$, of the AC magnetic susceptibility of $Ho_2Zr_2O_7$ measured at different static magnetic fields $1 \leq B \leq 4$ T, 0.9 mT AC excitation field, and $f = 40$ Hz, and (b) the static magnetic susceptibility, $\partial(\chi)/\partial T$, measured at the same applied DC magnetic fields.

5.3.2 Spin Freezing Below 1.8 K

Figure. 5.5 (a and b) shows the DC magnetic susceptibility of $Ho_2Zr_2O_7$ measured in the low temperature regime between 400 mK and 1 K in external magnetic fields of 10 $\leq B \leq$ 100 mT. At B = 10 mT, the susceptibility shows a clear irreversibility, below $T \approx 0.6$ K, between ZFC and FC measured data. χ_{ZFC} exhibits a broad peak centered at $T_{\mathrm{b}} \approx 0.6$ K and strongly decreases below this temperature but does not reach zero. In contrast, χ_{FC} is almost constant in the bifurcation regime which is a typical signature of spin-glass [49]. This behavior agrees well with other reports on spin ice pyrochlores where similar blocking temperatures $T_{\mathrm{b}} \approx 0.60 - 0.75$ K are observed for $A_2B_2O_7$ (A = Dy, Ho and B = Ti, Sn) [50–53]. The presence of similar blocking temperatures in systems with strongly different magnetic moments and hence strongly different magnetic couplings J_{nn} between rare-earth ions' moments in the pyrochlore structure indicates not T_{b} is rather independent on J_{nn} [33]. The irreversibility between ZFC and FC magnetic susceptibilities of $Ho_2Zr_2O_7$ persists under external applied magnetic fields and the blocking temperature shifts to lower values (see Fig. 5.5 (a and b)) with increasing the field until no irreversibility is observed in the accessible temperature regime at $B \leq 0.1$ T. At $B = 0$ T, the specific heat capacity shows a broad peak centered at $T = 0.5$ K as depicted in Fig. 5.5 (d). The nature of the peak of excludes the presence of a magnetic phase transition in$Ho_2Zr_2O_7$, instead it has been assigned to nuclear heat capacity resulting from the hyperfine interactions of Ho^{3+}, as it has been discussed in the first half of this chapter [27].

At T = 1.8 K, the isothermal magnetization M vs. B of $Ho_2Zr_2O_7$ initially increases steeply and shows a pronounced right-bending towards saturation (see Fig. 5.8). At T = 0.4 K, M(7 T) amounts to 5.6 μ_{B}/Ho^{3+}; linearly extrapolating the high-field regime to B = 0 T yields $\simeq$ 5.0 μ_{B}/Ho^{3+} (see Fig. 5.6. These values are much smaller than the theoretically expected saturation magnetization of M_{sat} = 10 μ_{B} (g = 1.25, J = 8) of free Ho^{3+} ions as M(0.4 K,7 T) is only about 55% of M_{sat} (see Fig. 5.6. Such a reduced value can be attributed to substantial single ion anisotropy and it is consistent with the saturation value recently obtained for $Ho_2Zr_2O_7$ [43], and for other pyrochlores such $Ho_2Ti_2O_7$ [53, 54], $Ho_2Sn_2O_7$ [51], $Ce_2Zr_2O_7$ [34], and $Pr_2Zr_2O_7$ [37]. With a closer look on the magnetization of $Ho_2Zr_2O_7$ and $Ho_2Sn_2O_7$ measured at 0.4 K, the data follows a quasi-linear behavior in the low-field regime ($B < 0.2$ T), and the former exhibits a lower slope with increasing the magnetic field. This is reflected in a broad hump in case of $Ho_2Zr_2O_7$ centered at B = 0.03 T compared to a sharp peak for $Ho_2Sn_2O_7$ at B = 0.1 T as shown in Fig. 5.4. Further, the magnetization saturation is less rapidly achieved as expected for free moments (see the comparison with the Brillouin function

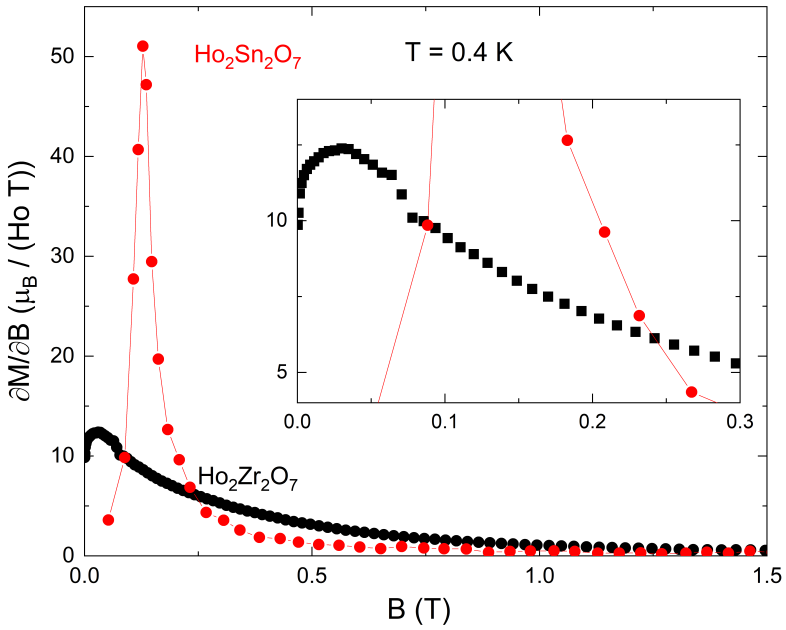

Figure 5.4: Magnetization derivatives of $Ho_2Zr_2O_7$, and $Ho_2Sn_2O_7$ measured at $T = 0.4$ K. The data of $Ho_2Sn_2O_7$ are adopted from [51]. Inset: A narrow scale of the main plot to emphasize the anomalies appear at $B < 0.3$ T.

in Fig. 5.6). The deviation from Brillouin function indicates the presence of short range correlations in $Ho_2Zr_2O_7$. These correlations are of antiferromagnetic type as inferred from the sign of the Weiss-temperature estimated earlier, and also evident when comparing the way to saturation in $Ho_2Zr_2O_7$ with that of $Ho_2Sn_2O_7$ as shown Fig. 5.6. Clearly, the later saturates faster consistent with the ferromagnetic correlations and exchange coupling of a few Kelvins between Ho^{3+} moments as reported in [51]. Spin freezing in $Ho_2Zr_2O_7$, which is evidence by thermal hysteresis in Fig. 5.5), appears also in the hysteresis of the isothermal magnetization measured below 0.6 K as depicted in Fig. 5.7. In this temperature regime, the magnetization exhibits small and narrow loops at 0.4 K and 0.5 K with a width of 9 mT and 3 mT, respectively. In the $M(B)$ curves, we observe initial left-bending in the up-sweep so that there is a broad hump in $\partial M/\partial B$ which (at 0.4 K) is centered at around 300 mT (see Fig. 5.4; in the down-sweep, there is no such hump. As expected, magnetization becomes reversible at higher temperatures as evidenced by the loop being fully closed at $T = 0.9$ K. Note, despite the presence of clear hysteresis at $T < T_b$, no conventional long-range thermodynamic ordering transition is observed as a function of temperature. This is evident by invoking the difference between χ_{FC} and χ_{ZFC} measurements of the dc magnetic susceptibility, $\Delta\chi = \chi_{FC} - \chi_{ZFC}$, as shown in Fig. 5.5 (c). Clearly, $\Delta\chi$ increases monotonically and smoothly through T_b with decreasing

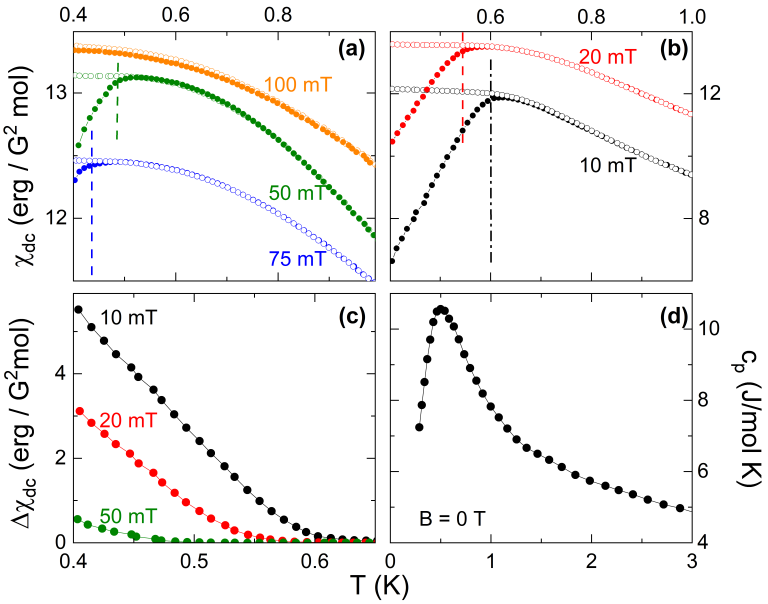

Figure 5.5: (a,b) Temperature dependence of the static magnetic susceptibility in various external magnetic fields $10 \leq B \leq 100$ mT. Empty and filled symbols refer to FC and ZFC measurement protocols (χ_{FC} and χ_{ZFC}), respectively. Dashed lines indicate the blocking temperature; T_b. (c) Difference between FC and ZFC magnetic susceptibility $\Delta\chi = \chi_{FC} - \chi_{ZFC}$ measured at different external fields. (b) Specific heat capacity at $B = 0$ T.

the temperature at all applied magnetic fields, and there is no evidence of any anomalies around or below T_b.

5.4 Discussion

Our heat capacity, DC and AC magnetization studies show that $Ho_2Zr_2O_7$ does not exhibit long-range magnetic order at least down to $T = 280$ mK. Instead, it has a disordered ground state with short-range antiferromagnetic correlations. Specifically, due to geometrical frustration, the system tends to go into a frozen state below $T_b = 0.60$ K, which is preceded by two field-induced spin relaxation processes at $T_{g1} = 7(1)$ K, and $T_{g2} = 0.9(1)$ K [43]. The field-induced spin freezing at high temperatures far above the frozen state ($T_{g1} = 7(1)$ K in case of $Ho_2Zr_2O_7$) seems to be an universal phenomenon in pyrochlore lattices with classical large magnetic ions. For instance, the anomalies observed in $Ho_2Zr_2O_7$'s AC magnetization data at $T_{g1} = 7(1)$ K resemble the peaks observed in the canonical spin ice systems $Dy_2Ti_2O_7$ and $Ho_2Ti_2O_7$ [44, 45], at $T = 15(1)$ K. It is also very similar to the peaks observed in χ' of the disordered-fluorite $Tb_2Zr_2O_7$ [41] at $T = 25$ K and the pyrochlore system $Tb_2Ti_2O_7$ at $T = 20$ K [48]. To follow this phenomenon, the

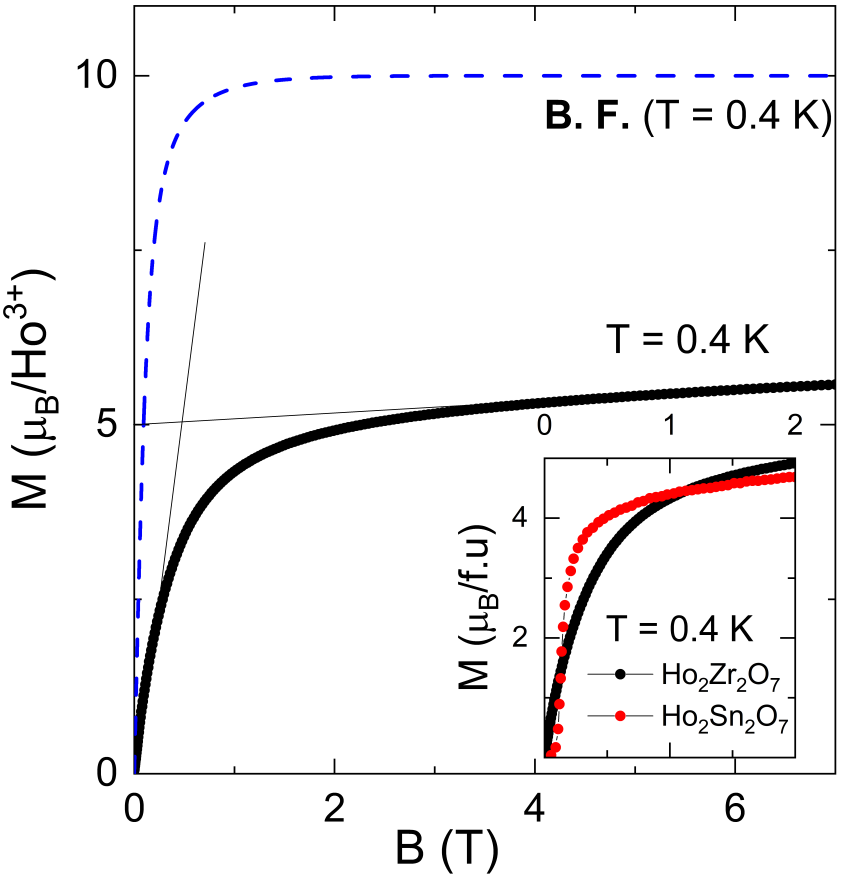

Figure 5.6: Magnetic field dependence of the isothermal magnetization of $Ho_2Zr_2O_7$ measured at 0.4 K in the upsweep mode and Brillouin function (dashed blue line) corresponding to non-interacting Ho^{3+} ions with $g_J = 1.25$, $J = 8$ at the same temperature. Inset: comparison of the magnetization of $Ho_2Zr_2O_7$ and $Ho_2Sn_2O_7$, which is taken from ref. [51].

spin freezing temperatures T_g, and their relaxation characteristic times (τ_o) of $RE_2B_2O_7$; RE = Ho, Dy, and B = Ti, Zr are listed in Table 5.1. At $B = 0$ T, the characteristic time reported for $Ho_2Zr_2O_7$ [43] from the frequency dependence of $T_{g2} = 1$ K, is two orders of magnitude lower than the one reported for the canonical spin ice $Ho_2Ti_2O_7$ [44, 55]. While, at $B = 1$ T, the characteristic time ($\tau = 2.1 \times 10^{-8}$) estimated for $Ho_2Zr_2O_7$ from the frequency dependence of $T_{g1} = 7(1)$ K (see inset in Fig. 5.2) has the same order of magnitude as the one reported for $Ho_2Ti_2O_7$.

Spin ice model based on Monte Carlo simulations of the nearest-neighbor interactions predicted [56] that systems with spin ice state would have a magnetization plateau at 3.33 μ_B/ion and magnetization saturation at 5.00 μ_B/ion for the magnetization measured along $B||$ [111] of the pyrochlore single crystal. These predictions were verified in the magnetization data, M vs B at $T = 1.8$ K, of $Ho_2Ti_2O_7$ single crystals [57]. Since the system at hand is a polycrystal, we compare its magnetization measured, at 1.8 K, with the

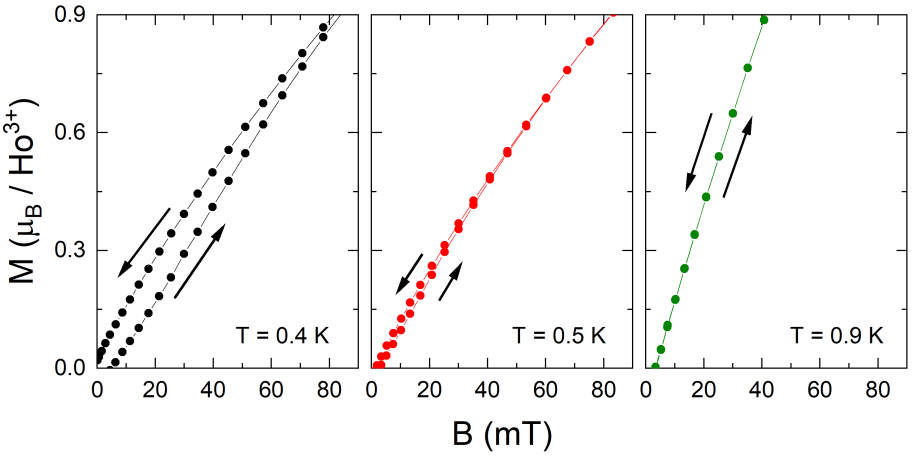

Figure 5.7: Magnetic field dependence of the isothermal magnetization of $Ho_2Zr_2O_7$ measured at 0.4 K, 0.5 K and 0.9 K. The up and down black arrows refer to the up and down magnetic field sweeps, respectively.

magnetization of $Ho_2Ti_2O_7$ polycrystal [54] as displayed in Fig. 5.8. From the comparison we draw the following remarks:

- At $B = 7$ T, $Ho_2Zr_2O_7$'s $M_{sat} = 5.1(1)$ μ_B/Ho^{3+}, whereas that of $Ho_2Ti_2O_7$ equals 4.6 μ_B/Ho^{3+}. While our M_{sat} agrees with the spin ice model predictions, the magnetization of $Ho_2Zr_2O_7$ and $Ho_2Ti_2O_7$ polycrystals do not show the predicted plateaux even at low temperature as $T = 400$ mK shown in Fig. 5.6 for $Ho_2Zr_2O_7$.

- The way to saturation is different in the two systems. In case of $Ho_2Ti_2O_7$, the saturation effect sets in at $B = 0.6(1)$ T, while in $Ho_2Zr_2O_7$ it is shifted to $B = 1.4(2)$ T. These difference signifies antiferromagnetic correlations into $Ho_2Zr_2O_7$ in comparison to the ferromagnetic correlations into $Ho_2Ti_2O_7$ [54, 57].

Table 5.1: Comparison of the relaxation processes' characteristic times (τ_o), and spin freezing temperatures (T_g) in $RE_2B_2O_7$; $RE = Ho$, Dy, and $B = Ti$, Zr.

Material	B_{dc} (T)	T_{g2} (K)	T_{g1} (K)	τ_o^2 (sec)	τ_o^1 (sec)	Ref.
$Dy_2Ti_2O_7$	0	1	15(1)	5×10^{-11}	2.2×10^{-10}	[45, 58]
$Ho_2Ti_2O_7$	0	1	-	1.6×10^{-11}	-	[44, 55]
$Ho_2Zr_2O_7$	0	1	-	8×10^{-13}	-	[43]
$Ho_2Ti_2O_7$	1	-	15(1)	-	5×10^{-8}	[44]
$Ho_2Zr_2O_7$	1	-	7(1)	-	2.1×10^{-8}	This work

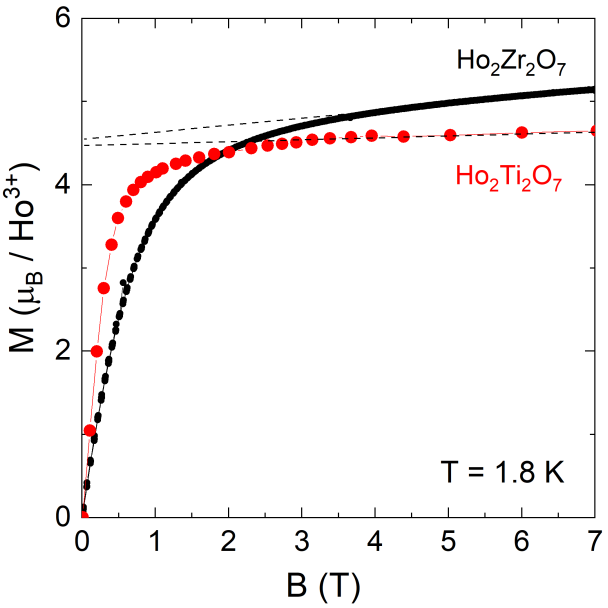

Figure 5.8: Magnetic field dependence of the isothermal magnetization of $Ho_2Zr_2O_7$, and $Ho_2Ti_2O_7$ measured at 1.8 K. The latter is taken from Ref. [54] for comparison.

Qualitatively, the spin freezing evidences in $Ho_2Zr_2O_7$, i.e., the irreversible magnetic susceptibility, the absence of a magnetic phase transition in the heat capacity down to 280 mK, and the frequency dependence of the maximum visible in χ'_{ac} at 0.9(1) K [43] are in a good agreement with spin-glass freezing observed in both highly disordered systems and in site-ordered geometrically frustrated antiferromagnets [52, 59–62]. Further, with a closer look on the evolution of the position of the blocking temperature T_b with the magnetic field, we observe that it is shifted to lower values and suppressed very fast by low magnetic fields. Such magnetic field effect agrees very well with the spin ice system $Ho_2Ti_2O_7$ [53], but contradicts what had been observed in the spin ice system $Dy_2Ti_2O_7$ [52]. Where in the latter T_b not only persists under much higher magnetic fields, but also shifts to higher values with increasing the field. This might be attributed to the differences between Dy^{3+} and Ho^{3+} magnetic ions, where the former, unlike Ho^{3+}, is a Kramers' ion.

Finally, the features appeared in χ_{dc}, $M(B)$, χ'_{ac}, χ''_{ac}, and their derivatives are used to construct the phase diagram of $Ho_2Zr_2O_7$ shown in Fig. 5.10. Upon cooling, $Ho_2Zr_2O_7$ passes by a field-induced spin relaxation region, starting at $T = 18$ K. Interestingly, this the regime where the Curie-Weiss analysis indicate the presence of a weak antiferromagnetic coupling of 20 mK. Further cooling, the system enters a frozen phase below $T_b = 0.6$ T. This phase resembles very much the frozen phase reported in $Ho_2Ti_2O_7$ single crystals [53], which is constructed from magnetization data measured along $B||$ [111] axis and also appears below 0.6 K. Notably, pyrochlore structures with the formula $A_2B_2O_7$ (A = Dy,

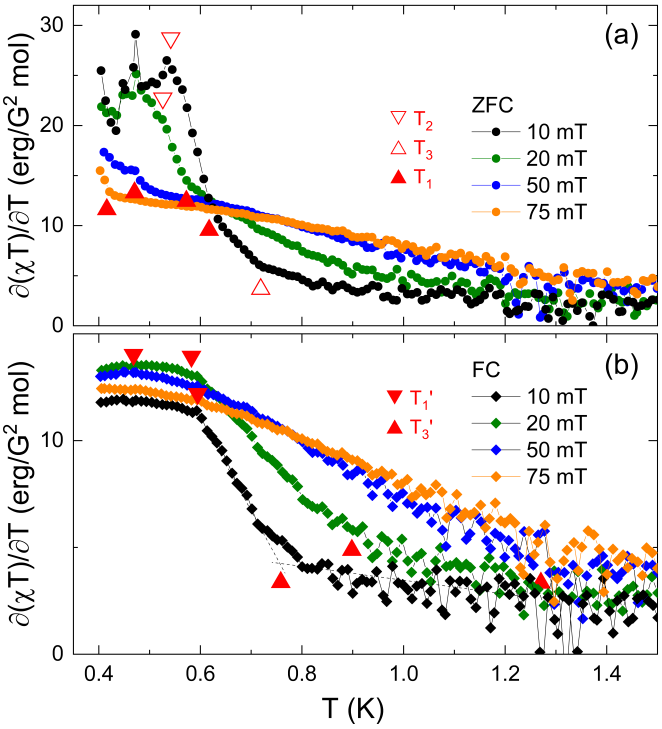

Figure 5.9: Magnetic heat capacity of $Ho_2Zr_2O_7$ derived from the magnetic susceptibility $\chi_{dc}(T)$ measured at $B \leq 0.075$ T: (a) in ZFC mode and (b) FC mode. Triangles mark the features appeared in the data.

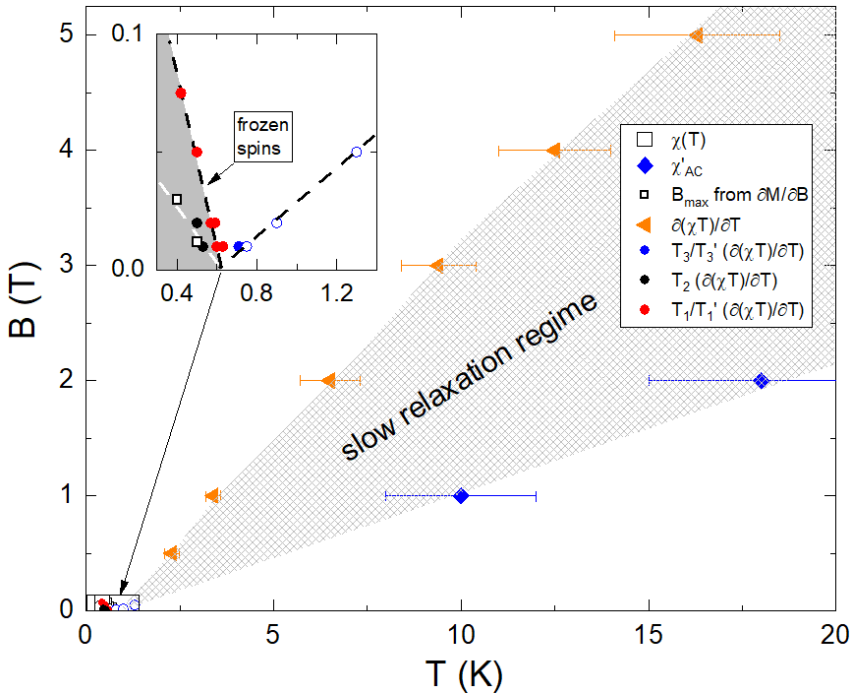

Figure 5.10: How spins freeze in $Ho_2Zr_2O_7$. Below $T = 0.6$ K and in the presence of magnetic fields of $B < 0.1$ T, the system enters a complete frozen state.

Ho and B = Ti, Sn) exhibit $T_{\rm b} \approx 0.60 - 0.75$ K [50–53]i.e., $T_{\rm b}$ is rather independent on $J_{\rm nn}$ [33].

5.5 Summary

In sum, our heat capacity, DC, and AC magnetization studies show that $Ho_2Zr_2O_7$ does not exhibit a long-range magnetic order down to T = 280 mK. Instead, it has a disordered ground state with short-range antiferromagnetic correlations. Further, due to geometrical frustration, the spins tend to go into a frozen state below T = 0.6 K, which is preceded by two spin relaxations processes and $T_{\rm g1} = 7(1)\ K$ and $T_{\rm g2} = 0.9(1)$ K. To conclude, like the spin ice systems $Ho_2Ti_2O_7$, and $Dy_2Ti_2O_7$, the frozen state in $Ho_2Zr_2O_7$ is driven by slow spin relaxation processes at higher temperatures.

Chapter 6

Nd_3BWO_9 and Pr_3BWO_9

6.1 Introduction

Theoretical predictions of a spin-liquid state in S = 1/2 Kagomé antiferromagnet [13, 63, 64] remained untested for a long time until the synthesis of Herbertsmithite ($ZnCu_3(OH)_6Cl_2$), a structurally perfect Kagomé system of quantum spin $S = \frac{1}{2}$; Cu^{2+} [65]. $ZnCu_3(OH)_6Cl_2$ exhibits the fingerprints of fractionalized excitations and continuous spin excitations [66, 67]. Nevertheless, deep understanding of the spin-liquid state through investigations of $ZnCu_3(OH)_6Cl_2$ is hindered by two natural obstacles in the chemistry of the compound. First, the antisite defect, resulting from the mixing of Cu^{2+} and Zn^{2+} due to their similar ion radii. Second, the difficulty in chemical substitution or doping at the magnetic sites of Cu^{2+} [68]. The same problems hold for other kagome systems based on $3d$ metals such as $SrCr_{8-x}Ga_{4+x}O_{19}$ (Cr^{3+}; $S = \frac{3}{2}$), and $D_3OFe_3(SO_4)_2OD_6$ (Fe^{3+}; $S = \frac{5}{2}$) [69, 70]. Additionally, Dzyaloshinskii-Moriya interactions, and single-ion anisotropies, in the $3d$-based systems, act as perturbations and complicate the investigation of the spin-liquid state.

Kagomé systems based on rare-earth magnetic ions [71–74] are studied to realize new spin-liquid state, avoiding the perturbations found in $3d$-transition metal-based ones. Rare-earth systems, with their distinct single-ion anisotropies, spin-orbit coupling, and dipolar interaction, would lead to diverse magnetic ground state. Further, in the rare-earth systems, the induced spin dynamics due to geometrical frustration is expected to emerge at low temperatures far below the first excited crystal-field level.

This chapter is devoted to investigate the magnetic ground state of two distorted Kagomé systems, namely Nd_3BWO_9 and Pr_3BWO_9. The two systems belong to the newly synthesized family rare-earth boratotungstates with the formula RE_3BWO_9; RE= Nd, Pr, Sm, Gd, Tb, or La [75–78]. In Sm_3BWO_9, antiferromagnetic long-range order at $T_N = 0.75$ K

is revealed by heat capacity, and an incommensurate magnetic order of spin density wave (SDW) type is suggested by nuclear magnetic resonance (NMR) studies [78]. Gd_3BWO_9 has antiferromagnetic ground state with $T_N = 1\ K$ and it exhibits substantial magnetocaloric effect [76]. Nd_3BWO_9 and Pr_3BWO_9 crystallize in a hexagonal coordinated structure with space group $P6_3$ (no. 173), where the Nd^{3+}, and Pr^{3+} magnetic ions lay on a distorted Kagomé lattice connections within the ab-plane and stacked in an AB-type fashion along the c axis [75, 77, 79]. Recent calorimetric and neutron scattering studies [79] on Nd_3BWO_9 single crystals reveal that it behaves as a strongly interacting effective spin-1/2 moment below 100 K and there is static magnetic order evolves at $T_N =$ 300 mK. Below T_N and at low temperatures as 120 mK, there are magnetization plateaus for all field orientations each of which has a different magnetic structure. In Pr_3BWO_9, NMR studies [77] show a persistent cooperative paramagnetic state down to $T = 0.09$ K. Further, the NMR data suggest a spin gap opened at the antiferromagnetic wave vector whose size further shows a linear field dependence.

This chapter presents heat capacity, and magnetization (DC, AC, and pulse-field) studies on polycrystalline samples of Nd_3BWO_9 and Pr_3BWO_9. DC magnetization data, in the range $0.4 \geq T \leq 350$ K, indicate significant differences in the magnetic ground states of these two materials. Nd_3BWO_9 exhibits a static long-range magnetic order, whereas Pr_3BWO_9 does not. Additionally, Nd_3BWO_9 shows a washed-out magnetization plateau in low applied fields, which is absent in the case of Pr_3BWO_9. AC magnetization studies rule out the presence of glassy states at least down to 1.8 K in Nd_3BWO_9 and Pr_3BWO_9. However, the cooperative paramagnetic state in Nd_3BWO_9 differs from that of Pr_3BWO_9; the former exhibits field-induced spin freezing at $T^* = 4.3(5)$ K, while the latter is barely affected by the magnetic field. This suggests a distinct slow spin relaxation mechanism in Nd_3BWO_9 compared to Pr_3BWO_9. Furthermore, pulsed field (0–60 T) magnetization measurements were performed at temperatures down to 540 mK, revealing notable distinctions in the dynamic magnetic responses of Nd_3BWO_9 and Pr_3BWO_9. In both systems, the theoretical saturation magnetization is not reached even in high-fields of $B = 58$ T, and there are no magnetization plateaus in the high field regimes.

6.2 Samples and Experimental Details

Nd_3BWO_9 and Pr_3BWO_9 samples have been provided by P. Khuntia, Department of Physics, Indian Institute of Technology Madras, Chennai 600036, India. The samples are polycrystals pressed into pellets with different sizes and weights.

The DC magnetization measurements of Nd_3BWO_9 and Pr_3BWO_9 were performed in

the temperature range from 1.8 to 350 K, using a Magnetic Properties Measurement System (MPMS3, Quantum Design). The samples had masses of 9.1(3) and 6.6(2) mg, respectively.

For measurements down to 400 mK, the MPMS3 was equipped with the iQuantum He3 setup. The DC magnetization were obtained in two ways: (a) after cooling the sample in the external magnetic measurement field (field-cooled; FC), and (b) by applying the magnetic field after cooling the sample to the lowest temperature (zero-field-cooled; ZFC). For the low-temperature regime, the Nd_3BWO_9 and Pr_3BWO_9 samples had masses of 13.2(3) and 6.6(2) mg, respectively.

The AC magnetization measurements of Nd_3BWO_9 were conducted in the temperature range from 1.8 to 60 K, with 5 - 7 Oe AC excitation fields, up to 5 T DC magnetic fields and frequencies ranging from 10 Hz to 0.8 kHz. These measurements were conducted using the AC option of the MPMS3 on samples with masses of 9.1(3) mg and 2.3(1) mg for Nd_3BWO_9, and Pr_3BWO_9, respectively.

To measure the specific heat capacity of the samples, a relaxation method is employed using the heat capacity option of the PPMS. Specifically, for Pr_3BWO_9, the measurements were carried out for temperatures in the range of 1.8 to 200 K on a sample with a mass of 6.6(2) mg under applied magnetic fields $0 \leq B \leq 14$ T. For Nd_3BWO_9, the measurement was carried out in the temperature range from 0.3 to 1 K using PPMS incorporated with a dilution refrigerator (DR) on a sample with a mass of 5.1(2) mg and only at $B = 0$ T.

Pulsed-field magnetization was measured up to 60 T at Helmholtz Zentrum Dresden-Rossendorf by an induction method using a coaxial pick-up coil system [25]. The pulse raising time was 7 ms. The pulsed-field magnetization data were calibrated using static magnetic field magnetization data obtained by means of MPMS.

6.3 Experimental Results

6.4 Nd_3BWO_9

6.4.1 Static and Dynamic Magnetization Above 1.8 K

Figure 6.1 shows the temperature dependence of the DC magnetic susceptibility, $\chi(T)$, and its inverse χ^{-1} of Nd_3BWO_9. Clearly, there is no evidence of a magnetic transition above 1.8 K, and the susceptibility exhibits a paramagnetic-like behaviour, where it increases monotonically with decreasing the temperature. To clarify the type of magnetic correlations in the system, the Curie–Weiss law is used to fit the data over two different

temperature regimes. These regimes are chosen in the light of the recent inelastic neutron scattering (INS) studies [79] on Nd_3BWO_9, which have revealed the existence of three excited crystal electric field (CEF) levels at 180 K, 380 K and 507 K. Consequently, the χ^{-1} data, at low temperatures between 7 and 40 K far below the first excited CEF level, and at high temperatures between 200 and 310 K far below the second excited CEF level, are fitted. Note, the data used for fits were corrected by subtracting a temperature-independent term $\chi_0 = 1.812 \times 10^{-4}$ emu mol^{-1} Oe^{-1}. The fits yield a Curie constant $C_1 = 1.1(1)$ erg K mol^{-1} G^2, a Weiss-temperature Θ_{W1} = -2.8(2) K, and $C_2 = 1.7(1)$ erg K mol^{-1} G^2, Θ_{W2} = -47(2) K, for the low and high temperature regimes, respectively. The negative value of the Weiss-temperatures obtained from the low as well as the high temperature fits indicates a dominating antiferromagnetic (AFM) exchange interactions between Nd^{3+} moments and its reduced value at low temperature fit reflects the significant effect of the crystal field on the exchange interactions. As listed in Table 6.1, μ_{eff} obtained from the high temperature fit is slightly higher than the theoretical value $\mu_{eff} = g_J\sqrt{J(J+1}} = 3.62$ μ_B; $g_J = 0.72$ and $J = 9/2$, expected for a Nd^{3+} free ion. upon cooling, μ_{eff} is reduced to 82% of the theoretical value. Overall, our results agree well with literature on single crystals [79] as well as polycrystals [75].

Table 6.1: Comparison of the Weiss-temperature (Θ_W) and the effective magnetic moment (μ_{eff}) obtained from the Curie–Weiss law fits shown in Fig. 6.1 with those found in the literature of Nd_3BWO_9 poly and single crystalline samples.

Field-direction	Θ_{W1} (K)	μ_{eff} (μ_B)	Θ_{W2} (K)	μ_{eff} (μ_B)	Ref.
$B\|\|a^*$	-3.78	2.94	-54.3	3.76	[79]
$B\|\|b$	-3.82	2.90	-54.7	3.79	[79]
$B\|\|c$	-3.68	2.91	-59.2	3.77	[79]
Polycrystal	-2.20(5)	2.85(6)	-49.2(1)	3.7(1)	[75]
Polycrystal	-2.80(2)	2.96(2)	-46(2)	3.70(3)	[This work]

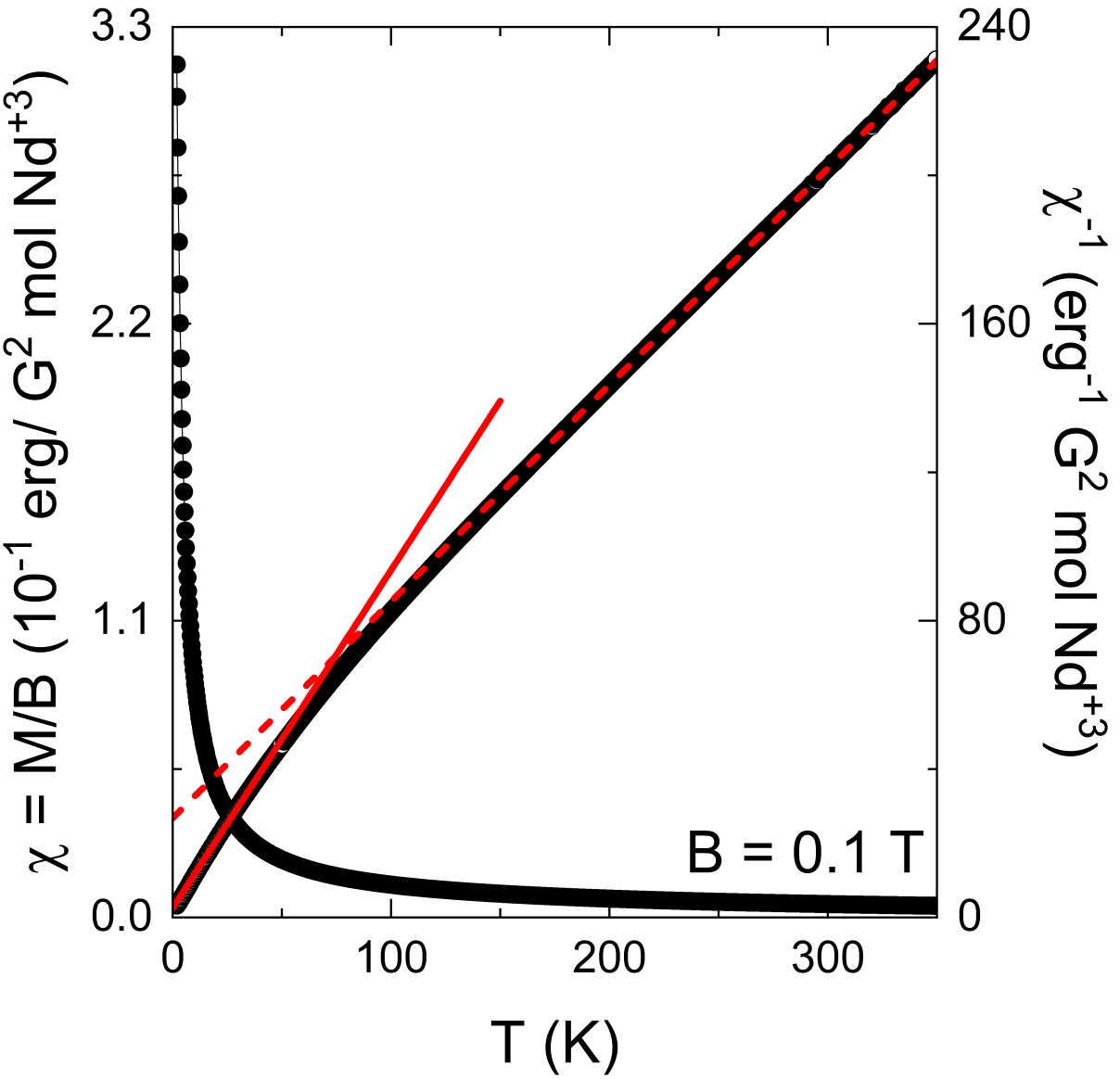

Figure 6.1: Temperature dependence of the DC magnetic susceptibility, $\chi = M/B$, and its inverse χ^{-1} of Nd_3BWO_9 measured at an applied magnetic field of 0.1 T, after being cooled from room temperature in zero magnetic field (ZFC). The dashed (solid) red line represents the high (low) temperature Curie–Weiss law fit to the data.

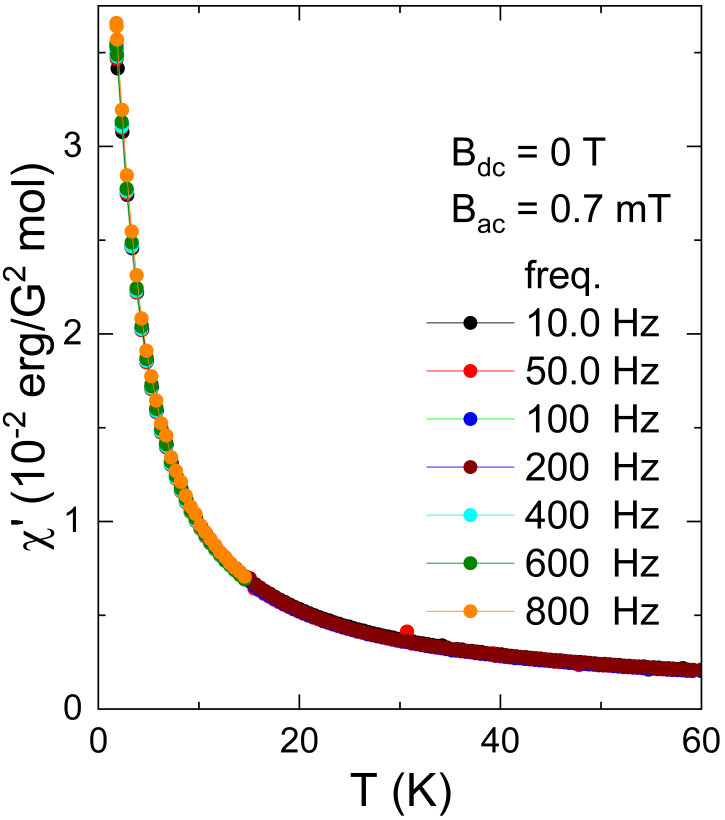

Figure 6.2: Temperature dependence of the real part $\chi'_{\rm ac}$ of the AC magnetic susceptibility for Nd_3BWO_9 polycrystal sample. The susceptibility is measured at $B_{dc} = 0$ T, excitation filed $B_{ac} = 0.7$ mT, and under different frequencies in the range of $10 \leq f \leq 800$ Hz.

To obtain information on the spin dynamics of Nd_3BWO_9, AC magnetic susceptibility measurements were performed with and without applied DC magnetic field. At $B_{dc} = 0$ T and $10 \leq f \leq 800$ Hz, the real part $\chi'_{\rm ac}$, displayed in Fig. 6.2, increases monotonically with decreasing the temperature in a paramagnetic-like behaviour consistent with the DC susceptibility. Even at temperatures far below the estimated Weiss-temperatures, the data show no anomaly, nor any frequency dependence. Noticeably, this paramagnetic-like behaviour and the frequency independence of the $\chi'_{\rm ac}$ data exclude the possibility that Nd_3BWO_9 exhibits a glassy-state in the studied temperature regime and might imply that the characteristic spin-fluctuation rate in Nd_3BWO_9 is beyond the kilohertz region.

Switching on the DC magnetic field results in a more complex behavior for both $\chi'_{\rm ac}$ and the imaginary part $\chi''_{\rm ac}$ as shown in Fig. 6.3. At $B = 0.5$ T, $\chi'_{\rm ac}$ in Fig. 6.3 (b) shows a field dependent behaviour, at roughly $T = 7(1)$ K, with respect to the zero field data. Further, there is a slight change in the slope of the data below this temperature. With increasing the DC magnetic field, the field dependence of $\chi'_{\rm ac}$ appears at higher temperatures and a broad hump emerges at lower temperatures. In case of $\chi''_{\rm ac}$ [see Fig. 6.3(a)], the anomaly

observed in χ'_{ac} is translated into a peak centered at $T^* = 4.4(3)$ K, which agrees with the Kramer-Kronig relations. The peak shifts to higher temperatures with increasing the applied magnetic field, and its amplitude increases at B $\leq$ 2 T but it fades out again at higher fields.

6.4.2 DC Magnetization Below 1.8 K

Figure 6.4 (b) shows the temperature dependence of the specific heat capacity of Nd_3BWO_9 poly (open black circles) and single crystal samples measured at $B = 0$ T, the latter is taken from [79]. The data exhibit a broad hump centered at $T = 0.80(2)$ K, as marked by black solid triangles. The magnetic nature of this hump is confirmed when Fisher's magnetic specific heat $\partial(\chi T)/\partial T$, depicted in Fig. 6.4 (a), is considered [80]. On further cooling, c_p^{tot} signals a magnetic phase transition at $T_N = 0.3$ K, which is not visible in our DC magnetization data, because it is below the base temperature of our He-3 option. Further cooling below T_N the c_p^{tot} decreases gradually as expected for a ground state with a long-range magnetic order. At $B \geq 0.9$ T, the broad hump in $\partial(\chi T)/\partial T$ and c_p^{tot} completely vanishes as marked by dashed circles and solid triangles in Fig. 6.4. Further, the magnetic phase transition at $T_N = 0.3$ K is developed into abroad peak and shifted to a higher temperature $T = 0.43(2)$ K. Simultaneously, our magnetic heat capacity $\partial(\chi T)/\partial T$ shows an anomaly $T = 0.44(1)$ K. Despite similarities between these two anomalies, its hard to conclude if they share the same origin or not.

The broadness of the hump seen in $\partial(\chi T)/\partial T$, c_p^{tot}, and its evolution in the applied magnetic field excludes the probability of a proper thermodynamic phase transition at $T = 0.80(2)$ K, instead it is suggested to be the onset of short-range magnetic correlations [79, 81]. Similar behaviours have been observed in frustrated antiferromagnets [82], distorted Kagomé system $SrCr_8Ga_4O_{19}$ [70], and in quasi-1D antiferromagnets [83, 84]. The evolution of this hump in the applied magnetic fields of 0.005 T $\leq B \leq$ 1.2 T is shown in Fig. 6.5 and the general remarks reads as follows:

- The hump is independent of the measurement protocol, i.e. it does exist in zero field cooling as well as field cooling measurement.
- At 0.005 T $\leq B \leq$ 0.1 T [see Fig. 6.5 (a)], the hump more or less is field independent.
- At 0.4 T $\leq B \leq$ 1.2 T [see Fig. 6.5 (b)], the hump gradually flattens with increasing the applied field and its center shifts to lower temperatures until it completely vanishes at $B \geq 0.9$ T (as marked by the open circle).

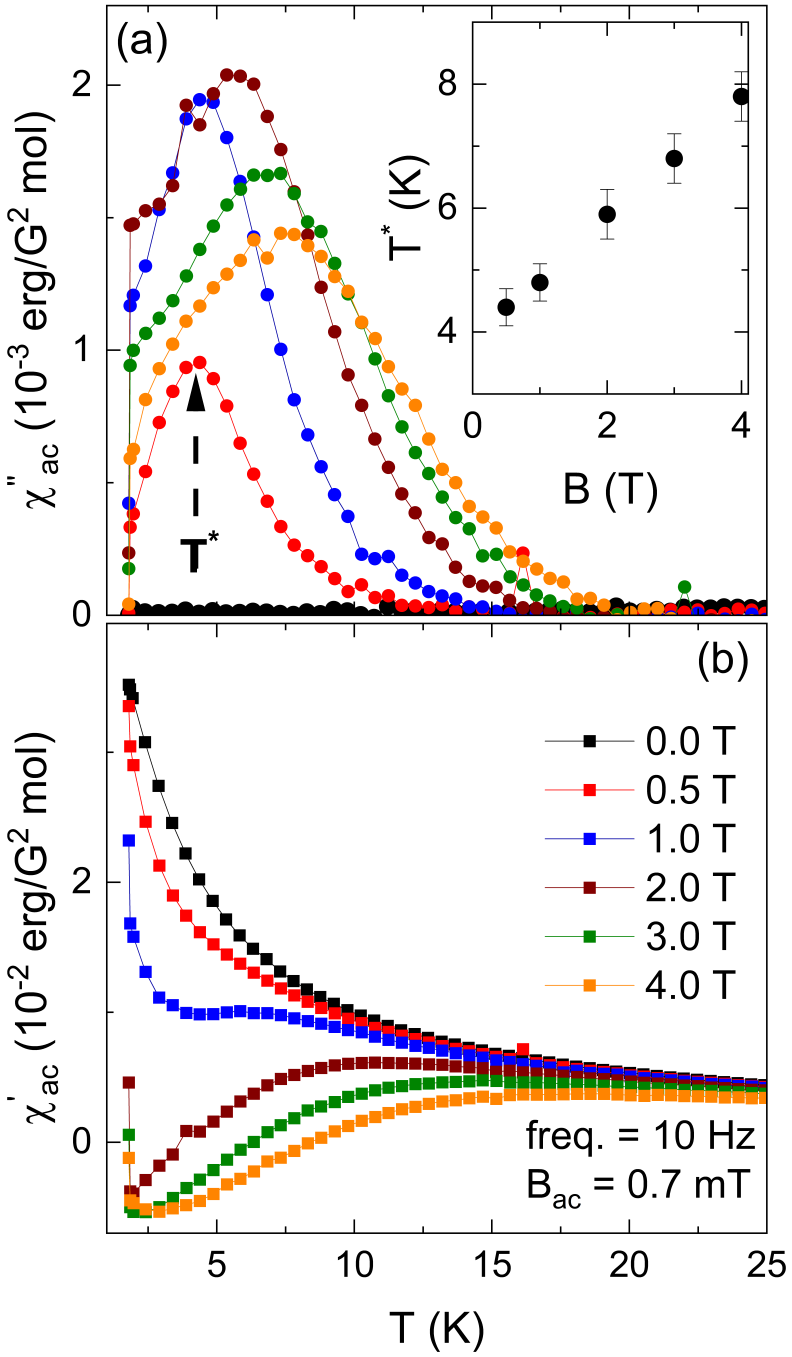

Figure 6.3: Temperature dependence of the AC magnetic susceptibility of Nd_3BWO_9 polycrystal sample. The susceptibility is measured at $f = 10$ Hz, excitation field $B_{ac} = 0.7$ mT, and under different DC magnetic fields in the range of $0 \leq B \leq 4$ T. (a) and (b) are the imaginary and the real parts of the AC susceptibility, respectively. The dashed black arrow marks the field induced peak at T^* in the imaginary part χ''_{ac} at $B = 0.5$ T . Inset: The magnetic field dependence of T^*, which increases linearly in the field.

- At 0.6 T $\leq B \leq$ 0.9 T, there is an emergent upturn at $T = 0.44(2)$ K as marked by empty triangles. The restricted field dependence of this anomaly agrees well the low field anomaly (B_{c1}) visible in the isothermal magnetization as will be shown below.

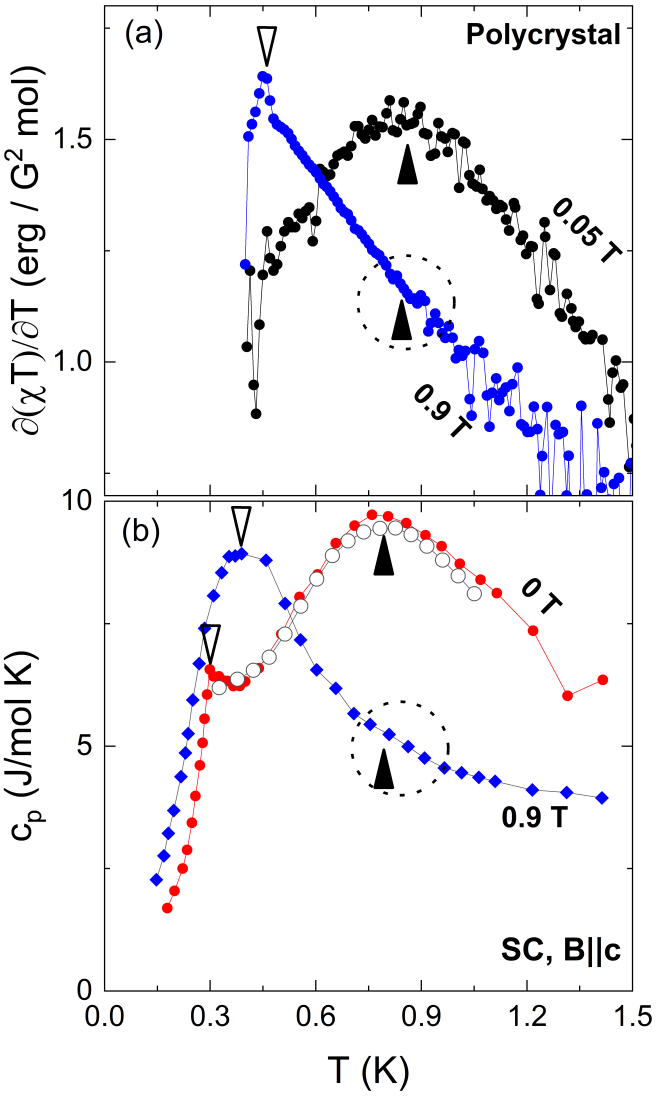

Figure 6.4: Temperature dependence of (a) Fisher's magnetic specific heat, $\partial(\chi T)/\partial T$ of Nd_3BWO_9 polycrystalline sample, and (b) the specific heat capacity of Nd_3BWO_9 polycrystalline (open circles) and single crystal (solid circles) measured at $B||c$ axis. The latter is adopted from [79]. The c_p^{tot} measured at $B = 0$ T, and at $B = 0.9$ T, while $\partial(\chi T)/\partial T$ measured at $B = 0.05$ T, and at $B = 0.9$ T. Solid triangles mark the presence of a hump at $B \simeq 0$ T, and the solid triangles plus dashed circles mark its disappearance at $B = 0.9$ T. Empty triangles mark the evolution of anomalies in finite external field.

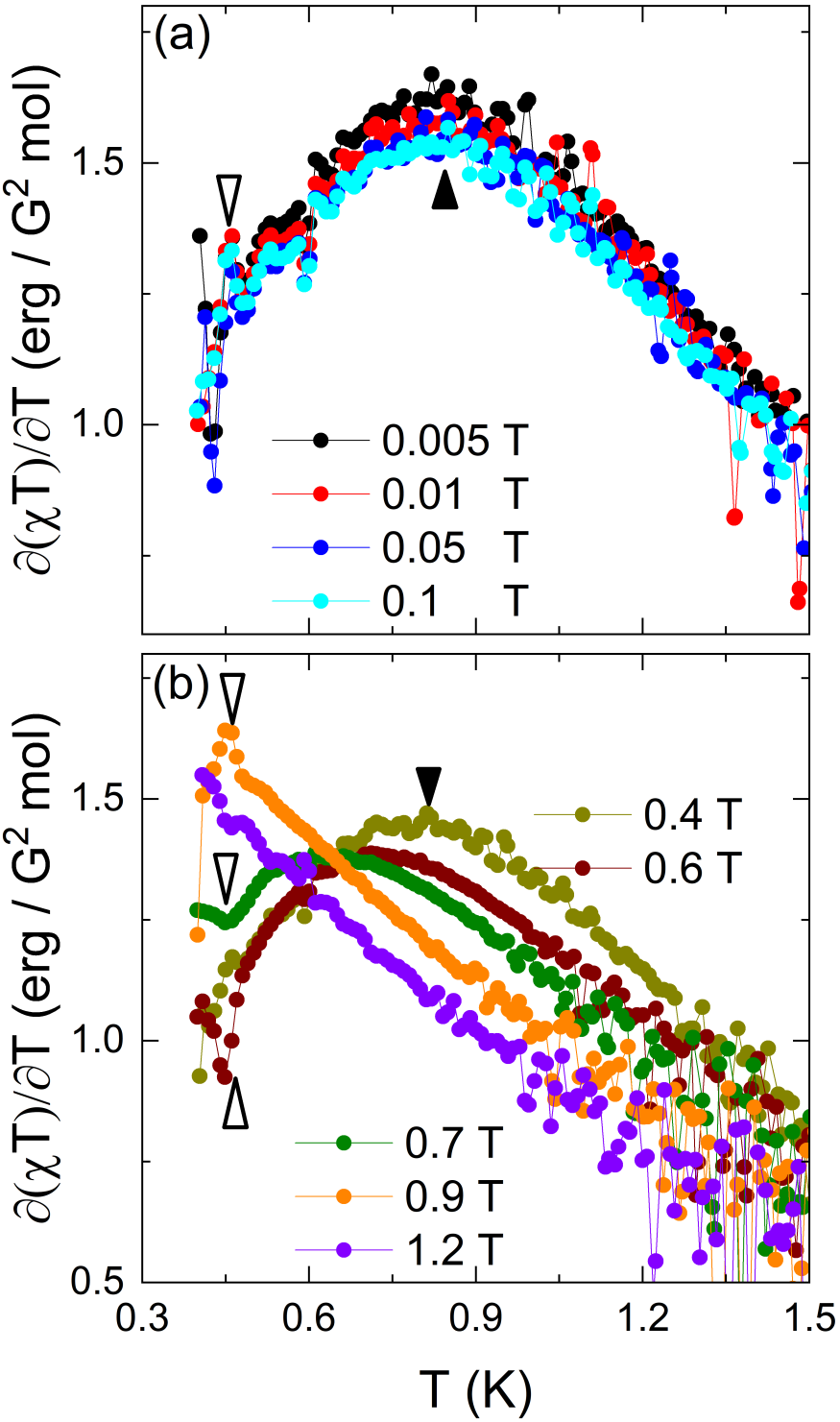

Figure 6.5: Temperature dependence of Fisher's magnetic specific heat $\partial(\chi T)/\partial T$ as derived from the DC magnetic susceptibility of Nd_3BWO_9 at different magnetic fields 0.05 T $\leq B \leq$ 1.2 T. The black solid, and open triangles mark the evolution of the anomalies observed at high and low temperatures, respectively.

The isothermal magnetization data of Nd_3BWO_9 measured at $T = 400$ mK are shown in Fig. 6.6. The magnetization per Nd^{3+} ion increases in quadratic-like manner below 0.4(1) T. This behaviour differs from the magnetization reported in Nd_3BWO_9 single crystals (see Fig. 6.11c) at $T = 120$ mK, where all crystallographic directions exhibit a zero magnetization phase extends up to 0.5 T. Further, Nd_3BWO_9's magnetization demonstrates a narrow washed-out plateau, spans fields of 0.67 - 0.86 T, with a value consistent with a fractional $M = 1/3M_{\mathrm{sat}}$ as displayed in the inset in Fig. 6.6. After the plateau-like feature, the magnetization increases monotonically, and finally the saturation sets in at $B_{\mathrm{sat}} = 1.85(2)$ T.

Magnetization derivative $\partial M/\partial B$ (right axis in Fig. 6.6) shows couple of features, namely shoulder-like anomaly ($\uparrow$), and two peaks at critical fields B_{C1} ($\downarrow$), B_{C2} ($\downarrow$), and minima at B_{min} correspond to the beginning, end, and center of the plateau-like feature, respectively. With the rise of temperature, as shown in Fig. 6.7, the shoulder-like anomaly ($\uparrow$) shifts to lower fields and disappear at $T > 0.5$ K. The anomaly at B_{min} slightly shifts to higher fields and also disappears at $T > 0.5$ K. Likewise, the peak at B_{C1} is shifted to higher magnetic fields, and it is gradually smeared out until it is not detectable anymore at $T > 0.5$ K. The peak at B_{C2} is shifted to lower magnetic fields with increasing the temperature, and it swallows the anomaly at B_{C1}, whereas the two anomalies merge into one to form a broad hump at $T \geq 0.6$ K.

At $B = 7$ T, the highest applied field in the quasi-static measurement, the magnetization exhibits saturation value $M_{\mathrm{sat}} \simeq 1.56\ \mu_{\mathrm{B}}/\mathrm{Nd}^{3+}$ independent of the temperature of the measurement as depicted in Fig. 6.7. Such reduced values agree well with the data in [79] (see Fig. 6.11c) and with other magnetization data of Nd-based frustrated magnets [85]. Simultaneously, the data show temperature dependent saturation field B_{sat}, where B_{sat} amounts to 1.85 T at 400 mK and increases to 2.6 T at 1.5 K. Finally, there is no hysteresis between up and downsweeps over the whole applied field regime.

6.4.3 Pulsed-Field Magnetization

The pulsed-field magnetization data of Nd_3BWO_9 measured at 540 mK and 11.5 K are shown in Fig. 6.9. The magnetization per Nd^{3+} does not reach the expected theoretical value of 3.24 μ_{B} even at the highest applied magnetic field of 60 T for the measurement at 11.5 K. No magnetization plateaus are observable either at low or high fields in measurements at 540 mK and 11.5 K. Note, the 540 mK pulsed field data are measured using a He-3 cryostat, while the 11.5 K pulsed field data are measured using a He-4 cryostat, and the pulsed-field rates are different. The pulsed-field data are scaled to the quasi-static

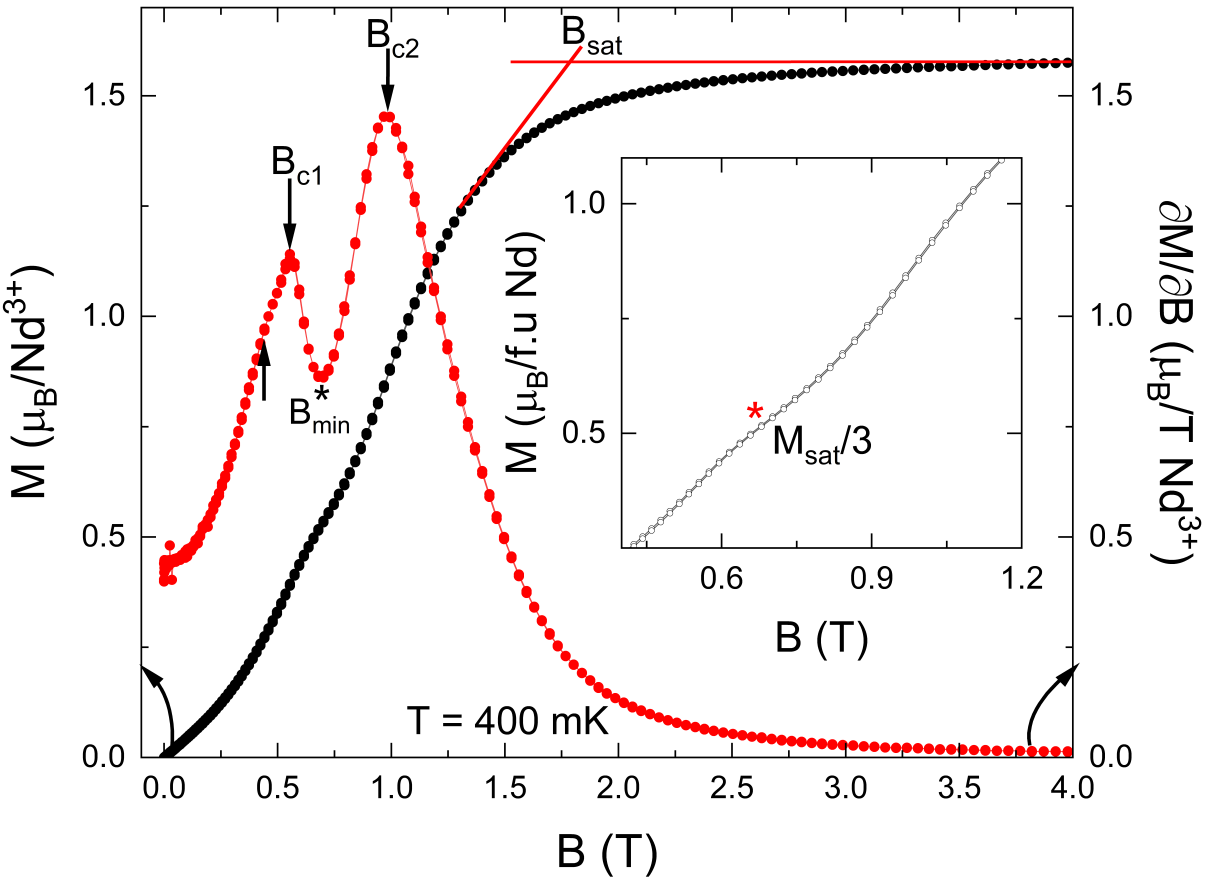

Figure 6.6: Magnetic field dependence of the isothermal magnetization, M, of Nd_3BWO_9, and its corresponding derivative $\partial M/\partial B$ on the right-axis. The data are obtained form up and down field sweeps at $T = 400$ mK. Black up arrow marks the shoulder-like anomaly in $\partial M/\partial B$, and down arrows mark the critical fields at B_{C1} and B_{C2}. The black asterisk marks B_{min}, and the intersection of red solid lines marks the saturation field B_{sat}. Inset: Magnetic field dependence of M, which highlights the narrow $\frac{1}{3}$-magnetization plateau visible in the data. The red asterisk refers to the center of the plateau. Note, M_{sat} is determined from pulsed-field magnetization measured at 540 mK and up to 33 T.

data measured up to 7 T using SQUID MPMS-3, we observe a clear difference between the pulsed-field and the static data in the range 1 T $< B <$ 5.80 T. In case of 11.5 K data, the pulsed field data are higher than the static one in the range 1 T $< B <$ 5.80 T. Below 1 T and above 6 T, the pulsed-field data show good agreement with the static one. This behaviour might be an artefact from the pulsed-field measurement or due to differences in the field sweep rates between the pulsed and the static measurements. In case of the 540 mK data, the pulsed field magnetization data are lower than the static one in the range 1 T $< B <$ 5.80 T.

The pulsed-field data at 11.5 K exhibits a smooth right bending over a wide range of

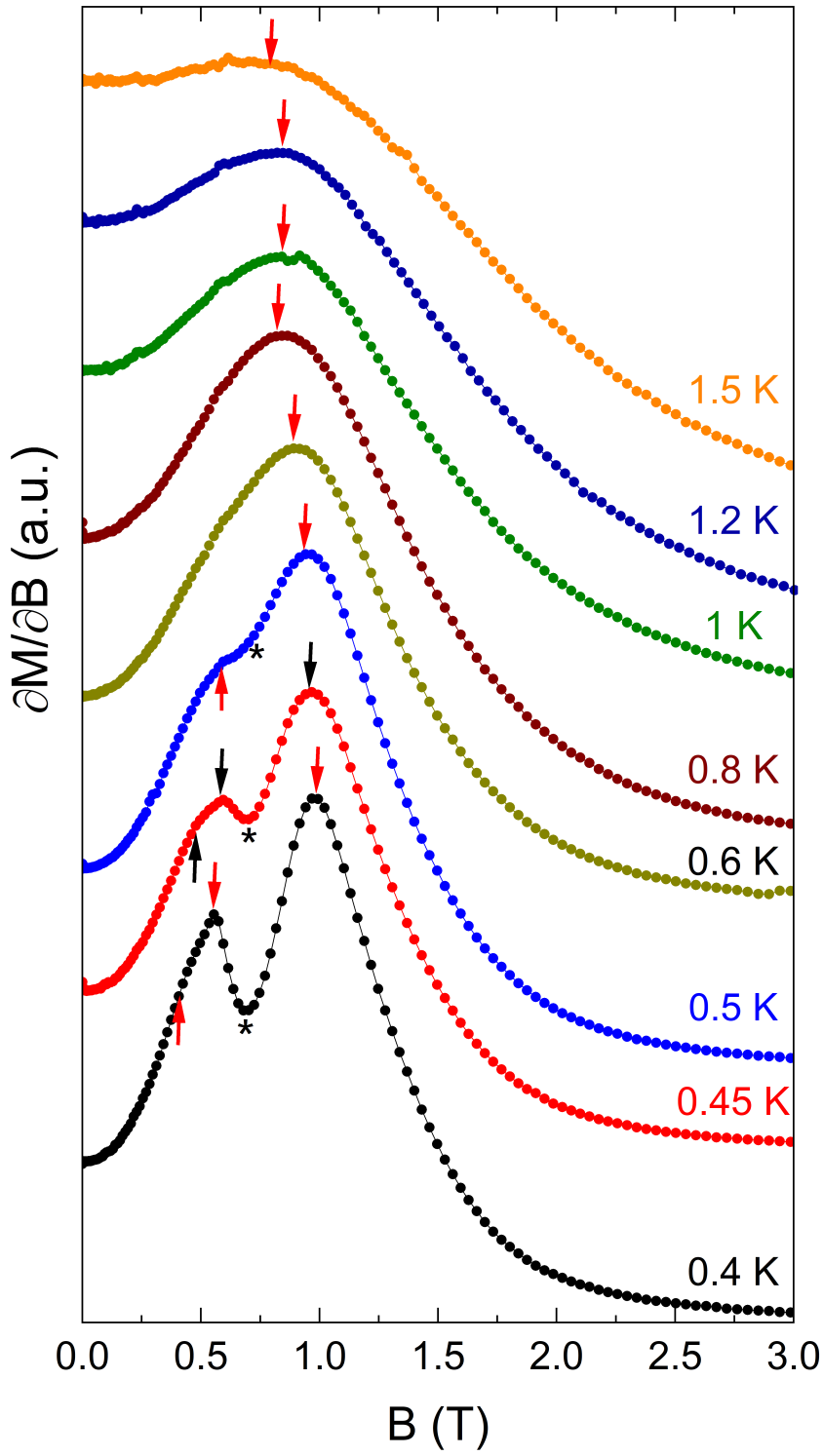

Figure 6.7: Magnetic field dependence of the magnetic susceptibility $\partial M/\partial B$ of Nd_3BWO_9. The data are obtained form up field sweep measurements at $0.4 \leq T \leq 1.5$ K. Up arrows mark the evolution of shoulder-like anomaly with increasing the temperature, and down arrows mark the evolution of critical fields at B_{C1} and B_{C2}.

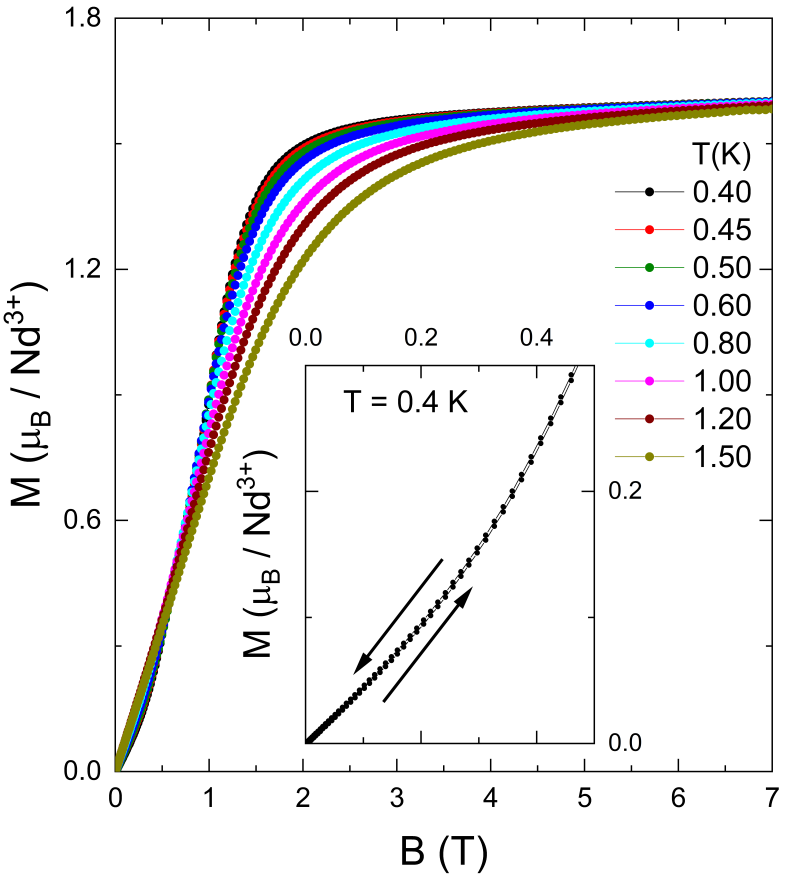

Figure 6.8: Magnetic field dependence of the isothermal magnetization, M, of Nd_3BWO_9 measured at different constant temperatures in the range $0.4 \leq T \leq 1.5$ K. Inset: a closer look on the low field dependence of M measured at $T = 400$ mK; up and down black arrows refer to the upsweep and downsweep, respectively.

magnetic fields. Fitting the data using a Brillouin function, which corresponds to the non-interacting paramagnetic Nd^{3+} ions with $J = 9/2$, the fit diverges (see light gray line in Fig. 6.10), indicating the absence of a pure paramagnetic state in the system even at 11.5 K. Instead, fitting the data by the sum of a Brillouin function B_J and a linear term, denoted as $M_{sat}B_J(x)+\chi_0\times B$; $x = g\mu_B JB/[k_B(T)]$ with M_{sat} the saturation magnetization of the right-bending term, total angular momentum J, field-independent susceptibility χ_0, Boltzmann constant k_B, Bohr magneton μ_B, and the g-factor. The linear term mainly reflects the response of the short-ranged AFM correlations. The fit reasonably represent the data and yields $\chi_0 = 0.01278$ μ_B/T Nd^{3+}, $M_{sat} = 1.23$ μ_B/Nd^{3+}.

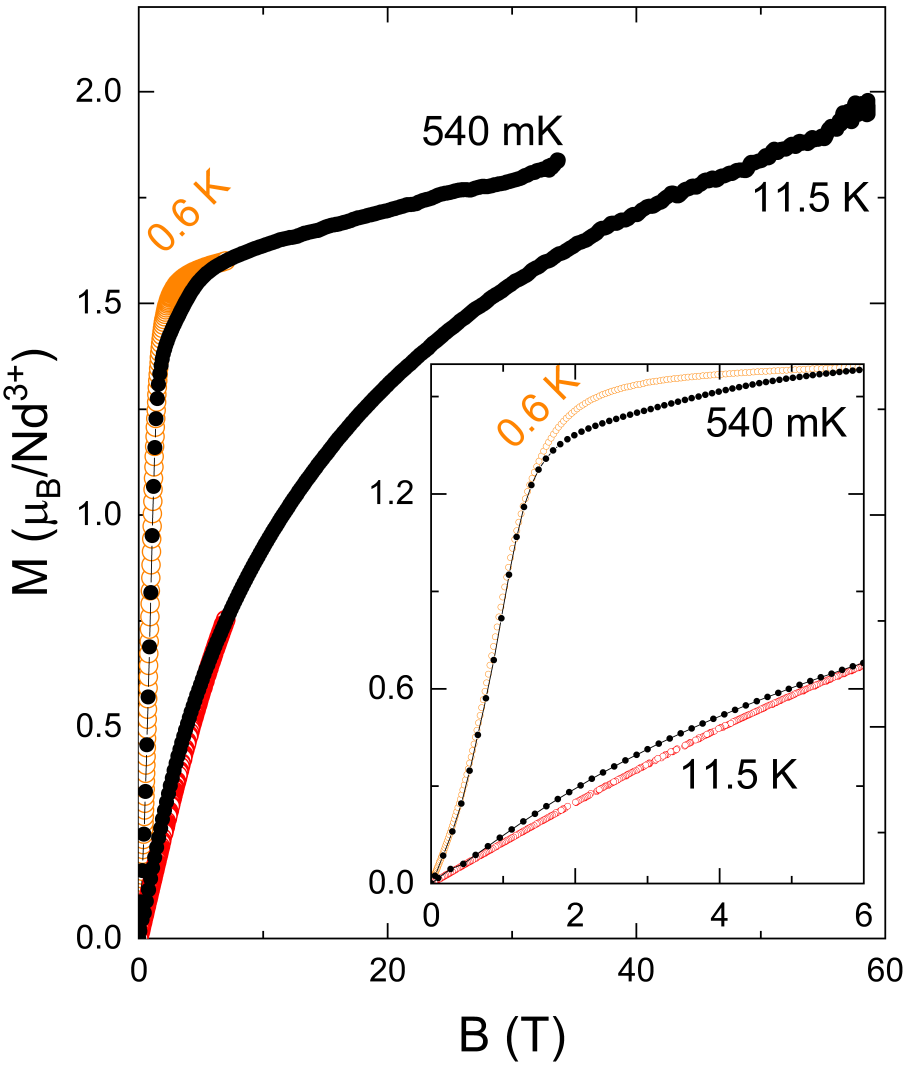

Figure 6.9: Magnetic field dependence of the upsweep magnetization of Nd_3BWO_9 polycrystals obtained in quasi-static (open circles) and pulsed (solid circles) magnetic field. Inset: the magnetization low field dependence, which highlights the differences between the static and pulsed-field data at 1 T $< B <$ 5.80 T.

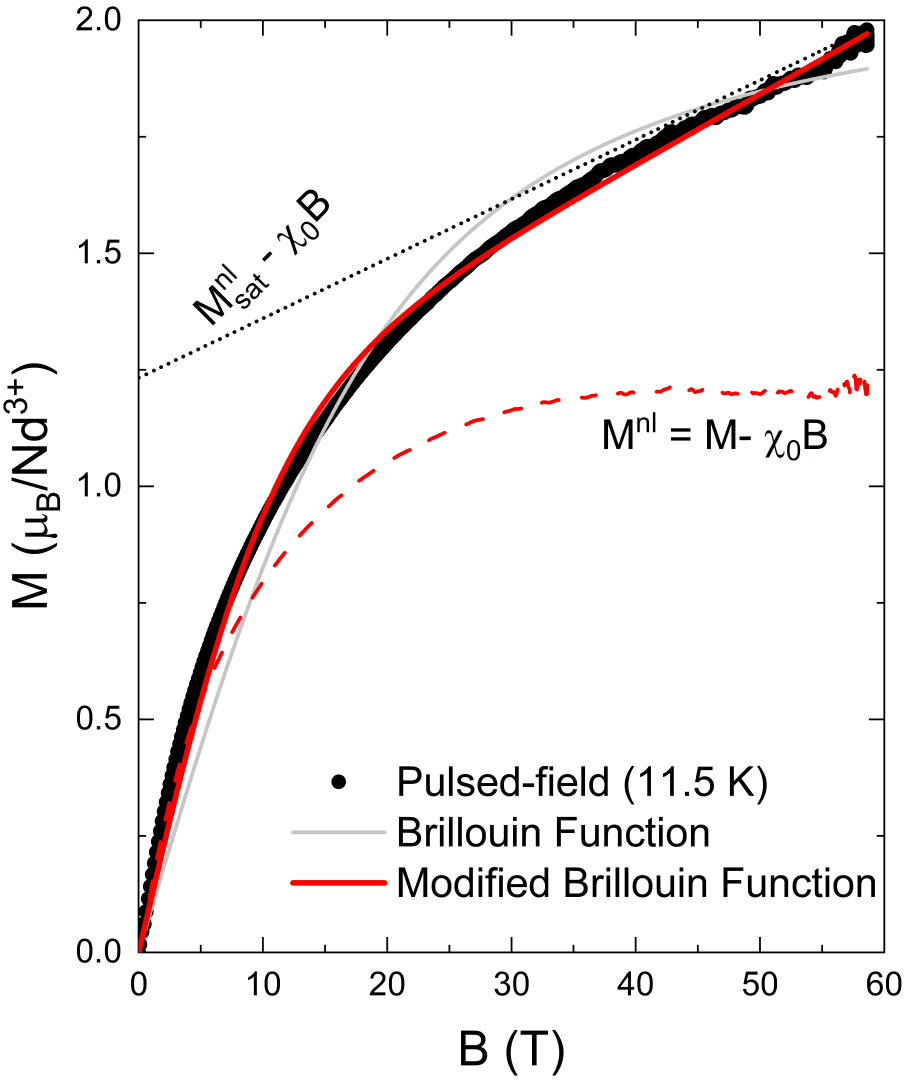

Figure 6.10: Magnetic field dependence of the upsweep pulsed-field magnetization of Nd_3BWO_9 measured at 11.5 K. The data of Nd_3BWO_9 are reasonably described by the sum of Brillouin function and a linear term $\chi_0 \times B$ (solid red line). The red dashed line shows the nonlinear magnetisation $M_{\rm nl} = M - \chi_0 \times B$

6.4.4 Magnetic Phase Diagram

Distinct anomalies visible in temperature dependence of c_{p} and $\partial(\chi T)/\partial T$ (see Figs. 6.4 and 6.5) and field dependence of magnetization (see Figs. 6.6, 6.7, and 6.8) of Nd_3BWO_9 polycrystal are combined with the features reported in magnetic field dependence of c_{p}, and M (see Fig. 6.11 of Nd_3BWO_9 single crystal to extend and complete the magnetic phase diagram of Nd_3BWO_9 reported in [79]. The extended version of the magnetic phase diagram is shown in Fig. 6.12. The following remarks can be drawn from the combined phase diagram:

- The phase labeled (A) forms a confined dome, which spans a restricted field range from 0 to $\sim$ 0.6 T. This phase does exist for magnetic fields applied along c and a^* crystallographic directions. This phase is hardly magnetizable up to $B \sim 0.5$ T, as evident from the magnetization at 120 mK (see Fig. 6.11c) suggesting a gapped state in this field range [79]. Notably, the magnetization data in the polycrystalline sample, which is measured at 400 mK, shows a different behaviour and increases with field in a quadratic-like manner.

- At $B > 0.6$ T and T = 120 mK, Nd_3BWO_9 exhibits field-induced ordered phase, namely B and C phases for the fields applied along a^* and c axes, respectively.

- While both B and C phases show similar 1/3 magnetization plateaus, the magnetic order within the phases is different where the former characterized by propagation vector $Q = (0, 1/2, 1/2)$, the latter has $Q = (1/3, 1/3, 1/3)$ [79]. The phases B and C phases form confined domes, which spans a restricted field range from 0.55 to $\sim$ 1.2 T, from 0.55 to $\sim$ 1 T, respectively.

- Similar to B and C phases in the single crystal data, the polycrystalline data show a reminiscent phase labeled D in Fig. 6.12. The phase D forms a confined dome, which spans a restricted field range from 0.55 to $\sim$ 1 T. Specifically, at $B > 0.5$ T and $T = 400$ mK, Nd_3BWO_9's magnetization shows a narrow washed-out plateau, spans 0.67 - 0.86 T, with a magnetization value also consistent with a fractional $M = 1/3M_{\mathrm{sat}}$. The presence of 1/3 plateau feature and the similarity in the form of D-phase with respect to B and C phases, suggest the phase D as a new ordered phase in Nd_3BWO_9.

- On cooling, the broad hump features in $\partial(\chi T)/\partial T$ and c_{p} represent a crossover from a paramagnetic-like phase phase to the pseudospin polarized phase (FPP).

The latter is confined between $B > 1$ T and the saturation magnetic fields obtained from magnetization.

- At $T > 0.80$ K, Nd_3BWO_9 behaves like an unconventional paramagnet.

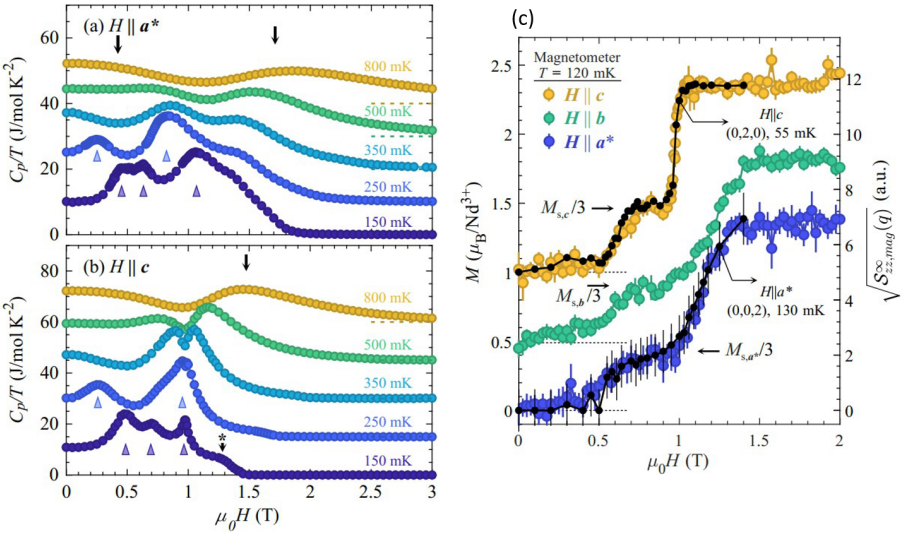

Figure 6.11: Magnetic field dependence of Nd_3BWO_9 Specific heat measured at constant temperature with fields applied along (a) $B||c$ and (b) $B||a^*$. Solid filled triangles show features associated with the phase transitions. Black arrows signal the existence of broad double-hump features. (c) Magnetization (left axis) per Nd^{3+} measured at 120 mK in Nd_3BWO_9 for magnetic fields applied along the crystallographic directions a^*, b, and c. Magnetization extracted from neutron diffraction (right axis) intensity of nuclear reflections is superimposed to the corresponding bulk data. The figures are taken from [79]

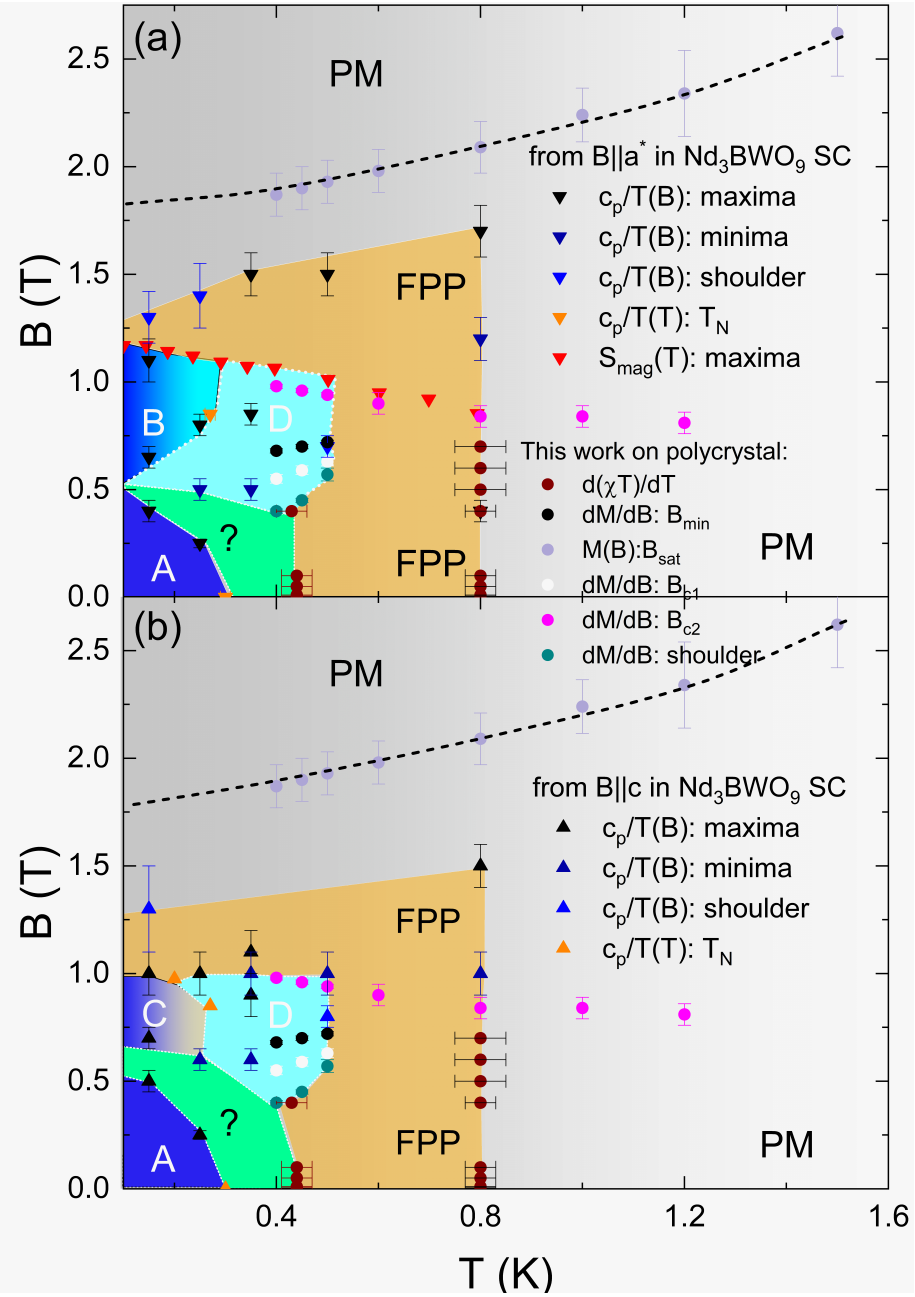

Figure 6.12: Magnetic phase diagram of Nd_3BWO_9 in a magnetic field applied along the principal directions: (a) a^*, (b) c, the data are taken from [79]. The features observed in the magnetization studies from this work for Nd_3BWO_9's polycrystalline sample are combined with the single crystal's features to complete the magnetic phase diagram. The different phases are labeled as: A, B, C, D, Fully Polarized Pseudospin (FPP), and paramagnet (PM).

6.5 Pr_3BWO_9

6.5.1 Static and Dynamic Magnetization Above 1.8 K

Similar to Nd_3BWO_9, the magnetic susceptibility of Pr_3BWO_9 does not indicate long-range magnetic order above 1.8 K, and it also increases on cooling. Again, the susceptibility is analyzed by performing Curie–Weiss law fits at low temperatures (10-25 K) and high temperatures (150-350 K) as shown in Fig. 6.13. The fit results show that at low temperatures, $C_1 = 1.09(1)$ erg K mol^{-1} G^2, $\Theta_{W1} = -6.5(4)$ K, while at high temperatures, $C_2 = 1.4(1)$ erg K mol^{-1} G^2, $\Theta_{W2} = -31(2)$ K. Similar to Nd_3BWO_9, AFM interactions dominate the low and high fit regimes. Interestingly, the Weiss-temperature from the high temperature fit is lower than that of Nd_3BWO_9, but the one from the low-temperature fit is approximately three times higher. Finally, comparing the fit results with those in the literature, as listed in Table 6.2, μ_{eff} obtained from the high temperature fit is roughly 92% of the theoretical value $\mu_{\text{eff}} = g_J\sqrt{J(J+1}} = 3.58\ \mu_{\text{B}}$; $g_J = 0.8$ and $J = 4$, expected for a Pr^{3+} free ion. On cooling, μ_{eff} as well as the Weiss-temperature are significantly reduced. Overall, our results agree well with literature on polycrystals [75] and with μ_{eff} reported for $B \perp c$ axis in Pr_3BWO_9 single crystal [77]. Surprisingly, Ref. [77] reports $\Theta_W > 0$ for $B||c$ axis, while $\Theta_W < 0$ for $B \perp c$ axis.

Table 6.2: Comparison of the Weiss-temperature (Θ_W) and the effective magnetic moment (μ_{eff}) obtained the Curie–Weiss law fits shown in Fig. 6.13 with those found in the literature of Pr_3BWO_9 poly and single crystalline samples.

Field-direction	Θ_W (K)	μ_{eff} (μ_{B})	Θ_W (K)	μ_{eff} (μ_{B})	Ref.
$B\|\|c$	-5.40	3.5	3.3	3.50	[77]
$B \perp c$	-6.10	2.73	-72	3.67	[77]
Polycrystal	-6.88	3.09	-40.30	3.55	[75]
Polycrystal	-6.8(2)	2.95(1)	-31(2)	3.33(3)	[This work]

The AC magnetic susceptibility of Pr_3BWO_9 is shown in Fig. 6.14. At $B_{dc} = 0$ T and $10 \leq f \leq 600$ Hz, the real part χ'_{ac} displayed in Fig. 6.14 (a) increases monotonically with decreasing the temperature in a pretty similar behaviour to that of Nd_3BWO_9 and consistent with the DC susceptibility in Fig. 6.13. Noticeably, the frequency independence of the χ'_{ac} data in the studied regime implies that there is no glassy-state in the system and/or the characteristic spin-fluctuation rate in Pr_3BWO_9 is beyond the kilohertz region. The latter argument is supported by NMR studies (MHz frequencies), which show the existence of short-ranged collective spin excitations [77]. In contrast to Nd_3BWO_9, the application of DC magnetic fields barley affect the behavior of Pr_3BWO_9's χ'_{ac}, see Fig. 6.14

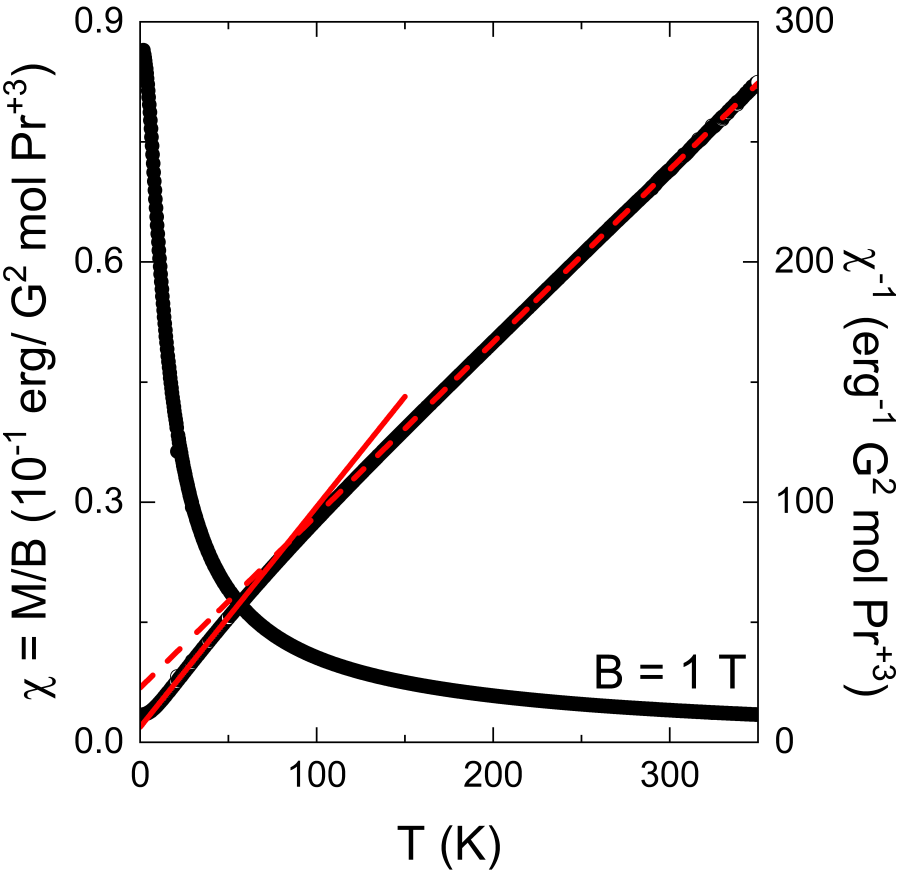

Figure 6.13: Temperature dependence of the DC magnetic susceptibility, $\chi = M/B$ and its inverse χ^{-1} of Pr_3BWO_9, measured at an applied magnetic field of 1 T (ZFC). The dashed (solid) red line represents the high (low) temperature Curie-Weiss fit to the data.

(b), and does not induce clear anomalies. Generally, the AC susceptibilities suggest that the spin relaxation rates in the two systems are completely different. speculatively, the spin relaxation rates in Pr_3BWO_9 are higher than that of Nd_3BWO_9. Consequently, the application of magnetic fields in the latter induces a kind of freezing feature. Additionally, this picture is consistent with the much stronger AFM interactions in Pr_3BWO_9 compared to those in Nd_3BWO_9.

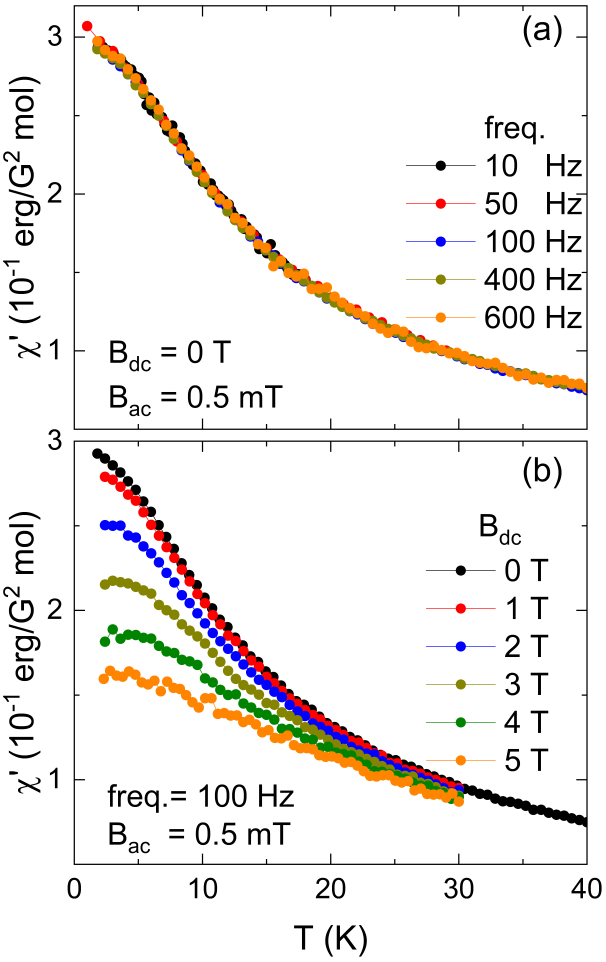

Figure 6.14: Temperature dependence of the AC magnetic susceptibility of Pr_3BWO_9 polycrystal sample. (a) shows the data measured at $B_{dc} = 0$ T, an excitation AC filed $B_{ac} = 0.5$ mT, and using different frequencies in the range of $10 \leq f \leq 600$ Hz and (b) shows the data measured at $f = 100$ Hz, an excitation AC filed $B_{ac} = 0.5$ mT, and under different DC magnetic fields in the range of $0 \leq B \leq 5$ T.

6.5.2 Heat Capacity

Figure 6.15 (a) shows the specific heat of Pr_3BWO_9 and of its non-magnetic counterpart La_3BWO_9, as reported by Flavían *et al.* in [79]. At $B = 0$ T and low temperatures, c_p of Pr_3BWO_9 exhibits an anomaly at about 5.7(4) K, which can not be attributed to a phase transition. In other words, our data show the absence of a long-range magnetic order in Pr_3BWO_9 down to 1.8 K, in a agreement with DC and AC data shown earlier, and with the heat capacity data reported by Zeng *et al.* [77]. Subtracting the specific heat capacity of La_3BWO_9 (lattice contribution) from the total specific heat of Pr_3BWO_9, yields the non-phononic heat capacity (c_p^{el}) of the latter, which extends up to about $T = 30$ K and fades out at $T > 30$ K as shown in Fig. 6.15 (b). The non-phononic specific heat is supposed to be associated with magnetic degrees of freedom, accordingly the integral of (c_p^{el} /T) from 1.8 K to 90 K gives the changes in magnetic entropy, S_{mag} as shown in Fig. 6.15 (b). We obtain $\Delta S_{mag} = 5.42$ J/(mol K) above 30 K. Additionally, estimating the magnetic entropy changes below 1.8 K down to 90 mK at 0.11 J/(mol K), based on heat capacity data reported in [77], we end up with $\Delta S_{mag} = 5.53$ J/(mol K) for $T > 90$ mK. This value is only 30% of the full expected magnetic entropy of $R\ln(8) = 18.26$ J/(mol K) for Pr^{3+} with $J = 4$, but surprisingly it represents 96% of the expected value ($R\ln 2 = 5.76$ J/(mol K)) of a two-level system with $J_{eff} = 1/2$, where R is the universal gas constant. Notably, the magnetic entropy of the isomorphic Nd_3BWO_9 is also well described by a two-level system [79]. Nonetheless, the saturation of the magnetic entropy changes in Nd_3BWO_9 sets at $T = 3$ K. This temperature is only one tenth of the saturation temperature shown in Pr_3BWO_9.

Table 6.3: The parameters, n the concentration of Schottky centers, and Δ the splitting gap, obtained from fitting the c_p^{mag} of Pr_3BWO_9 to a two-level Schottky model at different applied magnetic fields.

Magnetic Field (T)	n	Δ (K)
0	2.57(1)	18.2(1)
1	2.58(1)	18.5(1)
2	2.57(1)	18.9(1)
4	2.62(2)	19.8(2)
6	2.61(2)	21.2(2)
8	2.58(1)	23.1(2)
10	2.54(2)	25.2(3)
12	2.48(2)	27.3(4)
14	2.41(1)	29.5(6)

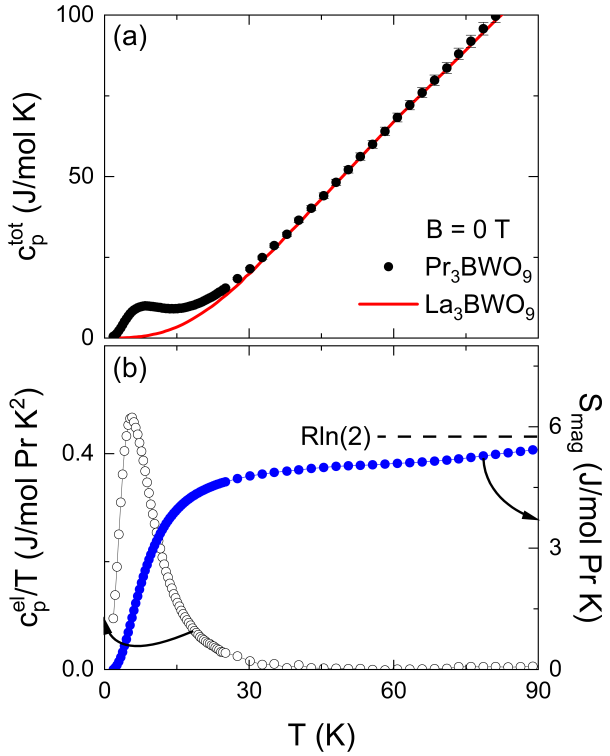

Figure 6.15: Temperature dependence of (a) specific heat of Pr_3BWO_9 and La_3BWO_9 polycrystalline samples measured at $B = 0$ T; the latter data are taken from [79]. (b) c_p^{el}/T, and calculated magnetic entropy S_{mag} of Pr_3BWO_9. The dashed line marks the expected theoretical value of $S_{mag} = R\ln(2)$.

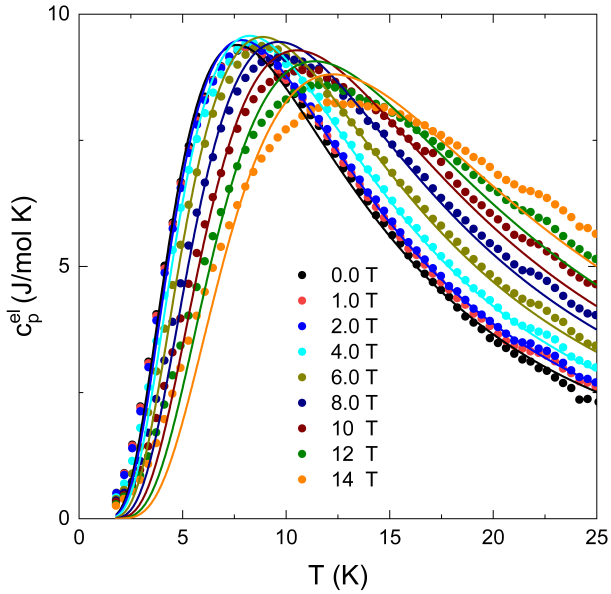

Figure 6.16: Temperature dependence of the $c_p^{el}$of Pr_3BWO_9 polycrystalline sample measured at different applied magnetic fields. The $c_p^{el}$is obtained by the subtraction of the heat capacity of La_3BWO_9 , which is taken from [79]. The solid lines represent the fits to the two-level Schottky function as described in text.

Figure 6.16 shows the temperature dependence of the electronic specific heat, $c_{\mathrm{p}}^{\mathrm{el}} = c_{\mathrm{p}}^{\mathrm{tot}}$ - $c_{\mathrm{p}}^{\mathrm{ph}}$, of Pr_3BWO_9. At B = 0 T, the $c_{\mathrm{p}}^{\mathrm{el}}$exhibits a broad peak at T = 5.7 (4) K, with a relatively large heat capacity of 8.5 J/(mol K). The shape of the peak and its large value cannot be explained by electronic, lattice, or even magnon contributions. Instead, it arises from the Schottky-like anomaly caused by electronic excitations in the split energy levels of Pr^{3+} ions. The Schottky nature of the peak becomes more clear with the application of magnetic fields, which gradually shift the peak's position to higher temperatures, broadens and suppresses its amplitude. For the non-Kramer's ion Pr^{3+} with J = 4, the crystal field interactions result in nine singlet states, some of which may have accidental or near-degeneracies [77, 86]. To quantify the energy gap separation between the ground state and the first excited levels, a two-level system with energy degeneracy, as described by Gopal [16] and Tari [14] is employed:

$$C_{\mathrm{Schottky}} = n \cdot R \left(\frac{\Delta}{T}\right)^2 \left(\frac{g_0}{g_1}\right)^2 \frac{e^{\frac{\Delta}{T}}}{\left[1 + \left(\frac{g_0}{g_1}\right) e^{\frac{\Delta}{T}}\right]^2} \tag{6.1}$$

where n is the concentration of Schottky centers, R is the gas constant, Δ is the splitting gap of Pr^{3+} electronic orbital levels in magnetic fields, and (g_0/g_1) is the degeneracy of energy levels. Considering n, Δ, as free fit parameters, and $(g_0/g_1) = 1$, produce good-fitting curves as represented by solid lines in Fig. 6.16). The fit results are listed in Table 6.3. Notably, the best fits are achieved with (g_0/g_1) as a constant, which implies the magnetic field effect on the level's degeneracy in Pr_3BWO_9 is negligible. Further, the fits yields n $\simeq$ 2.5(1), under different applied magnetic fields, which means only 82(3)% of magnetic ions Pr^{3+} contribute to the Schottky specific heat. It is noteworthy to mention that in the same temperature regime where the Schottky anomaly appears, the low temperature Curie–Weiss law fit in Fig. 6.13 yields μ_{eff} of 2.95 μ_{B} / Pr^{3+}, which also represents 82% of the theoretical μ_{eff}. The magnetic field dependence of the obtained Δ is plotted in Fig. 6.17 as black solid circles. Obviously, Δ increases monotonically with the field, in particular at B $\geq$ 4 T, which agrees very well with the spin excitation gaps (red and blue solid circles in Fig. 6.17) as reported by Zeng *et al.* [77] from NMR measurement. Notably, our results support their speculation regarding the presence of a nonzero spin gap at zero field and indicate that the excitation gap is inherent rather than field-induced.

Figure 6.18 compares the Pr_3BWO_9's $c_{\mathrm{p}}^{\mathrm{el}}$ /T with the spin-spin relaxation time $1/^{11}T_2$, which is reported by Zeng *et al.* for a Pr_3BWO_9 single crystal under magnetic fields applied parallel and perpendicular to the c axis [77]. Firstly, it should be noted that comparing $c_{\mathrm{p}}^{\mathrm{el}}$ /T and $1/^{11}T_2$ is not straightforward, given that these two quantities originate from

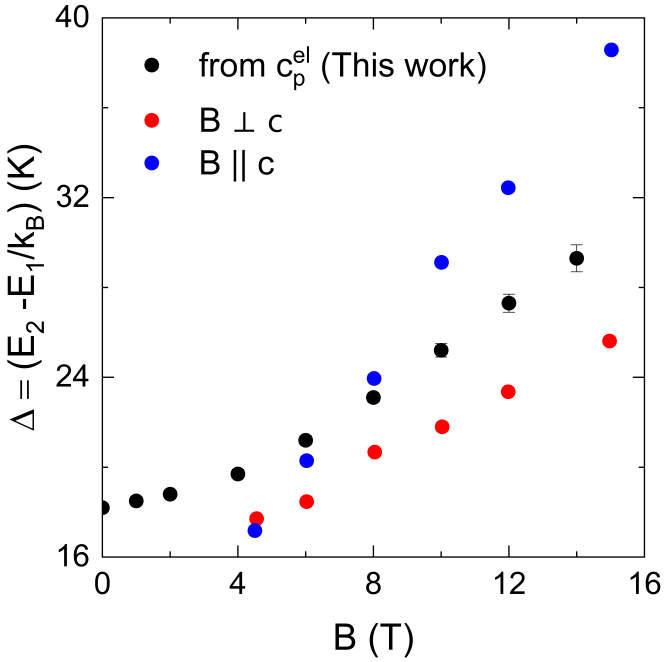

Figure 6.17: Magnetic field dependence of the Zeeman splitting gap Δ (black circles) obtained from the analysis of Pr_3BWO_9's c_p^{el}. The spin excitation gaps obtained from the Arrhenius plot of $1/^{11}T_1$ versus 1/T with magnetic fields applied perpendicular (red) and parallel (blue) to the c axis of Pr_3BWO_9 single crystal [77] are shown for comparison.

different physics concepts. However, since we argue the causation of the hump at ≈ 5 K in both quantities is the same, i.e. crystal electric field excitations. This argument is supported by the observation of a similar hump at 8 K in the NMR data of Pr_3BWO_9's counterpart Sm_3BWO_9 which has been also linked to crystal electric field excitations [78]. Additionally, a similar hump has been reported in both c_p^{el} and NMR data of the distorted Kagomé system $Pr_3Ga_5SiO_{14}$ [72] as well as in the frustrated antiferromagnet $Yb(BaBO_3)_3$ [87]. Now back to the data, luckily, the NMR wipe-out effect does not occur for Pr_3BWO_9 and the $1/^{11}T_2$ amounts to few tens of milliseconds below $T \approx 5$ K, which enables us to compare the c_p^{el}/T and the relaxation time over a relatively wide range. At a glance, the c_p^{el}/T and the $1/^{11}T_2$ measured in the vicinity of $B = 4$ T exhibit the same form. Precisely, both quantities show a broad peak centered at $T \approx 5$ K. This similarity in form can be attributed to the increasing occupation of the Pr^{3+} ion ground state at low temperatures. Below $T \approx 5$ K, the occupation of the ground state by the electron spins rapidly increases with decreasing the temperature and both $1/^{11}T_2$ and c_p^{el}/T drop to low limit values. A similar behaviour was reported for the distorted Kagomé system $Pr_3Ga_5SiO_{14}$ [72].

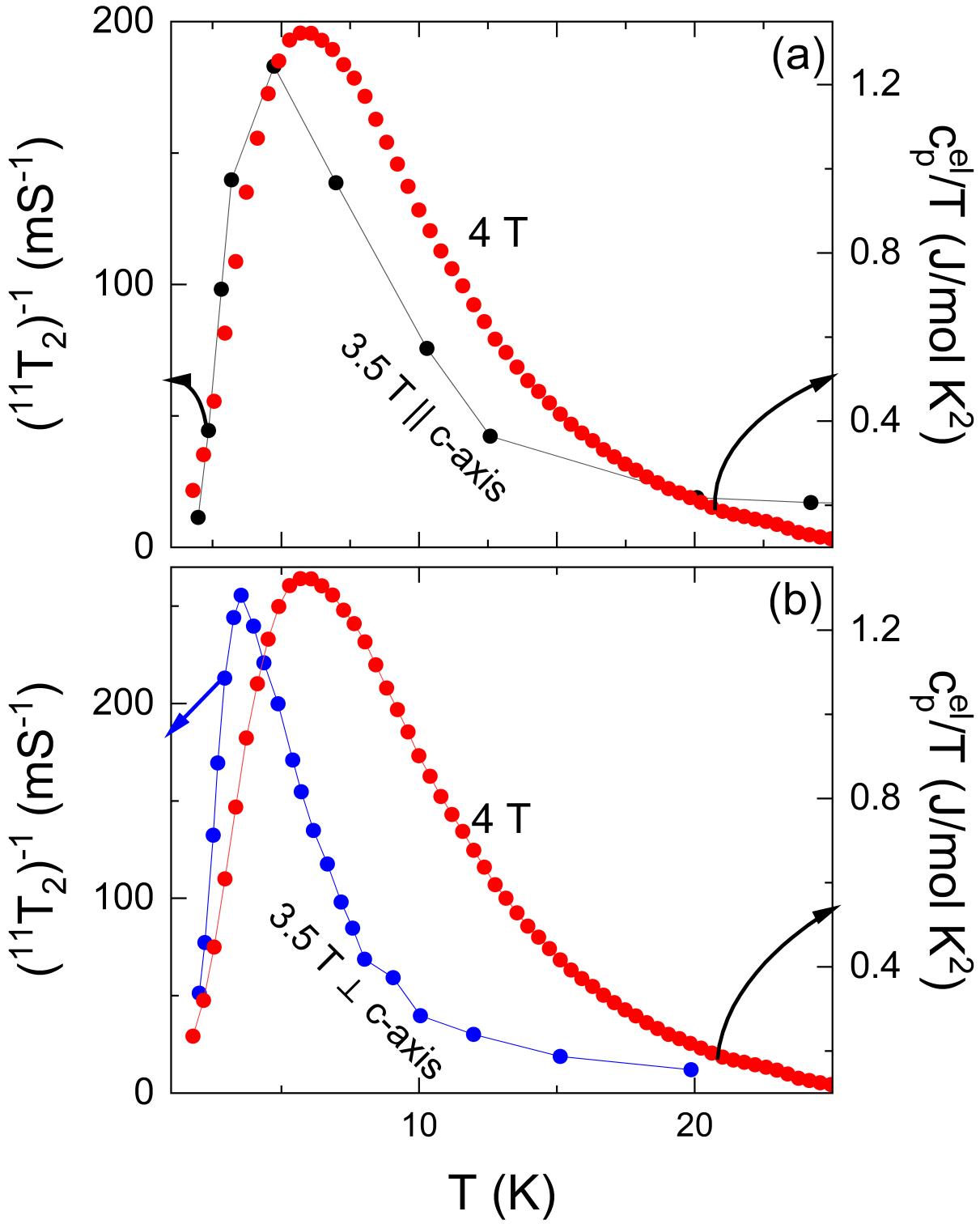

Figure 6.18: Temperature dependence of spin-spin relaxation rates ($1/^{11}T_2$) of Pr_3BWO_9 single crystals measured at B = 3.5 T parallel and perpendicular to c axis (the data are adopted from [77], together with the c_p^{el} of Pr_3BWO_9 polycrystal measured at B = 4 T.

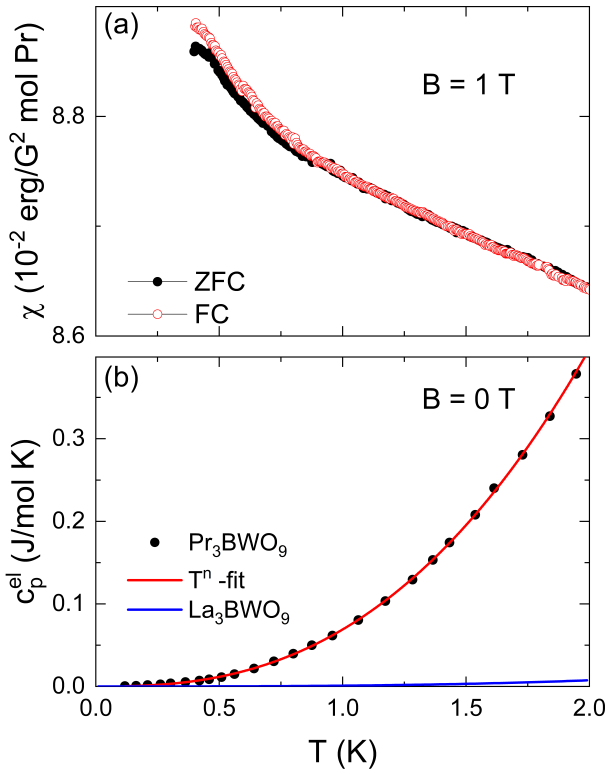

Figure 6.19: (a) Magnetic susceptibility $\chi(T)$ of Pr_3BWO_9 polycrystalline sample measured in ZFC (black circles) and FC (red circles) modes at $B = 1$ T, and (b) c_p^{el} of Pr_3BWO_9 single crystal obtained by the subtraction of La_3BWO_9's c_p reported in [79] from c_p^{tot} reported in [77]. The solid red line is a power-law fit(see the text).

6.5.3 Static Magnetization Below 1.8 K

The absence of long-range magnetic order in Pr_3BWO_9 down to 400 mK is evident from the temperature dependence of the DC magnetic susceptibility shown in 6.19 (a). $\chi(T)$ increases monotonically with decreasing the temperature without anomalies or changes in the slope down to the lowest temperature. Additionally, there is no bifurcation between ZFC and FC measurements at least down to 470 mK, which excludes the presence of spin-glass state in this regime. Simultaneously, c_p^{el} derived from subtracting the specific heat of La_3BWO_9 [79] from c_p^{tot} of Pr_3BWO_9 [77] shows no anomalies down to 90 mK. Fitting c_p^{el} data by means of a power law $c_p^{el} \simeq T^n$, where A is a constant, yields a reasonable fit to the data with $n = 2.4(1)$ as shown in 6.19 (b). It is noteworthy to mention that in a 2D ordered magnet, the magnon excitations would give $c_p^{mag} \propto T^2$. Nonetheless, in 2D kagomé-like systems such as $SrCr_{8-x}Ga_{4+x}O_{19}$ [70] and Pr_3GaSiO_14 [72], $c_p^{el} \sim T^2$ even in the absence of a long-range order.

6.5.4 Pulsed-Field Magnetization

Figure 6.20 shows the magnetizations of Pr_3BWO_9 polycrystalline sample measured at 3, and 5.1 K. The pulsed-field magnetization data (solid circles) show no plateaus neither at low fields nor at high fields. The data have been normalized to M(B) data measured in quasi-static fields up to 7 T. Notably, the pulsed-field data and quasi-static field data show the same behaviours. At the maximum applied magnetic field of 58 T, the magnetizations amount to 1.60(2), and 1.40(2) μ_B/Pr^{3+}, for measurements at 3, and 5.1 K, respectively. Although these values are far from the theoretical saturation magnetization M_{sat} = 3.2 μ_B/Pr^{3+} expected for free Pr^{3+} ions, they agree well with the values reported for distorted Kagomé system $Pr_3Ga_5Si_3O_{14}$ [85] from pulsed-field magnetization data, and with other Pr^{3+}-based frustrated magnets $Pr_3M_2Sb_3O_{14}$ (M = Mg, Zn) [88, 89]. Note, the quasi-static magnetization of Pr_3BWO_9 polycrystal sample reported in [75] gives $M_{sat} = 1.2$ μ_B/Pr^{3+} at the highest field of 14 T and measurement at 2 K.

With a closer look on the magnetization in Fig. 6.20, we note a continuous, and monotonic behavior with no signs of a magnetic phase transition. Notably, the magnetization curves exhibit smooth right-bending and there is a kind of saturation effect sets in above B = 18(2) T. The absence of long-range order down to 400 mK might suggest a purely paramagnetic state. However, this contradicts the magnetic field dependence of non-interacting paramagnetic Pr^{3+} ions with $J = 4$, which saturates much more rapidly at such a low temperature (see black dashed line in Fig. 6.20), indicating a significant influence of antiferromagnetic correlations at the studied temperatures. Consequently, the Pr_3BWO_9 magnetization can only be described by the sum of a Brillouin function B_S and a linear term, denoted as $M_{sat}B_J(x)+\chi_0\times B$; $x = g\mu_B SB/[k_B(T)]$ with M_{sat} the saturation magnetization of the right-bending term, spin S, field-independent susceptibility χ_0, Boltzmann constant k_B, Bohr magneton μ_B, and the g-factor. The linear term mainly reflects the response of the short-ranged AFM correlations. The fits yield $\chi_0 = 0.0059$ μ_B/T Pr^{3+}, $M_{sat} = 1.26$ μ_B/Pr^{3+}, and $\chi_0 = 0.0011$ μ_B/T Pr^{3+}, $M_{sat} = 1.32$ μ_B/Pr^{3+} for the data measured at 3 K and 5.1 K, respectively.

6.6 Discussion

Comparing the results of the DC magnetic susceptibility for the studied systems, we note that Nd_3BWO_9 exhibits a higher Weiss temperature in the high-temperature regime ($\Theta \sim -47$ K) compared to Pr_3BWO_9 ($\Theta \sim -31$ K), suggesting stronger AFM exchange interactions in the former. Using Weiss-temperature values and $T_N = 0.3$ K, magnetic frustration factors of $f > 65(5)$, and $f = |\Theta_W|/T_N \sim 10(1)$ are estimated for Nd_3BWO_9,

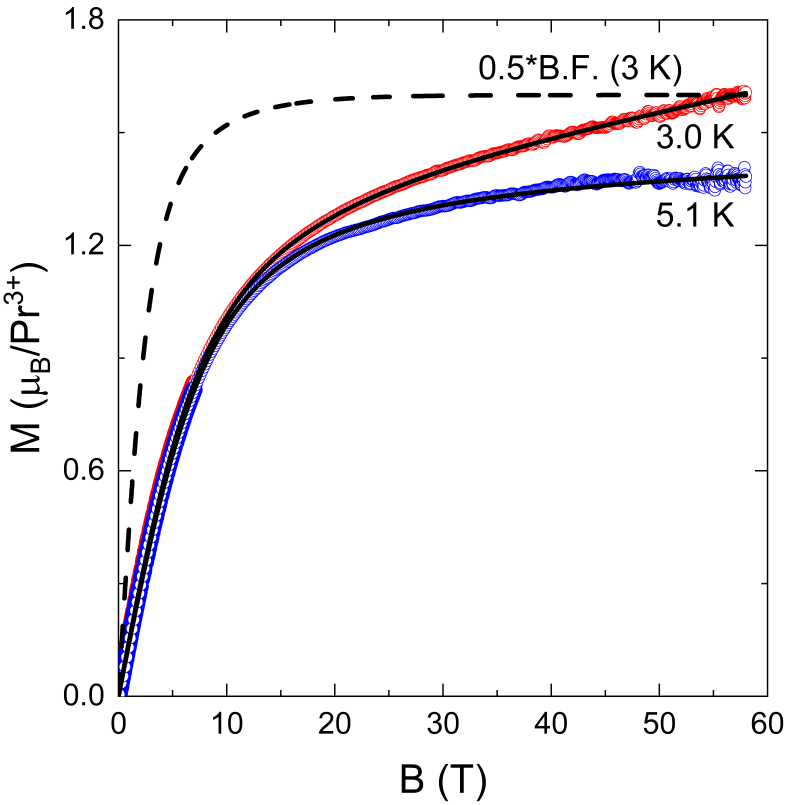

Figure 6.20: Magnetic field dependence of DC (open circles) and pulsed (solid circles) magnetizations of Pr_3BWO_9 polycrystalline sample measured at different temperatures under up sweeps of magnetic fields up to 7 T and 58 T respectively. Black solid lines represent fits to the data by the sum of Brillouin function and a linear term $\chi_0 \times B$ (see the text). The dashed line represents the Brillouin function corresponding to non-interacting Pr^{3+} ions with $g_J = 0.8$, J = 4 at T = 3 K, and it is scaled to the pulsed-field data measured at T = 3 K.

and Pr_3BWO_9, respectively, as there no long-range order in the latter above 90 mK. With a closer look on the fits in Figs. 6.1 and 6.13, we note that the Curie–Weiss law is valid well below Weiss temperatures, which is a fingerprint of a cooperative paramagnetic state in the static magnetic susceptibility of classical frustrated magnets [90]. Nonetheless, at 1.8 $\leq T \leq$ 10 K, as depicted in Fig. 6.21, Pr_3BWO_9's susceptibility exhibits a right-bending, while Pr_3BWO_9's shows left-bending, which might result from differences in the magnetic frustration, and exchange interactions in the systems.

AC magnetic susceptibility results shown in Figs. 6.2 and 6.14 (a) rule out the presence of glassy states down to 1.8 K in Nd_3BWO_9 and Pr_3BWO_9. However, the cooperative paramagnetic state in Nd_3BWO_9 differs from that of Pr_3BWO_9; the former exhibits field-induced spin freezing at T^*, while the latter is barely affected by the magnetic field. This suggests a distinct slow spin relaxation mechanism in Nd_3BWO_9 compared to Pr_3BWO_9.

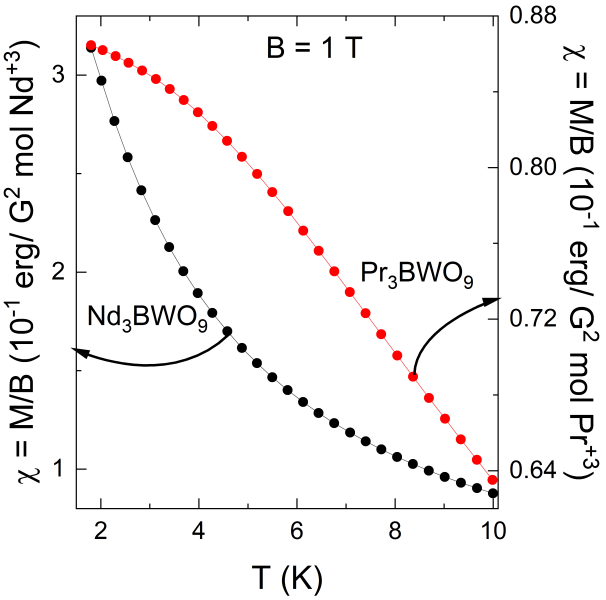

Figure 6.21: Comparison of DC magnetic susceptibility of Nd_3BWO_9 and Pr_3BWO_9 measured at $B = 1$ T.

6.7 Summary

In sum, static, dynamic, pulsed magnetization and heat capacity bulk probes have been employed to study the magnetic ground state of Nd_3BWO_9 and Pr_3BWO_9 with distorted Kagomé lattice. Analysis of magnetic susceptibility data shows that Nd_3BWO_9's Weiss temperature ($\Theta \sim -47$ K) is higher than that of Pr_3BWO_9 ($\Theta \sim -31$ K), suggesting a stronger AFM exchange interactions in the former. Magnetic frustration parameters of $f > 65(5)$, and $f = |\Theta_W|/T_N \sim 10(1)$ are estimated for Nd_3BWO_9, and Pr_3BWO_9, respectively. AC magnetization studies rule out the presence of glassy states at least down to 1.8 K in Nd_3BWO_9 and Pr_3BWO_9. However, the cooperative paramagnetic state in Nd_3BWO_9 differs from that of Pr_3BWO_9; the former exhibits field-induced spin freezing at $T^* = 4.3(5)$ K, while the latter is barely affected by the magnetic field. This suggests a distinct slow spin relaxation mechanism in Nd_3BWO_9 compared to Pr_3BWO_9. Absence of long-range magnetic order in Pr_3BWO_9 is further confirmed by the heat capacity studies, where only a Schottky anomaly is observed at $T = 5.7(4)$ K. Estimation of magnetic entropy changes gives $\Delta S_{mag} = 5.53$ J/(mol K) for $T > 90$ mK. This value represents 96% of the expected value ($R \ln 2 = 5.76$ J/(mol K)) of a two-level system with $J_{eff} = 1/2$. Likewise, the magnetic entropy changes of Nd_3BWO_9 are also well described by a two-level system. Nonetheless, the saturation of the magnetic entropy changes in Nd_3BWO_9 sets

in at $T = 3$ K, which is one tenth the saturation temperature in comparison to that of Pr_3BWO_9. On further cooling, and at $B = 0$ T, Nd_3BWO_9 orders antiferromagnetically at $T_N = 0.3$ K, while there no long-range magnetic order in Pr_3BWO_9 at least down to $T = 90$ mK. DC magnetization, at $T = 400$ mK, shows that the magnetization of Nd_3BWO_9 per Nd^{3+} increases in a quadratic-like manner below $B = 0.4(1)$ T, and it demonstrates a narrow washed-out plateau, spans 0.67 - 0.86 T, with a value consistent with a fractional $M = 1/3M_{\rm sat}$. After the plateau feature, the magnetization increases monotonically, and the saturation sets in at $B_{\rm sat} = 1.85(2)$ T, and the maximum magnetization at $B = 7$ T equals to 1.6 $\mu_{\rm B}/Nd^{3+}$. In Pr_3BWO_9, the magnetization increases monotonically with increasing the field with no signs of plateaus or saturation, and the maximum magnetization at $B = 7$ T equals to 0.9 $\mu_{\rm B}/Pr^{3+}$. The pulsed-field magnetization of Nd_3BWO_9, measured at 540 mK and 11.5 K, shows no magnetization plateaus, and does not reach the expected theoretical value of 3.24 $\mu_{\rm B}$ even at $B = 60$ T for the measurement at 11.5 K. The pulsed-field data at 11.5 K exhibits a smooth right bending over a wide range of magnetic fields. Fitting the data using a Brillouin function, the fit diverges. This indicates the absence of a conventional paramagnetic state in Nd_3BWO_9 even at 11.5 K. Instead, the data are nicely fitted by the sum of the Brillouin function and a linear term, which mainly reflects the response of the short-ranged AFM correlations. Similar to Nd_3BWO_9, the pulsed-field data of Pr_3BWO_9, measured at 3 K, and 5.1 K, show no plateaus neither at low fields nor at high fields. The magnetization does not reach the theoretical saturation value even at $B = 58$ T, and also the data follow a sum of the Brillouin function and a linear term, which again indicates the relevant of the short-ranged AFM correlations in Pr_3BWO_9.

Chapter 7

Overall Summary

The aim of this work is to experimentally investigate the magnetic ground state of electron correlated systems with competing interactions as realized by the mixed antiferromagnet system $Ni_{0.25}Mn_{0.75}TiO_3$, the spin ice candidate; $Ho_2Zr_2O_7$, and the distorted Kagomé systems; Nd_3BWO_9, and Pr_3BWO_9 by means of heat capacity and magnetization techniques. The heat capacity is measured using a relaxation method provided by the PPMS heat capacity option. The measurements are performed under applied magnetic fields up to 14 T, and over two separate temperature regimes: the standard regime spans from 1.8 K to 300 K and the low temperature regime spans from 0.05 K to 4 K, where the PPMS is equipped with the dilution refrigerator probe. DC, AC, and pulsed-field magnetizations are combined with the heat capacity studies to build the magnetic phase diagrams of the studied systems.

$Ni_{0.25}Mn_{0.75}TiO_3$ belongs to the mixed ilmenite-structured titanates, $A_xMn_{1-x}TiO_3$ (A = Fe, Co, and Ni), where the dopants A are randomly distributed in the structure. The parent compound $MnTiO_3$ exhibits G-type AFM order with the easy magnetization axis along the crystallographic direction c. In contrast, $NiTiO_3$ shows A-type AFM order with an easy-plane-like anisotropy perpendicular to the c axis. This suggests different exchange interactions and competing anisotropies in $Ni_{0.25}Mn_{0.75}TiO_3$. At $B = 0$ T, $Ni_{0.25}Mn_{0.75}TiO_3$ exhibits antiferromagnetic long-range order at $T_N = 34.8(6)$ K and a spin reorientation at $T_R \sim 14.8(4)$ K observed through specific heat, static and dynamic magnetic susceptibility studies. The transition at T_R is of discontinuous nature and attributed to competing magnetic anisotropies of Mn^{2+} and Ni^{2+} magnetic moments. Further, these transitions are associated with noticeable lattice changes, as indicated by anomalies in thermal expansion. Cooling further, AC susceptibility χ'_b shows a glassy feature at $T^* \approx 3.7$ K, which corresponds to the onset of a thermal hysteresis between χ_{dc}^{ZFC} and χ_{dc}^{FC}. Additionally,

in the same temperature regime, the magnetic specific heat shows no anomaly, but follows a $c_{\mathrm{p}}(T) \propto T^{1.3}$ behaviour instead of T^3 behaviour expected for an antiferromagnet with long-range order. Pulsed-field magnetization, measured at $T = 1.4$ K, indicates that ≈ 15 % of all Mn^{2+}-spins are weakly antiferromagnetically-coupled in $Ni_{0.25}Mn_{0.75}TiO_3$. The magnetic transitions visible in the static magnetic susceptibility become weaker as the magnetic field increases and completely vanish at magnetic fields $B \geq 0.8$ T. In contrast, in c_p at $B = 14$ T, while the anomaly at T_{R} is completely suppressed, the one at T_{N} is only very slightly shifted to lower temperatures. In thermal expansion, applying a field of $B = 1$ T yields a significant decrease (increase) of T_{R} when applied along the b axis (c axis). Notably, for $B||b$ axis, the anomaly at T_{R} changes its sign from positive to negative for $B \geq 1$ T and up to $B = 14$ T. Note, the sign change in α_{b} at T_{R} is accompanied by the disappearance of the anomalies observed in χ_{b}. The main effects of 25 % Ni-doping on pure $MnTiO_3$ are as following: (a) T_{N} is suppressed from 64 K to ≈ 35 K and its anomaly size is significantly reduced to only ≈ 3 % of the expected mean-field value, (b) In $Ni_{0.25}Mn_{0.75}TiO_3$ below T_{N}, the magnetic entropy is consumed in a quasi-linear manner, which qualitatively differs from the behavior in $MnTiO_3$, (c) In $Ni_{0.25}Mn_{0.75}TiO_3$ short-range magnetic order is persistence up to $\simeq 4 \times T_{\mathrm{N}}$, compared to $\simeq 3 \times T_{\mathrm{N}}$ in $MnTiO_3$.

$Ho_2Zr_2O_7$ belongs to a series of rare-earth oxides with the formula $RE_2Zr_2O_7$ with RE = Ce, Pr, Nd, Gd, Tb, Dy, or Ho. The system features Ho^{3+}, which its free ion magnetism is described by $S = 5$, $L = 3$, and $J = 8$. In $Ho_2Zr_2O_7$, the ratio between the radii of the magnetic and nonmagnetic ions is $\frac{r(Ho^{3+})}{r(Zr^{4+})} \approx 1.40$, which yields the defected-fluorite structure with space group $Fd\bar{3}m$. This structure is geometrically frustrated and presents a platform to investigate the spin ice state. Heat capacity, DC, and AC magnetization studies show that $Ho_2Zr_2O_7$ does not exhibit a long-range magnetic order down to $T =$ 280 mK. Instead, it has a disordered ground state with short-range antiferromagnetic correlations. Further, due to geometrical frustration, the spins tend to go into a frozen state below $T = 0.6$ K, which is preceded by two spin relaxations processes at $T_{\mathrm{g1}} =$ 7(1) K and $T_{\mathrm{g2}} = 0.9(1)$ K. Similar to the canonical spin ice systems $Ho_2Ti_2O_7$, and $Dy_2Ti_2O_7$, the frozen state in $Ho_2Zr_2O_7$ is driven by slow spin relaxation processes at higher temperatures. At $T = 400$ mK, $Ho_2Zr_2O_7$'s isothermal magnetization measured amounts to 5.5 (1) μ_{B}, which is only about 55% of the theoretical saturation value, M_{sat} = 10 μ_{B}. This is attributed to substantial single ion anisotropy. Further, the route to saturation in $Ho_2Zr_2O_7$ is different compared to that in $Ho_2Ti_2O_7$. In the latter, saturation effect sets in at $B = 0.6(1)$ T, which is delayed to $B = 1.4(2)$ T in case of $Ho_2Zr_2O_7$. These difference signifies antiferromagnetic correlations in $Ho_2Zr_2O_7$ in comparison to the

ferromagnetic correlations in $Ho_2Ti_2O_7$.

Nd_3BWO_9 and Pr_3BWO_9 belong to a family of rare-earth boratotungstates with the formula RE_3BWO_9; RE= Nd, Pr, Sm, Gd, Tb, or La. Nd_3BWO_9 features Nd^{3+}, which its free ion magnetism is described by $S = 3/2$, $L = 3$, and $J = 9/2$, and Pr_3BWO_9 features Pr^{3+} ions leading to $S = 1$, $L = 3$, and $J = 4$. Both systems crystallize in a hexagonal structure with space group $P6_3$ (no. 173), where the Nd^{3+}, and Pr^{3+} ions lay on a distorted Kagomé lattice connections within the ab-plane and stacked in an AB-type fashion along the c axis. Analysis of magnetic susceptibility data shows that Nd_3BWO_9's Weiss temperature ($\Theta \sim -47$ K) is higher than that of Pr_3BWO_9 ($\Theta \sim -31$ K), suggesting a stronger AFM exchange interactions in the former. Magnetic frustration parameters of $f > 65(5)$, and $f = |\Theta_W|/T_N \sim 10(1)$ are estimated for Nd_3BWO_9, and Pr_3BWO_9, respectively. AC magnetization studies rule out the presence of glassy states at least down to 1.8 K in Nd_3BWO_9 and Pr_3BWO_9. However, the cooperative paramagnetic state in Nd_3BWO_9 differs from that of Pr_3BWO_9; the former exhibits field-induced spin freezing at $T^* = 4.3(5)$ K, while the latter is barely affected by the magnetic field. This suggests a distinct slow spin relaxation mechanism in Nd_3BWO_9 compared to Pr_3BWO_9. Absence of long-range magnetic order in Pr_3BWO_9 is further confirmed by the heat capacity studies, where a Schottky anomaly is observed at $T = 5.7(4)$ K. Estimation of magnetic entropy changes gives $\Delta S_{mag} = 5.53$ J/(mol K) for $T > 90$ mK. This value represents 96% of the expected value ($R \ln 2 = 5.76$ J/(mol K)) of a two-level system with $J_{eff} = 1/2$. Likewise, the magnetic entropy changes of Nd_3BWO_9 are also well described by a two-level system. Nonetheless, the saturation of the magnetic entropy changes in Nd_3BWO_9 sets in at $T = 3$ K, which is one tenth the saturation temperature in comparison to that of Pr_3BWO_9. On further cooling, and at $B = 0$ T, Nd_3BWO_9 orders antiferromagnetically at $T_N = 0.3$ K, while there no long-range magnetic order in Pr_3BWO_9 at least down to $T = 90$ mK. DC magnetization, at $T = 400$ mK, shows that the magnetization of Nd_3BWO_9 per Nd^{3+} increases in a quadratic-like manner below $B = 0.4(1)$ T, and it demonstrates a narrow washed-out plateau, spans 0.67 - 0.86 T, with a value consistent with a fractional $M = 1/3M_{sat}$. After the plateau feature, the magnetization increases monotonically, and the saturation sets in at $B_{sat} = 1.85(2)$ T, and the maximum magnetization at $B = 7$ T equals to 1.6 μ_B/Nd^{3+}. In Pr_3BWO_9, the magnetization increases monotonically with increasing the field with no signs of plateaus or saturation, and the maximum magnetization at $B = 7$ T equals to 0.9 μ_B/Pr^{3+}. The pulsed-field magnetization of Nd_3BWO_9, measured at 540 mK and 11.5 K, shows no magnetization plateaus, and does not reach the expected theoretical value of 3.24 μ_B even at $B = 60$ T for the measurement at 11.5 K. The pulsed-field data at 11.5 K exhibits a smooth right bending

over a wide range of magnetic fields. Fitting the data using a Brillouin function, the fit diverges. This indicates the absence of a conventional paramagnetic state in Nd_3BWO_9 even at 11.5 K. Instead, the data are nicely fitted by the sum of the Brillouin function and a linear term, which mainly reflects the response of the short-ranged AFM correlations. Similar to Nd_3BWO_9, the pulsed-field data of Pr_3BWO_9, measured at 3 K, and 5.1 K, show no plateaus neither at low fields nor at high fields. The magnetization does not reach the theoretical saturation value even at $B = 58$ T, and also the data follow a sum of the Brillouin function and a linear term, which again indicates the relevant of the short-ranged AFM correlations in Pr_3BWO_9.

Appendix A

Magnetization of $Mn(NO_3)_2$

This appendix presents low-temperature DC magnetization studies on $Mn(NO_3)_2$; which is supposed to resemble an antiferromagnetic kagomé system with $S = 5/2$. Polycrystalline samples of $Mn(NO_3)_2$ were synthesized as described in [91–93] by the group of Prof. A. N. Vasiliev, Low Temperature Physics and Superconductivity Department, Physics Faculty, M.V. Lomonosov Moscow State University, Moscow 119991, Russia. The samples have been obtained for the measurements presented below in 2021.

A.1 Experimental Details

The DC magnetization of $Mn(NO_3)_2$ polycrystalline samples have been studied by means of a Magnetic Properties Measurement System (MPMS-3, Quantum Design) over a wide temperature range from 0.4 K and up to 300 K. For measurements below 1.8 K down to 0.4 K, the MPMS-3 was equipped with the iQuantum He3 setup. DC magnetization data were obtained either after cooling the sample in the external magnetic measurement field (field-cooled; FC) or the field was applied after cooling the sample to the lowest temperature (zero-field-cooled; ZFC) on a sample with mass of 13.0(2) (mg).

A.2 Experimental Results

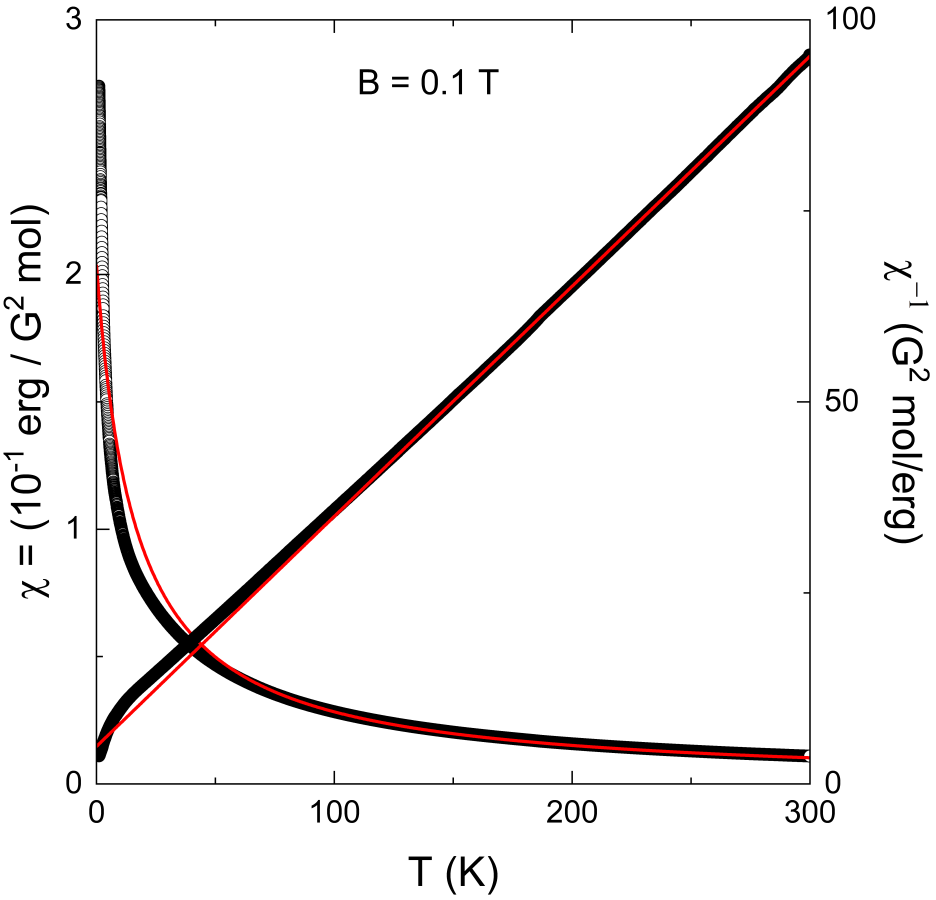

Figure A.1: Temperature dependence of the DC magnetic susceptibility, $\chi = M/B$ and its inverse χ^{-1} of $Mn(NO_3)_2$. The measurement was done at an applied magnetic field of $B = 0.1$ T (ZFC). The solid red lines represent a fit by the Curie–Weiss law, $\chi_{dc} = C/(T + \Theta_W)$, which yields Curie constant $C = 3.32$ emu/mol, and the Weiss-temperature $\Theta_W = -16(2)$ K.

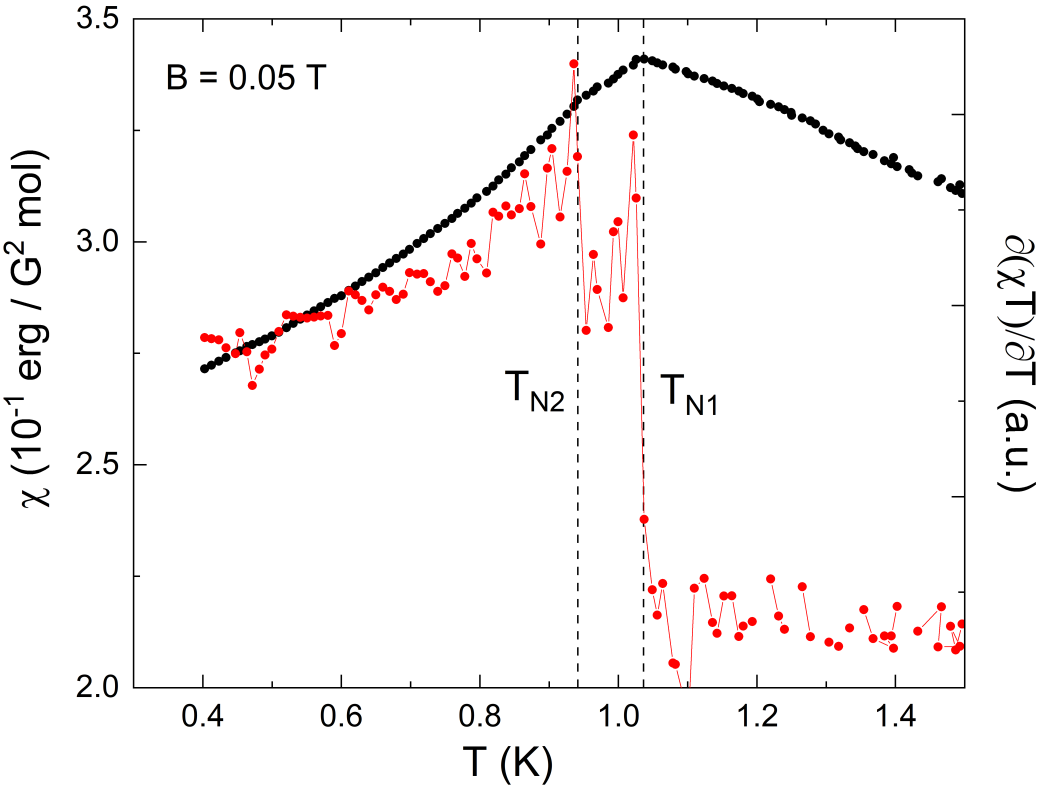

Figure A.2: Temperature dependence of the DC magnetic susceptibility, $\chi = M/B$ and its corresponding Fisher's magnetic specific heat, $\partial(\chi T)/\partial T$, of $Mn(NO_3)_2$. The The measurement was done at an applied magnetic field of 0.05 T(ZFC). The black dashed lines mark the magnetic phase transitions at T_{N1} and T_{N2}.

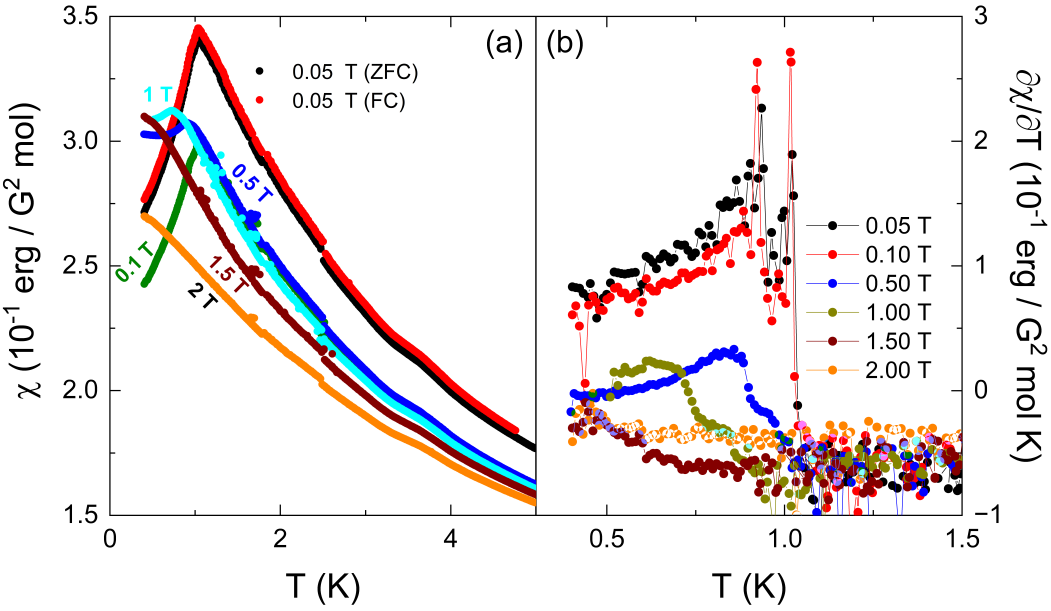

Figure A.3: Temperature dependence of (a) the DC magnetic susceptibility, $\chi = M/B$, and (b) its derivative, $\partial\chi/\partial T$, of $Mn(NO_3)_2$. The susceptibility measured at different magnetic fields in the range of $0.05 \leq B \leq 2$ T, after being cooled from 10 K in zero magnetic field (ZFC).

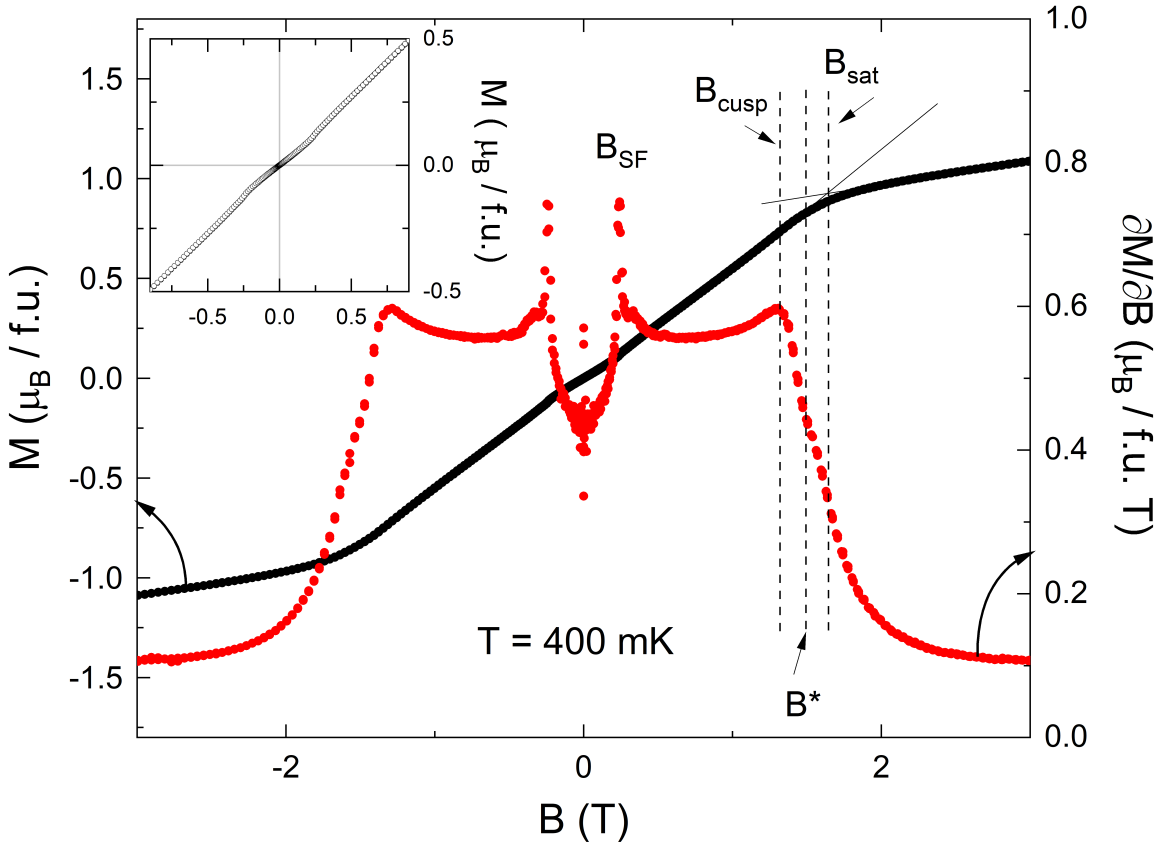

Figure A.4: Isothermal magnetization of $Mn(NO_3)_2$ at T = 400 mK, and its derivative $\partial M/\partial B$. Inset: the magnetization behaviour in the vicinity of zero magnetic field. The anomalies at $B_{\rm cusp}$, B^*, and $B_{\rm sat}$ are marked by Dashed lines.

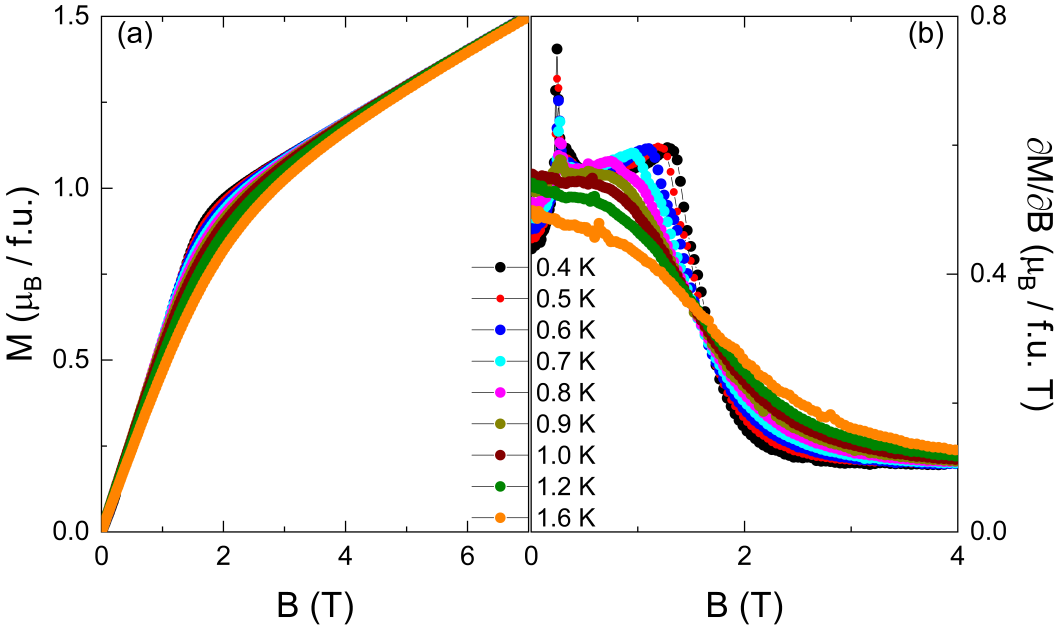

Figure A.5: Magnetic field dependence of (a) the upsweep isothermal magnetization, and (b) its derivative, $\partial M/\partial B$, of $Mn(NO_3)_2$ measured at different temperatures in the range of $0.4 \leq T \leq 1.6$ K.

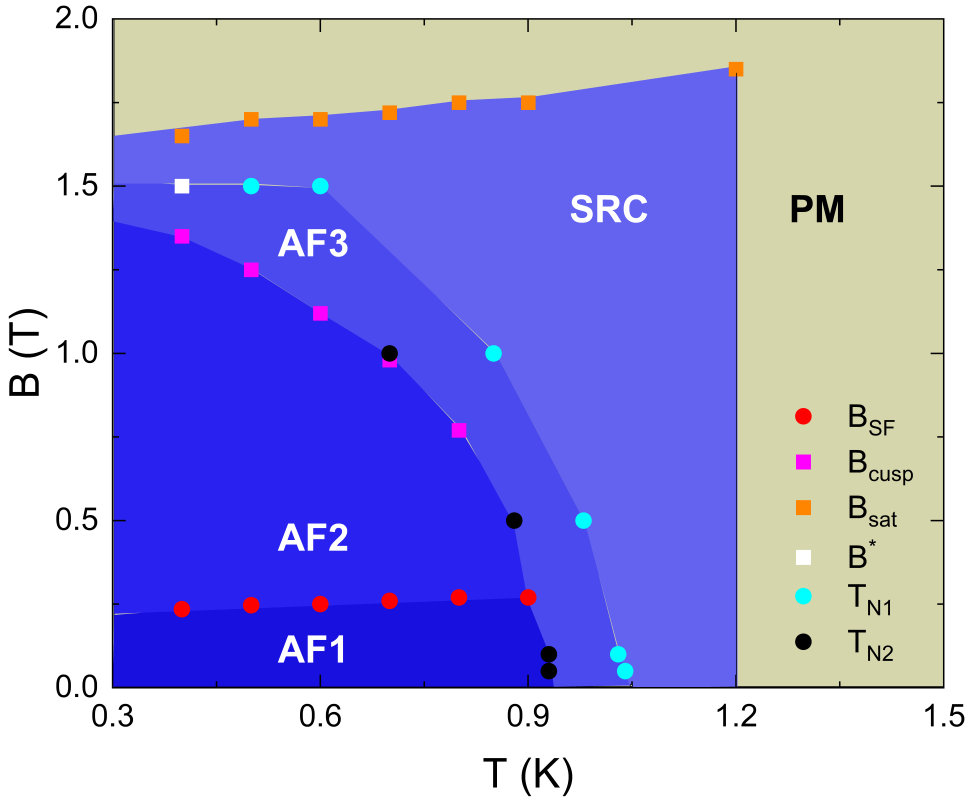

Figure A.6: Magnetic phase diagram of $Mn(NO_3)_2$. AF1, AF2, and AF3 refer to different antiferromagnetic phases. SRC, and PM refer to short-range correlated and paramagnetic phases, respectively.

Appendix B

Heat Capacity and Magnetization of $Ba_3ErB_9O_{18}$

This appendix presents heat capacity and magnetization studies on $Ba_3ErB_9O_{18}$, a triangular frustrated magnet. The low temperature DC magnetization data in Figs. B.4, B.5, and B.6 have been published as a part of a regular article in Physical Review B, under the title "Magnetic properties of the triangular-lattice antiferromagnets $Ba_3RB_9O_{18}$ (R = Yb, Er) [94].

B.1 Material Background

Polycrystalline samples of $Ba_3ErB_9O_{18}$ were prepared by a conventional solid-state reaction method as described in [94]. Samples in the form of pressed pellets were provided by P. Khuntia, Department of Physics, Indian Institute of Technology Madras, Chennai 600036, India.

B.2 Experimental Details

The DC magnetization (isotherm) of $Ba_3ErB_9O_{18}$ was measured at different temperatures in the range 2 K $\leq T \leq$ 50 K by means of the VSM option of the Physical Properties Measurement System (PPMS, Quantum Design) on a sample with mass of 22.0(3) mg. For measurements below 1.8 K down to 400 mK, the Magnetic Properties Measurement System (MPMS-3) was equipped with the iQuantum He-3 probe and a sample with mass of 21.56(7) mg was used. The temperature dependence of the magnetization (at three different fields) was obtained either after cooling the sample in an external magnetic field (field-cooled; FC) or the field was applied after cooling the sample to the lowest tem-

perature (zero-field-cooled; ZFC). The isotherm magnetization was measured at different temperatures in the range 0.4 K $\leq T \leq$ 1.6 K.

The AC magnetization was measured in the temperature range from 1.8 to 60 K, with 5 Oe AC excitation field, up to 7 T DC magnetic fields and frequencies ranging from 10 Hz to 0.6 kHz, using the AC option of the MPMS-3 on a sample with 1.3(3) mg mass.

The specific heat capacity was measured using the heat capacity option of the Physical Properties Measurement System (PPMS). The measurements were carried out in a wide temperature range from 1.8 to 200 K on a pressed pellet sample with a mass of 7.58(5) mg. The measurements were obtained under applied magnetic fields in the range 0 T $\leq B \leq$ 14 T.

Pulsed-field magnetization was measured up to 60 T at Helmholtz Zentrum Dresden-Rossendorf by an induction method using a coaxial pickup coil system [25]. The pulse raising time was $\approx$ 7 ms. The pulsed-field magnetization data were calibrated using static magnetic field magnetization data obtained by means of PPMS.

B.3 Experimental Results

B.3.1 Magnetization and Heat Capacity Above 1.8 K

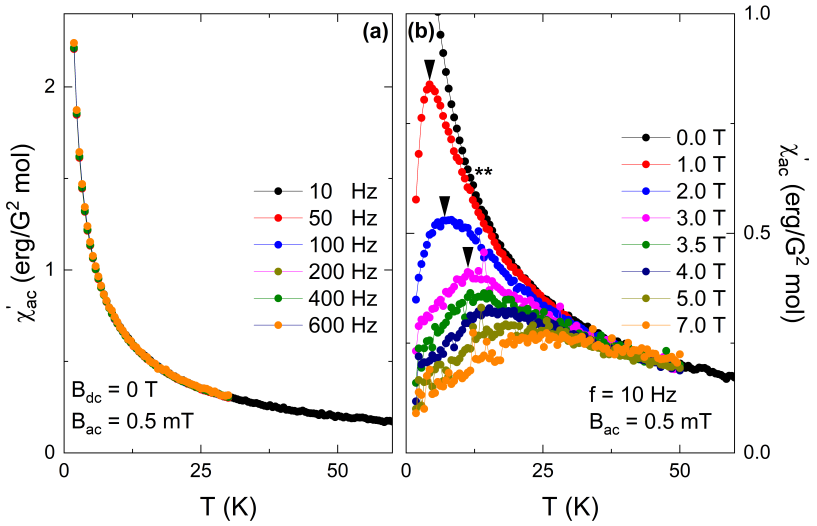

Figure B.1: Temperature dependence of the real part $\chi'_{\rm ac}$ of the AC magnetic susceptibility for $Ba_3ErB_9O_{18}$ polycrystalline sample: (a) $\chi'_{\rm ac}$ is obtained at $B_{\rm dc} = 0$ T, excitation filed $B_{\rm ac} = 0.5$ mT, and under different frequencies in the range 10 Hz $\leq f \leq$ 600 Hz, and (b) $\chi'_{\rm ac}$ is obtained at $f = 10$ Hz, excitation filed $B_{\rm ac} = 0.5$ mT, and under different DC magnetic fields in the range of 0 T $\leq B_{dc} \leq$ 7 T. The solid black triangles in (b) mark the evolution of the induced anomaly at $T = 4.2(2)$ K with increasing the field, and ** marks the onset temperature of the field dependence regime with respect to the zero field data.

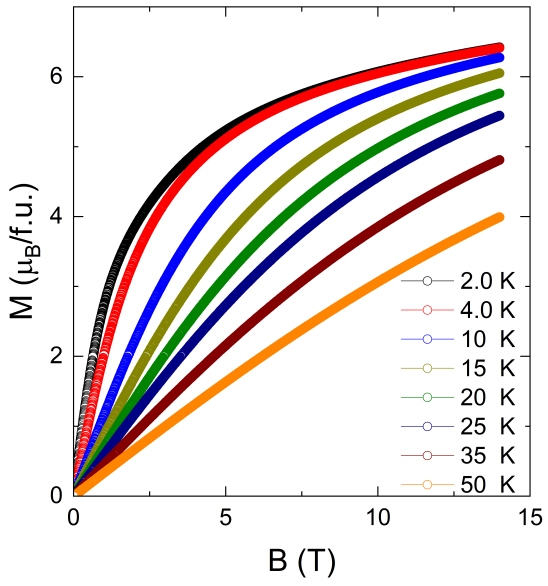

Figure B.2: $Ba_3ErB_9O_{18}$'s isotherm magnetization measured in an upsweep mode at different constant temperatures in the range 2 K $\leq T \leq$ 50 K.

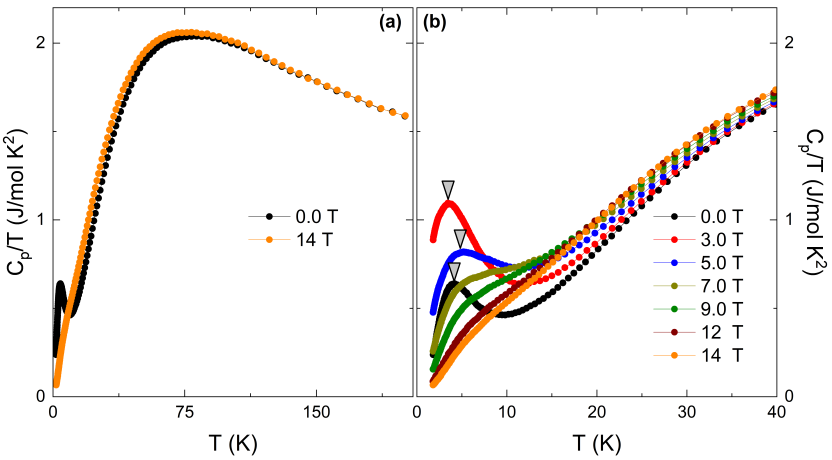

Figure B.3: Temperature dependence of $Ba_3ErB_9O_{18}$'s (c_p/T) measured: (a) at 0 T and 14 T over a wide temperature regime, and (b) at different magnetic fields in the range of $0 \leq B \leq 14$ T over a narrow temperature regime. The gray triangles in (b) mark the magnetic field effect on the Schottky-like anomaly.

B.3.2 Low Temperature DC Magnetization

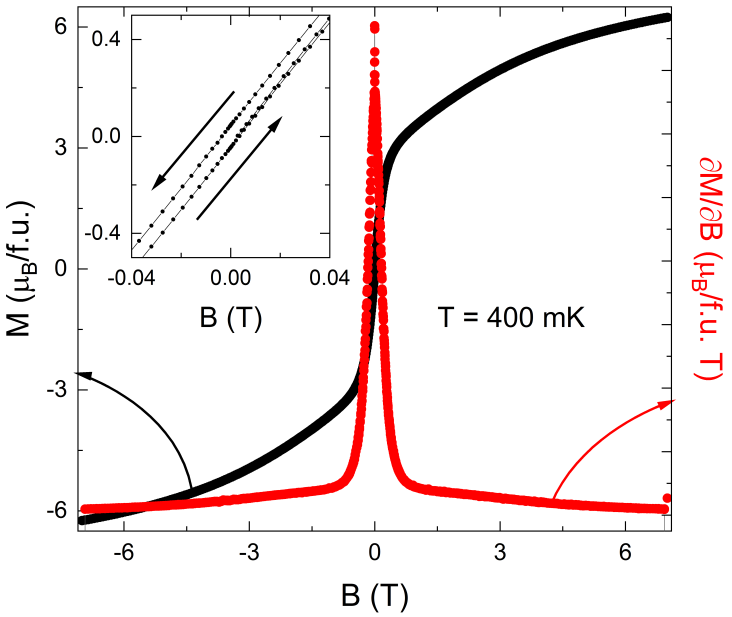

Figure B.4: Isothermal magnetization of $Ba_3ErB_9O_{18}$ at T = 400 mK, and its corresponding magnetic susceptibility $\partial M/\partial B$ are shown on the left and right axes, respectively. Inset: the magnetization behaviour in the vicinity of zero magnetic field.

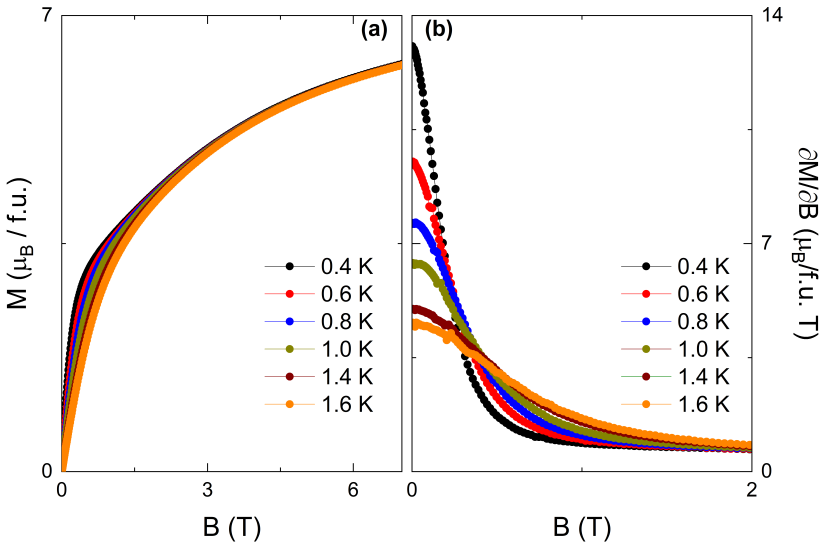

Figure B.5: (a) $Ba_3ErB_9O_{18}$'s magnetization (isotherm) obtained from an upsweep mode, and (b) its corresponding magnetic susceptibility $\partial M/\partial B$. The data were measured at different constant temperatures in the range 0.4 K $\leq T \leq$ 1.6 K.

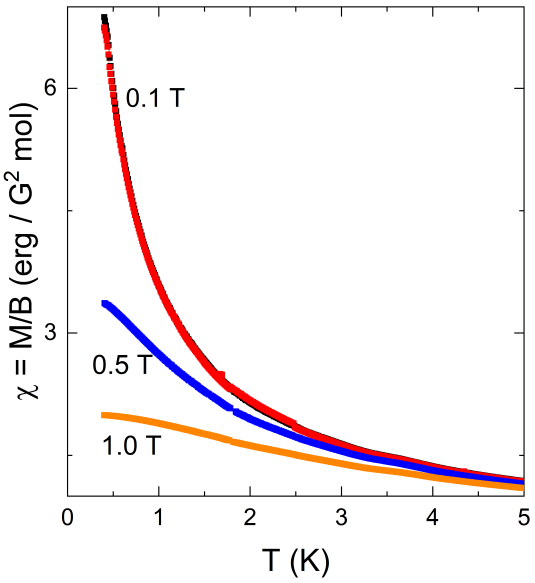

Figure B.6: Temperature dependence of $Ba_3ErB_9O_{18}$'s static magnetic susceptibility, $\chi = M/B$, measured at different magnetic fields in the range 0.1 T $\leq B \leq$ 3 T. Note, the red data at $B = 0.1$ T were obtained in a field-cooled (FC) mode.

B.3.3 Pulsed-Field Magnetization

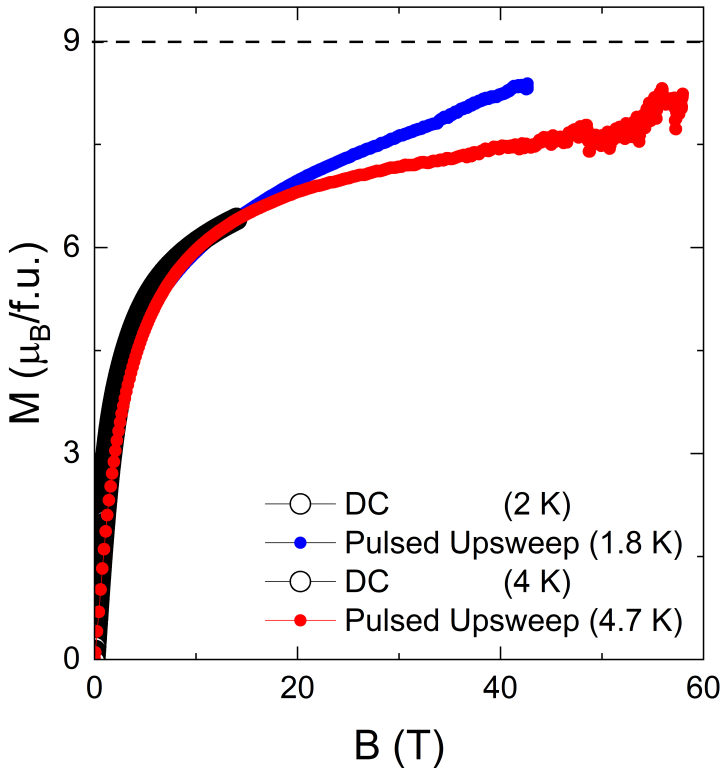

Figure B.7: Pulsed-field magnetization of $Ba_3ErB_9O_{18}$ measured at 1.8 K (blue), and at 4.7 K (red). The data were scaled to the quasi-static magnetization (black open circles) obtained by VSM measurements at 2 K and 4 K in fields up to 14 T. The horizontal dashed line marks the theoretical saturation magnetization (9 μ_B) expected for Er^{3+} free ions.

Appendix C

Heat Capacity of $GdInO_3$

This appendix presents specific heat data of $GdInO_3$, which is a geometrically frustrated magnet. All the data shown below are unpublished except, the specific heat data measured at $B = 0$ T, shown in Fig. C.3. These data are part of a recently submitted article to Physical Review B, and it is also available on arXiv under the title "1/3 plateau and 3/5 discontinuity in the magnetization and the magnetic phase diagram of hexagonal $GdInO_3$" [95].

C.1 Material Background

The single crystal used for the heat capacity studies was grown by Ning Yuan (KIP, Heidelberg University) using a high-pressure optical floating-zone furnace. A full description of the crystal growth recipe is available on arXiv [95].

C.2 Experimental Details

The specific heat capacity was measured using the heat capacity option of the Physical Properties Measurement System (PPMS). The measurements above 1.8 K and under different magnetic fields in the range 0 T $\leq B||c \leq$ 14 T were obtained using the standard heat capacity option on a single crystal sample with mass of 5.42 mg. For measurements below 1.8 K down to 50 mK, and in fields 0 T $\leq B||c \leq$ 7 T, the PPMS was equipped with the dilution refrigerator (DR) probe, and a single crystal sample with mass of 4.17 mg was used.

C.3 Experimental Results

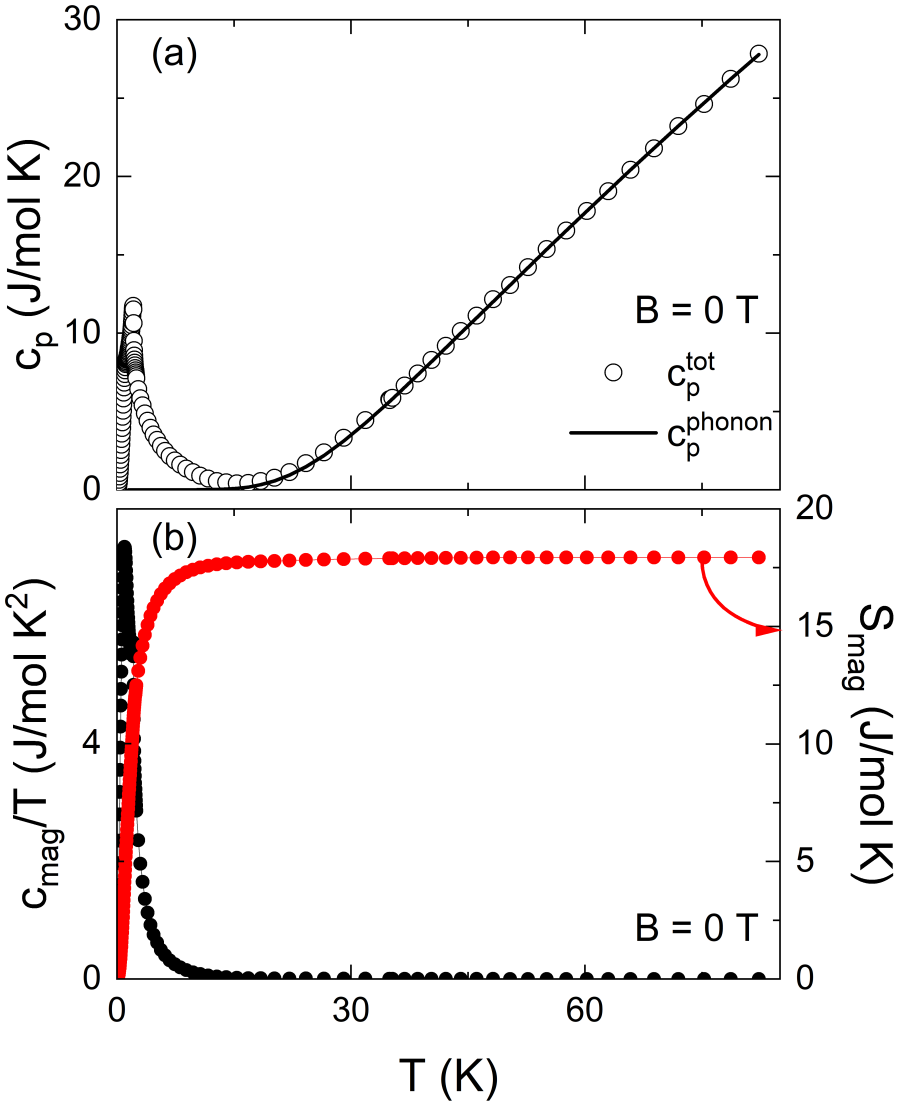

Figure C.1: Temperature dependence of (a) specific heat of $GdInO_3$ single crystal sample measured at $B = 0$ T, and the black line represents a phononic fit to the data based on 1 Debye and 1 Einstein mode according to Eq. 2.39, (b) $c_{\mathrm{p}}^{\mathrm{mag}}/T$, and the estimated magnetic entropy S_{mag} on the right-axis.

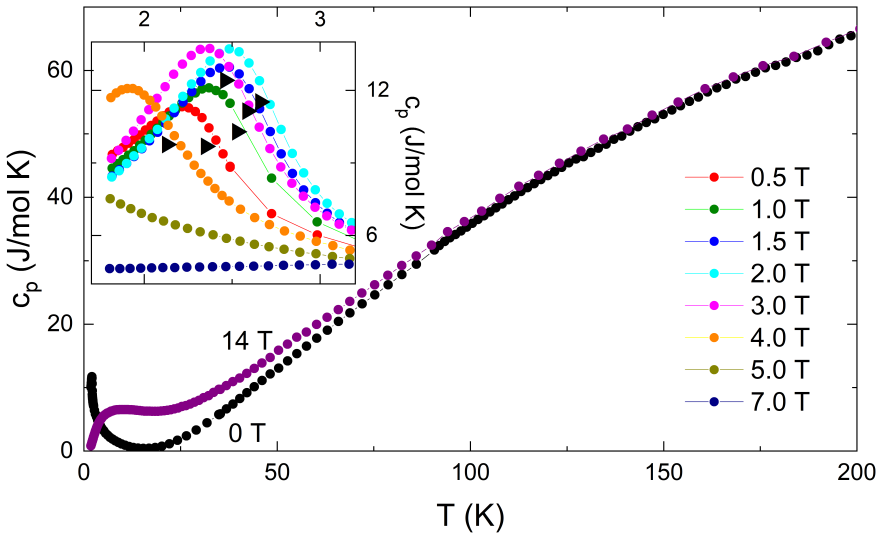

Figure C.2: Temperature dependence of $GdInO_3$'s c_p measured at 0 T and 14 T over a wide temperature regime. Inset: c_p measured at different magnetic fields in the range of $0.5 \leq B||c \leq 7$ T over a narrow temperature regime, and the black triangles mark the evolution of T_N in field.

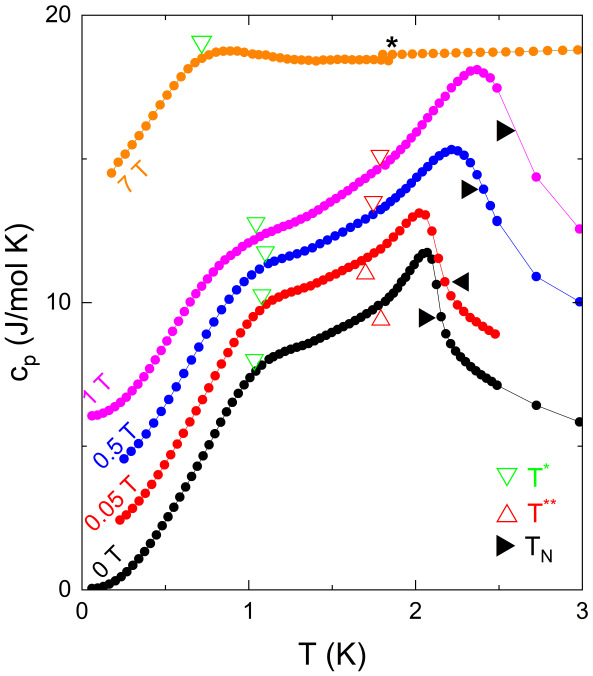

Figure C.3: Temperature dependence of $GdInO_3$'s c_p measured at temperatures below 3 K down to 50 mK, and different applied magnetic fields in the range $0 \leq B||c \leq 7$ T. The black, red, and green triangles mark the magnetic effect on the features at T_N, T^{**}, and T^*, respectively. The black asterisk refers to the data overlap arising from slight variations between the measurements taken at 7 T using the standard heat capacity option and those obtained using the dilution refrigerator.

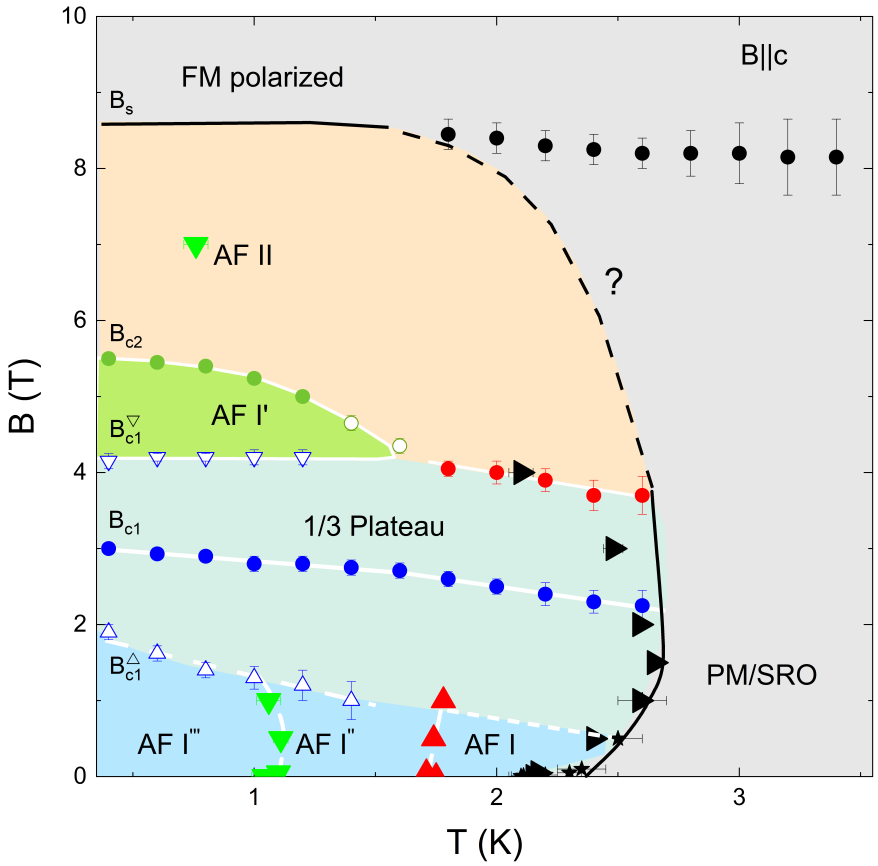

Figure C.4: Magnetic phase diagram of $GdInO_3$ for $B||c$, which is taken from [95]. The features appeared in heat capacity data at T_N, T^{**}, and T^* as shown in Figs. C.2, and C.3 are presented in the phase diagram as black, red, and green triangles, respectively.

Appendix D

Heat Capacity of $Sr_2Ni(SeO_3)_2Cl_2$

This appendix presents specific heat data of $Sr_2Ni(SeO_3)_2Cl_2$; a quasi-one-dimensional $S = 1$ magnet. This magnet represents a potential realization of the Haldane conjecture of a gapped spin liquid. All the data shown below are unpublished except, the specific heat data measured at $B = 0$ T, shown in Fig. D.1 (a) were included as a part of an open access article in Scientific Reports under the title "Quasi-1D XY antiferromagnet Sr2Ni(SeO3)2Cl2 at Sakai-Takahashi phase diagram $Sr_2Ni(SeO_3)_2Cl_2$" [96].

D.1 Material Background

The strontium nickel selenite chloride, $Sr_2Ni(SeO_3)_2Cl_2$, was obtained from $SrSeO_3$ and anhydrous $NiCl_2$ precursors [96, 97]. The crystal structure details found in [98]. Samples in the form of a powder were provided by A. N. Vasiliev, Low Temperature Physics and Superconductivity Department, Physics Faculty, M.V. Lomonosov Moscow State University, Moscow 119991, Russia.

D.2 Experimental Details

The specific heat capacity was measured using the standard heat capacity option of the Physical Properties Measurement System (PPMS). The measurements were performed over a wide temperature range from 1.8 K to 300 K, and under different magnetic fields in the range 0 T $\leq B \leq$ 14 T on a polycrystalline sample (pressed into a circular disc) with mass of 18.0 (1) mg.

D.3 Experimental Results

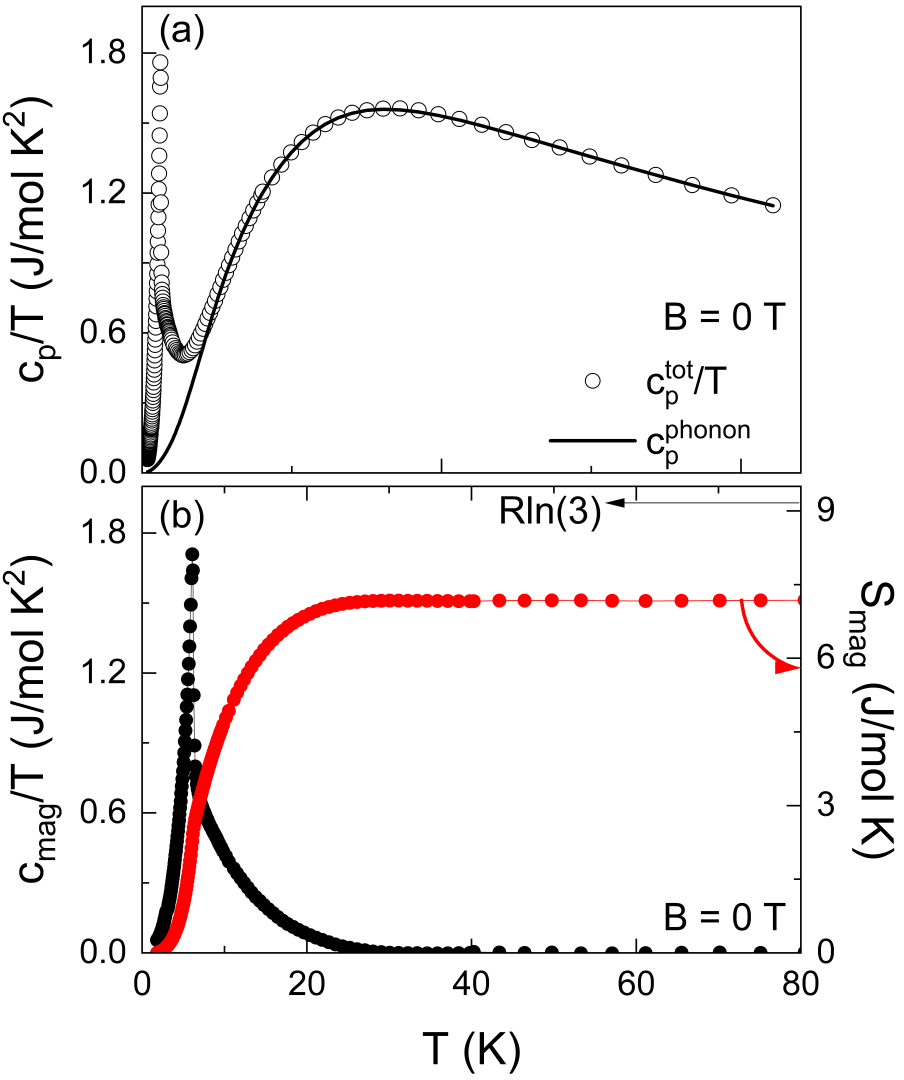

Figure D.1: Temperature dependence of (a) c_{p} $/T$ of $Sr_2Ni(SeO_3)_2Cl_2$ polycrystalline sample measured at $B = 0$ T, the black line represents a phononic fit to the data based on 1 Debye and 2 Einstein modes according to Eq. 2.39, and (b) $c_{\mathrm{p}}^{\mathrm{mag}}$ $/T$, and the estimated magnetic entropy S_{mag} on the left and right axes, respectively. The black arrow marks the expected magnetic entropy of $Rln(3)$ for $S = 1$ system.

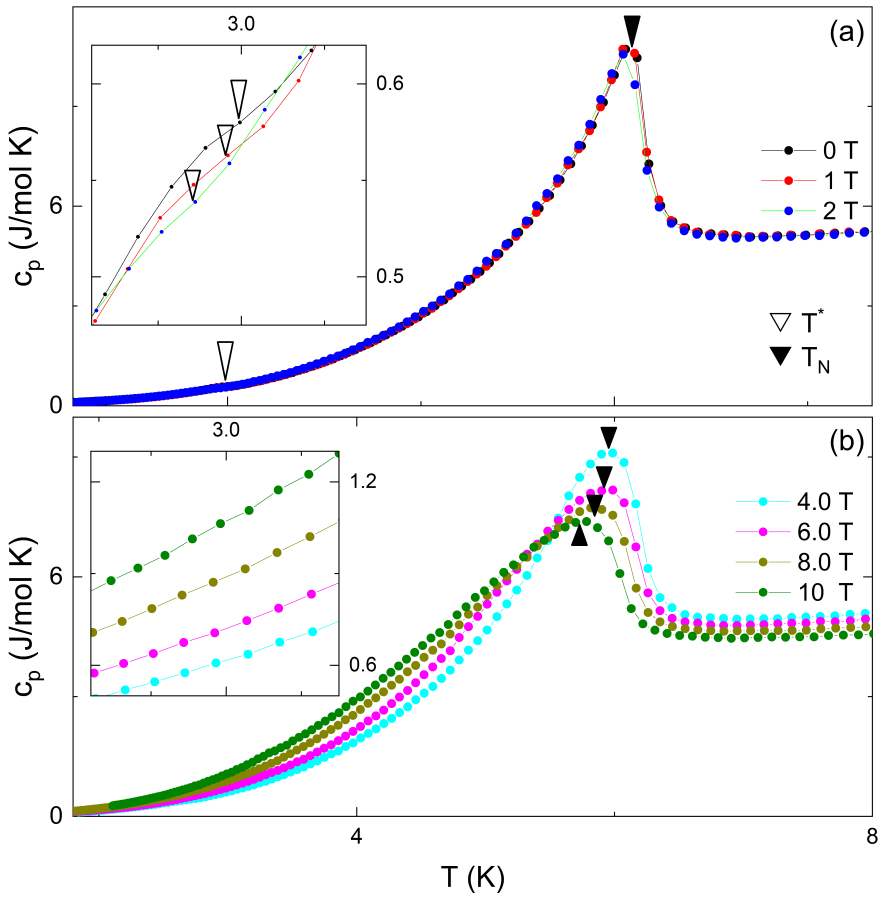

Figure D.2: Temperature dependence of $Sr_2Ni(SeO_3)_2Cl_2$'s c_p measured: (a) at $B \leq 2$ T; empty and filled black triangles mark the anomalies at T^* and T_N, respectively. (b) at higher fields in the range $4 \leq B \leq 10$ T filled black triangles mark the anomalies at T_N. Note, the change in the shape of the anomaly with increasing the field and its shift to lower temperatures. Inset: in (a) highlights the field effect on the anomaly at T^*, and in (b) emphasizes its disappearance at higher fields.

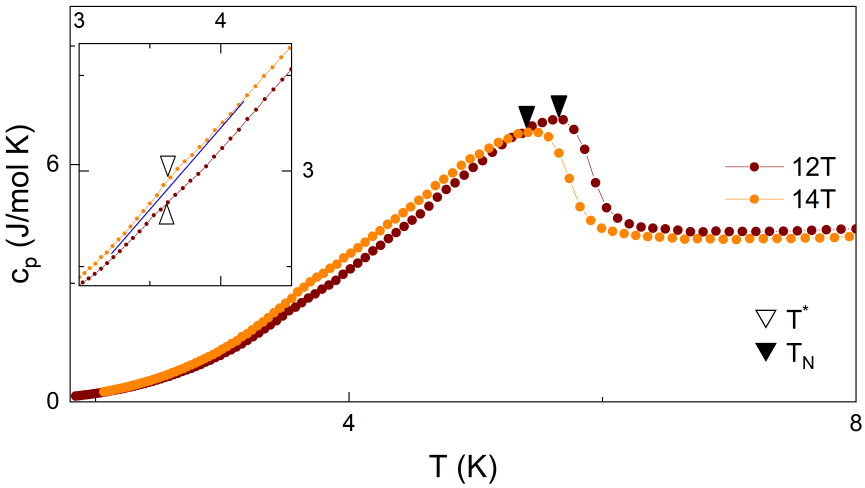

Figure D.3: Temperature dependence of $Sr_2Ni(SeO_3)_2Cl_2$'s c_p measured at 12 T and 14 T empty and filled black triangles mark the anomalies at T^* and T_N, respectively. Inset: highlights the reappearance of the T^* anomaly, and the blue line is a baseline guides the eye to estimate the height of the anomaly.

List of Publications

1. **A. Elghandour**, L. Gries, L. Singer, M. Hoffmann, S. Spachmann, M. Uhlarz, K. Dey, and R. Klingeler, Magnetic anisotropy, magnetoelastic coupling, and the magnetic phase diagram of in $Ni_{0.25}Mn_{0.75}TiO_3$, Phys. Rev. B 108, 014406, (2023).

2. Ning Yuan, **A. Elghandour**, W. Hergett, R. Ohlendorf, L. Gries, and R. Klingeler, 1/3 plateau and 3/5 discontinuity in the magnetization and the magnetic phase diagram of hexagonal $GdInO_3$, cond-mat arXiv:2308.04935, (2023).

3. L. Gries, M. Jonak, **A. Elghandour**, and R Klingeler, Role of magnetoelastic coupling and magnetic anisotropy in $MnTiO_3$, Phys. Rev. B 106, 174425, (2022).

4. J Khatua, M Pregelj, **A. Elghandour**, Z Jaglicic, R Klingeler, A Zorko, and P Khuntia,Magnetic properties of triangular lattice antiferromagnets $Ba_3RB_9O_18$ (R= Yb, Er) Phys. Rev. B 106, 104408, (2022).

5. Sheetal, **A. Elghandour**, R Klingeler, and C S Yadav, Field induced spin freezing and low temperature heat capacity of disordered pyrochlore oxide $Ho_2Zr_2O_7$, J. Phys.: Condens. Matter 34 245801, (2022).

6. S Spachmann, **A. Elghandour**, S Selter, B Büchner, S Aswartham, and R Klingeler, Strong effects of uniaxial pressure and short-range correlations in $Cr_2Ge_2Te_6$, Phys. Rev. Research 4, L022040, (2022).

7. S Spachmann, **A. Elghandour**, M. Frontzek, W. Löser, and R. Klingeler, Magnetoelastic coupling and phases in the skyrmion lattice magnet Gd_2PdSi_3 discovered by high-resolution dilatometry, Phys. Rev. B, 103, 184424 (2021).

8. ES Kozlyakova, AV Moskin, PS Berdonosov, VV Gapontsev, SV Streltsov, M Uhlarz, S Spachmann, **A. Elghandour**, R Klingeler, and AN Vasiliev, Quasi-1D XY antiferromagnet $Sr_2Ni(SeO_3)_2Cl_2$ at Sakai-Takahashi phase diagram, Scientific Reports, 11, 15002 (2021).

Bibliography

[1] P. Curie, "Propriétés magnétiques des corps à diverses températures [thesis presented to the faculty of sciences, university of paris, for the degree of docteur ès sciences physiques]", *Paris: Gautheir-Villars*, 1895.

[2] P. Weiss, "L'hypothèse du champ moléculaire et la propriété ferromagnétique", *J. Phys. Theor. Appl.*, vol. 6, no. 1, pp. 661–690, 1907.

[3] W. Gerlach and O. Stern, "Der experimentelle nachweis der richtungsquantelung im magnetfeld", *Zeitschrift für Physik*, vol. 9, no. 1, pp. 349–352, 1922.

[4] W. Heisenberg, "Zur theorie des ferromagnetismus", *Zeitschrift für Physik A Hadrons and Nuclei*, vol. 49, no. 9, pp. 619–636, 1928.

[5] L. Néel, "Propriétés magnétiques des ferrites; ferrimagnétisme et antiferromagnétisme", in *Annales de physique*, vol. 12, 1948, pp. 137–198.

[6] L. Néel, "Propriétés magnétiques de l'état métallique et énergie d'interaction entre atomes magnétiques", in *Annales de physique*, vol. 11, 1936, pp. 232–279.

[7] P. W. Anderson, "Antiferromagnetism. theory of superexchange interaction", *Physical Review*, vol. 79, no. 2, p. 350, 1950.

[8] J. G. Bednorz and K. A. Müller, "Possible high t c superconductivity in the ba- la- cu- o system", *Zeitschrift für Physik B Condensed Matter*, vol. 64, no. 2, pp. 189–193, 1986.

[9] S. Blundell, *Magnetism in condensed matter*. OUP Oxford, 2001.

[10] J. M. Coey, *Magnetism and magnetic materials*. Cambridge university press, 2010.

[11] S. H. Simon, *The Oxford solid state basics*. OUP Oxford, 2013.

[12] C. Lacroix, P. Mendels, and F. Mila, *Introduction to frustrated magnetism: materials, experiments, theory*. Springer Science & Business Media, 2011, vol. 164.

[13] A. Ramirez, "Strongly geometrically frustrated magnets", *Annual Review of Materials Science*, vol. 24, no. 1, pp. 453–480, 1994.

[14] A. Tari, *The specific heat of matter at low temperatures*. World Scientific, 2003.

[15] F. Pobell, *Matter and methods at low temperatures*. Springer Science & Business Media, 1996.

[16] E. Gopal, *Specific heats at low temperatures*. Springer Science & Business Media, 2012.

[17] C. Kittel and P. McEuen, *Introduction to solid state physics*. John Wiley & Sons, 2018.

[18] Q. Design, *Heat Capacity Option User's Manual*. 2017.

[19] R. Küchler, A. Wörl, P. Gegenwart, M. Berben, B. Bryant, and S. Wiedmann, "The world's smallest capacitive dilatometer, for high-resolution thermal expansion and magnetostriction in high magnetic fields", *Review of Scientific Instruments*, vol. 88, no. 8, 2017.

[20] J. Werner, W. Hergett, M. Gertig, J. Park, C. Koo, and R. Klingeler, "Anisotropy-governed competition of magnetic phases in the honeycomb quantum magnet na 3 ni 2 sbo 6 studied by dilatometry and high-frequency esr", *Physical Review B*, vol. 95, no. 21, p. 214 414, 2017.

[21] L. Gries, *Experimentelle untersuchung der ilmenit-titanate mntio3 und mn0.75ni0.25tio3 mittels hochauflosender kapazitatsdilatometrie*, 2021.

[22] Q. Design, *Magnetic Property Measurement System: SQUID VSM AC Option User's Manual*. 2010.

[23] Q. Design, *Vibrating Sample Magnetometer (VSM) Option User's Manual*. 2017.

[24] Q. Design, *Physical Property Measurement System: AC Measurement System (ACMS II) Option User's Manual*. 2017.

[25] Y. Skourski, M. Kuz'Min, K. Skokov, A. Andreev, and J. Wosnitza, "High-field magnetization of ho 2 fe 17", *Physical Review B*, vol. 83, no. 21, p. 214 420, 2011.

[26] A. Elghandour, L. Gries, L. Singer, M. Hoffmann, S. Spachmann, M. Uhlarz, K. Dey, and R. Klingeler, "Magnetic anisotropy, magnetoelastic coupling, and the magnetic phase diagram of ni 0.25 mn 0.75 tio 3", *Physical Review B*, vol. 108, no. 1, p. 014 406, 2023.

[27] Sheetal, A. Elghandour, R. Klingeler, and C. S. Yadav, "Field induced spin freezing and low temperature heat capacity of disordered pyrochlore oxide ho2zr2o7", *Journal of Physics: Condensed Matter*, vol. 34, no. 24, p. 245 801, Apr. 2022. DOI: 10.1088/1361-648X/ac5fd8. [Online]. Available: https://dx.doi.org/10.1088/1361-648X/ac5fd8.

[28] M. J. Harris, S. Bramwell, D. McMorrow, T. Zeiske, and K. Godfrey, "Geometrical frustration in the ferromagnetic pyrochlore ho 2 ti 2 o 7", *Physical Review Letters*, vol. 79, no. 13, p. 2554, 1997.

[29] A. P. Ramirez, A. Hayashi, R. J. Cava, R. Siddharthan, and B. Shastry, "Zero-point entropy in 'spin ice'", *Nature*, vol. 399, no. 6734, pp. 333–335, 1999.

[30] J. D. Bernal and R. H. Fowler, "A theory of water and ionic solution, with particular reference to hydrogen and hydroxyl ions", *The Journal of Chemical Physics*, vol. 1, no. 8, pp. 515–548, 1933.

[31] L. Pauling, *The nature of the chemical bond 301–304*, 1945.

[32] E. Reynolds, P. E. Blanchard, B. J. Kennedy, C. D. Ling, S. Liu, M. Avdeev, Z. Zhang, G. J. Cuello, A. Tadich, and L.-Y. Jang, "Anion disorder in lanthanoid zirconates gd2–x tb x zr2o7", *Inorganic Chemistry*, vol. 52, no. 15, pp. 8409–8415, 2013.

[33] B. C. den Hertog and M. J. Gingras, "Dipolar interactions and origin of spin ice in ising pyrochlore magnets", *Physical review letters*, vol. 84, no. 15, p. 3430, 2000.

[34] B. Gao, T. Chen, D. W. Tam, C.-L. Huang, K. Sasmal, D. T. Adroja, F. Ye, H. Cao, G. Sala, M. B. Stone, *et al.*, "Experimental signatures of a three-dimensional quantum spin liquid in effective spin-1/2 ce2zr2o7 pyrochlore", *Nature Physics*, vol. 15, no. 10, pp. 1052–1057, 2019.

[35] J. Gaudet, E. Smith, J. Dudemaine, J. Beare, C. Buhariwalla, N. Butch, M. Stone, A. Kolesnikov, G. Xu, D. Yahne, *et al.*, "Quantum spin ice dynamics in the dipole-octupole pyrochlore magnet ce 2 zr 2 o 7", *Physical review letters*, vol. 122, no. 18, p. 187 201, 2019.

[36] B. Gao, T. Chen, H. Yan, C. Duan, C.-L. Huang, X. P. Yao, F. Ye, C. Balz, J. R. Stewart, K. Nakajima, *et al.*, "Magnetic field effects in an octupolar quantum spin liquid candidate", *Physical Review B*, vol. 106, no. 9, p. 094 425, 2022.

[37] K. Kimura, S. Nakatsuji, J. Wen, C. Broholm, M. Stone, E. Nishibori, and H. Sawa, "Quantum fluctuations in spin-ice-like pr2zr2o7", *Nature communications*, vol. 4, no. 1, pp. 1–6, 2013.

[38] H. Blöte, R. Wielinga, and W. Huiskamp, "Heat-capacity measurements on rare-earth double oxides r2m2o7", *Physica*, vol. 43, no. 4, pp. 549–568, 1969.

[39] E. Lhotel, S. Petit, S. Guitteny, O. Florea, M. C. Hatnean, C. Colin, E. Ressouche, M. Lees, and G. Balakrishnan, "Fluctuations and all-in–all-out ordering in dipole-octupole nd 2 zr 2 o 7", *Physical Review Letters*, vol. 115, no. 19, p. 197 202, 2015.

[40] J. Xu, V. Anand, A. Bera, M. Frontzek, D. L. Abernathy, N. Casati, K. Siemensmeyer, and B. Lake, "Magnetic structure and crystal-field states of the pyrochlore antiferromagnet nd 2 zr 2 o 7", *Physical Review B*, vol. 92, no. 22, p. 224 430, 2015.

[41] J. Ramon, P. Silva, J. S. Gardner, and R. S. Freitas, "Glassy correlated state induced by disorder in the frustrated antiferromagnet tb2zr2o7", *Journal of Magnetism and Magnetic Materials*, vol. 565, p. 170 215, 2023.

[42] J. G. A. Ramon, C. Wang, L. Ishida, P. Bernardo, M. Leite, F. M. Vichi, J. Gardner, and R. Freitas, "Absence of spin-ice state in the disordered fluorite d y 2 z r 2 o 7", *Physical Review B*, vol. 99, no. 21, p. 214 442, 2019.

[43] J. G. A. Ramón, "Geometrically frustrated magnetism in the pyrochlore er2ti2-xsnxo7 and in the disordered fluorites r2zr2o7 (r= dy, ho, tb)", Ph.D. dissertation, Universidade de São Paulo, 2020.

[44] G. Ehlers, A. Cornelius, T. Fennell, M. Koza, S. Bramwell, and J. Gardner, "Evidence for two distinct spin relaxation mechanisms in 'hot'spin ice ho2ti2o7", *Journal of Physics: Condensed Matter*, vol. 16, no. 11, S635, 2004.

[45] J. Snyder, J. Slusky, R. Cava, and P. Schiffer, "How 'spin ice'freezes", *Nature*, vol. 413, no. 6851, pp. 48–51, 2001.

[46] H. Stanley, *Introduction to Phase Transitions and Critical Phenomena* (International series of monographs on physics). Oxford University Press, 1987, ISBN: 9780195053166. [Online]. Available: `https://books.google.de/books?id=C3BzcUxoaNkC`.

[47] D. Gatteschi, R. Sessoli, and J. Villain, *Molecular nanomagnets*. Oxford University Press on Demand, 2006, vol. 5.

[48] B. Ueland, G. Lau, R. Cava, J. O'Brien, and P. Schiffer, "Slow spin relaxation in a highly polarized cooperative paramagnet", *Physical review letters*, vol. 96, no. 2, p. 027 216, 2006.

[49] S. Nagata, P. Keesom, and H. Harrison, "Low-dc-field susceptibility of cu mn spin glass", *Physical Review B*, vol. 19, no. 3, p. 1633, 1979.

[50] O. Petrenko, M. R. Lees, and G. Balakrishnan, "Titanium pyrochlore magnets: How much can be learned from magnetization measurements?", *Journal of Physics: Condensed Matter*, vol. 23, no. 16, p. 164 218, 2011.

[51] K. Matsuhira, Y. Hinatsu, K. Tenya, and T. Sakakibara, "Low temperature magnetic properties of frustrated pyrochlore ferromagnets ho2sn2o7 and ho2ti2o7", *Journal of Physics: Condensed Matter*, vol. 12, no. 40, p. L649, 2000.

[52] J. Snyder, B. Ueland, J. Slusky, H. Karunadasa, R. Cava, and P. Schiffer, "Low-temperature spin freezing in the dy 2 ti 2 o 7 spin ice", *Physical Review B*, vol. 69, no. 6, p. 064 414, 2004.

[53] C. Krey, S. Legl, S. Dunsiger, M. Meven, J. Gardner, J. Roper, and C. Pfleiderer, "First order metamagnetic transition in ho 2 ti 2 o 7 observed by vibrating coil magnetometry at milli-kelvin temperatures", *Physical review letters*, vol. 108, no. 25, p. 257 204, 2012.

[54] S. Bramwell, M. Field, M. Harris, and I. Parkin, "Bulk magnetization of the heavy rare earth titanate pyrochlores-a series of model frustrated magnets", *Journal of Physics: Condensed Matter*, vol. 12, no. 4, p. 483, 2000.

[55] G. Ehlers, A. Cornelius, M. Orendac, M. Kajnakova, T. Fennell, S. Bramwell, and J. Gardner, "Dynamical crossover in 'hot'spin ice", *Journal of Physics: Condensed Matter*, vol. 15, no. 2, p. L9, 2002.

[56] M. Harris, S. Bramwell, P. Holdsworth, and J. Champion, "Liquid-gas critical behavior in a frustrated pyrochlore ferromagnet", *Physical review letters*, vol. 81, no. 20, p. 4496, 1998.

[57] A. Cornelius and J. Gardner, "Short-range magnetic interactions in the spin-ice compound ho 2 ti 2 o 7", *Physical Review B*, vol. 64, no. 6, p. 060 406, 2001.

[58] K. Matsuhira, Y. Hinatsu, and T. Sakakibara, "Novel dynamical magnetic properties in the spin ice compound dy2ti2o7", *Journal of Physics: Condensed Matter*, vol. 13, no. 31, p. L737, 2001.

[59] A. Ramirez *et al.*, "Handbook of magnetic materials", *Amsterdam: Elsevier Science*, vol. 13, p. 423, 2001.

[60] A. Ramirez, G. Espinosa, and A. Cooper, "Strong frustration and dilution-enhanced order in a quasi-2d spin glass", *Physical review letters*, vol. 64, no. 17, p. 2070, 1990.

[61] P. Schiffer and I. Daruka, "Two-population model for anomalous low-temperature magnetism in geometrically frustrated magnets", *Physical Review B*, vol. 56, no. 21, p. 13 712, 1997.

[62] A. Wills, "Long-range ordering and representational analysis of the jarosites", *Physical Review B*, vol. 63, no. 6, p. 064 430, 2001.

[63] C. Broholm, G. Aeppli, G. Espinosa, and A. Cooper, "Antiferromagnetic fluctuations and short-range order in a kagomé lattice", *Physical review letters*, vol. 65, no. 25, p. 3173, 1990.

[64] C. Waldtmann, H.-U. Everts, B. Bernu, C. Lhuillier, P. Sindzingre, P. Lecheminant, and L. Pierre, "First excitations of the spin 1/2 heisenberg antiferromagnet on the kagomé lattice", *The European Physical Journal B-Condensed Matter and Complex Systems*, vol. 2, no. 4, pp. 501–507, 1998.

[65] M. P. Shores, E. A. Nytko, B. M. Bartlett, and D. G. Nocera, "A structurally perfect s= 1/2 kagome antiferromagnet", *Journal of the american chemical society*, vol. 127, no. 39, pp. 13 462–13 463, 2005.

[66] J. Helton, K. Matan, M. Shores, E. Nytko, B. Bartlett, Y. Yoshida, Y. Takano, A. Suslov, Y. Qiu, J.-H. Chung, *et al.*, "Spin dynamics of the spin-1/2 kagome lattice antiferromagnet zncu 3 (oh) 6 cl 2", *Physical review letters*, vol. 98, no. 10, p. 107 204, 2007.

[67] T.-H. Han, J. S. Helton, S. Chu, D. G. Nocera, J. A. Rodriguez-Rivera, C. Broholm, and Y. S. Lee, "Fractionalized excitations in the spin-liquid state of a kagome-lattice antiferromagnet", *Nature*, vol. 492, no. 7429, pp. 406–410, 2012.

[68] T. Imai, M. Fu, T. Han, and Y. S. Lee, "Local spin susceptibility of the s= 1 2 kagome lattice in zncu 3 (od) 6 cl 2", *Physical Review B*, vol. 84, no. 2, p. 020 411, 2011.

[69] A. Wills, A. Harrison, S. Mentink, T. Mason, and Z. Tun, "Magnetic correlations in deuteronium jarosite, a model s= 5/2 kagomé antiferromagnet", *Europhysics Letters*, vol. 42, no. 3, p. 325, 1998.

[70] A. Ramirez, B. Hessen, and M. Winklemann, "Entropy balance and evidence for local spin singlets in a kagome-like magnet", *Physical review letters*, vol. 84, no. 13, p. 2957, 2000.

[71] H. Zhou, B. Vogt, J. Janik, Y.-J. Jo, L. Balicas, Y. Qiu, J. Copley, J. Gardner, and C. Wiebe, "Partial field-induced magnetic order in the spin-liquid kagomé nd 3 ga 5 sio 14", *Physical review letters*, vol. 99, no. 23, p. 236 401, 2007.

[72] L. Lumata, T. Besara, P. Kuhns, A. Reyes, H. Zhou, C. Wiebe, L. Balicas, Y. Jo, J. Brooks, Y. Takano, *et al.*, "Low-temperature spin dynamics in the kagome system pr 3 ga 5 sio 14", *Physical Review B*, vol. 81, no. 22, p. 224 416, 2010.

[73] H. Zhou, C. Wiebe, Y.-J. Jo, L. Balicas, R. Urbano, L. Lumata, J. Brooks, P. Kuhns, A. Reyes, Y. Qiu, *et al.*, "Chemical pressure induced spin freezing phase transition in kagome pr langasites", *Physical review letters*, vol. 102, no. 6, p. 067 203, 2009.

[74] V. Simonet, R. Ballou, J. Robert, B. Canals, F. Hippert, P. Bordet, P. Lejay, P. Fouquet, J. Ollivier, and D. Braithwaite, "Hidden magnetic frustration by quantum relaxation in anisotropic nd langasite", *Physical review letters*, vol. 100, no. 23, p. 237 204, 2008.

[75] M. Ashtar, J. Guo, Z. Wan, Y. Wang, G. Gong, Y. Liu, Y. Su, and Z. Tian, "A new family of disorder-free rare-earth-based kagome lattice magnets: Structure and magnetic characterizations of re3bwo9 (re= pr, nd, gd–ho) boratotungstates", *Inorganic Chemistry*, vol. 59, no. 8, pp. 5368–5376, 2020.

[76] Z. Yang, H. Zhang, M. Bai, W. Li, S. Huang, S. Ruan, and Y.-J. Zeng, "Large magnetocaloric effect in gadolinium borotungstate gd 3 bwo 9", *Journal of Materials Chemistry C*, vol. 8, no. 34, pp. 11 866–11 873, 2020.

[77] K. Zeng, F. Song, Z. Tian, Q. Chen, S. Wang, B. Liu, S. Li, L. Ling, W. Tong, L. Ma, *et al.*, "Local evidence for collective spin excitations in the distorted kagome antiferromagnet pr 3 bwo 9", *Physical Review B*, vol. 104, no. 15, p. 155 150, 2021.

[78] K.-Y. Zeng, F.-Y. Song, L.-S. Ling, W. Tong, S.-L. Li, Z.-M. Tian, L. Ma, and L. Pi, "Incommensurate magnetic order in sm3bwo9 with distorted kagome lattice", *Chinese Physics Letters*, vol. 39, no. 10, p. 107 501, 2022.

[79] D. Flavián, J. Nagl, S. Hayashida, M. Yan, O. Zaharko, T. Fennell, D. Khalyavin, Z. Yan, S. Gvasaliya, and A. Zheludev, "Magnetic phase diagram of the breathing-kagome antiferromagnet Nd_3BWO_9", *Phys. Rev. B*, vol. 107, p. 174 406, 17 May 2023. DOI: 10.1103/PhysRevB.107.174406. [Online]. Available: https://link.aps.org/doi/10.1103/PhysRevB.107.174406.

[80] M. E. Fisher, "Relation between the specific heat and susceptibility of an antiferromagnet", *Philosophical Magazine*, vol. 7, no. 82, pp. 1731–1743, 1962.

[81] S. Dutton, M. Kumar, M. Mourigal, Z. G. Soos, J.-J. Wen, C. L. Broholm, N. H. Andersen, Q. Huang, M. Zbiri, R. Toft-Petersen, *et al.*, "Quantum spin liquid in frustrated one-dimensional licusbo 4", *Physical review letters*, vol. 108, no. 18, p. 187 206, 2012.

[82] P. Schiffer, A. Ramirez, D. Huse, P. Gammel, U. Yaron, D. Bishop, and A. Valentino, "Frustration induced spin freezing in a site-ordered magnet: Gadolinium gallium garnet", *Physical review letters*, vol. 74, no. 12, p. 2379, 1995.

[83] C. Rüegg, K. Kiefer, B. Thielemann, D. McMorrow, V. Zapf, B. Normand, M. Zvonarev, P. Bouillot, C. Kollath, T. Giamarchi, *et al.*, "Thermodynamics of the spin luttinger liquid in a model ladder material", *Physical review letters*, vol. 101, no. 24, p. 247 202, 2008.

[84] D. Blosser, V. K. Bhartiya, D. Voneshen, and A. Zheludev, "Z= 2 quantum critical dynamics in a spin ladder", *Physical Review Letters*, vol. 121, no. 24, p. 247 201, 2018.

[85] M. Hoch, H. Zhou, E. Mun, and N. Harrison, "Pulsed field magnetization in rare-earth kagome systems", *Journal of Physics: Condensed Matter*, vol. 28, no. 4, p. 046 001, 2016.

[86] A. Scheie, M. Sanders, J. Krizan, A. D. Christianson, V. O. Garlea, R. J. Cava, and C. Broholm, "Crystal field levels and magnetic anisotropy in the kagome compounds nd 3 sb 3 mg 2 o 14, nd 3 sb 3 zn 2 o 14, and pr 3 sb 3 mg 2 o 14", *Physical Review B*, vol. 98, no. 13, p. 134 401, 2018.

[87] K. Zeng, L. Ma, Y. Gao, Z. Tian, L. Ling, and L. Pi, "Nmr study of the spin excitations in the frustrated antiferromagnet yb (babo 3) 3 with a triangular lattice", *Physical Review B*, vol. 102, no. 4, p. 045 149, 2020.

[88] M. B. Sanders, J. W. Krizan, and R. J. Cava, "Re3sb3zn2o14 (re= la, pr, nd, sm, eu, gd): A new family of pyrochlore derivatives with rare earth ions on a 2d kagome lattice", *Journal of Materials Chemistry C*, vol. 4, no. 3, pp. 541–550, 2016.

[89] M. B. Sanders, K. M. Baroudi, J. W. Krizan, O. A. Mukadam, and R. J. Cava, "Synthesis, crystal structure, and magnetic properties of novel 2d kagome materials re3sb3mg2o14 (re= la, pr, sm, eu, tb, ho): Comparison to re3sb3zn2o14 family", *physica status solidi (b)*, vol. 253, no. 10, pp. 2056–2065, 2016.

[90] R. Moessner, "Magnets with strong geometric frustration", *Canadian journal of physics*, vol. 79, no. 11-12, pp. 1283–1294, 2001.

[91] O. Volkova, V. Mazurenko, I. Solovyev, E. Deeva, I. Morozov, J.-Y. Lin, C. Wen, J. Chen, M. Abdel-Hafiez, and A. Vasiliev, "Noncollinear ferrimagnetic ground state in ni (no 3) 2", *Physical Review B*, vol. 90, no. 13, p. 134 407, 2014.

[92] E. B. Deeva, A. V. Merkulova, S. I. Troyanov, M. A. Zakharov, V. A. Tafeenko, V. F. Kozlovskii, and I. V. Morozov, "Nitrosonium nitratometallates no [m (no3) 3](m= co, ni): New synthetic approach and crystal structures", *Mendeleev Communications*, vol. 26, no. 5, pp. 421–422, 2016.

[93] I. Danilovich, E. Deeva, K. Bukhteev, A. Vorobyova, I. Morozov, O. Volkova, E. Zvereva, O. Maximova, I. Solovyev, S. Nikolaev, *et al.*, "Co (no 3) 2 as an inverted umbrella-type chiral noncoplanar ferrimagnet", *Physical Review B*, vol. 102, no. 9, p. 094 429, 2020.

[94] J. Khatua, M. Pregelj, A. Elghandour, Z. Jagličic, R. Klingeler, A. Zorko, and P. Khuntia, "Magnetic properties of the triangular-lattice antiferromagnets ba 3 r b 9 o 18 (r= yb, er)", *Physical Review B*, vol. 106, no. 10, p. 104 408, 2022.

[95] N. Yuan, A. Elghandour, W. Hergett, R. Ohlendorf, L. Gries, and R. Klingeler, "1/3 plateau and 3/5 discontinuity in the magnetization and the magnetic phase diagram of hexagonal gdino _3", *arXiv preprint arXiv:2308.04935*, 2023.

[96] E. Kozlyakova, A. Moskin, P. Berdonosov, V. Gapontsev, S. Streltsov, M. Uhlarz, S. Spachmann, A. ElGhandour, R. Klingeler, and A. Vasiliev, "Quasi-1d xy antiferromagnet sr2ni (seo3) 2cl2 at sakai-takahashi phase diagram", *Scientific Reports*, vol. 11, no. 1, p. 15 002, 2021.

[97] O. A. Dityatiev, P. Lightfoot, P. S. Berdonosov, and V. A. Dolgikh, "Srseo3 from a combined x-ray and neutron powder diffraction study", *Acta Crystallographica Section E: Structure Reports Online*, vol. 63, no. 6, pp. i149–i150, 2007.

[98] P. S. Berdonosov, A. V. Olenev, A. N. Kuznetsov, and V. A. Dolgikh, "A group of new selenite-chlorides of strontium and d-metals (co, ni): Synthesis, thermal behavior and crystal chemistry", *Journal of Solid State Chemistry*, vol. 182, no. 1, pp. 77–82, 2009.

Acknowledgements

Firstly, I would like to express my gratitude to my supervisor and mentor, Prof. Dr. Rüdiger Klingeler, for offering me the opportunity to join his group at the Kirchhof Institute for Physics at Heidelberg University. Our one-on-one discussions on the experimental data were invaluable and have greatly influenced my current mindset as a physicist. I deeply appreciate his patience, and support, as well as the trust he placed in me throughout my projects.

Secondly, I would like to extend my thanks to Prof. Dr. Maurits Haverkort for taking the responsibility as the second referee.

Completing a PhD in experimental physics is a challenge on its own, but in a foreign country with two children, a different language, and culture, it becomes even more demanding. I'm grateful to my caring wife, Fatma, who is the cornerstone of happiness in our small family. Her constant support, patience, and consideration played a crucial role in helping me finish this journey on time. Abdelrahman and Hanaa, I loved our daily tram rides to kindergarten, where your endless questions brought joy. Watching your mental development was a privilege, and you gave me the chance to relive the bedtime stories I missed as a child.

I'm thankful for my parents' support and proud of them. To my brothers Abdou and Mohammed, our daily chats, shared thoughts, and occasional online meetings brought happiness.

I would like to express my sincere gratitude to all members of the F25 group, both the current and former generations, with whom I had the privilege of sharing my academic journey. From the moment I joined, it felt like I had found a second home. In particular, I want to thank my officemate, Martin Jonak. Martin was not just a colleague but also a true and sincere friend who walked alongside me throughout my PhD journey, offering invaluable support. I extend my gratitude to Jan Arenth, whose companionship during conferences in Jordan and Regensburg added depth to our conversations, not to mention

the humor and laughter we shared. I'd like to acknowledge my colleague Kaustav Dey for growing high-quality single crystals and Lukas Gries for measuring thermal expansion, both playing vital roles in my research projects. Equally I thank Sven Spachmann for the collaboration and his sincere friendship. A special thanks to Lennart Singer for the enjoyable discussions we had during our lunchtime rambles. I would also like to thank Ning for her positive attitude. I want to say thanks to Timo, my officemate over the past few months. We worked together on heat capacity measurements. Our discussions were really helpful.

Special thanks to Rudolf Eitel for his essential work on helium liquefaction, which made my experiments possible. I'd also like to thank Natalia Tristan and her team at Quantum Design company for their assistance with technical issues in our PPMS, He-3, and Dilution refrigerators. I would like to express my gratitude to the individuals at HGSFP. I learned a lot during the graduate days and on Friday's Kolloquium. Your efforts are really appreciated. Thanks to Beatrice Schwoebel, the F25 group secretary, for her continuous support that made my life easier. I appreciate Ms. Koball from Die Continentale health insurance for her prompt payment reimbursements.

I'm grateful to my friends Amr, Emad, and Hesham, whose friendship and our online reading club have had a positive impact on my thinking. Lastly, I'd like to thank Mahmoud Abdelhafiez for his friendship and support.